PPPL- 5020

PPPL- 5020

Energetic Particle Physics In Fusion Research in Preparation For Burning Plasma Experiments

N.N. Gorelenkov, S.D. Pinches, K. Toi

APRIL, 2014

Prepared for the U.S. Department of Energy under Contract DE-AC02-09CH11466.

Princeton Plasma Physics Laboratory
Report Disclaimers

Full Legal Disclaimer

This report was prepared as an account of work sponsored by an agency of the United States Government. Neither the United States Government nor any agency thereof, nor any of their employees, nor any of their contractors, subcontractors or their employees, makes any warranty, express or implied, or assumes any legal liability or responsibility for the accuracy, completeness, or any third party's use or the results of such use of any information, apparatus, product, or process disclosed, or represents that its use would not infringe privately owned rights. Reference herein to any specific commercial product, process, or service by trade name, trademark, manufacturer, or otherwise, does not necessarily constitute or imply its endorsement, recommendation, or favoring by the United States Government or any agency thereof or its contractors or subcontractors. The views and opinions of authors expressed herein do not necessarily state or reflect those of the United States Government or any agency thereof.

Trademark Disclaimer

Reference herein to any specific commercial product, process, or service by trade name, trademark, manufacturer, or otherwise, does not necessarily constitute or imply its endorsement, recommendation, or favoring by the United States Government or any agency thereof or its contractors or subcontractors.

PPPL Report Availability

Princeton Plasma Physics Laboratory:

http://www.pppl.gov/techreports.cfm

Office of Scientific and Technical Information (OSTI):

http://www.osti.gov/bridge

Related Links:

U.S. Department of Energy

Office of Scientific and Technical Information

Fusion Links

Energetic particle physics in fusion research in preparation for burning plasma experiments

N.N.Gorelenkov[1], S.D. Pinches[2], K. Toi[3]
[1]Princeton Plasma Physics Laboratory, Princeton University, Princeton, New Jersey 08543, USA
[2]ITER Organization, Route de Vinon-sur-Verdon, 13115, St. Paul-lez-Durance, France
[3]National Institute for Fusion Science, Toki 509-5292, Japan

Abstract

The area of energetic particle (EP) physics of fusion research has been actively and extensively researched in recent decades. The progress achieved in advancing and understanding EP physics has been substantial since the last comprehensive review on this topic by W.W. Heidbrink and G.J. Sadler [1]. That review coincided with the start of deuterium-tritium (DT) experiments on Tokamak Fusion Test reactor (TFTR) and full scale fusion alphas physics studies.

Fusion research in recent years has been influenced by EP physics in many ways including the limitations imposed by the “sea” of Alfvén eigenmodes (AE) in particular by the toroidicity-induced AEs (TAE) modes and reversed shear Alfvén (RSAE). In present paper we attempt a broad review of EP physics progress in tokamaks and spherical tori since the first DT experiments on TFTR and JET (Joint European Torus) including helical/stellarator devices. Introductory discussions on basic ingredients of EP physics, i.e. particle orbits in STs, fundamental diagnostic techniques of EPs and instabilities, wave particle resonances and others are given to help understanding the advanced topics of EP physics. At the end we cover important and interesting physics issues toward the burning plasma experiments such as ITER (International Thermonuclear Experimental Reactor).

1. Introduction.

It seems timely to overview the area of energetic particle (EP) physics that is being developed as a constituent part of broader fusion research. We focus here on relatively recent studies in this area starting from the comprehensive review by W.W.Heidbrink and G.J.Sadler [1] to present days. It is remarkable that the time of that last review coincided with the start of tritium experiments on TFTR (Tokamak Fusion Test Reactor) where charged fusion products, α-particles, were studied for the first time on a full scale [2] [3]. Around that time experimental studies of toroidicity-induced Alfvén eigenmodes (TAEs), the key subject of EP research had begun [4] [5].

We organize this review in an introductory format across various EP physics problems. We review the selected problems in a way that introduces most important physic elements of the topic to be used by the experts in plasma physics and students studying fusion. EP physics development is often sufficiently complex and broad that it seems hard to encompass existing literature without the guidance of a review like ours. In many places we keep the introduction to the problems concise, but provide extensive references for further reading.

Where possible new or very recent developments are chosen in this review. However, since many of the pioneering EP studies were done on TFTR where a substantial focus was placed on Deuterium – Tritium (DT) products and fusion alphas, we therefore use them as examples for introductions to those areas. Alfvén eigenmode (AE) studies are very important for future burning experiments and are considered in details because of their link to the development of predictive modelling capabilities. In particular, work by the ITPA (International Tokamak Physics Activity) Topical Group on Energetic Particle Physics is described that covers the benchmarking and validation of various numerical models in Section 7.1.

Various review papers on several aspects of EP physics have been published over recent decades that cover many elements of EP physics in great detail [3] [6] [7] [8] [9] [10] [11] [12] [13][1]. They are natural extensions of earlier reviews [14] [15] [16] [17]. The progress in the EP area is so notable that it deserves such wide coverage from different authors (and different approaches) although we would recommend the present introductory review to be read first. We are trying to present this review using traditional EP physics topics. However, we cover them in a way that highlights new contributions or new diagnostic studies.

Energetic particles are common to tokamaks and stellarators/helical devices as all of them need to compensate the thermal plasma energy loss due to the transport and turbulence processes. Specific attention is devoted to 3D configurations with their peculiarities and similarities to tokamaks. This is in contrast to most of previous reviews that were written primarily for tokamaks. Normally the topics discussed are introduced for tokamaks first, and then, if appropriate, for stellarators/helical devices. Some topics such as drift particle motion and effects due to magnetic field ripple are common for both geometries.

The number of selected topics is inevitably limited as the field has grown wide, which is evidenced by the breadth of this review's citations. This does not make the present review sufficiently comprehensive. For introductory purposes we leave only those topics that seem to be more interesting, relevant to the subject or insufficiently covered by earlier review papers. Not all works on a given topic are reviewed equally, but only those which bring basic physics understanding of the problem. It should be noted that the topics chosen include issues identified in a recent topical review [11] (see Section 6 of that paper) as interesting for the future. We try to avoid repetitions with previous comprehensive or topical reviews. The criteria for choosing certain topics are dictated by the new specific diagnostics employed in the studies and/or newly developed theoretical techniques that show the subject in a novel and different aspect. Once the topic is identified we attempt to focus its presentation basing on the underlying physics and outline the outstanding issues if possible. The introductory style and finite length of this review mean that some of the topics presented cannot be covered to the depth required for a full understanding.

This review is organized according to the table of contents; going from single particle motion to their interactions with electromagnetic fields, to various collective effects and to the predictive models for burning plasmas (BP) and ITER in particular. Several sections devoted to burning plasmas appear at the end (section 7 contains examples of predictive studies for ITER). Since many existing works consider EP physics in ITER, and in particular the AE stability, whilst taking many different approaches, we attempt to introduce and summarize them in a systematic way in Secs.7.2 and 7.5. We do not cover one important topic, namely on runaway electrons. However the global mode excitation by suprathermal electrons is included within the context of wave-particle interactions.

For introductory purposes the following topics can be recommended: Alfvén eigenmodes (Sec. 4.2.2), EP and fluctuation diagnostic systems (Sec. 2), quasi-linear diffusion (Sec 5.2), drift integrals conservations (Sec. 3.1), resonance interaction between EPs and waves (Sec. 4.2.1), toroidal magnetic field ripple effect (sec. 3.2), and implications for burning plasmas (sec. 7).

The summary of the review lists some outstanding issues which we have identified for near and long-term future EP research. Additional areas for specific future research are indicated in the appropriate sub-sections.

Typical EP and plasma parameters are important to keep in mind when reading the whole review paper. Their relative position among the present day tokamaks, stellarators and TFTR, JET and a planned ITER tritium experiment is systematized in Section 4.2.6. In all these experiments the plasma and EPs have the following parameters: $T_{i,e} = 1 - 25\ keV$, $B = 0.1 - 10$ T, $a/R < 1$, $E_f = 0.03 - 10\ MeV$, $\beta_f < \beta_{pl} = 0.1 - 10\ \%$, $v_{Ti} \ll v_A \sim v_f \ll v_{Te}$.

---

[1] After the submission of our review we learned that another topical review on Alfvénic modes was published [13] with detailed studies of the problem ranging from ideal to kinetic approaches.

In this review, equations and figures are enumerated according to the section number to which they belong. For example, Eq. (4.1.1.2) is the second equation in Section 4.1.1 and likewise Fig. 5.5.1 is the first figure in Section 5.5. At the end of the review we include an appendix describing the used nomenclature.

2. Measurements of energetic particles and MHD fluctuations

Even though the major EP sources – neutral beam injection (NBI), ion cyclotron resonance heating (ICRH) and nuclear fusion have not evolved much in recent years our knowledge and understanding of the underlying physics has evolved through the use of new diagnostic techniques. This section aims at introducing fundamental experimental techniques on plasma diagnostics relevant for EP physics, instead of detailed and specific descriptions. In Sec. 2.1 powerful diagnostics for measuring confined and lost EPs are introduced. Fluctuation measurements of EP-driven global instabilities and the usual pressure and/or current driven magneto hydro dynamic (MHD) instabilities are also important to fully understand the interactions between EPs and these instabilities. Some newly developed diagnostic systems for the fluctuation measurements are introduced in 2.2.

2.1 Main diagnostics development for EP research

Direct measurement of EPs is essential for understanding the generation, confinement and loss of EPs. The principal diagnostics for EPs, briefly described in this section, are active and passive Neutral Particle Analyzer (NPA), neutron and gamma-ray spectroscopy, Fast Ion Dα diagnostic (FIDA)/FIDA imaging, collective Thomson scattering (CTS), and fast ion loss detector (FILD)/scintillator lost ion probe (SLIP). It is important to describe the physics of these diagnostics in order to understand their use and limitations.

2.1.1 Active and passive Neutral Particle Analyzer (NPA)

The use of the PCX diagnostic, which is one of the active NPAs and consists of a pellet injector and a neutral particle energy analyzer (NPA), is perhaps the most detailed way to directly measure the ICRH minority ion distribution function, because the neutralization of energetic fuel ions is considerably enhanced by the interaction with an ablation cloud of injected low Z impurities such as Li and C pellet [18]. As an example of the application of PCX we describe here H^+ minority (protons) distribution measurements [19]. Two characteristic features of the H^+ minority distribution function are worth highlighting here.

First is the pitch angle distribution. Theory predicts that the distribution is dominated by trapped particles with the bounce point at the ICRH resonance layer [20]. The width of the distribution in pitch angles corresponds to its radial localization and is determined by the heating scheme, scattering mechanisms and so on. The PCX diagnostic was able to measure this specific dependence, which is illustrated in figure 2.1.1.1. Here the active PCX signal is shown versus the pellet flight time for one of the NPA channels for neutrals leaving the plasma at energy $E_H = 0.72 MeV$. The signal corresponds to the density of ICRF-accelerated H^+ ions in the deuterium plasma. What is remarkable is that the characteristic width is very narrow and is comparable to the fast ion Larmor radius. This is in qualitative agreement with theoretical expectations [20] [21].

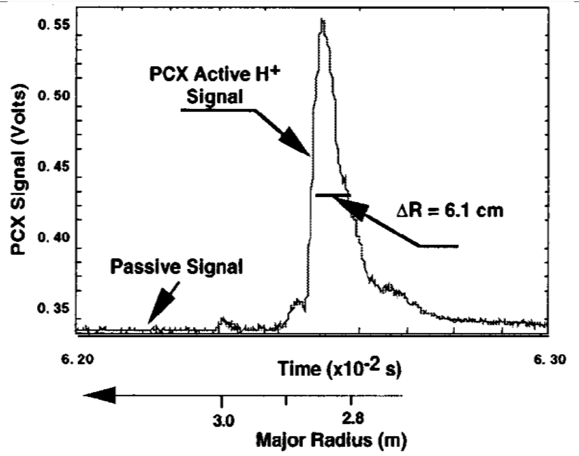

Fig.2.1.1.1 *PCX measured radial position and shape of the* H^+ *minority distribution during ICRH in TFTR deuterium plasma. The radial position of the pellet is derived from the measured pellet velocity. The figure is adopted from* [19].

The second feature of the H^+-minority distribution is its energy dependence, which is expected to be linear for the argument of the exponent according to [20]. It was measured by the PCX diagnostic in TFTR experiments before and after the sawtooth crash as illustrated in Fig. 2.1.1.2 [19]. The slope of the logarithm of the distribution function in energy is almost constant (or its energy dependence is almost exponential) and is reduced after the crash. This figure shows that the effective energy or temperature of H^+-minority ions is reduced by a sawtooth crash.

A passive NPA with the natural diamond detector (NDD) was also applied to the TFTR discharges using the charge exchange process between the H^+ and intrinsic impurity of a plasma C^{5+} [22] [23]. However, the signals were limited by poor statistics in those experiments. The spectrum obtained is nonetheless useful in one aspect since it allowed the so-called critical energy to be deduced, which is important in the theory of EP redistribution due to the sawtooth crash and will be considered in section 4.2.5.

ICRH modifies the EP motion since it is an effective scattering or velocity space diffusion operator pulling particles to higher perpendicular energy. ICRH competes with the collisional equilibration of the distribution function in both the perpendicular and parallel directions [21]. That is why the PCX diagnostic measurements of EPs at fixed λ are well suited for studies of energy dependence only.

The PCX has an advantage in extracting spatially resolved EP information in the plasma

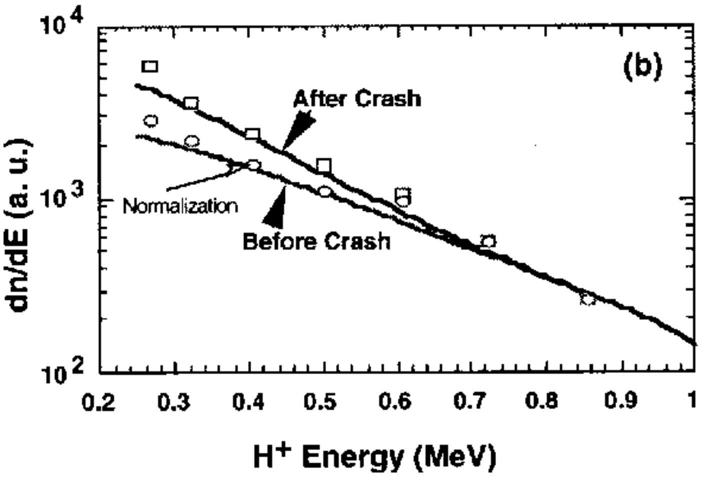

Fig. 2.1.1.2 *Minority ions energy spectra before and after the sawtooth crash versus*H^+ *energy as measured by PCX diagnostics on TFTR* [19].

core region. During PCX operation, the injected pellet does not disturb the target plasma considerably and reaches the required radial position in large hot plasmas. A passive NPA, where recently silicon-diodes or NDD are often used as the detectors, is still routinely employed in present-day fusion devices. In order to get information on the energetic ions in the MeV energy range, the charge exchange process between H+, D+ or T+ and hydrogen-like low Z impurity ions such as C^{5+} intrinsically existing in the plasma is employed instead of hydrogenic neutral beams because of their high neutralization cross-section in the MeV range [19]. This NPA is complementary to the active NPA, PCX. The distribution function of minority EPs generated by ICRH was measured by using the passive NPA approach in JET [24] and by a compact NPA (CNPA) using biased silicon-diode detectors in C-Mod [25].

2.1.2 Neutron diagnostics

For consistency of the presented material we show five fusion reactions of a DT plasma and the energy yields associated with them:

$$\begin{gathered} D+D\rightarrow He^3(0.82MeV)+n(2.45MeV)+3.27MeV \\ D+D\rightarrow T+p+4.03MeV \\ He^3+D\rightarrow He^4+p+18.3MeV \\ T+D\rightarrow He^4(3.5MeV)+n(14.1MeV)+17.6MeV \\ T+T\rightarrow He^4+2\mathrm{n}+11.3MeV \end{gathered} \tag{2.1.2.1}$$

The fourth of these reactions is that targeted by magnetic fusion research at the moment due to the accessibility of its conditions in the laboratory (accessible plasma temperatures $\sim 10keV$). It produces alpha particles and neutrons with the birth energies $E_\alpha = 3.52MeV$ and $E_n = 14.1MeV$ respectively. The other reactions are important for the diagnosis of neutral beams, thermal ions and the plasma itself. The first three reactions are employed to study EP physics in present-day fusion devices. The dominant reactions in a self-sustained reactor plasma will be between the plasma ions, whereas in present day toroidal devices beam-plasma reactions are dominant.

Neutron and gamma-ray cameras for 2D emission measurements provide the source profiles of fusion reaction or fusion products such as alpha particles. Neutron cameras are often employed in present day tokamaks because of their relatively simple but powerful capability to measure the neutron emission profile [26] [27]. In tokamak plasmas, neutron emission is dominated by beam-plasma reactions and the signals give information about the EP density. For example, it was successfully employed to study AE-induced EP transport on JT-60U [28]. Neutron emission is not constant on magnetic surfaces but is rather localized to the regions occupied by the EP orbits. On ITER a set of radial and vertical neutron cameras are planned to be installed to measure the 2D EP density profile [29].

Due to its high energy resolution and good statistics (high counting rate) neutron emission spectroscopy is a very powerful diagnostic for determining the velocity distribution of EPs and studying their interaction with MHD instabilities if the emission is high enough, as expected in ITER or with high harmonic ICRF heating. Various aspects of neutron diagnostics were extensively reviewed by Wolle in his review article [30]. Since the first D-T experiments on TFTR and JET, neutron spectroscopy has been further advanced using various approaches and developed towards application on ITER. Neutron spectroscopy has been attempted by the following three main techniques: the first is using NDD and was first applied in TFTR. The other two techniques which have been developed and progressed for the last decade on JET are the Time-Of-Flight Optimized for Rate (TOFOR) spectrometer [31] [32] and the (upgraded) Magnetic Proton Recoil (MPRu) spectrometer [33] [32].

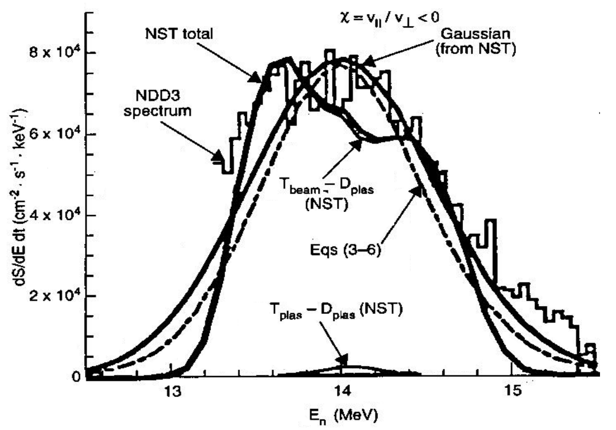

***Fig. 2.1.2.1** Neutron spectrum measured using a NDD in TFTR DT experiments and its comparison with modeling using the NST code and the approximate formula (2.1.2.2) as indicated* [22].

The study of the source spectrum by neutron spectroscopy using a NDD [34] was a unique and pioneering contribution of the DT experiments on TFTR [2]. One of the aspects not included in the review [30] was the energy distribution of the fusion source. This new development is covered here. Its determination is relatively simple and can be used to quantitatively evaluate beam characteristics using only NDD measurements. 14 MeV neutrons from DT fusion produce pulsed signal in the diamond through the ^{12}C(n, ^{4}He)^{9}Be reaction which has an energy threshold of 5.7 MeV [34]. NDDs have considerable potential for application to burning plasmas where diagnostics opportunities are limited. It can also be used as a diagnostic for lost alphas and to detect other escaping particles with sufficient energy. NDDs allow the study of the spectrum of 14 MeV neutrons produced in DT fusion reactions. Since such fusion produced neutrons have the same birth energy distribution as the fusion α-particles, the latter thus becomes directly measurable.

Due to the importance of neutron diagnostics in burning plasmas we here present the formulation behind the natural neutron source spectroscopy as an example of potential possibilities. It turns out that a semi-analytic expression can be used for the neutron source spectrum which is based on the formulation for thermal ions in the plasma [35]. The following expressions were approximated for balanced D and T beams injection. The source spectrum was expressed in the form:

$$f(E_n) = \frac{\exp[-(E_n - \langle E_n \rangle)^2 / 2\sigma_E^2]}{\sqrt{2\pi}\sigma_E}, \qquad (2.1.2.2)$$

where $E_n - \langle E_n \rangle = \mathit{\Delta} E_n = 180\sqrt{T_{eff}}$, T_{eff} is the effective “temperature” for beam injection into the plasma in keV and the definition of the angle brackets is given below. For beam-plasma interactions, the characteristic energy width is

$$\sigma_E^2 = \frac{4m_n\langle E_n \rangle}{m_n + m_\alpha} \frac{T_\parallel T_\perp}{[\sqrt{T_\parallel} + \chi^2(\sqrt{T_\perp} - \sqrt{T_\parallel})]^2}, \qquad (2.1.2.3)$$

where $T_\parallel \equiv T_{\parallel ij} = \frac{m_D T_{\parallel Di} + m_T T_{\parallel Tj}}{m_D + m_T}$, $\chi = v_\parallel / v$ and

$$T_{\parallel Di} = \langle E_{\parallel Di} \rangle,\ T_{\perp Di} = \langle E_{\perp Di} \rangle / 2,\ T_{\parallel Ti} = \langle E_{\parallel Ti} \rangle,\ T_{\perp Ti} = \langle E_{\perp Ti} \rangle / 2. \qquad (2.1.2.4)$$

The DT neutron average energy for such an anisotropic plasma also depends upon the neutron pitch angle χ relative to the equilibrium magnetic field at birth point:

$$\langle E_n \rangle = \frac{m_\alpha}{m_n + m_\alpha} Q + \frac{3}{2}\left(\frac{m_n}{m_n + m_\alpha} T_{eff} + \frac{m_\alpha}{m_n + m_\alpha} \frac{m_D T_T + m_T T_D}{m_n + m_\alpha}\right) + \\ + \frac{m_\alpha}{m_n + m_\alpha} \mathit{\Delta} E_\parallel + \sqrt{2} \frac{m_D \langle v_{\parallel Di} \rangle + m_T \langle v_{\parallel Tj} \rangle}{m_n + m_\alpha} \sqrt{\frac{m_n m_\alpha Q}{m_n + m_\alpha}} \chi, \qquad (2.1.2.5)$$

where $T_{D,T} = T_{\parallel D,T} + T_{\perp D,T}$, $\Delta E_{\parallel} \equiv \Delta \mathrm{E}_{\parallel ij} = \frac{(\langle v_{\parallel Di}\rangle - \langle v_{\parallel Tj}\rangle)^2 m_D m_T}{m_D + m_T}$, Q is the nuclear energy release of the reaction, and $\langle v_{\parallel Di}\rangle$ and $\langle v_{\parallel Tj}\rangle$ are averaged over the distribution function velocities of D and T ions. m_n, m_D, m_T, and m_α are the masses of neutron, D, T ions and α-particles, and i and j are the indexes of beams and plasmas correspondingly.

The application of the formula (2.1.2.2) to DT experiments is shown in Fig.2.1.2.1, which demonstrates that it was able to capture important measurable quantities such as the beam injection anisotropy and its radial profiles [22]. This is promising in its possible application to burning plasmas as can be seen from the figure, where the spectrum corresponds to the beam injection with only a weak contribution from plasma - plasma reactions. Detailed spectrum measurements with sufficient accuracy can serve as a diagnostic of the beam injection which is very valuable for reactor plasma conditions where the neutron flux will be strong and may affect the instruments.

The unique and powerful neutron diagnostics, TOFOR and MPRu neutron spectrometers have been developed and successfully applied to JET plasmas heated by NBI alone, by a combination of NBI and third harmonic ICRF heating, and also the most recent set of DT experiments. Here, only three typical results are introduced. In the TOFOR neutron spectrometer, the spectra are measured by recording the time delay of signals from two detectors for scattered neutrons [31] [32]. The TOFOR spectrometer is placed outside the concrete shielding in the roof of the JET torus hall and views the JET plasma through collimators. The first detector placed at the bottom of the system consists of a 5-element detector whilst the second has a ring shape with 32 detectors equally arranged in the azimuthal direction. Figure 2.1.2.2 (left) shows the TOFOR data (counts) shown as a function of the time delay t_{TOF} between the two detectors from a JET plasma heated by 4 MW of 3rd harmonic deuterium heating to accelerate ~100 keV deuterium ions from the NBI system [36]. The distribution function of deuterium ions inferred from the TOFOR data is shown in the right figure. The energetic ion tail clearly extends up to the cut-off energy of 3.1 MeV predicted from the RF heating theory. The MPRu spectrometer shows that a fraction of the neutrons (10^{-4}) is converted to a flux of proton recoils of (nearly) the same energy distribution apart from a broadening, which reflects the finite instrumental energy resolution. The energy of the protons is analyzed by a momentum-dispersing magnet, which provides a recoil spectrum expressed as a function of the detector position. That is, the MPRu is a kind of high accuracy magnetic spectrometer. Figure 2.1.2.3 shows an example of the MPR spectrum for 14 MeV neutron emission in the DT plasma that achieved the record fusion energy (21.7 MJ) [32]. The MPR spectrum can be fitted very well with the thermal reaction component (TH), two supra-thermal (epithermal (ET) and high-energy (HE)) components and a component scattered from the wall and structural materials (SC).

In the first D-T plasmas on JET, a signature of suprathermal fuel ions generated by elastic collisions between fast alpha particles and D/T ions was first detected in neutron emission spectra obtained by MPR spectrometer [37]. This alpha knock neutron emission provides important information of energetic alpha source function in burning plasmas.

Moreover, in the JET shot with the high neutron rates [38], the counting rate of the TOFOR spectrometer was such that the time evolution of the energetic ion fluxes could be obtained with a time resolution of around 50 ms. In the phase of the shot where TAEs and tornado modes were simultaneously destabilized, the time behaviors of the two high energy TOFOR signals indicated the redistribution of energetic deuteron ions due to this Alfven eigenmode activities. In ITER, neutron spectrometers with a high time resolution should allow the determination of the temporal evolution of the energetic ion distribution function and be a powerful aid to studying the effects of MHD modes on energetic particles.

Neutron spectroscopy based on NDD, TORFOR and MPRu spectrometers is a very powerful tool for studying burning plasma experiments such as ITER, where very high neutron emission rates are expected. Note that the TOFOR and MPRu spectrometers can also be applied to the measurements of DD neutrons as well as DT neutrons.

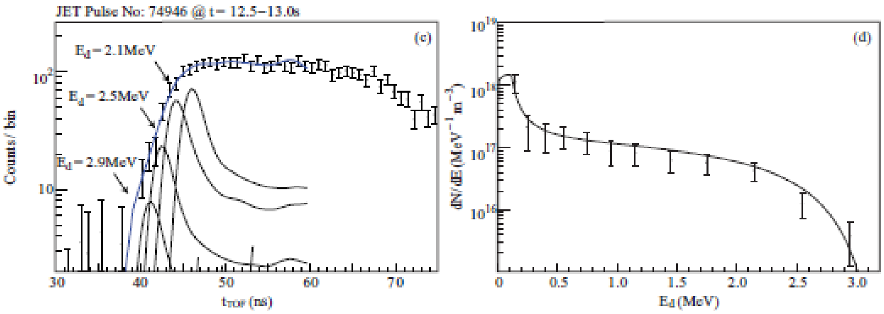

Fig.2.1.2.2 *(left) TOFOR data of JET deuterium plasma with NBI and 3rd ICRF heating, (right)* [36]. *Deuterium ion distribution function inferred from TOFOR data. Note the clear energetic ion tail extending up to the expected cut-off energy of 3.1 MeV.*

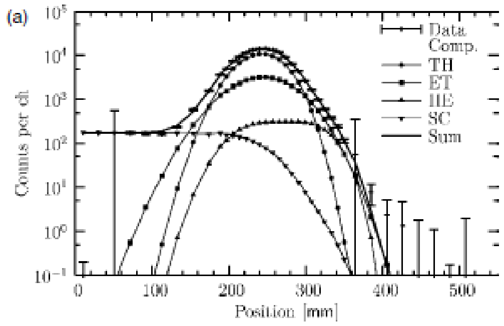

Fig.2.1.2.3 *Example of MPR spectrum for 14 MeV neutron emission from a JET DT plasma* [32].

2.1.3 Gamma-ray spectroscopy and its 2D imaging

Gamma ray spectroscopy is also a very powerful tool to obtain information about the fusion reaction source and fusion products in addition to the neutron spectroscopy discussed above. γ–rays are born in nuclear reactions between fast ions and impurities in the main plasma and/or the plasma fuel ions. As pointed out above (see Sec. 2.1.2) there are three sources of EPs in fusion plasmas. First, fusion products such as fast tritons, protons, ^{3}He- and ^{4}He-ions with energies in the MeV range. Second, the H- and ^{3}He-minority ions accelerated to the MeV energy range by higher harmonic ICRF waves. Other fuel ions such as D, T and ^{4}He can also be accelerated by ICRH scenarios. Third, NBI heating introduces D, H, T, ^{4}He or ^{3}He ions with energies below or around 1 MeV. Here we review this diagnostic technique using nuclear reaction rates and nuclear reaction product densities at high temperatures [39].

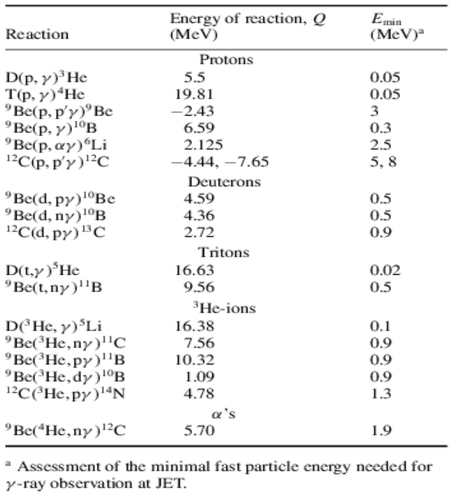

Reaction	Energy of reaction, Q (MeV)	$E_{\min}$ (MeV)[a]
	Protons	
$D(p,\gamma)^3He$	5.5	0.05
$T(p,\gamma)^4He$	19.81	0.05
$^9Be(p,p'\gamma)^9Be$	−2.43	3
$^9Be(p,\gamma)^{10}B$	6.59	0.3
$^9Be(p,\alpha\gamma)^6Li$	2.125	2.5
$^{12}C(p,p'\gamma)^{12}C$	−4.44, −7.65	5, 8
	Deuterons	
$^9Be(d,p\gamma)^{10}Be$	4.59	0.5
$^9Be(d,n\gamma)^{10}B$	4.36	0.5
$^{12}C(d,p\gamma)^{13}C$	2.72	0.9
	Tritons	
$D(t,\gamma)^5He$	16.63	0.02
$^9Be(t,n\gamma)^{11}B$	9.56	0.5
	^{3}He-ions	
$D(^3He,\gamma)^5Li$	16.38	0.1
$^9Be(^3He,n\gamma)^{11}C$	7.56	0.9
$^9Be(^3He,p\gamma)^{11}B$	10.32	0.9
$^9Be(^3He,d\gamma)^{10}B$	1.09	0.9
$^{12}C(^3He,p\gamma)^{14}N$	4.78	1.3
	α's	
$^9Be(^4He,n\gamma)^{12}C$	5.70	1.9

[a] Assessment of the minimal fast particle energy needed for γ-ray observation at JET.

Table 1 *γ-ray spectrum obtained during NBI heated deuterium plasma on JET, where 2.5 MA plasma current, 2.4 T toroidal magnetic field and 17.8 MW injection were applied* [41].

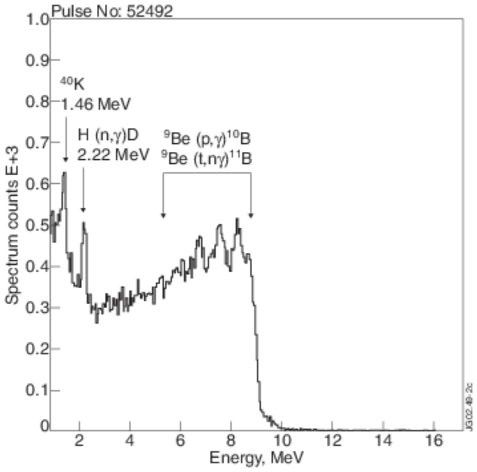

Fig. 2.1.3.1. *γ–ray spectrum obtained during NBI heated deuterium plasma on JET, where 2.5 MA plasma current, 2.4 T toroidal field and 17.8 MW injection were applied* [41].

The contributions from thermal ions heated by NBI and beam-beam reactions to the overall γ–ray production are small, but beam-plasma reactions are important for the γ–ray emission. Nuclear reactions of fast ions with fuel ions and low Z impurities such as C and Be produce γ–ray line spectra. This was proposed as a promising technique for studying EPs in fusion devices in this reference [40]. Neutrons generated by the fusion reactions, Eq. (2.1.2.1), give rise to a continuous γ–ray background through their interactions with the structural materials of the torus. Table 1 lists the nuclear reactions identified by γ-ray spectra in NBI/ICRH JET plasmas [41]. A typical γ–ray spectrum obtained in a JET plasma heated by NBI alone is shown in Fig. 2.1.3.1. This consists of four components: The line at 1.46 MeV is due to the radioactive decay of ^{40}K and is part of the natural background. The continuum background up to 10 MeV arises from the reaction of neutrons with the structural material of the torus. The neutron capture γ–line at 2.22 MeV is produced by the H(n,γ)D reaction in the polythene plug in the collimator. Several of the lines from 5 MeV to 9 MeV are generated by nuclear reactions between fusion products (proton and triton) and Be which is the main low Z impurity in JET plasmas. The excitation function of the reactions in Table 1 is well established and exhibits a threshold and/or a resonant nature. This allows a quantitative comparison between measured spectra and numerical modeling based on the well-established reaction data and enables the identification of the different fast ion species present and an assessment of their effective temperatures and relative concentrations if the Be ion density profile is known by spectroscopic method such as charge exchange spectroscopy. The reaction identified in ICRH heated JET plasmas $^9Be(\alpha,n\gamma)^{12}C$ (i.e., $^9Be(^4He,n\gamma)^{12}C$ in Tab.2.1.3.1) is induced by energetic alpha particles and is very important for the measurement of fusion-born alpha particles [42]. This is a resonant reaction with a threshold. The γ–rays generated by nuclear reactions between fusion-born alpha particles and Be impurities was first observed in JET D-T experiments [43]. In addition to the gamma-ray spectroscopy, a 2D imaging measurement of γ–rays was successfully performed in ICRH heated JET plasmas [41] [44]. High-resolution γ–ray spectrometry measurements of nuclear reactions between energetic D, ^{3}He and ^{4}He and main plasma impurities such as C and Be enabled the effective tail temperature of the energetic ions to be accurately derived through the detailed analysis of the gamma ray emission intensities and the spectral shapes [45] [46]. This technique is expected to be powerful for understanding and controlling burning plasma experiments such as those in ITER.

In addition, absolutely calibrated ^{235}U fission chambers have been successfully used to monitor the production of protons in the MeV energy range by ICRF heating on JT-60U, complementing the measurements of the time-resolved gamma-ray spectra with a NaI(Tl) scintillator [47]. These techniques are conventional but can still be applied to current fusion devices as well as ITER. Figure 2.1.3.2 shows the time evolution of the neutron yield and 2.1 MeV and 4.4 MeV gamma ray lines produced by nuclear reactions between MeV range energetic protons and the elements of the boron-carbide tiles (boron and carbon) $^{11}B(p,p'\gamma)^{11}B$ and $^{12}C(p,p'\gamma)^{12}C$, respectively. These reactions have thresholds in the proton energies of 2.5MeV and 5.0 MeV, respectively. These neutron and gamma-ray emission signals become good monitors of the energetic ion loss to the wall. Since these nuclear reactions have a threshold in energy, the signals also provide the minimum energy of the lost energetic ions.

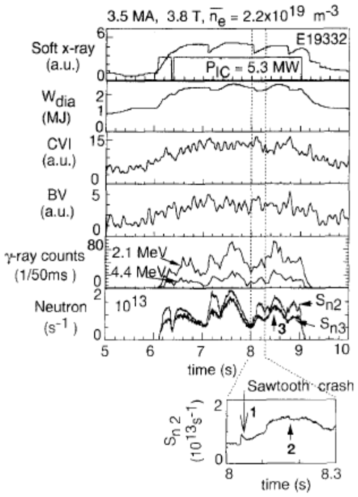

Fig.2.1.3.2 *Time evolution of 2.1 MeV and 4.4 MeV gamma ray emission lines and neutron yield in giant sawtoothing plasma heated by ICRF heating on JT-60U* [47].

2.1.4 Fast Ion D_α measurement

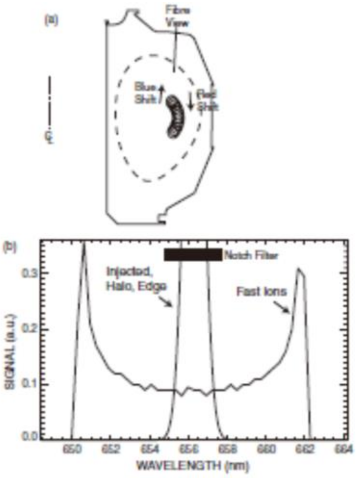

Fig. 2.1.4.1 *(a) Cross section of DIII-D tokamak and the projection of a fast ion orbit. The fast ion orbit emits red-shifted and blue shifted emission due to the gyro-motions. (b) Emission spectrum produced by mono-energetic 80 keV deuterons. The figure is adopted from* [49].

Fast ion D_α diagnostics (FIDA) work in a similar way as charge exchange recombination spectroscopy (detailed review paper on FIDA is available [48]). The n=3 to n=2 transition (λ_{D_α}=656.1 nm) of the Balmer-alpha line is used in FIDA because of the easy detection of visible light. However, the FIDA emission generated by charge exchange between fast ions and injected neutral beams is relatively easily contaminated by other bright emissions such as those caused by relatively cold neutrals in the plasma edge, warm halo neutrals produced by charge exchange between injected neutral beams and bulk deuterium ions, bremsstrahlung and various impurity line emissions. These bright emissions are shifted away from the FIDA emission by selecting appropriate viewing geometries. In addition, low density ($< 10^{20} m^{-3}$) and lowZ_{eff} plasmas are preferred to minimize background emission due to Bremsstrahlung and impurity radiations.

A two-channel FIDA system with a vertical view of the D_α emission was first developed in DIII-D (Doublet III D) [49]. In the vertical view of the beam, no Doppler shift of D_α is generated and the red- and blue-shifted emissions arise from the gyro-motion of fast ions, as shown in Fig. 2.1.4.1. The background due to bremsstrahlung and impurity line emissions can be subtracted by employing a beam modulation technique. The one-dimensional multichannel system was recently employed in DIII-D for a confinement study of fast ions produced by various NBI heating scenarios: co/counter tangential and co/counter perpendicular injections [50].

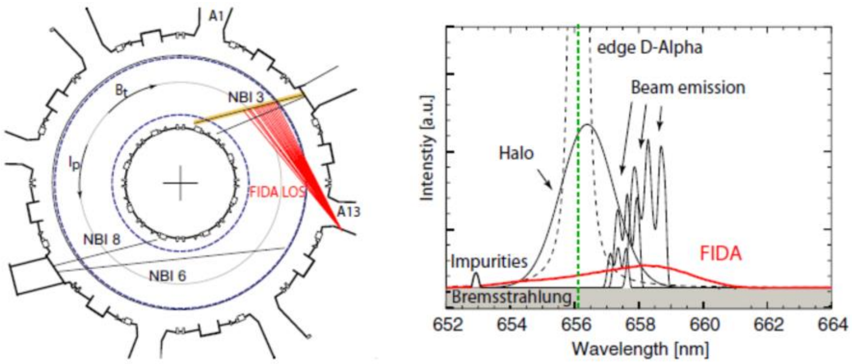

Fig.2.1.4.2 *FIDA viewing geometry in AUG and accompanying simulatedFIDA emission and other signals coming from the plasma edge: halo and impurity ions, and beam emission splitting* [51].

Another possible viewing is toroidal, nearly tangential to the magnetic surfaces on the outboard side as adopted in AUG (ASDEX Upgrade - Axially Symmetric Divertor Experiment

Upgrade) [51]. The geometry and a simulated emission profile in the D_α wavelength range are shown in Fig. 2.1.4.2. With this viewng geometry, the right wing of the spectrum is dominated by the FIDA emission. In AUG, the background emission is subtracted by a flat offset model in low density, low Z_{eff} plasmas without the need for beam modulation enabling the time evolution of the fast ion radial profile to be obtained. Toroidal (or tangential) viewing geometry can be extended to 2D imaging of FIDA emission (as discussed in Sec. 2.1.5) [50].

A dual viewing FIDA system has also been installed to measure radially resolved information about the fast ion density and its distribution in energy and pitch angle in MAST (Mega Amp Spherical Tokamak) . Both toroidally and vertically-directed collection lenses are employed to detect both passing and trapped particle dynamics, with reference views used to subtract the background [52]. Dedicated experiments on MAST have quantified significant changes in the fast ion distribution associated with the presence of internal n = 1 chirping modes (so-called fishbones). The FIDA system sees a depletion of fast ions in the core associated with the fishbone activity [53] [54].

The relationship between the measured FIDA spectra and fast ion distribution function is complicated by the energy dependence of the charge exchange cross section. An ideal way is to use an algorithm that would relate the measured spectrum shape $dI/d\,\lambda$ with the desired fast ion distribution function, $f_f(E,\chi)$. The signal intensity is not linearly proportional because the neutralization rate is a strong function of the relative energy between the fast ions and injected neutrals, having a peak at $\sim 27\ keV/amu$ [49]. This leads to complexity in the analysis. The FIDA technique can also be applied to measure fast ions produced by ICRH and fusion reactions using neutral beam injection as the fast neutral source and where an appropriate injection angle is chosen so that the neutralization rate is maximized [49]. Fast ion confinement studies based on the FIDA diagnostic in DIII-D and AUG have shown that EP confinement is classical in a quiescent plasma without any Alfvénic instabilities, as discussed in Sec.3. A FIDA system called FICXS has also been developed for the stellarator/helical device LHD (Large Helical Device) [55]. The effects of AEs on EP confinement are discussed in Secs.4 and 5.

2.1.5 NBI EP source imaging

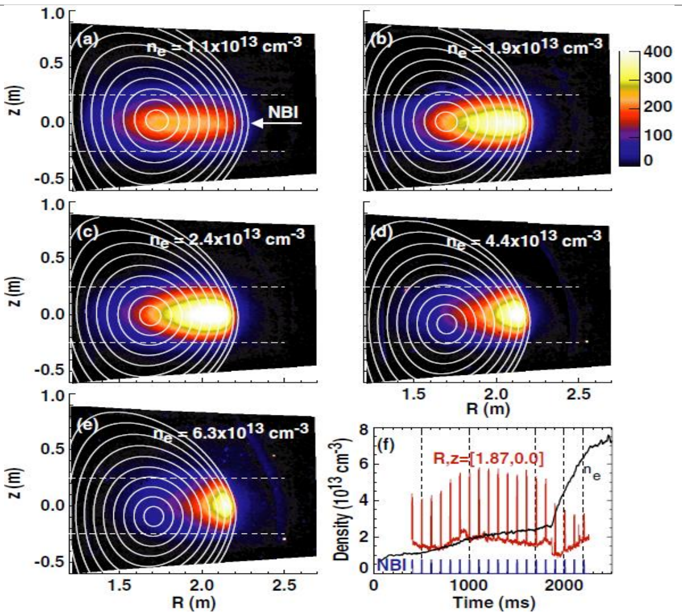

Fig. 2.1.5.1 *Figures (a) through (e) show the plasma cross-section including magnetic surfaces superimposed with the D_α imaging data* [56] *from DIII-D discharge number 135851 representing a change in the active signal as the density rises. The beam propagates from right to left (on each subfigure) in the plasma with the plasma densities as indicated. The images shown are obtained by subtracting the background signal from the signal when NBI is present.*

We present the results of NBI imaging diagnostics in DIII-D that help to visualize beam confinement. These modern techniques represent a breakthrough in the development of EP diagnostics [56]. It is important to note that these techniques are applied not only to achieve better visualization but are also extremely helpful in getting a deeper physics insight and validating a whole range of integrated plasma simulations. Fig. 2.1.5.1 shows 2D images of the D_α emission from the injected neutrals and halo neutrals produced by the bulk ions through the charge exchange with injected neutrals. The 2D images are helpful to visualize the profile of the beam deposition.

Several different emission measurement techniques have been explored including 2D imaging of Doppler-shifted, Balmer alpha (D_α) emission from charge exchange processes between high energy injected neutrals and bulk fuel ions (deuterons). Note that the FIDA emission discussed above is negligibly weak compared to the D_α emission discussed here. Tangential NB injection allowed direct imaging of the source of confined NBI ions over the plasma cross-section [56]. D_α emission is capable of showing the full 2D structure of the beam injected into the plasma, its divergence and the density dependence of NBI attenuation. The D_α emission signal is proportional to the density of injected neutrals. We present a D_α imaging signal in Fig. 2.1.5.1 using DIII-D data from Ref. [56]. All the images have the same color scale as that given in the upper right subfigure. The plane presented is a cut parallel to the beam propagation. Subfigure (f) shows the evolution of the line-averaged plasma density at the location of beam interaction, $(R, z) = (1.87, 0)m$ (solid red). The times of the subfigures (a-e) correspond to the vertical dashed lines in (f).

The application of the fast-framing technique to Bremsstrahlung imaging has recently been reported and provides wide field-of-view measurements of core MHD [57] [58]. This 2D technique based on a tangential viewing geometry was also applied to imaging of the Doppler-shifted D_α from re-neutralized beam ions. It has provided spatially resolved measurements of the EP distribution (2D FIDA imaging) [50] [59] and is discussed in the next section of this review. Other applications in tokamaks and stellarators [60] [61] have been recently developed and provide detailed 2D measurements of neutral beam deposition and plasma kinetic profiles. Even though the conditions with high neutron fluxes are very challenging, there seems no reason why these imaging diagnostics should not find their way into applications for burning plasmas, at least in the initial non-nuclear phase of operation when the plasma performance will be studied.

2.1.6 Fast Ion Collective Thomson Scattering (CTS)

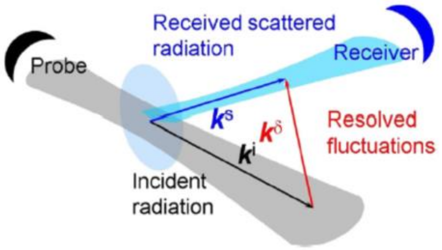

Fig. 2.1.6.1 *Scattering geometry of CTS diagnostics* [62]. *The wave vectors of resolved fluctuations and of the incident and scattered waves are denoted with $\mathbf{k}^\delta$, $\mathbf{k}^i$ and $\mathbf{k}^s$, respectively. The blue ellipse at the intersection of the beam denotes the scattering volume.*

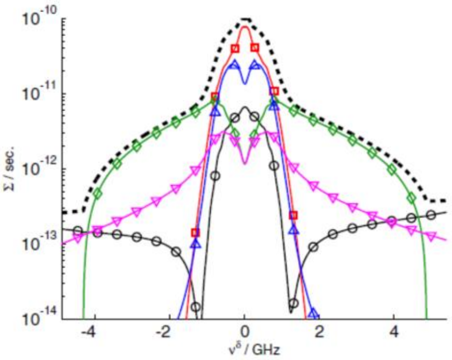

Fig. 2.1.6.2 *Calculated scattering function for ^{3}He minority heating with 2 % ^{3}He density* [63] *and nearly perpendicular velocities. Diamond, triangle, reversed triangles, squares and circles denote the contributions of alphas, tritons, ^{3}He, bulk ions and electrons respectively. The sum is shown with a broken curve. The horizontal axis* ν_δ *is the frequency shift* ν_δ *from the probe beam frequency* ν_i.

Another diagnostic method for measuring the EP energy distribution is collective Thomson scattering (CTS) by gyrotrons or a CO_2 laser. By using waves with a mm wavelength launched by gyrotrons, collective scattering dominates over a wide range of scattering angles. A schematic drawing of the CTS geometry is shown in Fig.2.1.6.1 [62]. For CTS based on gyrotrons, good spatial localization and flexible scattering geometries are possible. The expected CTS signal calculated for an ITER plasma heated by He^3 minority ICRH is shown in Fig. 2.1.6.2 where the calculation is for the low field side CTS in ITER [63]. The main problems in CTS are refraction and electron cyclotron emission (ECE) radiation from high temperature plasma. Those effects can be minimized or removed by selection of optimal scattering conditions, power modulation of the gyrotron probe beams and so on. In JET, the fast ion CTS was first used to detect EPs in the MeV energy range produced by ICRH [64]. The mm waves were launched at the top of the torus with an elliptical polarization and the scattering signals were detected near the bottom. A super-heterodyne detection system with 32 channels was adopted by reduction of stray radiation with the help of notch filters. Noise caused by ECE corresponded to 0.1 to $2keV$, detector noise $\sim 0.1keV$, and low frequency electrical pickup. The first attempt in JET showed the diagnostic capability of such a measurement of the EP distribution function, even though the diagnostic performance was far from optimal. Subsequently, CTS was applied to TEXTOR (Tokamak Experiment for Technology Oriented Research) plasmas to study fast ion dynamics and the results obtained were in good agreement with a simple Fokker-Planck model [65] (see also Sec.4.2.5).

The derivation of the fast ion velocity distribution from FIDA and CTS is not straightforward and requires sophisticated computational methods. One example is the weight function technique introduced in Ref. [66] for FIDA analysis to demonstrate the ICRH acceleration of fast ions above the injection energy. A new reconstruction method for the 2D fast-ion velocity distribution is proposed through a combination of CTS and 1D- FIDA data [67]. A tomographic test to reconstruct 2D fast ion distributions with combined model data of two CTS views and two FIDA views has demonstrated that the distribution functions can be inferred successfully if uncorrelated Gaussian noise of the data of CTS and FIDA is suppressed within a certain value [68]. This approach is quite promising. CTS techniques have also been developed in the stellarator/helical device LHD using a 77 GHz gyrotron [69].

2.1.7 Fast ion loss detector / Lost ion probe

The measurement of EPs produced by nuclear fusion reactions and NBI/ICRH in a toroidal plasma were discussed in the above sub-sections. EPs produced in the manners described might be lost due to non-uniformity of the magnetic field structure and EP driven instabilities, as will be discussed in Sections 3 and 5. EP loss to the wall is a serious concern for the lifetime of the plasma facing components (PFC) inside the vacuum vessel of the torus due to local heating. The local heating can be monitored by high speed infrared (IR-) cameras that view the vessel wall and divertor target plates. IR cameras are important for machine safety as well as for understanding orbit losses. When EPs are lost outside the plasma confinement domain through the plasma edge and scrape-off/divertor regions, bursts of H_α/D_α emission are often observed. The bursts may be generated by bulk plasma disturbances induced by rapid EP transport near the edge, in addition to the EP losses themselves. Although the H_α/D_α emission bursts indicate events induced by EP losses, they are not necessarily a direct indicator of EP losses. Fast ion loss detectors (FILD) or scintillator-based lost ion probes (SLIP) are powerful diagnostic tools to simultaneously obtain information on the energy and pitch angle of lost fast ions. A FILD/SLIP is typically inserted at a position near the plasma boundary behind the limiter. The geometrical structure of a typical detector head is shown in Fig. 2.1.7.1 [70]. This diagnostic is a kind of mass spectrometer. The energy (i.e. gyro-radius) of lost ions is discriminated by a double aperture at the entrance, i.e. pinhole and slit shown in Fig. 2.1.7.1. The pitch angle is discriminated using the width of the aperture. The pitch angle resolution is relatively good ($\Delta\chi$~ 5 deg.), while the energy resolution is appreciably larger ($\Delta E/E$~0.3-0.4 depending on E). In the FILD/SLIP system, the visible light emitted from a scintillator by bombardment of lost fast ions is guided by a lens assembly to a half mirror where the light is divided into two detector systems: a fast framing camera (CMOS camera) and a multi-channel detector array such as a photo diode array or photomultiplier tubes. The bright spots on the scintillator screen are captured by the camera, whose image provides the gyro radius and pitch angle of the lost ions simultaneously, albeit with the relatively slow time response of the camera. The fast time evolution of lost ion fluxes is monitored using a multichannel detector array with a fast response (typically in the range of microseconds). Fluctuations by energetic ion driven instabilities such as AEs are detected in the lost ion signals on AUG, and are a clear indication of fast ion losses due to resonant interactions with these instabilities [71]. This lost ion detector system is also employed to monitor energetic ion losses by AEs and MHD modes in stellarator/helical devices [72] [73]. Details are discussed in Sec.5. In an ITER plasma, a FILD/SLIP head would be heated by the heat flux from the core plasma to the scrape-off layer (SOL) region and lost EP fluxes, and could reach several 100 degrees C. In such conditions the sensitivity of the scintillator will noticeably decrease. To overcome this problem, a fast ion loss detector system based around a Faraday cup array has also been developed. This type of loss detector has been installed on JET [74], however there remain some technical issues associated with the energy resolution.

Neutron and gamma ray emissions due to nuclear reactions between lost energetic ions and wall materials will provide information on energetic ion losses to the wall, as is briefly discussed in sub-section 2.1.3 [47]. For a basic study of energetic ion transport, a directional Langmuir probe was developed in the CHS helical/stellarator device and successfully used to detect the resonant losses of energetic beam ions due to energetic particle modes (EPMs). The probe was inserted inside the last closed flux surface of plasmas heated by low power NBI [75].

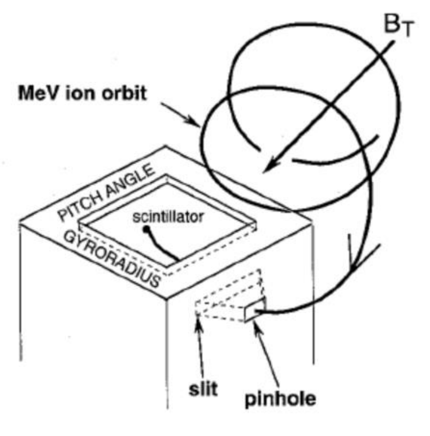

Fig.2.1.7.1 *A schematic drawing of a FILD/SLIP. Figure is adopted from Ref.* [70].

2.2 New fluctuation measurements for MHD instabilities

Fast particles can destabilize Alfvén eigenmodes and other MHD instabilities. In order to study the interactions between these instabilities and EPs, knowledge about the mode frequency, propagation direction and spatial structure of the fluctuations is essential. The most conventional fluctuation measurement technique is by using arrays of magnetic probes (MP), which are simple but powerful at determining the toroidal and poloidal wave vectors, polarization and propagation directions. However, they are not able to derive internal information on the fluctuations. Many fluctuation diagnostics have been developed in addition to MPs. Powerful diagnostics which are able to measure the internal structure of the fluctuations with a good radial resolution without strong constraints on their application have emerged such as ECE/ECEI systems, microwave reflectometer and beam emission spectroscopy (BES).

According to ideal MHD theory, electron density and temperature fluctuations δn_e and δT_e are expressed as:

$$\frac{\delta n_e}{n_e} = -\nabla \cdot \vec{\xi} - \frac{\vec{\xi} \cdot \nabla n_e}{n_e} \text{ and } \frac{\delta T_e}{T_e} = -(\Gamma - 1)\nabla \cdot \vec{\xi} - \frac{\nabla \vec{\xi} \cdot \nabla T_e}{T_e}. \quad (2.2.1)$$

According to these expressions, δn_e and δT_e have strong contributions from the convective terms (second terms on the right hand sides of Eq.s 2.2.1) across the radial gradient regions of the equilibrium n_e and T_e profiles in addition to from the plasma compressibility $\nabla \cdot \vec{\xi}$. In a large toroidal plasma, the n_e profile tends to be fairly flat and its gradient exists only at the plasma edge, whereas the T_e profile is generally peaked. Nevertheless, small density fluctuations are induced even in a plasma with a flat n_e-profile by $\nabla \cdot \vec{\xi}$, which is approximated as $-2\vec{\xi} \cdot \vec{R}/R$ [76]. The eigenfunction of an MHD mode can be derived from the experimentally obtained n_e and T_e fluctuations based on the Eq. (2.2.1). The ECE/ECEI systems mentioned above can be used to measure T_e fluctuations, and reflectometer and BES to measure n_e fluctuations.

2.2.1 Electron cyclotron emission (ECE) radiometer and the ECE imaging diagnostic (ECEI)

High temperature plasma emits electromagnetic radiation in the electron cyclotron frequency (f_{ce}) range. Under conditions of favorable optical thickness, the 2nd harmonic electron cyclotron emission (ECE) is proportional to the electron temperature as black body radiation. In the plasma core region except for low T_e regions (usually only found at the very edge), a suitable optical thickness is usually ensured for ECE. The ECE frequency is determined by f_{ce} and, of course, is in proportion to the magnetic field strength at the emission point. Since f_{ce} is a decreasing function of the major radius of a toroidal plasma, the radiation positions of ECE at various frequencies are uniquely identified. This enables us to derive the 1D-radial profile of T_e and its fluctuation profiles. Radial mode structures of TAE and RSAE were successfully measured in DIII-D and showed good agreement with theoretical predictions [77]. The details will be discussed in Sec.4.2.2. By extending the measurements to 2D in a radially and vertically extended cross section of the plasma, ECEI systems have been developed and recently applied to image T_e fluctuations due to Alfvénic instabilities [78] [79] including the 2D mode structures of TAE and RSAE in DIII-D. The measurements revealed that the mode structure is twisted poloidally in the ion diamagnetic drift direction due to non-perturbative effects arising from the fast ion populations [80]. In AUG, ECEI has also been employed to measure the 2D structures of reversed shear AE (RSAE) and beta-induce AE (BAE) [79]. The details are discussed in Sec. 4.2.2. Since the T_e fluctuation amplitude is typically ~ 0.1 - 0.5 %, singular value decomposition (SVD) and Fourier decomposition are employed to derive the detailed mode structure.

2.2.2 Millimeter wave reflectometer

When millimeter waves are launched into a dense plasma with a peaked density profile, the waves are reflected due to the presence of the cutoff layer [81]. Depending on the polarization, the launched O-mode is reflected at the O-mode cutoff corresponding to f_{pe}. The X-mode launched is reflected at the right-hand cutoff layer whose frequency depends upon f_{pe} and f_{ce}. The X-mode reflectometer can also be effectively applied to a plasma with a slightly hollow density profile at a higher magnetic field. The radial profile of n_e fluctuations is obtained by sweeping the frequency of the launched waves.

The radial information is derived using the equilibrium electron density profile and the magnetic field structure. This diagnostic is broadly applied to tokamaks and stellarators. For example, it was successfully applied to reveal the anti-ballooning mode structure of TAEs on TFTR [82].

2.2.3 Beam emission spectroscopy (BES)

When high energy hydrogen-isotope neutral beams are injected into a plasma, Balmer lines are emitted through various neutral sources, as seen in Fig. 2.1.3.2 from Sec. 2.1.3. The intensity is determined by impact excitation in collisions with electrons, hydrogen-isotope fuel ions and impurity ions. The intensity of beam emission is approximately proportional to the electron density. Accordingly, the fluctuation gives us the information about the n_e fluctuations. Such a diagnostic to measure the beam emission is called BES [83]. With hydrogen or deuterium neutral beam injection, H_α/D_α Balmer lines are monitored along an appropriate viewing geometry. The viewing line is carefully selected to separate the target beam emission from the very bright edge plasma radiation by introducing a Doppler shift which is induced by the tangential beam velocity to the sight line. The sight line is also adjusted to view the plasma tangentially to the magnetic surfaces. Therefore, the beams that are injected and have a finite toroidal velocity component provide the beam Doppler shift. Due to beam attenuation, BES focuses on density fluctuation measurements on the low field side (larger R side of a toroidal plasma). First application of BES diagnostics to measure TAE radial structure and poloidal spectrum was done on TFTR and showed good agreement with simulations [84]. Such diagnostics are routinely employed to measure density fluctuations due to energetic ion driven global instabilities [85].

2.2.4 Other fluctuation diagnostics

Other potential diagnostics for fluctuation measurements have been developed and applied to study EP driven instabilities under various specific conditions. For instance, mm wave and far-infrared (FIR) interferometers, FIR scattering, phase contrast imaging of laser light, heavy ion beam probes (HIBP) and so on have all been applied to various plasma experiments. The interferometer is the most popular and widely used diagnostic method for density measurements and although it provides only line-integrated signals, it can nevertheless be used to monitor AE fluctuations localised in the plasma interior which magnetic probes may not be able to detect [86] [85] [87]. FIR scattering can also be applied to support other fluctuation diagnostics [85]. Phase contrast imaging measures fluctuations as line integrated signals and has been successfully employed for studying RSAE in sawtoothing plasmas in C-mod [88]. HIBPs are a unique fluctuation diagnostic and have also been applied to studies of EP driven fluctuations in stellarator/helical devices [89] [90].

Polarimeter using a FIR laser [91] is another diagnostic technique used to measure the internal magnetic fluctuations of EP driven modes directly. It has not been used to study EP driven modes until recently [92] where detailed internal radial structure was reported for reversed-field pinch configuration. In its studies on tokamaks and stellarators we expect the polarimetry to provide important information on internal magnetic fluctuations of EP driven modes.

Data from the fluctuation diagnostics in this section in conjunction with EP loss information measured using the diagnostics discussed in the last section enable the scaling of EP losses with mode amplitude to be determined, as well the establishment of a threshold in mode amplitude for an enhanced radial transport of EPs to take place.

3 Single particle confinement

3.1 Drift motion and TF ripples in different confinement geometries

Here we review the advances in physics understanding of basic properties of EP trajectories in toroidal magnetic fields. The geometry of the equilibrium magnetic fields in toroidal systems can be complex. We show representative examples of the magnetic field variation at an interior magnetic surface in various toroidal systems in Fig. 3.1.1. These are shown on the left against the so-called ballooning poloidal (nonperiodic) variable, ϑ [93]. This special variable is taken along the magnetic field line with the origin point at the midplane on the low field side. The results are simulations shown for the LHD (Large Helical Device [94]) stellarator, the quasi-axisymmetric design of NCSX (National Compact Stellarator Experiment [95] and its symmetrized (tokamak-like) version - NCSX-SYM [96]), the quasi-isodynamic W7-X (Wendelstein 7-X [97]), the quasihelically symmetric HSX (Helical Symmetric Experiment [98]), and the QPS (Quasi-Poloidal Symmetric Stellarator [99]). These devices either exist or are planned for construction based upon theoretically proposed confinement properties.

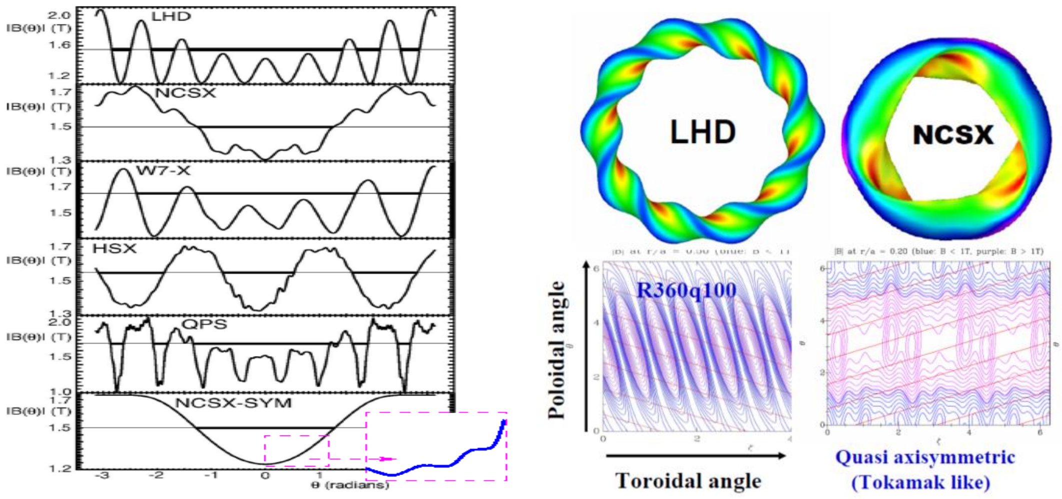

Figure 3.1.1 *In the left figure we show the variation of the magnetic field in several toroidal plasmas for the machines indicated on each subfigure. Shown as solid horizontal lines are the projections of the low energy trapped particle orbits. (The graphics are adapted from Ref.* [96]*.) The two figures on the right correspond to the magnetic surfaces in the LHD and NCSX stellarators computed using the VMEC code* [101] [102].

The field variation on a certain flux surface in a toroidal configuration is seen more clearly from a contour plot of the field strength in the plane defined by the poloidal and toroidal angle variables of the Boozer coordinate θ_B and φ_B [100]. Two examples for LHD and NCSX are shown in the lower right inserts of figure 3.1.1 that are adopted from [101] [102]. The contours of $|B|$ in the $\vartheta_B - \varphi_B$ plane are important to understand the characteristics of the quasi-symmetries in 3D toroidal magnetic configurations. Since the particle orbits are determined only by the spectrum of $|B|$ in Boozer coordinates, these contours can be used to understand the characteristics of orbits of thermal plasma particles and EPs, which have a gyro radius that is finite and small enough compared to the scale length of the magnetic field non-uniformity. A certain kind of quasi-symmetry can reduce particle losses by minimizing orbit deviation from the flux surfaces. Note that the analyses of EP confinement using Boozer coordinates are limited by the last closed flux surface (LCFS), i.e. to where the coordinates are defined, namely inside the LCFS. EPs that return from the vacuum region to the plasma region cannot be treated by this approach, and a more complete and sophisticated treatment is necessary.

What follows from the illustrations presented is that stellarators with their equilibrium properties are prone to enhanced particle transport on a drift time scale due to magnetic field ripples. As can be seen from the figure, the extent of the drift trajectories of trapped particles is limited in the ballooning variable by the region of low magnetic field. The extent or length of the trapped particle drift trajectory on that figure reflects the variation in helical transform the particle experiences during its drift motion. If it is small, the particle drifts vertically out of the trapped region. For comparison, passing particle trajectories would be represented as horizontal lines above the B-curves in these figures (not shown). More on the properties of the (transport) optimizations of stellarators can be found in the tutorial in this reference [103].

It can be shown that in LHD plasmas there are a significant number of locally trapped particles (see trajectories in the deep wells of the B field in Fig. 3.1.1). They can drift vertically or be de-trapped through a transition to passing orbits without collisions. Special numerical studies of neoclassical transport optimization in LHD (such as Ref. [104]) rely upon ripple diffusion, and were used for positioning the magnetic axis of the vacuum field. It is shifted inward from the axis of the helical coils to move the region of high field ripple to a location with better curvature, i.e. a smaller R region. In a tokamak with a small toroidal field ripple (cf. NCSX-SYM dependence in the above Fig. 3.1.1 where the B field variation deviates from the ideal axisymmetric tokamak noticeably as one approaches the LCFS) the local wells are not as deep (shown on the insert) and are located near the origin $\vartheta = 0$. Tokamaks are therefore well suited to ripple diffusion studies, both theoretically and experimentally, because of their relative simplicity [105].

The subject of ripple induced EP transport in stellarators has not been so extensively studied experimentally. In LHD work was done with using NDD and $ICRH$ generated trapped ions [106] [107] and focused on the tail in the ion velocity distribution that was compared with the Stix theory. Good confinement of EPs generated by tangential NBI and ICRH was confirmed in an inward-shifted LHD configuration where the helical ripple is reduced compared to the outward-shifted configuration [108]. The simulation results by the GNET code where the drift kinetic equation in 5D phase space is solved were found to agree well with the experimental data [109] [110]. The ripple-induced loss mechanism was concluded to be the main loss mechanism in the reported experiments. In regimes that are more relevant to thermal plasma confinement [103] [111] [112], i.e. when collisions are essential, theoretical studies were undertaken. As it was pointed out in [103], EPs are highly insensitive to the electrostatic potential present in the plasma, which cannot be higher than the plasma temperature and hence is much less than the EP energy. In this case the EP orbits (excluding trapped particles) are determined entirely by the structure of the $|B|$. This is useful for understanding even the orbits of thermal particles and low energy EPs having a sufficiently small gyro-radius. Numerical studies on this topic have been published but for introductory purposes it seems reasonable to focus here on the effects of TF ripples in tokamaks (see Sec. 3.2.).

It follows from the publications on numerical studies that the confinement of EPs in stellarators is in general a serious problem [113] [114] that has not been the focus of transport optimization studies to date. Tangential injection is considered to be the best way to minimize ripple losses in the present day machines. Simulations show [114] that a quasi-asymmetric stellarator (QAS) configuration scaled up to the size necessary for a reactor shows a relatively high α-loss rate compared to simulations for the ITER-98 EDA design [115]. As indicated above, alpha-particle loss simulations tend to overestimate the losses because the EPs that can reenter the plasma (with small pitch angles) are counted as lost by the simulations. Alpha particles having large pitch angles should exist in the velocity domain close to the passing-trapped boundary. However they would be considered lost in this model. Reduction of the alpha loss rate through a lowering of the field ripples should be a high priority in the search for QAS reactor configurations [114]. The mitigation of alpha particle losses in a stellarator-based reactor is aimed at minimizing the slowing down time with the help of high density and relatively low temperature operating scenarios [116].

The study of ripple diffusion is predominantly a numerical activity as helical systems are not generally amenable to an analytic treatment. Numerical results have been successfully compared with experimental studies in LHD, as discussed above.

3.1.1 Conservation of magnetic moment in low field machines such as spherical tokamaks

The equilibrium magnetic field in a reactor has to be strong enough to confine charged particles, ions and electrons of the thermonuclear plasma. In STs (spherical torus or tokamak) this is not easy to achieve due to the required high current in the toroidal field coils. Thus the ST line of tokamak devices has low B field and high plasma β. With these characteristics, STs [117] such as the Current Drive Experiment (CDX) [118], Small Tight Aspect Ratio Tokamak (START) [119], National Spherical Torus Experiment (NSTX) [120] [121], Mega Ampere Spherical Tokamak (MAST) [122], GLOBUS-M [123] and others, have unique operating scenarios and unusual EP orbits. The charged particle trajectories in STs can, of course, still be treated in the same way as in conventional aspect ratio tokamaks within the drift approximation when certain functions of their space and velocity coordinates, known as adiabatic constants of motion, are conserved as shown, for example, in Refs. [105] [124]:

$$\mu = \mathcal{E}_{\perp}/B\,;P_{\varphi} = v_{\varphi}\,cRM/e - \psi_p \tag{3.1.1.1}$$

They are called the adiabatic magnetic moment and the canonical angular momentum respectively or COM (constant of motion). The magnetic moment is conserved in the case that the field quantities are almost constant around a single gyro-orbit, whilst the canonical angular momentum is exactly conserved in a perfectly axially symmetric system. The conservation of μ and P_{φ} is thus expected in tokamak geometries, whereas in helical systems only the first one is conserved. P_{φ} is approximatly conserved in a periodic helical system with a large toroidal period number N. That is in helical systems such as LHD (at $N = 10$), P_{φ} is approximately conserved for deeply passing EPs, as discussed later (See sec. 3.1.2).

In STs, μ and P_{φ} are also conserved but the expression for μ in Eq. (3.1.1.1), oscillates in time [125] if it is written using the drift approximation, i.e. $\vec{v} = \vec{v}_{\perp} + \vec{v}_{\parallel} + \vec{v}_{dr}$ and v_{φ} is included in $\vec{v}_{\parallel}$ term only. Such an approach is often used and requires several iterations to converge to the exact angular momentum given by the second equation (3.1.1.1) and v_{φ} is the instantaneous value of the particle velocity. For test particle simulations, it is sufficient to know that there are expressions for μ and P_{φ} that are conserved but that the explicit expressions are not required. They are only required for calculations when the phase of the particle drift motion is needed, such as for studing the cyclotron instabilities discussed in Sec. 4.2.3.

The issue of the confinement of the magnetic moment became important in view of recent ST experiments. Several groups were involved in the theoretical [126] [127] [128] and numerical work [129] we introduce here in an attempt to understand the EP COM conservation in ST plasmas when the ratio of the fast ion gyro-radius to the gradient scale length of the magnetic field is finite. The theoretical work has some similarity to earlier work carried out on mirror machines [130]. It seems appropriate here to present an illustration (see Fig. 3.1.1.1) showing the possibility for μ to have jumps from a single particle motion point of view.

We schematically show two charged particle orbits in a magnetic field which is stronger on the left side from the dashed line. If we take two particles that differ only by their gyro-phase as shown in the figure after a drift motion through the region “x” we can estimate the characteristic jump of its magnetic moment due to different gyro-center locations and different magnetic field values in those locations. So we can write

$$\Delta\mu \approx \mu\frac{\Delta B}{B} \approx \mu\frac{\rho_f}{R}, \tag{3.1.1.2}$$

where ρ_f is the Larmor radius of the fast ion. We should note that in Fig. 3.1.1.1, the illustration is of only a single jump of the EP magnetic moment. In a toroidal plasma, this jump happens at the point where the EP crosses the midplane (marked as "x" on the figure) [127] due to the same phasing of its motion. In careful theoretical work, the expression for the change of μ for an EP which experiences a characteristic jump was obtained [127]

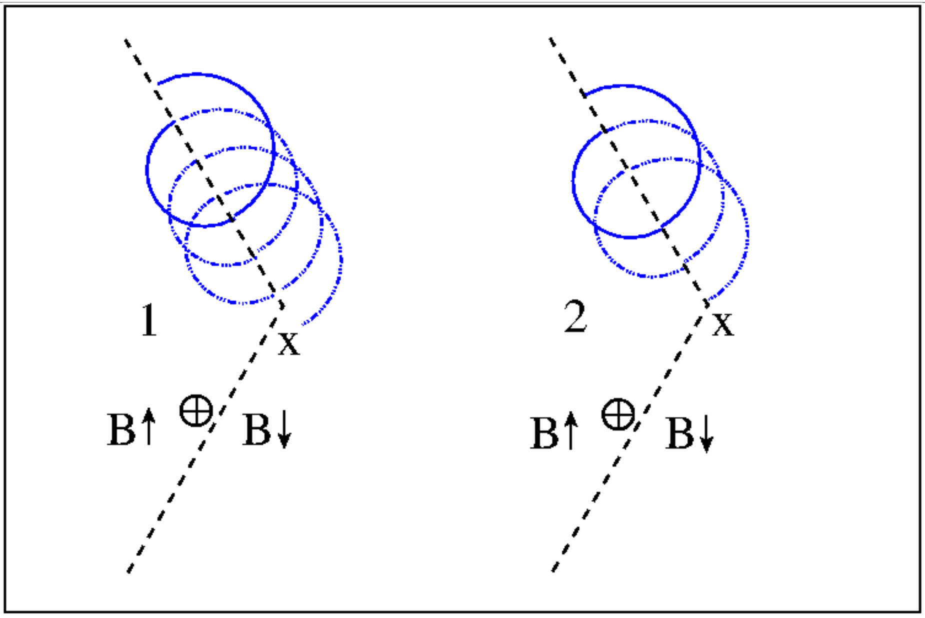

Figure 3.1.1.1 *Illustrations of charged particle gyro-orbit drift motion in the presence of the magnetic field gradient, which is stronger on the left and weaker on the right of the dashed line (the guiding center trajectory also indicated by the dashed line), as indicated by arrows. Shown are two EP gyro-orbits with different gyro-phases.*

$$\frac{\Delta\mu}{\mu} = -\pi\frac{v}{v_\perp}\Re\left(\exp[-\frac{\alpha_\rho}{\varepsilon_\rho}]\right)O(1), \tag{3.1.1.3}$$

where the expression for the phase is coming from an accurate evaluation of the magnetic field and the change of the magnetic moment is described by the real part of the exponent, denoted by $\Re$. The above estimate is valid provided the gyro-radius is large enough and the stochasticity condition is satisfied

$$\varepsilon_\rho \approx \frac{\rho_L}{R} > \varepsilon_{\rho cr} \approx \frac{\alpha_\rho}{\ln(M_*)}, \tag{3.1.1.4}$$

where α_ρ is of order unity and $M_* \approx q/\varepsilon \gg 1$.

A different way to evaluate the jumps in the magnetic moment was proposed in Ref. [126] for passing particles (trapped particle contributions were argued to be small) and was written in terms of the pitch angle variable λ as

$$\frac{\Delta\lambda}{\lambda} = \frac{4\pi q}{\chi\sqrt{2\lambda}}J_s(s\varepsilon), \tag{3.1.1.5}$$

where $s \gg 1$ is the integer number of the relevant high order cyclotron resonance $\langle\omega_c\rangle = s\omega_b$ and J_s is the Bessel function of order s. Evaluations of the associated pitch angle diffusion resulted in a negligible effect on fast beam ions in NSTX $\Delta\lambda\sqrt{\tau_{se}/\tau_b} \ll 1$. Nevertheless, the authors did not rule out the importance of non-adiabatic diffusion in the plasma periphery. Both expressions (3.1.1.3) and (3.1.1.5) have the same asymptotic behavior in the limit of large s.

Numerically, a similar conclusion for non-adiabatic diffusion being negligible was found in Ref. [129]. Although the results obtained in Refs. [127] [128] predict possible stochastic non-adiabatic diffusion experimentally, it was not studied in detail. However, experimental studies of EP confinement in NSTX did not find an effect from the non-adiabatic behavior of the EP magnetic moment, at least within the measured accuracy of 20-30% [131] [132]. These studies were done in so-called MHD quiescent plasmas. Further topics relevant to this regime are covered in sections 3.3.1 and 5.5.

We would like to note that the numerical study of the non-adiabaticity diffusion effect of fusion products seems to be very important for reactor scale STs. One of the reasons for this is that there are groups of EPs, such as potato orbits and eye-drop locally trapped orbits, which are beyond the analytic analysis and require a numerical treatment to make accurate predictions.

It seems natural to expect more conclusive numerical confirmation of stochastic diffusion, especially in ST-based reactors with relatively low magnetic fields. Such effects may also play some role in predictions of the behavior in future laboratory scale devices.

3.1.2 Conservation of toroidal canonical angular momentum in 3D plasmas

In 3D plasmas the toroidal angular momentum in Eq. (3.1.1.1) is not an adiabatic invariant due to the lack of toroidal field symmetry. However, an adiabatic invariant or COM is found for a wide class of 3D geometries such as stellarator/helical devices where the rotational transform per toroidal field period is small, $(\iota/2\pi)/N \ll 1$, and the variation of the field strength due to toroidicity is small compared to the variation along the field line due to helical ripple, i.e. $\epsilon_\varphi\,(\iota/2\pi)/(\varepsilon_h N) \ll 1$ [133]. In these devices, two classes of particles exist. Particles of one class are trapped in local ripple wells whilst the other are untrapped. The first group of particles (trapped particles) have a bounce invariant or a modified second adiabatic invariant J^* and the latter ones (passing particles) also have an invariant. For passing particles with small pitch angle, the invariant becomes equivalent to the toroidal angular momentum P_φ. The J^* conservation has successfully been applied to the study of particle orbits in the Advanced Toroidal Facility (ATF) torsatron device that satisfies both requirements: $(\iota/2\pi)/N \ll 1$ and $\epsilon_\varphi\,(\iota/2\pi)/(\varepsilon_h N) \ll 1$ [134]. In LHD plasmas with large $N = 10$, the toroidal angular momentum is conserved for passing EPs under this approximation. These requirements are however not satisfied for quasi-axisymmetric (QAS) devices with small $N = 2$ or 3. Nevertheless, in QAS configurations such as NCSX, the toroidal angular momentum is approximately conserved due to the quasi-symmetry of the magnetic fields, similar to a rippled tokamak. Note that QAS is usually appreciably violated in the plasma edge region because the external coils are close to the plasma boundary and the invariance is violated by the toroidal perturbations to the field. In a similar manner, the conservation may be broken in the rippled edge region of a tokamak. Note that in such optimized configurations where quasi-symmetries are found, the drift approximation ignores the gyro-radius, which is not always small for EPs. It should also be noted that the above requirements are satisfied even near the plasma edge and P_φ is approximately conserved from the plasma core to the edge.

3.2 Ripple effects

The deviation of the toroidal magnetic field from exact axisymmetry by the presence of magnetic field ripples may strongly influence the fast ion drift orbits as we will here discuss.

Let us consider the effects of the deviation of the toroidal magnetic field from axisymmetry on EP motion via the ripple of the confining magnetic field. Ripples are present in toroidal systems due to the fact that a finite number of coils with finite dimensions are used to generate the magnetic field and that the B field is stronger closer to the coil. One can represent this for a tokamak with N toroidal field coils in the form (see for example [135] [136])

$$B = B_0[1 - (r/R)\cos\vartheta + \delta\cos N\varphi], \qquad (3.2.1)$$

where $\delta = (B_{max} - B_{min})/(B_{max} + B_{min})$. The magnitude of δ is typically on the order of 1%

and is an exponential function of major radius becoming negligibly small at the magnetic axis. At that level this results in a few percents of α losses, whereas at $\delta \sim 5\%$ about half of the alphas may be lost in a device like ITER [137]. One of the consequences of the rippled magnetic field strength in a tokamak is the dependence of the losses upon toroidal angle if $\gamma = r/R\, Nq\delta < 1/|\sin\vartheta|$, where the particle is locally trapped at $v_\parallel/v < \sqrt{\delta}$. The rate with which the trapped particles drifts out of the plasma is fast, $v_d = R\omega_c(\rho_f/R)^2$.

Trapped particles in general are prone to experience strong effects on their drift orbits due to ripples as near the bounce points of their drift trajectories the magnetic moment is approximately $\mu \simeq E/B$ and small changes in B field can cause significant changes in trapped particle parallel velocity $v_\parallel$ as well as the position of its reflection or turning points. We show the calculated magnetic field ripple in Fig. 3.2.1 of the Tore Supra tokamak [138] and JET [139]. Here the largest ripple value for each figure is on the low field side of the cross section in the mid-plane where the toroidal field coils are furthest apart.

In addition to the local trapping of charged particles mentioned above, which we call the first mechanism, two other mechanisms of particle diffusion due to ripples are also known. The second one is described by the cyclotron interaction of energetic particles with the rippled magnetic field when the number of TF coils is large [140] [141]. In that case, the effective wave-number of the TF induced perturbation is $k_\parallel = N/R$ and the possibility for a resonance with the cyclotron frequency arises: $k_\parallel v_\parallel = \omega_{cf}$. This condition is satisfied only at a few points along an EP's trajectory where the adiabatic invariants experience jumps. The amount of change in the invariant due to a single pass through such a cyclotron resonance can be on the order of a ripple amplitude $\Delta\mu \sim \delta$. A detailed study of this mechanism was recently undertaken in Ref. [126] for STs. Using the wave-particle interaction formalism it showed that passing beam injected D-ions should not be strongly affected by this mechanism. On the other hand, trapped and marginally circulating ions are affected with the following estimate for the amount of radial diffusion resulting:

$$\frac{\Delta r}{r} \approx \frac{Nq\Delta\lambda}{2\kappa}\frac{\rho_f^2}{r^2} \tag{3.2.2}$$

This can be of order one if the width of the cyclotron resonance is sufficient for many resonances to overlap. Here κ is the ellipticity. Detailed experimental studies of beam ion confinement with this effect is very challenging and needs to be done for a variety of plasma conditions in both tokamaks and stellarators.

The third particle diffusion mechanism is collisionless banana diffusion and has been studied in great detail (see for example the discussion on this topic in [105]) both experimentally and theoretically. When trapped particles drift toroidally due to precession with the frequency ω_φ they see the rippled magnetic field as a perturbation with frequency $\omega = N\omega_\varphi$. In other words, their velocity is modulated in this case due to μ conservation and a (ripple) variation in the B field. Given the toroidal ripple $\delta$the trapped particles of interest will precess in $\Delta t = 2\pi\, R/Nv\sqrt{\delta}$ during which it will change its phase by $\Delta\varphi = N\omega_\varphi\Delta t = 2\pi q\, \rho_f/\sqrt{\delta}\, a$. In nominal tokamak plasma conditions, the phase change is larger than 2π and one cannot make use of the adiabatic theory to compute the probability of the particle orbit transformation [142]. If the ripple is small, $\gamma \gg 1$ and the main effect comes from collisionless banana diffusion [143], which is often referred to as GWB (after the authors Goldston, White, Boozer) diffusion.

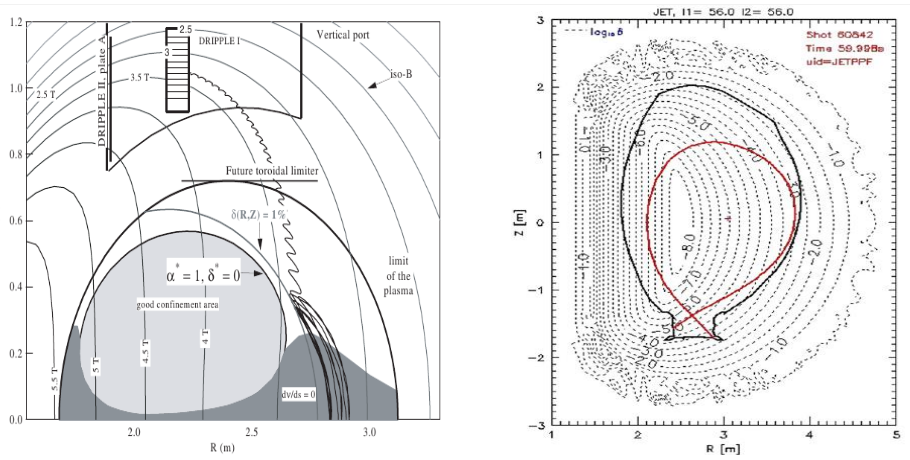

***Figure 3.2.1**. The left figure is the toroidal field ripple map of the Tore Supra circular tokamak* [138]. *It is shown as a shaded area near the bottom of the figure. The solid black lines are the computed trajectories of guiding center trapped particles and unconfined locally trapped orbits that drift out. In the right figure, we show the realistic toroidal magnetic field ripple map for JET with 32 coils all carrying the same current* [139]. *The dotted lines identify surfaces of equal ripple amplitude using a logarithmic scale. The actual plasma equilibrium used for the experimental analysis is shown as a continuous (red) line.*

The toroidal drift of trapped particle in a tokamak plasma is uncompensated by the rotational transform near the bounce points that introduces the possibility for stochastic diffusion via the violation of axisymmetry by the TF ripples. As a consequence such diffusion occurs with a radial step size that was found by employing a perturbative technique for circular plasmas [105] $\Delta r \approx \left(\frac{N\pi}{|\sin\vartheta_b|}\right)^{1/2}\left(\frac{q}{\epsilon}\right)^{3/2}\rho_f\delta\sin(N\varphi_b)$, where all the parameters are evaluated at the bounce point. This radial displacement becomes indeed diffusive if either one of the following decorrelation mechanisms (a factor $\sin(N\varphi_b)$ helps to make the process stochastic) are present: either the effect of the collisions becomes important or the toroidal drift becomes appreciable in such a way that the particle “forgets” its initial phase. For EPs the toroidal drift dominates when the modification of the bounce point becomes large and comparable with the ripple phase $N\varphi_b'\Delta > 1$ [143]. This expression was reduced for the case of low β, cylindrical equilibrium and at a bounce point $\vartheta_b = \pi/2$:

$$\delta > \delta_{cr} = \left(\frac{\epsilon}{N\pi q}\right)^{3/2}\frac{1}{2\rho_f q'} \tag{3.2.3}$$

This is the familiar GWB critical ripple magnitude which is often used for quick analysis of the ripple strength. Normally, experimental studies are focused on the ripple diffusion boundaries and/or the fraction of the losses of charged particles and their distribution over the wall [1] [3]. The pivotal point in the above derivation is that the particle transport should be of the *diffusion* motion. We will review this next, i.e. that the diffusion of the trapped particles was seen directly with the use of the PCX diagnostic in TFTR [18].

A complete theory of ripple induced particle loss can be found in this reference [144].

3.2.1 Ripple diffusion experiments and their modeling

Both NDD and PCX (via NPA [18]) were used in TFTR in similar ways to study ripple diffusion. PCX was used to directly measure the stochastic diffusion boundary dependence on the EP energy. Because it was targeting the trapped particles, PCX was well suited to measure one of the dominant EP loss mechanisms - stochastic ripple loss diffusion [18]. This was possible in part due to the noted dependence of the diffusion boundary on the EP energy. Additional analysis with the help of the FPPT code [145] allowed the illustration of the diffusive nature of trapped particle

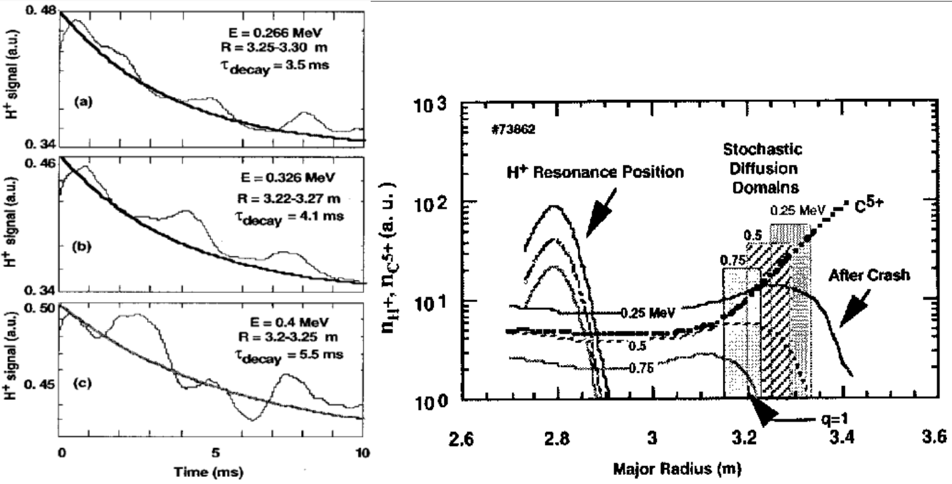

Figure 3.2.1.1 *Illustrations of the PCX experiments on the ripple diffusion performed on TFTR* [19]. *The left figure shows (fitted to the exponent) the decrease of the signal of the H^+ minority ions after the sawtooth crash due to the ripple diffusion. Modeling of the measured signal is done by the FPPT code* [145] *as discussed in the text. The figure on the right depicts the minority ion stochastic diffusion domains for different energies. The EP densities taken at different energies are shown before (indicated as H^+ resonance position) and after the sawtooth as was modeled by the FPPT code and discussed in Sec. 4.2.5.*

confinement in the ripple domain and to quantify the confinement boundaries for the measured energies, which compared favorably with the predictions by theory [146].

The FPPT code [145] solves the drift kinetic equation employing the method of characteristics (see also [147]) using the assumption of low EP density, which is justified by definition of their large characteristic energy. It finds the solution of the EP distribution function, F, including orbit width effects. Ripple diffusion was introduced via an effective loss time term in the drift kinetic equation:

$$\frac{\partial F}{\partial t} = < St(F) > + < S_f > - \frac{F}{\tau_{loss}}, \tag{3.2.1.1}$$

where τ_{loss} can be substituted with the ripple diffusion time τ_δ. A useful approximate formula describing a smooth transition from a confinement to a stochastic regime was obtained earlier [146],

$$\tau_\delta = \tau_b \frac{(r-a)^2}{\varrho_L^2} \frac{2\varepsilon^3 \sin\vartheta_b}{\pi q^3 N \delta^2(r_b,\vartheta_b)} \left(1 + e^{6.9-5.5\alpha_r}\right). \tag{3.2.1.2}$$

The phase in the exponent $\alpha_r \sim \delta$ takes into account the ripple well depth and describes the sharp boundary for the ripple diffusion to be effective.

It turns out that the diffusive nature of the ripple effects on EPs was seen from the time dependence of the PCX signal which was collected by the NPA diagnostics right after the sawtooth crash event when H^+ minority ions from the center are redistributed radially to the periphery [19]. The measured EP density before and after the sawtooth crash are shown in the figure 3.2.1.1, right. Minority ions reach the outer regions where the magnetic field ripples are strong and where they moderate the EP confinement described by the effective loss time given above and according to the theory [146]. The figure on the left illustrates that the PCX measured minority signal is exponential (decreasing) in time and that the effective-loss-time model captures this important dependence. Figure 3.2.1.1 (right) shows that the energy dependence of the stochastic diffusion domain agrees with the model as well.

The simulations show that the approximated formula for the diffusion time, Eq. (3.2.1.2), is extremely useful for quantitatively describing single particle confinement in the presence of toroidal field ripple. It would thus appear to be beneficial to include it in future integrated modeling efforts that aim at a holistic description including the influence of TF ripple on EP confinement.

3.2.2 Ripple mitigation and other axisymmetry breaking effects on EP confinement

To achieve burning plasma conditions the ripple diffusion needs to be mitigated to allow the charged fusion products to replenish the energy loss from the plasma. The approach adopted in ITER is to include FS (ferritic steel) inserts, which were analyzed and summarised in Ref. [137]. As follows from Eq. (3.2.3), the GWB diffusion is stronger for high q plasmas for which the associated ripple-induced magnetic perturbation is increased relative to plasmas with low q values. For projects such as ITER, the loss of energetic particles could impact the fusion gain, Q, especially at high q and a careful assessment is necessary. The suggested FS inserts were analyzed by several codes and were shown to be very effective at reducing the fusion alphas power loss by about an order of magnitude [137]. We would like to specifically point out here two publications on the calculations of this effect using the codes HYBRID [148] and OFMC (orbit following Monte-Carlo) [149]. Both calculations were consistent with each other, and predicted a similar (near order of magnitude) reduction of the α-particle ripple loss.

There are some other potential modifications to the plasma worth mentioning here that can break the axisymmetry and affect EP confinement. One of them is the planned set of TBMs (Test Blanket Modules) [150]. Each TBM will be about 1 $tonne$ of a steel ferromagnetic alloy, which is a neutron tolerant martensitic steel. They will perturb the nearby plasma through a $\sim 1\%$ reduction of the B-field. One of the concerns associated with the TBMs is that their introduction will cause a $n = 1$ perturbation of the field due to being sited next to each other on one side of ITER [151]. This is especial concerning as it may introduce locked modes, large magnetic islands, rotation braking and so on. The influence of TBMs on EP confinement was investigated in DIII-D experiments [151] that showed that TBMs seem to only have a small effect (within the error bars of the measurements). A special numerical analysis of DIII-D experiments was performed [152] and suggested that some of the observed head load enhancement in these experiments was in part due to prompt beam ion losses. The study was carried out using several different codes ranging from the full-orbit following codes SPIRAL [153], ASCOT [154] to the guiding-center codes OFMC [155] and DELTA5D [156]. A very recent study though of DIII-D experiments showed that TBM losses can be enhanced and localized [157] that warrants further investigations and can be problematic for ITER discharges.

Finally, new tools are becoming available to numerically simulate 3D tokamak plasmas [158]. Techniques that have been developed for stellarators can be applied to tokamaks allowing a non-perturbative treatment of magnetic equilibria with field ripples. Particular examples are self-consistent magnetic equilibria including the effects of TF ripple, TBMs and finite plasma pressure. They led to several new physics results that would not otherwise have been predicted. The first is that the flux surfaces are shifted through the fixed B-field gradient. EP confinement is influenced by these 3D effects and results in deeply trapped particle losses. Although using 3D configurations are more computationally intensive to handle, they can lead to new physical insights of practical importance.

Another example of interesting phenomenon not addressed in the literature is EP confinement during the formation of helical equilibria, which might appear in the high β_N plasmas with $q(0) > 1$ expected in the hybrid scenario envisioned for ITER [159]. A new limitation on the fast ion confinement, and thus future reactor performance, may take place in such operational scenarios.

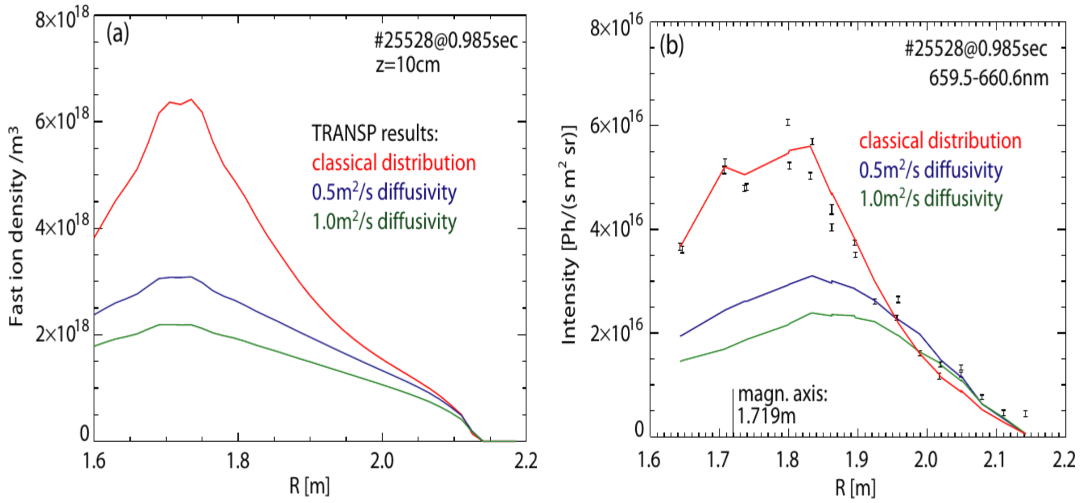

Fig. 3.3.1 *(a) Radial EP beam density profiles generated by TRANSP code for AUG discharge as indicated. The figure (b) gives the measured intensity of FIDA and its expectations with a classical DF of beam ions. Two values of the beam ion diffusivity were used to compute the profiles as indicated. The profiles correspond to* $E_{\|}$ *between* 25 *and* $42 keV$*. The error bars are from the statistical uncertainties of the measurement.* [51].

3.3 Measurements and modeling of fusion EP distribution function

As the EP distribution function (DF) is the consequence of many different physical effects, it is important to consider ways to measure and model it. Here we describe them for the case where only classical non-collective effects on the DF are present. That is, when the plasma is quiet and there are no waves or instabilities present. This restriction simplifies the interpretations of the measurements and helps to validate the diagnostics such as FIDA described in Sec. 2.1.

We would like to mention first the FIDA work on the DIII-D tokamak [160] to measure the beam ion distribution function (DF) and its modeling by the TRANSP code [161]. The beam ion DF was measured with the NBI injection geometry and D_α signal as described in section 2.1. A Monte Carlo simulation code was run afterwards to calculate the fast-ion D_α spectrum arising from the fast-ion distribution function calculated classically by TRANSP. The results showed that the spectrum agreed reasonably with the measurements within the experimental uncertainties. This was considered as validation of the TRANSP module used. An estimate was given for the possible EP diffusion coefficient which was around $0.1\, m^2/s$. These comparisons helped validate the use of FIDA diagnostics for future use.

Another set of experiments that exploited quiescent plasmas were those using the FIDA diagnostic in ASDEX Upgrade (AUG) [51]. We show in Fig. 3.3.1 an example of FIDA usage on AUG and its comparison with TRANSP modeling of the signal intensity. FIDA integrates the signal with a weighting function that goes from around $100 keV$ down to $20 keV$, and pitch angles $\chi = (v_{\|}/v) \sim -0.5$ down to -1.

One can see that good agreement is achieved for these plasmas in AUG. The same paper also studied of the “non-quiescent” effect on beam ions by examining a $q = 2$ sawtooth-like crash. In this case, a strong EP redistribution was reported.

3.3.1 Slowing down DF of fusion alphas in quiescent plasmas

It is appropriate here to show an example of the EP distribution that results from the classical (collisional) relaxation of a relatively well-known source of fusion DT alphas or NBI ions. We start with the generalized kinetic equation for the fast ion DF, Eq. (3.2.1.1), where we retain only the source and drag terms:

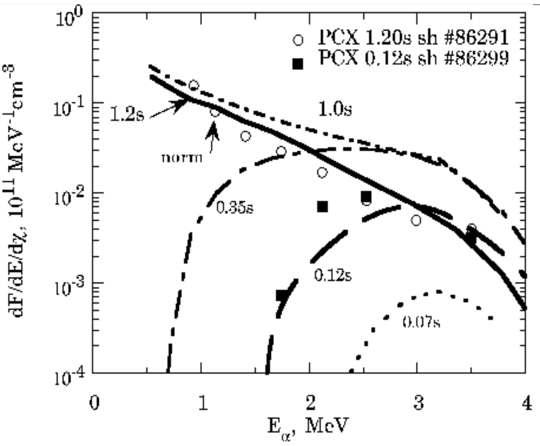

Fig. 3.3.1.1. *Evolution of the alpha energy DF spectra computed using the FPPT code for DT TFTR plasma (curves are computed* [145]*) and comparison with the measured alpha spectra for two times: (i) during the slowing-down phase shown as full circles corresponding to 1.2 s, and (ii) near the birth phase shown as full squares corresponding to 0.12 s.*

$$\frac{1}{\tau_{se}v^2}\frac{\partial}{\partial v}(v^3+v_*^3)f - S_f(v) = 0. \tag{3.3.1.1}$$

This equation can be readily solved for the delta-function source, $S_f(v) \sim \delta(v - v_{f0})$:

$$F_{se} \approx \frac{3}{2^5\pi^2}\frac{B^2\beta_f}{E_f(v^3+v_*^3)}, \tag{3.3.1.2}$$

which is the familiar slowing down distribution function. Here τ_{se} is the slowing down time and v_* is the critical velocity when slowing down on electrons and ions becomes equal. It is a Green function of the inhomogeneous first order differential equation (3.3.1.1) the solution of which can be written through the integral for any source function such as the Gaussian in velocity, $S_f(v) = S_{f0}\int \exp[-(v' - v_{f0})^2/\Delta_v^2]\delta(v' - v)dv'$. Substituting it and the Green function (3.3.1.2) into the equation (3.3.1.1) we obtain an expression for the fast ion DF the same as (3.3.1.2) if $v < v_{f0}$ and an integral of the EP source function near the birth velocity v_{f0}, which is a complementary error function, $erfc(x) = 1 - erf(x)$:

$$F = F_{se}erfc\,[(v - v_{f0})/\sqrt{\Delta_v}]/2, \tag{3.3.1.3}$$

which has a smooth behavior near the EP birth velocity, either α-particle birth or beam injection velocity.

The above distribution requires a finite time to settle which is the slowing down time τ_{se}. This process was captured on the TFTR tokamak with the PCX diagnostic [162] [145]. We show figure 3.3.1.1, which reflects this with the DF curves normalized only at one point (shown as norm). One can see how the DF evolves from the initial one close to the source at earlier times to the almost slowing down distribution at a later time.

The NPA measurements in JET DT plasmas showed quantitatively reasonable comparisons for alpha distributions in steady-state like plasma conditions [24] [163]. In those experiments, an impurity-induced neutralization technique was used as discussed in section 2.1, which although it has a lower flux, avoids perturbing the plasma during the measurements. In TFTR for comparison, the injected pellet terminated the discharge [164]. Nevertheless, a passive NPA on JET, without support from the PCX, allowed the study of important physics such as the slowing-down process, knock-on collisions via MeV deuteron measurements [163], ICRF minority ion heating [165] [166], and others [167].

3.3.2 Measuring the fast ion distribution and losses

Here we present an example of measurement techniques allowing NPA diagnostics to provide information about EP loss processes.

We reduce the DF kinetic equation (3.2.1.1) following [168] for the steady state case, keeping only the collisional drag term (accounting for EP slowing down)

$$\frac{1}{\tau_{se}v^2}\frac{\partial}{\partial v}(v^3+v_*^3)F-\frac{F}{\tau_{loss}}=0. \qquad (3.3.2.1)$$

This equation is valid with the source and the sink terms playing the roles of boundary conditions. The solution of this equation is again the slowing down distribution function, Eq.(3.3.1.2), for well confined EPs, i.e. for which τ_{loss} goes to infinity. If the loss time is finite the DF solution can be found from the above equation in the form [169]

$$F=F_{se}\left(\frac{v^3+v_*^3}{v_{f0}^3+v_*^3}\right)^{\tau_{se}/3\tau_{loss}}. \qquad (3.3.2.2)$$

From this equation it follows that the measured slope of the EP velocity distribution has information about the loss time of the measured group of particles. This is what was done in the work reported in reference [168] and shown in figure 3.3.2.1. In the early work [170], the time evolution of the EP distribution function was calculated by using the Fokker-Planck equation and also taking into account the EP losses such as due to charge exchange.

The loss time follows from this analysis by comparing the NPA signal DF slope with the TRANSP slowing down slope and with the slope in the model that gave $\sim 4ms$ given the slowing down time $\sim 60ms$. The exact cause of the losses was only speculated as some activity was observed in the TAE frequency range. Additional analysis is required to pinpoint the detailed characteristics of the loss mechanisms. Another implication for EP redistribution due to AEs is considered in Sec.4.2.3.

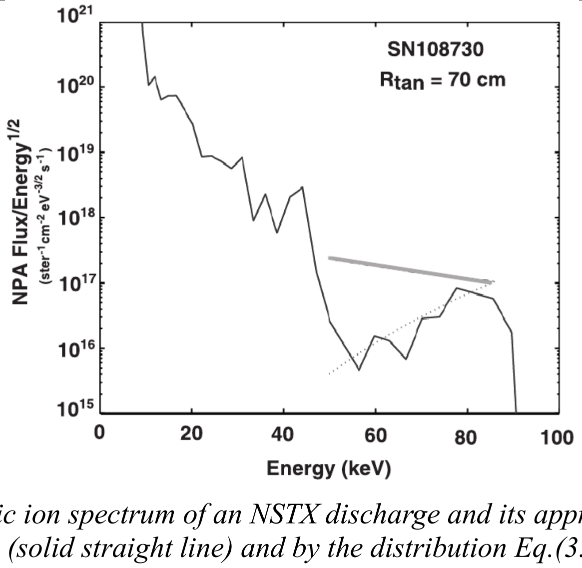

Fig. 3.3.2.1 *The NPA energetic ion spectrum of an NSTX discharge and its approximation at high energy by the slowing-down distribution (solid straight line) and by the distribution Eq.(3.3.2.2) with finite loss time (dotted line)* [168].

NPA measurements of fast ion distributions seem to be unique but can have limited applicability in future DT reactors due to high levels of radiation. The use of radiation resistant Natural Diamond Detectors (NDD) for undertaking the fast ion spectrum measurements is to be recommended. A caveat of NPA and PCX diagnostics is that they measure only single energy dependence (at one plasma radial location for PCX). Thus the information about the EP distribution function from NPA may not be relevant for other phase space locations. For more conclusive statements NPA measurements should be amended by other diagnostics.

3.3.3 Measurements of EP distribution profiles

As follows from section 2.1, a group of important diagnostics capable of measuring the radial and poloidal density profiles of energetic ions include FIDA, neutron and γ-ray emission profile monitors and their spectroscopy, CTS and the NPA diagnostics. The techniques employed involve an integral of the distribution inferred from the measurements that is proportional to the high energy part of the EP distribution. These techniques deserve to be carefully considered in present day devices given the limited information about the fusion alphas in a reactor.

NPA techniques designed to measure knock-on ions are attractive for future use in fusion reactors if applied to the thermal tritons that have a different charge to mass ratio than alphas or D ions. The T ions will therefore be well separated from alphas unlike deuterons. Furthermore, the impurity induced T neutralization is much more efficient than that of alphas and the potential lack of knowledge about the impurities has less effect on the measurements in the evaluation of the DT fuel ratio [163].

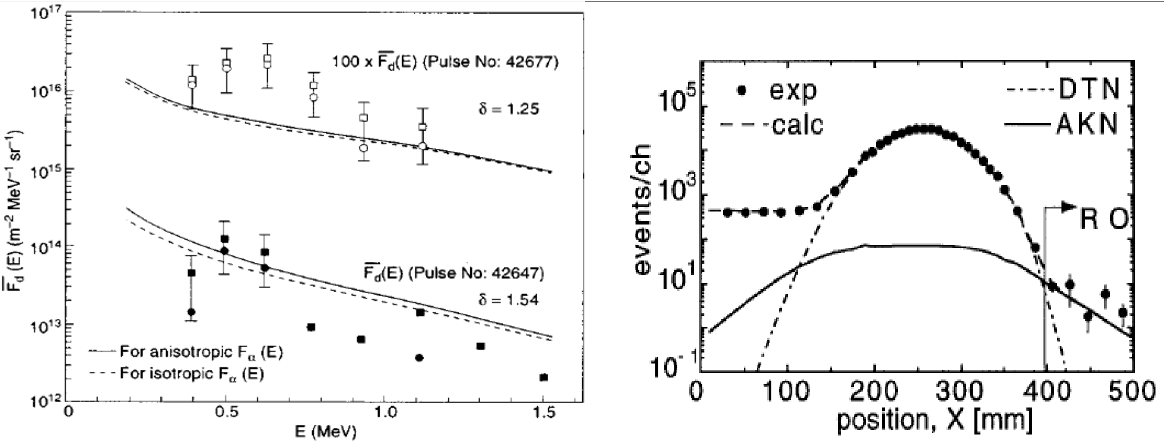

Figure 3.3.3.1 (Left) *JET NPA signal deduced distribution function of knock-on deuterons* [163]. *The error bars shown incorporate the counting statistics in the analysis. The dashed curves show the calculated knock-on distribution for isotropic alphas whereas the solid curves correspond to anisotropic alphas. Closed and open symbols are for two different plasmas for which the analysis produces different slopes. The upper spectra are multiplied by 100 for clarity of illustration (shifted up) on the logarithmic scale. Here δ is the degree of the pitch angle anisotropy and is responsible for the slope of the velocity dependence (Right.) The histogram of neutron emission obtained by MPR spectrometer in the first main DT plasma on JET. The solid and dash-dot curves respectively indicate the alpha knock-on contribution (AKN) and normal DT neutron (DTN) calculated assuming classical slowing down and no alpha particle loss. The part of the histogram in the range of X>400 m.* [37].

To calculate the source of knock-on deuterons the α-particle energy distribution is required, which should then be integrated with a certain weight function. This procedure allows one to obtain a measurable function that is also sensitive to such DF properties as the velocity space anisotropy. Figure 3.3.3.1 illustrates this by showing different measurable slopes of the knock-on deuterons' energy dependence. We note that the measured and predicted curves clearly correlate, which make this diagnostic technically feasible in a fusion reactor. The signature of the alpha knock-on was also observed in the neutron emission spectrum measured by a magnetic proton recoil (MPR) neutron spectrometer as shown in figure 3.3.3.1 (right), where the MPR diagnostic is discussed in Sec.2.1.2 [37]. This technique is also powerful for extracting important information on alpha particle source function in ITER burning plasmas with high fusion power output.

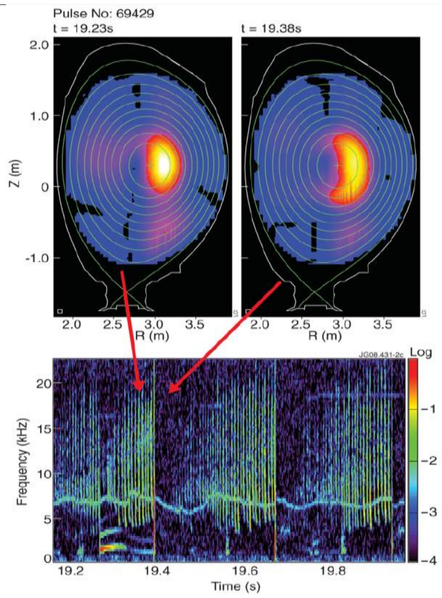

Figure 3.3.3.2. *Tomographic reconstructions of* γ *-ray emission profiles obtained with a* 2D γ *-camera in a* He^3*-minority ICRH heated JET discharge with* $I_P = 3MA, B_\varphi = 3.1T$*: left before a sawtooth crash; right after the crash; bottom is the spectrogram of the accompanying magnetic signal* [171].

Another method to measure the fast ion profiles that was mentioned above is the γ-ray diagnostics for confined EPs [40]. It provides the flux that is represented as an integral of the distribution over some energy range as pointed out in section 2.1 [41]. The signal measured by such diagnostics, can be reconstructed using tomographic methods and directly compared with numerical computations of the EP distribution integrated in the same way with the known cross-sections. The resulting 2D image of one particular measurement is shown in Fig. 3.3.3.2 [171]. The image makes use of the signal collected over $100ms$. A special modeling code helps to deduce such information as the effective tail temperature, identify the EP population and evaluate its density. The EP distribution function can also be derived from neutron emission spectroscopy in addition to gamma ray spectroscopy, as discussed in Sec.2.1.

3.3.4 Non-monotonic distribution of beam ions in STs

There are various observations of non-monotonic fast ion distribution functions made in STs [172] [173] [174]. STs appear to be vulnerable to effects leading to energy inverted distributions due to their relatively low equilibrium magnetic field and large ratio of EP Larmor radius (and drift orbit width) to tokamak major radius. These measurements of such fast ion distributions can be understood using the general ideas of ion loss effects on the DF described in sec. 3.1.1. It is noteworthy that other observations of inverted distributions in velocity are known and appeared in the comprehensive review Ref. [1].

On START, measurements were made to study the physics of fast ion confinement in STs using an NPA [172]. Those simulations used the LOCUST code that indicated that after beam injection, confined $E_f = 30\ keV$ ions with wide orbit widths were able to drift outside the plasma where large neutral densities resulted in their loss. This charge exchange loss mechanism was responsible for the formation of the inversed distribution function in ion energy. As a result, the bump-on-tail beam ion distribution emerged. Further estimates showed that for low-n TAEs, the positive velocity gradient makes a contribution to the drive comparable to the contribution coming from the radial pressure gradient. As the effect was primarily coming from the edge of the plasma, both simulations and NPA measurements indicated that the largest inverted velocity gradient was expected due to charge exchange processes at the plasma periphery.

Somewhat similar observations and explanations are given in a paper from MAST [173]. The use of an NPA on MAST gave direct access to the velocity dependence and helped to build a physical picture of the observations. According to this explanation, the injection of $40 - 70\ keV$ beams into the plasma created the inversed, bump-on-tail like, distribution in velocity in a similar way to the earlier START experiments. Two chief mechanisms were involved, Coulomb collisions and charge exchange, that support the classical behavior of fast ions in the analyzed discharges. Simulations by the TRANSP code further supported this conclusion in both L- and H- mode plasmas.

In a recent NSTX publication [174] observations were reported on the so-called HEF (high energy feature) during NBI. In NSTX plasmas the NPA diagnostic measures a sudden increase of the beam ion flux coming from a few high energy (near the injection energy) channels. The increase is up to 10 times for the peak-to-base ratio seen in H-mode plasmas with strong injection. Although the HEF does not seem to have any effect on plasma performance, it presents a challenge for EP research to explain. It was argued that the plasma in NSTX is very close to the first wall, so that fast ion neutralization at the edge can be excluded as a possible candidate for explanation.

In the same publication [174], a plausible mechanism responsible for the HEF was given in terms of the quasi-linear (QL) evolution of the fast ion DF in phase space. The underlying oscillations accounting for QL diffusion are suggested to be the high frequency modes (either global Alfvén eigenmodes - GAEs or compressional Alfvén eigenmodes – CAEs, see sec. 4.2.2.2) present in the plasmas considered. When beam ions slow down they interact with these modes. This results in fast ion losses and in a positive slope in the velocity distribution function with respect to velocity. The proposed mechanism leads to a distribution function evolution that is very similar to that observed by the NPA in NSTX and is illustrated in Fig.3.3.2.1.

For energetic ions produced in burning plasmas in the MeV energy range, the charge exchange cross-section with fuel ions near the edge can be neglected, as mentioned in Sec.2.1. Thus it is expected that the above inverted distribution function will not be produced in this case. However, the charge exchange process with hydrogenic low Z impurities in the edge plasma region may induce a non-monotonic DF of energetic ions such as deuterons.

Understanding the HEF mechanism (and other non-monotonic velocity dependences) is important for the development of theory as it may give a good handle to control various deleterious effects identified in Sec. 8. If the HEF were understood it may be useful to help to resolve the alpha-channeling problem (see sec. 4.2.7). Further theoretical and perhaps experimental studies are needed to establish the mechanism behind the HEF.

4 Wave particle interaction

In most interpretations of experimental observations the excitation of instabilities by fast ions in fusion plasmas requires three conditional elements to be identified. The first is the presence of (stable) eigenmodes. The second is the presence of a drive, i.e. the source of energy for the instability. The third is the group of resonant particles that can effectively exchange energy between the EP sources and the eigenmode. The phenomena observed in the experiments that we discuss in detail in this review, either have these elements or theory attempts to find them.

4.1 External perturbation effects on EP confinement

EP ions can interact with electromagnetic fields of plasma instabilities such as the Alfvénic modes considered in section 4.2.2 or with the externally excited or modified magnetic fields (see 3.2.2). One example of externally imposed fields is by using RMP (resonant magnetic perturbation) coils This is an axisymmetry breaking phenomenon that has attracted a lot of attention recently. In particular, one of the top technical challenges for future ITER discharges is the interaction between the burning plasma and the wall's solid material [175]. Near the plasma boundary, so-called edge localized modes (ELMs) can appear that affect the plasma performance and induce large heat loads to the divertor plates. ELM control becomes an important problem that may be solved by applying RMPs. The commonly accepted understanding of RMP stabilization of ELMs is through the reduction of the edge plasma pressure gradient that results in a more stable edge and suppresses ELMs. The initial applications of RMP coils reduced the amplitude and increased the frequency of ELMs without deteriorating the core plasma performance substantially [176]. The perturbation introduced can be strong enough to trigger additional secondary instabilities such as resistive wall modes and locked modes (or even neoclassical tearing modes (NTMs) and sawteeth) as the burning plasma is normally understood to be near the peak of its performance and stability.

Research on RMP studies has picked up with improved numerical tools. One recent example includes numerical simulations and experiments on ASDEX Upgrade (AUG) [177]. In these simulations, the perturbed magnetic field was not reduced by plasma shielding as was pointed out, representing a pessimistic estimate of RMP coil effects. Notable results were modeled for the parallel current drive beam when the losses increased by approximately four times. This could be a resonant effect but neither this nor its implications for ITER were discussed in this reference. A simulation based on the orbit following code OFMC showed that RMPs could bring noticeable losses of beam ions generated by the ITER NBI Heating and Current Drive system (HNB) if the plasma shielding effect is not taken into account [178].

Another experimental study of a relatively preliminary nature [179]has indicated an enhanced beam ion loss signal (measured by a FILD) during the application of RMP to successfully suppress ELMs on KSTAR. The mechanisms responsible for increase were not clearly resolved.

A recent experimental paper on the effects of both resonant and non-resonant magnetic perturbations on fast ion confinement argued in favor of the synergistic effect between the magnetic perturbations and internal fluctuations [180], such as tearing modes. The results obtained were based on measurements from DIII-D, AUG and KSTAR and lent support to the development of self-consistent numerical models in which the perturbations are screened by the plasma. Screening effects can significantly change the losses of the fast ions.

The influence of RMPs on EP confinement is being actively studied in many present day devices and is seen as important for future reactors. We consider it a high priority issue for reactor plasmas, as identified in Sec. 8.

4.2 Collective effects

From the above studies of single particle effects we move to the so-called collective effects for which it is essential that the group of charged particles is characterized by its MHD properties. These properties include the EP current and charge density in addition to their hydrodynamic density, mass, pressure and velocity. For collective effects, waves or organized motions of plasma are very important since the particles can interact over long ranges through their electric and magnetic fields.

4.2.1 MHD and kinetic descriptions

Linear stability of MHD modes has proven to be a powerful theoretical tool to analyze experimental data and to design new experiments for thermonuclear fusion research [181] [182]. The model of ideal MHD is based on the treatment of the plasma as a fluid that can carry the current and can be augmented by infinitely large conductivity, i.e., the vanished electric field along the magnetic field line, $E_{\parallel} = 0$. Within this model a range of plasma oscillations can be analyzed, such as internal and external kinks, ballooning modes, tearing modes, acoustic and Alfvénic modes, fast Alfvénic modes (or fast magnetosonic, compressional Alfvénic) and so on (see figure 4.2.2.2 for more complete classification of the various known eigenmode solutions).

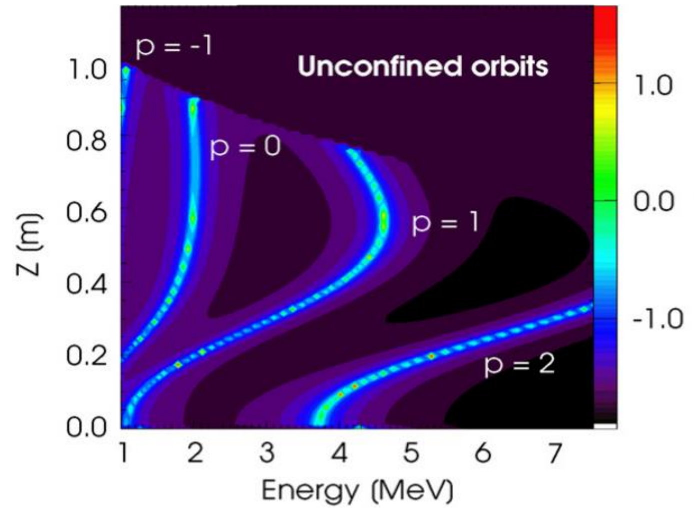

Figure 4.2.1.1 *Main resonances in energy and bounce point position for ICRH hydrogen ions that resonating with the* $n = 3$ *low shear TAE in JET* [194]. *Shown values of* p *indicate the bounce harmonics of a phase space resonances. In our notations* Ω_{np} *equals to the left hand side of Eq. (4.2.1.6) and p corresponds to resonance l.*

Many AEs were discovered by codes employing the ideal MHD approximation and it is also useful to start with the same restriction here. It is necessary to perform the initial stability analysis of ideal modes of the plasma with zero real frequency. For the stability of modes with finite frequencies, the theory utilizes the kinetic extension that is introduced below.

The equation of motion for plasma particles can be integrated to give a quadratic form

$$\delta W + \delta K = 0; \delta K = -\frac{\omega^2}{2}\int \rho\left(\vec{\xi}\right)^2 dx^3; \delta W = -\frac{1}{2}\int \vec{\xi} \bullet \vec{F}\left(\vec{\xi}\right) dx^3. \qquad (4.2.1.1)$$

The quadratic form is useful in providing the stability properties of the system within certain limits. From this form one can find that the real and imaginary parts of the oscillation frequency, two basic elements of the perturbed theory, should satisfy

$$\omega_r^2 = 2\delta\, W / \int\, \rho \vec{\xi}^2 dx^3, \quad \omega_i/\omega_r = -\Im \delta\, W / 2\, \delta K.. \qquad (4.2.1.2)$$

The real part of δW is given by MHD and making use of the force balance equation can be written in the form

$$\delta W = -\frac{1}{2}\int \left[\frac{1}{c}\vec{\xi}_{\perp}^{*} \bullet \delta(\vec{J} \times \vec{B}) - \vec{\xi}_{\perp}^{*} \bullet \nabla \delta p_c\right] d^3x, \tag{4.2.1.3}$$

where the plasma displacement includes both incompressible Alfvén and compressible acoustic parts. There are various forms of the potential energy of oscillations [183] [184] [181] [185] [186] that are omitted here.

However we note that the variational Lagrangian formalism [187] for linearized perturbations about an equilibrium configuration makes use of the above expressions and gives basic equations for the eigenmodes [188]. In the next section we present the eigenmode equations obtained this way. A quadratic form formalism can be used to derive a local version of the dispersion relation [189]

$$-i\frac{\omega}{\omega_A/q} + \delta W + \delta W_f = 0, \tag{4.2.1.4}$$

where $\omega_A = v_A/R$ with the Alfvénic speed v_A and the plasma major radius R

The EP contribution to the potential energy is typically proportional to EP beta and is thus small if it is done within the MHD framework only. This framework does not normally describe the excitation of specific EP instabilities. However, the situation is drastically different if the theory goes beyond MHD and becomes kinetic. Namely, the kinetic framework allows one to consider details of EP distribution in the phase space and to identify resonant particles with a certain plasma oscillation. That is the kinetic extension that allows the study of the stability of eigenmodes found by the MHD theory. This approach is presented well among others in such reviews as [14] [15].

The kinetic EP contribution to δW, i.e. δW_f relies on the derivation of EP perturbed distribution function given the perturbations obtained by solving the drift kinetic equation and represents the most general way to find the growth rate in the linear perturbative theory of tokamaks [190] [191]. In order to write the expressions for δW_f one has to employ the integrals of (or constants of) motion (COM) variables detailed in Sec.3. We write the EP contribution to the quadratic form neglecting cyclotron interactions the following way:

$$\delta W_f = -\frac{4\mathrm{m}_f^2\pi^2 c\omega}{e_f}\int dP_\varphi d\mu dE_f \tau_b \sum\nolimits_{mm\prime ll\prime} E_f^2 F_{fE_f}^{\prime} \; \frac{G_{m\prime l\prime}^{*} G_{ml}(1-\omega_*/\omega)}{\omega - n\bar{\omega}_D - l\omega_b}. \tag{4.2.1.5}$$

Here $\omega_* = n(F'_{fP_\varphi}/F'_{fE_f})$ and we explicitly introduced the toroidal mode number *n* in the resonant denominator to underline its role in the resonance condition. The parameters τ_b, ω_D and ω_b are respectively, the bounce time, toroidal precession angular frequency and the bounce angular frequency. When it equals to zero the denominator of this expression determines the resonances given by the poloidal harmonic number and the bounce frequency. Here coefficients G_{ml} are the harmonics of EP - wave interactions derived from the scalar product $\vec{v} \bullet \vec{E}$ averaged over time. The equation (4.2.1.5) together with Eq.(4.2.1.2) is standard to use in the perturbative theory to compute the growth and damping rates of a certain eigenmode such as the Alfvénic modes [14].

It is interesting to note that in the low frequency limit and MHD approximation only a fraction in the wave interactioin scalar product survives gyro averaging $\vec{v} \bullet \vec{E} \approx \vec{v}_d \bullet \vec{E}_{\perp}$, which means that in the absence of the magnetic field drift, the EP instabilities considered below are impossible. This is true for the cylindrical plasma in the homogeneous magnetic field.

The problem of AE stability is a problem considered/developed on a time scale longer than the Alfvén time, that is why matrix coefficients G_{ml} account for this by averaging vector product. Averaging is non-zero only for energetic particles near the resonances when the phase of EP – wave interaction accumulates (changes) integer number times 2π. In fact, even when this phase is a rational fraction of 2π there is a possibility for weak "resonance" like interaction [192] [193]. For resonant particles the resonance condition is thus (for generality we added the cyclotron frequency ω_c)

$$\omega - n\bar{\omega}_D - l\omega_b - j\omega_c = 0. \tag{4.2.1.6}$$

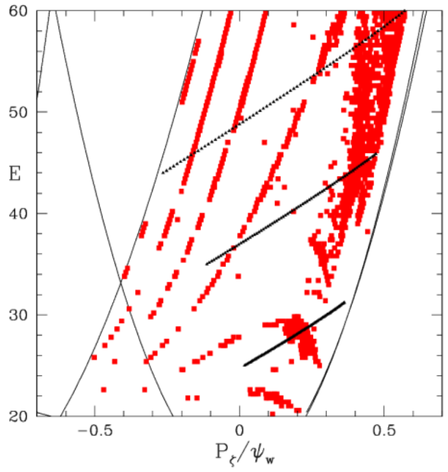

Figure 4.2.1.2. *Plane of* P_φ *(denoted* P_ζ *in the figure) and* E *with one value of* $\mu B_0 = 14\mathrm{keV}$ *for an* $81\mathrm{kHz}, n = 3$ *TAE mode with* $10 \leq m \leq 23$ *showing a kinetic Poincare plots along a line originating on the left at* $44\mathrm{keV}$ *modeled for DIII-D. Black lines indicate the variations of particle positions in the phase space due to considered TAE perturbation. The figure is adopted from Ref.* [196].

The resonant interaction formalism to be considered in section 4.2.6 is extremely useful describing the EP instabilities as we show below.

We show examples of the resonances for the low-shear TAE mode in JET discharge with ICRH in Fig. 4.2.1.1 as computed by HAGIS code [194]. The knowledge of the resonances in the phase space is important as it determine if the excitation of certain TAEs may or may not lead to effective particle transport.

An independent way to identify the wave particle interaction (WPI) resonances in simulations is offered in Refs. [195] [196] using the guiding center code ORBIT [197]. Instead of direct computations of the resonance conditions (such as Eq. (4.2.1.6)) a threshold condition for particle deviation from its original unperturbed COM trajectory is introduced. It defines how much the particle should deviate in energy and P_φ due to the perturbations with given amplitude. Thus a new method of determining domains of the phase-space in which good COM do not exist gives exact locations of the resonances and the island widths. This procedure is very advantageous to have in calculations as it can be implemented at any time step. Another advantage of this technique is that the introduced thresholds allow to single out the strongest resonances right away. An example of this technique application is given in Fig. 4.2.1.2 for one of the TAE modes analyzed in [195]. The black lines show directions of EP COM variations due to the phase space islands and the TAE perturbation. Further development of this technique allowed inferring the trapping frequencies inside the island with relatively simple calculations.

4.2.2 Alfvén Eigenmodes

The Alfvén wave is typically referred to as one of three fundamental MHD solutions. That is any MHD solution can be represented by a linear superposition of the fundamental solutions. They are introduced in this section and can exist either as decoupled as presented or coupled as in the case of CAE modes (see 4.2.3 for example). We identified the Alfvénic instabilities and their effects as one of the critical topics for fusion in Sec. 8.

The study of energetic particle physics can be traced back several decades to papers on cyclotron excitation of Alfvénic instabilities by alpha particles [198] [199] and on thermonuclear “drift” instabilities, i.e., those which are caused by the spatial inhomogeneity of alphas [200] [201]. It is important to note that Ref. [201] was the first to consider the shear Alfvén wave instability with the dispersion relation Eq. (4.2.2.2) (see below) excited by energetic ions.

Instabilities excited by fusion products were later reexamined as dangerous for alpha confinement in a reactor [202] [203] but this time were reconsidered at relatively low frequencies, much lower than the ion cyclotron frequency. These studies focused on localized instabilities that were not considered to be characterized by weakly damped eigenmode structures and thus prone to be damped due to short wavelength, i.e. intrinsic parallel electric field. Thus they were not considered seriously. The interest in these modes was renewed in the late 80th when the so-called toroidicity-induced Alfvén eigenmodes (TAE) were predicted theoretically [204] [185] and discovered experimentally shortly after [4] [5]. TAEs have rather global mode structure and therefore not affected by the parallel electric field damping due to short wavelength. Since then, TAEs have been considered the most likely candidates to limit the alpha particle confinement [205] and fusion reactor performance [137].

In a single fluid MHD theory of ideally conducting homogeneous plasma, one can cast the plasma oscillations in an equation for the plasma displacement vector, $\vec{\xi}$:

$$\frac{\partial^2 \vec{\xi}}{\partial t^2} = v_a^2 \nabla(\nabla \cdot \vec{\xi}) + v_A^2 \nabla_\perp(\nabla \cdot \vec{\xi}_\perp) + v_A^2 \frac{\partial^2 \vec{\xi}_\perp}{\partial z^2}. \tag{4.2.2.1}$$

This equation describes three types of waves each corresponding to each term on the right hand side of that equation. **Shear Alfvén** oscillations and their dispersion follow from this equation if the parallel component of the displacement to the magnetic field line and $\nabla\vec{\xi}_\perp = 0$ are zero and have the form

$$\frac{\partial^2 \vec{\xi}_\perp}{\partial t^2} = v_A^2 \frac{\partial^2 \vec{\xi}_\perp}{\partial z^2} \text{ or } \omega^2 = \omega_A^2 = v_A^2 k_\parallel^2. \tag{4.2.2.2}$$

Any solution of this equation can be represented as a superposition of waves propagating along z axis with the Alfvén speed v_A. One can obtain an equation for the **magnetoacoustic (or fast, or compressional) Alfvén** transverse oscillations in a low pressure plasma by ignoring the sound speed terms in the above equation and reducing to the following (and dispersion)

$$\frac{\partial^2 \nabla \cdot \vec{\xi}_\perp}{\partial t^2} = v_A^2 \Delta \nabla \cdot \vec{\xi}_\perp, \;\; \omega^2 = \omega_{cA}^2 = v_A^2 k^2. \tag{4.2.2.3}$$

Another branch is also characterized by $\nabla \cdot \vec{\xi}_\perp \neq 0$ and by nonzero parallel displacement $\xi_\parallel$, which satisfies

$$\frac{\partial^2 \xi_\parallel}{\partial t^2} = v_a^2 \frac{\partial^2 \xi_\parallel}{\partial z^2}, \;\; \omega^2 = \omega_a^2 = v_a^2 k_\parallel^2. \tag{4.2.2.4}$$

This is the **acoustic branch** or ion sound longitudinal wave. In the limit of $\beta \to 0$ the plasma displacement is along the B field line only, i.e. depends on *z*.

In a homogeneous magnetic field plasma, one can summarize these branch properties as follows: Shear (or slow) Alfvén wave is transverse, propagates parallel to $\vec{B}$ with the Alfvén phase velocity associated with $\delta\vec{B}$. The magnetosonic (or compressional Alfvén or fast Alfvén) wave is the longitudinal wave that propagates perpendicular or parallel to $\vec{B}$, associated with $\delta\vec{B}$. The sound (or acoustic) wave is longitudinal, propagates parallel to $\vec{B}$, the adiabatic sound velocity is the phase velocity not associated with the perturbed quantities $\delta\vec{E}$, $\delta\vec{j}$, or $\delta\vec{B}$. The MHD oscillations will be damped when the fluid is not perfectly conducting, but have a finite conductivity or if viscous effects are present.

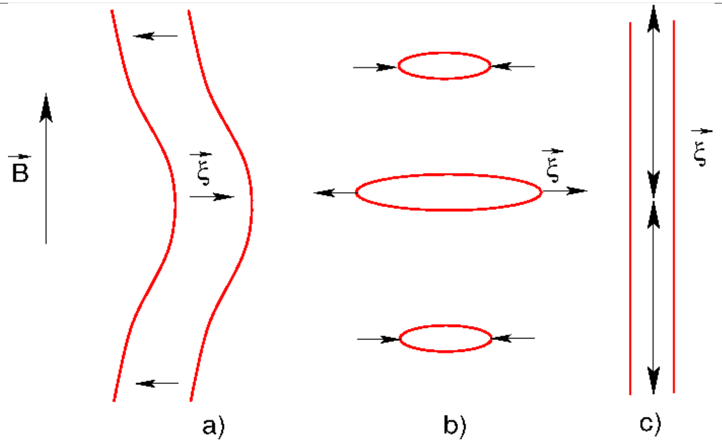

***Figure 4.2.2.1**. Illustrations of the plasma displacement in three fundamental MHD waves: (a) shear Alfvénic, (b) magnetosonic and (c) acoustic waves. We assume that the background magnetic field is directed vertically as shown by the vector $\vec{B}$.*

These branches can also be introduced using one of their primary properties, polarization, which determines the background plasma displacement orientation. It is widely used in experimental identification of plasma oscillations. Figure 4.2.2.1 illustrates the corresponding plasma displacements of shear Alfvén, fast Alfvén and acoustic branches. They are all relevant to the instabilities excited by EPs and observed in experiments, as we will discuss. However, in experiments they are observed normally as a dominant one fundamental oscillation with some coupling from others such as beta-induced Alfvén acoustic eigenmodes (BAAE) modes [206].

Consider one of those branches, the shear Alfvén wave. Its phase velocity is large in comparison with the thermal ion speed $v_A \gg v_i$, which is a straightforward consequence of a low plasma beta, $\beta_i \ll 1$. This allows resonances between the oscillations and energetic ions, which are added to the plasma for heating, that is $E_f \gg T_i$ and $v_f \sim v_A \gg v_i$. Because of this, thermal ions can interact with AEs only in the tails of their Maxwellian distribution.

Observed plasma oscillations in the form of plasma eigenmodes have characteristic frequency relations that follow from their dispersions, so that $\omega_{cA} \gg \omega_{sA} \gg \omega_a$. One can show that the effects of these modes on EPs are mostly spatial transport from sound and shear Alfvén waves and energy diffusion from compressional Alfvén waves which is based on their frequencies [207] (see Eq.3 of that reference). These waves do not exist in the plasma unless they are driven externally or the corresponding eigenmodes are excited by fast ions.

It can be shown that the low frequency oscillations, such as shear Alfvén branch, can interact with EPs and are dangerous for EP radial confinement, low frequency leads to radial particle redistribution [207]. The corresponding **shear Alfvén eigenmodes** are solutions of a more generalized system of coupled equations for plasma oscillations, which we can write in the form

$$\Sigma_{m,n}\hat{L}_{m,n}\Phi_{m,n} = 0, \qquad (4.2.2.5)$$

and has a form appropriate for both 3D and 2D geometries. The coupling itself comes from the dependencies of the coefficients in the eigenmode equation on the poloidal and toroidal angles. The simple coupling in a tokamak is coming from the dependence of the magnetic field strength on the poloidal angle and from the Shafranov shift, which also contributes to the poloidal variation. In 3D toroidal plasmas, toroidal mode coupling is in addition to the poloidal one as the geometrical matrix coefficients vary in both poloidal and toroidal directions. The characteristic Alfvén eigenmodes in 3D plasmas are discussed in more details in section 4.2.2.3.

There is no coupling in a tokamk plasma between the toroidal harmonics of the perturbed potential and the sum in that equation over the poloidal harmonics, which leaves only dominant $m \pm 1$ and m terms [208]. The important property of this is that it can be used to describe the so-called Alfvén continuum in a tokamak, which follows if we assume that the solution is singular in radius $r\,\partial/\partial\, r \gg \partial/\partial\,\theta$. It corresponds to the specific class of singular solutions with exact Alfvén wave polarization that may couple to realistic physical solutions and cause the so-called continuum damping.

One of the best tutorial explanations of the strong continuum “solution” damping is given in Ref. [8]. It can, however, also be explained in a different but complementary way. Consider high-n Alfvén wave in a cylindrical plasma having a safety factor profile $q(r)$, which consists of one poloidal harmonic. Then the eikonal of the perturbed potential $\phi = \phi_m \exp\left(-i\omega t + i\vec{k}\vec{r}\right)$ should satisfy the dispersion relation (4.2.2.2). To zeroth order Eq. (4.2.2.2) (right) is satisfied. The next order equation can be obtained advancing the oscillation frequency by the damping rate, $\omega_0 \rightarrow \omega_0 + i\gamma$, and the local Alfvén frequency by the radial wavelength, $\omega_{A0} \rightarrow \ \omega_{A0} + \omega_A'(ik_r^{-1})$. This results in the equation for the imaginary parts: $2\omega(i\gamma)\phi_m \approx -2\omega_A\omega_A'(ik_r^{-1})\phi_m$. Allowing $\omega = \omega_{sA}$ and $k_r \approx k_\theta$, the damping rate is thus $\gamma = -\,\omega_A'/k_\theta$, which reflects the fact that the pulse will quickly disperse in radius [8]. Here we have chosen signs for the damping rate to be negative.

Thus the continuum and its location indicate which frequencies and modes are not allowed or strongly damped. One can present the following form for the operators $\hat{L}_m, \hat{L}_{m\pm1}$ in a tokamak (see for example [209] [208] [210]):

$$\begin{gathered}\hat{L}_m = \frac{1}{r}\frac{\partial}{\partial r} r\left(\frac{\omega^2}{v_A^2} - k_{\parallel m}^2\right)\frac{\partial}{\partial r} - \left(\frac{\omega^2}{v_A^2} - k_{\parallel m}^2\right)\frac{m^2}{r^2} + \left(k_{\parallel m}^2\right)'\frac{1}{r}, \\ \hat{L}_{m\pm1} = \frac{1}{r}\frac{\partial}{\partial r} r\hat{\varepsilon}\frac{\omega^2}{v_A^2}\frac{\partial}{\partial r} + 2\frac{\omega^2}{v_A^2}\Delta_{Sh}'\frac{m(m\mp1)}{r}.\end{gathered} \tag{4.2.2.6}$$

The continuum equation can be obtained from the eigenmode equation by making the highest radial derivative (2nd) equal to zero, which is equivalent to the Alfvén dispersion relation given above and corresponds to a singular solution at the continuum point. In the system of equations the continuum has the same meaning but a more complicated expression involving sideband harmonics and can be represented as a matrix operator [204]. The presence of the sidebands turned out to be important for the existence of global modes, which were discovered numerically [204] and modeled analytically [211]. The sidebands break up the continuum and create gaps where the singular solutions can not be formed. The resulting gaps were noted to be analogous to the gaps that appear in the energy spectrum of valence electrons in a periodic potential well of the crystal lattice [212] with the essential difference that the Alfvén gaps result in extended radial solutions.

We present in Fig. 4.2.2.2 a typical Alfvén continuum obtained by the NOVA code [185] for the nominal ITER plasma with (nearly monotonic in radius) normal (positive) magnetic shear, s [213]. The equilibrium generated using the TRANSP code [135] shows the presence of slight q profile reversal inside $r/a \approx 0.3$ surface due to the sawtoothing plasma.

The gaps shown in figure 4.2.2.2 host eigenmodes that are due to neighboring poloidal harmonics coupling, such as m and $m \pm 1$ for TAEs, m and $m \pm 2$ for ellipticity-induced AEs (EAE) and so on. The corresponding continuum reflects not only the coupling of the Alfvénic branches but also explains the frequency shift due to the presence of BAEs introduced in Ref. [214] or GAMs [215] and introduced here in section 4.2.4. In the next section we consider TAEs that appear due to Alfvén harmonic coupling.

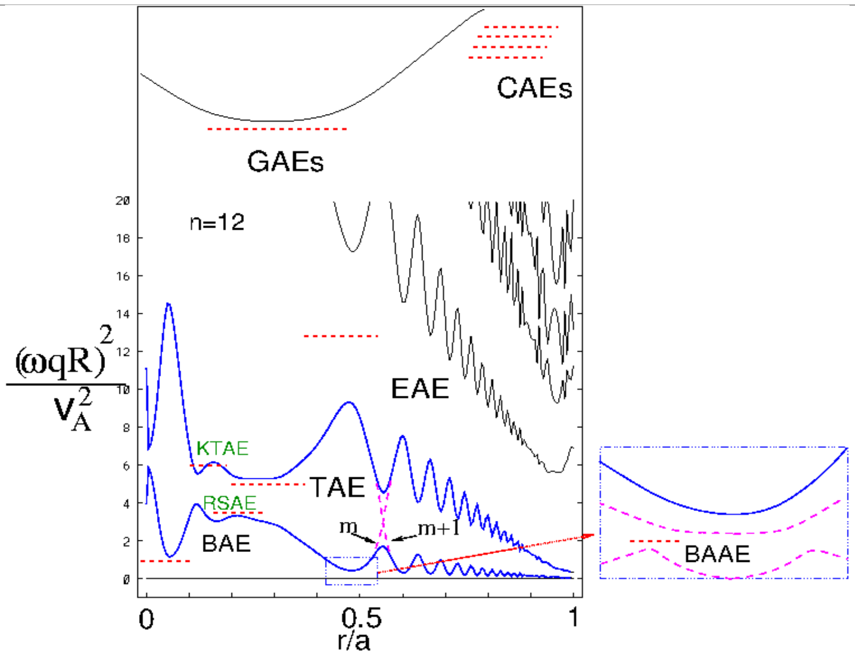

Figure 4.2.2.2 *Alfvén continuum (AC) for* $n = 12$ *in ITER tokamak* [213] *obtained by the ideal MHD code NOVA. Shown are the gaps in the continuum corresponding to the BAE, TAE, EAE and BAAE modes. The low frequency BAE gap is due to AC upshift by the coupling of the Alfvénic and acoustic waves as explained in section 4.2.4. This coupling also leads to the formation of a new gap near the rational magnetic surface called the BAAE gap shown in the insert. Dashed curves are added schematically on the insert due to coupling of the Alfvénic and acoustic waves. Dashed horizontal lines correspond to the global eigenmode solutions.*

Although in this review we are explaining the variety of *AE* modes it seems important to list them all in one place. The well-known toroidicity-induced eigenmodes (TAEs) [204] lie in the TAE gap and are primarily the Alfvénic polarization modes. In the same frequency range lie the reversed-shear AEs (RSAEs or ACM, section 4.2.2.2) [216] [217]. Below those reside the so-called beta-induced Alfvénic eigenmodes (BAEs, section 4.2.4.1) with strong influence from the acoustic waves [218] [219]. At lower frequencies there is the beta-induced Alfvén-acoustic (BAAE, section 4.2.4.1) gap and corresponding eigenmodes (see section 4.2.4) [206]. Immediately above the TAEs there is a group of relatively localized kinetic modes, kinetic TAEs (or KTAEs, section 4.2.2.4) [220]. Above the TAE gap there is an ellipticity induced AE (or EAE) gap [221] with the EAE modes and following the non-circularity induced gap (NAE) [222] [223]. At higher frequencies one can find the global AEs (GAEs, section 4.2.2.2) [224] and compressional AEs (or CAEs, section 4.2.3) [225], which do not require gaps in the continuum. GAEs in stellarators can exist in the same frequency range with TAEs as we discuss in Section 4.2.2.2.

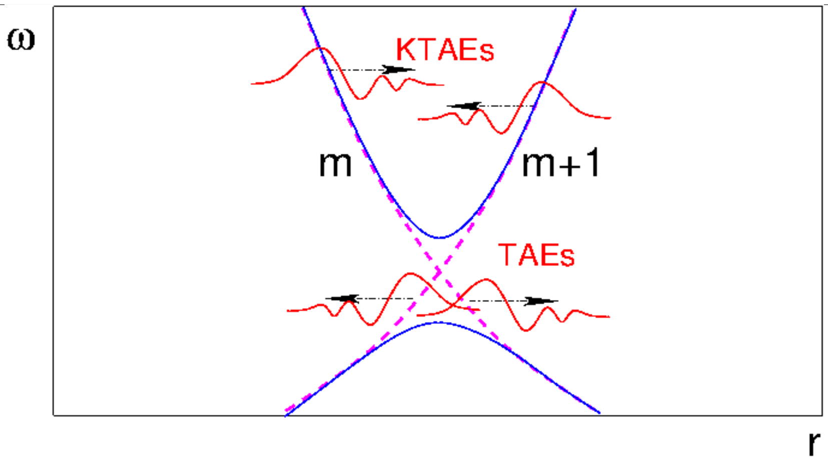

Figure 4.2.2.3 *KTAE and TAE mode formation making use of two poloidal harmonics* $m, m+1$. *Both KTAE and TAE solutions are not propagating in radial direction even though can be understood as coupled solutions of propagating local kinetic waves.*

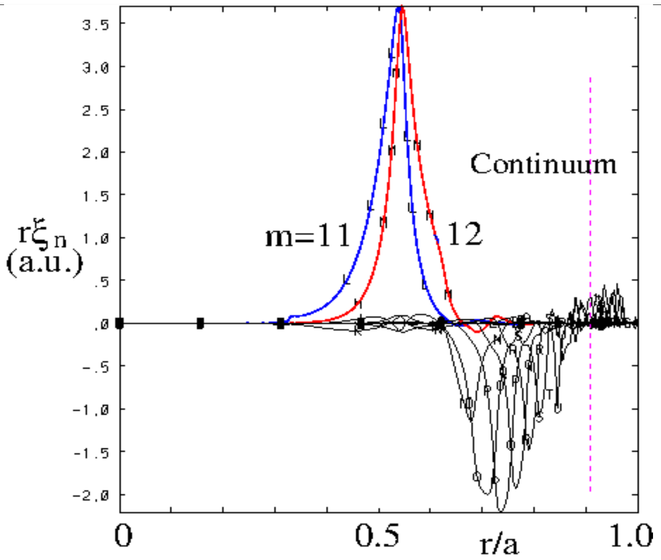

Figure 4.2.2.4 *N=12 TAE mode structure as computed by NOVA code for normal shear H-mode ITER equilibrium considered above in Fig. 4.2.2.2 with the poloidal mode numbers shown as indicated. The structure is dominated by two harmonics, which is known as a couplet.*

4.2.2.1 TAEs and some varieties, EAEs, NAEs

Axisymmetric plasma. Let us start with the coupling of m and $m+1$ harmonics when the so-called TAE couplet emerges. It can be a stand-alone eigenmode solution. The coupling is at the point where two continua intersect, $k_{\parallel m} = -k_{\parallel m+1}$ and thus $q_{TAE} = \frac{m+1/2}{n}$. The figure 4.2.2.3 shows a schematic of the couplet formation when two harmonics form the gap. When TAEs are formed, the kinetic Alfvén wave (KAW) from the m harmonic interacts with $m+1$ harmonic. This interaction is at a maximum of the KAW radial dependence, i.e. at a point close to the continuum (Fig. 4.2.2.4). The formation of the KTAE structure is mentioned again in section 4.2.2.3.

Correspondingly, the nominal frequency of the couplet $\omega_{TAE} = v_A/2q_{TAE}\,R$ is often considered as the nominal TAE frequency. If the magnetic shear is not too small the couplets can be combined into a global TAE solution to be found numerically [204]. In the plasma from the presented example well-aligned gaps from the plasma core to the edge lead to global type TAEs. A numerical global TAE solution for the same ITER equilibrium with nearly monotonic q-profile is shown in figure 4.2.2.4 [213]. Another interesting feature of this solution with the normalized frequency $(\omega\, qR/v_A)^2 = 1.97$ is that it tunnels to the right through the continuum at $r/a > 0.9$ with negligible damping because its harmonic goes exactly to zero at the continuum as predicted by theory [226].

A more sophisticated expression for the TAE frequency is obtained analytically in the low inversed aspect ratio and low-β approximation [227]:

$$\omega_{TAE}^2 = \left(\frac{v_A}{2qR}\right)^2 \left[1 + \frac{3}{2}\left(\frac{r_0}{R} + \Delta'_{Sh}\right)^2 + 4\frac{\Delta_{Sh}}{R} + \frac{r_0^2}{R^2} - 2\frac{r_0 \Delta'_{Sh}}{R} + 2g^2\right], \qquad (4.2.2.1.1)$$

where r_0 is the minor radius of the mode location, g^2 is the correction to the toroidal magnetic field. This dispersion already provides the plasma parameters' functional dependencies, which are important in diagnostics and in the study of the TAE stability. One consequence of this is the stabilization of TAEs by the frequency downshift and the subsequent mode merging into the continuum if the plasma pressure is sufficiently large. The width of the TAE frequency gap in the continuum was also obtained [227]:

$$\omega_{\pm}^2 = \omega_0^2 \left[1 \pm 2\left(\frac{r_0}{R} + \Delta'_{Sh}\right)\right] \qquad (4.2.2.1.2)$$

If the magnetic shear is low near the magnetic axis, a special kind of TAE emerges consisting of a single couplet that contains two poloidal harmonics. This is the so-called core-localized TAE (or cTAE) [228] [229] that was first observed in TFTR plasmas [230]. Further studies showed a multiplicity of eigenmodes could exist with mode frequencies lying in the gap instead of just one TAE solution [231]. Core localized TAEs having even or odd radial mode parity can exist and both were observed in JET [232].

Because the cTAEs exist in the center of the plasma they correlate strongly with the sawteeth oscillations. It was shown on TFTR that their excitation results in the loss of beam ions and can trigger monster sawtooth crashes [233] [234]. Similar measurements were performed on JET with ICRH minority ions providing the TAE drive [235].

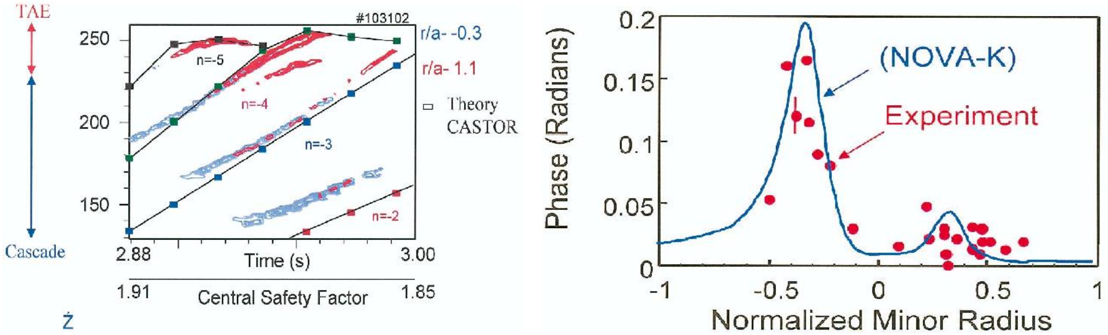

Figure 4.2.2.1.1 *The figure at left shows the contour plot of the observed TAE/RSAE activity in DT TFTR plasmas after the NBI was turned off. Shown in blue is the signal of the core density fulctuations (reflectometer at* $r/a \approx 0.3$ *on the high field side). Shown in red are the signals of the edge Mirnov magnetic measurements spectrum. Also shown as squares are the computed by the CASTOR code* [244] *TAE/RSAE frequencies for different* n *numbers. The right figure shows the measured radial structure of the RSAE mode and how it compares with the structure predicted by the NOVA code* [204] [185]. *The figures are adopted from Ref.* [243].

This approach to computing the global TAE structure and its dispersion relation numerically is the most accurate as it does not require large aspect ratio and small plasma pressure but it is still only one way to address the problem. However, it may take a lot of computer resources for high-

$n.m$ TAE analysis in a burning plasma. It is possible to achieve the goals of computing the mode frequency and its stability properties using the local calculations [236] and expanding them in the radial direction [237] [238]. The high-n TAE analysis was pioneered in the paper in which TAE solutions were found within the ballooning formalism and presented [211]. The ballooning formalism reduces the eigenmode problem to 1D equation for the electrostatic potential

$$\frac{\partial}{\partial\vartheta}\left[(1+s^2\vartheta^2)\frac{\partial}{\partial\vartheta}\phi\right]+\omega^2(1+2\epsilon\cos\vartheta)(1+s^2\vartheta^2)\phi+\alpha_p(\cos\vartheta+s\vartheta\sin\vartheta)\phi+Q\phi=0, \qquad (4.2.2.1.3)$$

where we added the kinetic terms in general form, Q, to account for kinetic contributions from fast ions and thermal plasma species. In the case of zero shear, s=0, this equation is reduced to the usual Mathieu equation, and no solutions exist in the gap. The ballooning formalism is often used for its simplicity and clarity but it lacks the realism of eigenmode structure and stability analysis. Often it is complementary to the global simulations, especially in cases in which the global ones have problems computing the finite structure near the point of the interaction with the continuum and when thermal ion FLR effects are important and need to be resolved.

One particular example that is hard to resolve using the ballooning formalism is the RSAE solution to be covered later in section 4.2.2.2. It first became known in tokamaks and greatly enriched our knowledge of AE stability in toroidal devices. Typically RSAEs are observed as oscillations that sweep up in frequency as q_{min} decreases during the plasma discharge.

As AEs may introduce a limit on a DT reactor's performance, it was of great interest to analyze the direct excitation of these modes by fusion alphas in TFTR. Initially, some reduction of the required drive for TAEs due to alphas was reported in Ref. [239]. An independent theoretical analysis was done first to understand the drive-damping balance for TAEs and it indicated that the damping from the injected beam ions was large and primarily due to the sub-Alfvénic EP injection velocity [240]. To minimize the beam damping by choosing appropriate timing for TAE instability was suggested even earlier [241]. The question was raised whether TAEs would be unstable after the NBI is turned off since its slowing down time was estimated to be $100ms$ whereas for alphas it was $500ms$. A special experiment on TFTR was subsequently conducted and confirmed the expected TAE like modes at the predicted time $\sim 100\mathrm{ms}$ after the NBI turn off [76]. The unstable mode number was within the range predicted by simulations. However, some inconsistencies in the explanation remained after the initial publication. Most importantly, the mode frequency sweeping and the poloidal dependence of the perturbation contradicted the numerical results. Only after some time and after the theory was sufficiently developed [216] [217] [209] it became clear that the observed modes were TAEs only at certain times when they were observed and were RSAEs (called ACM in [209] and RSAEs in [242]) at other times. RSAEs are discussed in more detail in section 4.2.2.2.

Important new insights resulted from the follow up study and are illustrated in figure 4.2.2.1.1 [243]. That figure shows the evolution of the AE frequencies during the transition from almost single harmonic RSAE to the TAE gap mode (couplet). Fig.4.2.2.1.1 was explained using Eq.(2.2.1), which couples acoustic and Alfvénic components of the mode. The coupling resulted in the dependence in the unexpected anti-ballooning AE radial structure Fig. 4.2.2.1.1 (right) [243], which was modeled using CASTOR [244] and NOVA codes [204].

We should note that the first observations of TAEs in TFTR [4] are still in the focus of research. They are carefully analyzed with the MEGA code and new insights into this problems were published [245] [246].

A similar method to the one used in the TFTR analysis was employed in the beam afterglow plasma of JET DT high performance experiments in attempt to excite TAE modes [247]. In hot ion H mode and shear optimized discharges unstable AEs were not observed even at the highest fusion power when the alpha-particle beta was $\beta_\alpha \approx 0.7\%$. A numerical analysis confirmed these observations and indicated that special KTAE solutions can exist in H mode discharges but cannot be effectively driven due to their antiballooning structure. No clear effect of fusion α's on AEs has been detected.

Extension to 3D Plasmas. Toroidal coupling due to the equilibrium in 3D plasmas has to be taken into account in addition to the poloidal coupling in order to analyze Alfvénic eigenmodes. The toroidal mode coupling of TAEs and EAEs depends on the toroidal period number $N$of the 3D stellarator magnetic configurations. TAEs and EAEs in stellarator plasmas with $N \gg 1$ have similar properties to those in the 2D case. This was confirmed for TAEs observed in helical/stellarator devices CHS with $N = 8$ [248], LHD with $N = 10$ [249], and W7-AS with $N = 5$ [250]. The toroidal mode coupling tends to lower the TAE gap frequency slightly (typically less than 10%), but the eigenfunction remains almost unchanged. Global and core-localized TAEs were observed in CHS [251] and LHD [249]. In LHD, it was found that even and odd parity cTAEs were excited concurrently [249] [10]. These cTAEs were considered theoretically [252]. Toroidal coupling plays an essential role in the formation of characteristic gaps in 3D plasmas in addition to the poloidal mode coupling. The gap is called the helicity-induced Alfvén eigenomodes (HAEs). This is discussed in detail in 4.2.2.3.

With the helical configuration observations we can say that TAEs were measured in all the toroidal, axi- and nonaxi- symmetric, devices. EPs are not always required to excite TAEs. In ASDEX tokamak TAEs were observed in Ohmically heated plasmas [253] and were attributed to TAE coupling to the Alfvénic turbulence.

4.2.2.2 Alfvén eigenmodes dominated by one harmonic: GAEs, RSAEs

A special set of the AEs was found theoretically [254] [255] [224] with the frequency just below the minimum of the Alfvén continuum and experimentally [256] [257] in tokamaks in search of plasma heating via the excitation of the relatively low frequency oscillations. These modes called *global Alfvén eigenmodes* are localized in the radial direction near the continuum minima outside the plasma center [255] [224] [258] or near the plasma center [259]. Their frequency allows them to avoid strong continuum damping and so they can be easily excited. We cover GAEs because of their importance in observations on STs and their role inducing electron transport that contribute to the outstanding issues in these topic (see section 6).

Here we call the modes localized below the Alfvén continuum (AC) minimum near the plasma center in tokamaks conventional GAEs. Others such as in stellarators [250] [260] [261] [262] are nonconventional GAEs (NGAEs), which are found in helical plasmas. Notably, they were studied theoretically in order to explain sudden drops of the plasma beta during the low frequency instabilities in the W7-AS shear-less stellarator due to subsequent electron heating of the plasma periphery. According to Ref. [261] NGAEs have frequencies above the AC maximum. In [10], however, there was no difference found in the GAE and NGAE mode structures using the AE3D code [263].

Other NGAEs are known from the literature [258], the solution found in tokamak equilibria theoretically were done for small m. Such modes violate a special condition of conventional GAEs existence. This condition was obtained for the conventional GAEs considered in the original papers [255] [225] and reads

$$g = \frac{-2\omega_A^2}{r\left(\omega_{sA}^2\right)''}\frac{\rho'}{\rho} > 1/4. \qquad (4.2.2.2.1)$$

(N)GAE structures typically have a Gaussian like shape for the radial dependence of their dominant poloidal harmonic peaked at the (extremum) minimum AC point.

An important feature of GAEs is that they are not bound in frequency, unlike TAEs which are bound by the TAE gap. The shear Alfvén wave dispersion $\omega = \omega_{sA} = v_A k_\parallel$ at AC extremum can be used as a good approximation for the GAE frequency and can have an almost arbitrary value determined by $k_{\parallel}$. This dispersion is used for GAE identification in STs [259]. Indeed GAE modes with different (m, n) pairs not only have different frequencies but they also have distinguishable temporal evolutions of their frequency, which was confirmed by a direct comparison with the Alfvén wave dispersion relation. In relatively low B field (ST) plasmas GAEs are associated with oscillations of subcyclotron instabilities, which are well above the typical TAE frequency range. They are observed together with the CAEs discussed in section 4.2.3. A multiplicity of GAEs has been observed in STs at high frequencies and they are candidates for the so-called alpha channeling or phase space engineering (see section 4.2.7). Note that the GAEs in stellarators and tokamaks can be seen around or slightly below the TAE frequency [250] [10]. They are in addition to the high frequency GAEs that have a different helicity ($m \cdot n < 0$) or n=0. The n=0 GAE in a tokamak plasma was theoretically studied analytically and numerically within the ideal MHD theory [264]. The paper suggested that the Alfven Frequency Modes observed in TFTR could be a n=0 GAE [265] and also the modes would be possible to excite by a set of saddle coils placed inside the vacuum vessel in JET [266]. An interesting observation of the identified n=0 GAEs was done on MAST [267]. What is interesting about them is that they were done in the Ohmic plasmas without the presence of the energetic ions.

Similar to the GAEs are the *RSAE* solutions formed primarily by a single poloidal harmonic. They also are known as ACM – Alfvén Cascade Modes [268] whereas the term RSAE was introduced in Ref. [242] (not to be confused with well-known Alfvén cascades from the turbulence theory). The essential difference is that GAEs can form an eigenmode potential even in the case in which only one harmonic is present so that the sideband harmonics can be ignored and the mode itself is essentially a cylindrical mode that makes it a very convenient topic for a study in a cylindrical geometry even in stellarator plasmas [10].

RSAEs essentially exist due to higher order corrections to the ideal MHD theory, an even higher order than the typically small toroidicity, plasma beta, ellipticity and other effects. In the search of these effects several important terms were sought and found theoretically. The first one was the EP contribution to the eigenmode equation [216], which doesn't require poloidal sidebands harmonics. Its essential contribution was that it modified the eigenmode equation in such a way that the EP contribution was proportional to the density gradient of the energetic particles, whereas it is typically determined by the EP pressure as their density is small. However, the EP density term is given by the non-resonant ions, which is not small and was stated to be important for the mode formation. It was demonstrated to lead to RSAEs in numerical simulations in realistic tokamak geometries [269].

It was found later that the EP contribution is sufficient but not necessary for RSAEs to exist. . In ICRF heating discharges in JT-60U, the AEs having characteristic frequency sweeps were already observed but they were not identified as RSAEs since their theory was not fully developed at that time [270] [271] [272]. Also in the analysis of the TFTR experiments as we noted above, the observed modes were identified as TAEs initially [76]. Further theory development led the authors to another paper and successful calculations of several observed properties, including the mode dispersion, the frequency evolution and the mode amplitude poloidal variation. These calculations were consistent with the properties of RSAEs [243]. RSAEs were identified in the JET ICRF heated plasma earlier [216].

Furthermore, it was shown in Ref. [209] that RSAEs can exist in MHD theory alone due to second order (in toroidicity) terms in the eigenmode equation. The same order as these toroidicity corrections are the terms due to the plasma pressure [204] [214] [215] and the pressure gradient [273] [274] [275]. Because the frequency of RSAEs is almost the same as the frequency of the AC maximum it is very hard to establish experimental validity of each of the terms affecting the mode formation. The most comprehensive validation of the RSAE theory has been performed on the DIII-D tokamak (see later in this section) using the ideal MHD code NOVA, which points out RSAEs as modes with well-determined structures excited perturbatively [276] [277], i.e. their structure does not change when the mode frequency evolves.

Summarizing various above-mentioned contributions, RSAEs that sweep up in frequency have dispersion relations as follows: If q_{min} decreases from its rational value m/n, the m^{th} harmonic continuum has its maximum point and is not coupled to its $m+1$ neighbor. This is the condition for the sweeping-up RSAE to be formed. At a point when q_{min} nears $(m-1/2)/n$ it is couple to the neighboring $m-1$ harmonic and the TAE gap couplet emerges. Until this point the dispersion relation of sweeping up RSAEs is $S_\omega = Q - \sqrt{Q}$, where

$$S_\omega \equiv \left(\bar{\omega}^2 - \bar{\omega}_{GAM}^2 - k_\parallel^2 R_0^2\right) m q_{min}^2 / |k_\parallel|\, R_0 r_0^2 q_{min}'', \qquad (4.2.2.2.2)$$

and,

$$Q \approx 2\frac{m\bar{\omega}q_{min}^2}{r_0^2 q_{min}''}\frac{\varepsilon(\varepsilon+2\Delta')}{1-4\mathrm{k}_\parallel^2 R_0^2 q_{min}^2} + \frac{m\alpha}{r_0^2 q_{min}''|k_\parallel|R_0}\left[\frac{4\bar{\omega}^2 q_{min}^2\Delta' - \alpha/2}{1-4\mathrm{k}_\parallel^2 R_0^2 q_{min}^2} + \varepsilon(1-q_{min}^{-2}) + \alpha/2\right]. \qquad (4.2.2.2.3)$$

Here $m \gg 1$, $\bar{\omega}_{GAM} = \sqrt{\Gamma\beta}$ and we ignored the EP contribution. This dispersion relation is in agreement with the numerical calculations [273] [275] and with the experimental data from [85] [278] [279] [280]. In the later [280], it was shown that the RSAE frequency nears the GAM frequency as q_{min} approaches unity, which follows from Eq. (4.2.2.2.3) and is important for theory validation. The theory of minimum frequency of RSAEs including various higher order corrections is summarized compactly in Ref. [281] and is quite useful for a quick check of experimental observations.

A multiplicity of RSAEs was reported from JET observations using techniques including interferometry and edge Mirnov coils [86] and from DIII-D experiments using a far infrared scattering diagnostic [282]. More on the RSAE discussion in tokamak plasmas with examples of the mode structure evolution is well summarized in the recent topical review [11] (see Figure 2 for RSAE structure evolution). We would also like to note that RSAEs were seen in many other tokamaks: Alcator C-mod [88], AUG [283], DIII-D [276], NSTX [278] and MAST [284]. Moreover, RSAEs are also observed in a reversed magnetic shear stellarator/helical plasma generated by counter NBCD in LHD, where the second derivative of the q-profile at the zero-shear layer is negative, i.e., positive shear, *s,* in the core and negative *s* towards the edge [87] [10]. Note that the net plasma current driven by counter NBCD reduces the rotational transform produced by the external helical coils. In the plasma, the RSAE frequency is swept down and then swept up taking the minimum frequency, for instance, when q_{max} increases from 2 passing through 3, as shown in Fig. 4.2.2.2.1. The EP contribution is essential for the existence of RSAE during the sweep-down phase when q_{max} increases. In the sweep-up phase, the bulk plasma pressure gradient plays an important role in the excitation and overcomes the negative contribution from the mainly counter going EPs. The minimum frequency is nearly equal to the GAM frequency and also equal to the frequency of the n=0 mode (EP driven GAM) excited concurrently in the plasma [87] [10]. This is in clear contrast with RSAEs in tokamaks where the downward sweeping is rarely observed as discussed below. At higher bulk plasma toroidal beta (~1.2%) than the beta in the shot shown in Fig.4.2.2.2.1 (~0.4%), the RSAEs with n=1 and n=2 are simultaneously excited together with n=0 EP driven GAM on LHD, where the sweep rate of n=2 RSAE frequency is doubled from n=1 RSAE frequency rate.

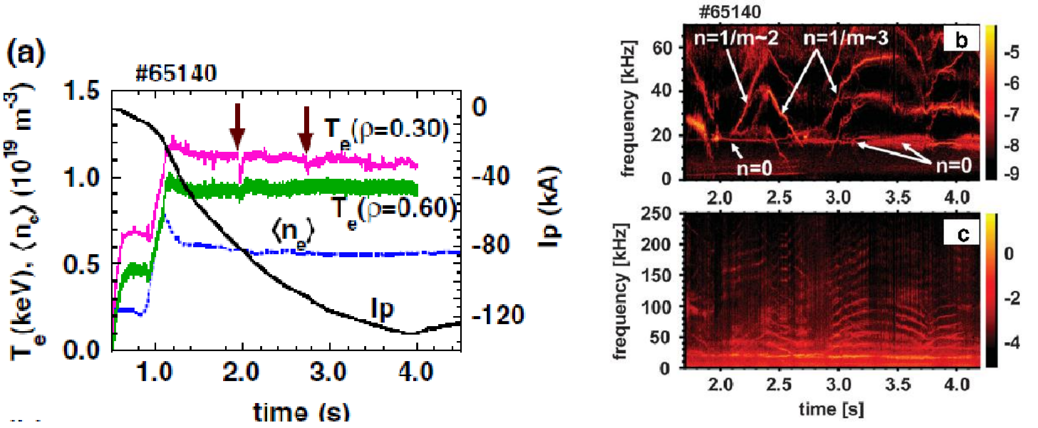

***Figure 4.2.2.2.1** Figure (a) shows time evolution of electron temperature measured by a calibrated ECE radiometer, line averaged electron density and plasma current driven by counter NBI in LHD. Two arrows indicate the q_{max} passes 2 and 3. Magnetic probe's spectrograms to the right (b) and microwave interferometer (c) signals. The RSAE frequency takes the minimum when q_{max} takes 2 and 3. Nonlinear coupling of RSAE and GAM generates a multitude of frequency sweeping modes. The figures are adopted from Ref.* [87].

A less studied topic is on *RSAEs whose frequency sweeps down* and which are rarely observed in tokamaks. There are several papers published on this topic [285] [286] [287] [288] [289] [290] [291]. The explanations given in those references take different approaches. Refs. [286] [287] and Ref. [288] have similar physics. They are developed by one of us (NNG) and independently by other groups and are reviewed below. In Ref. [285] a pure kinetic solution for this problem was offered, which has the radial scale of ρ_i and should be radially localized and potentially strongly damped. There is an alternative explanation to down sweeping RSAEs driven by trapped EPs in JET when an attempt is given to explain them in terms of the radially propagating structures – quasimodes, which are not eigenmodes. Nevertheless the authors were able to compute the drive and the damping of those structures. The details of this model can be found in the already mentioned topical review paper [11] or in Ref. [289]. A pure MHD description of these modes is given in Refs. [290] [291]. The first one treats the underlying instability as internal AEs (IAEs). These modes can exist in flat or weakly reversed-shear plasmas. The IAEs were not considered for the stability analysis. Only continuum damping was estimated perturbatively and shown to be small. Ref. [291] proposed an MHD explanation (i) with the RSAE frequency laying below the continuum or (ii) the safety factor containing local maximum or (iii) the hollow plasma rotation flow profile. All of the above mentioned interpretations are interesting models but remain to be compared with experiments beyond the preliminary comparison published recently [292].

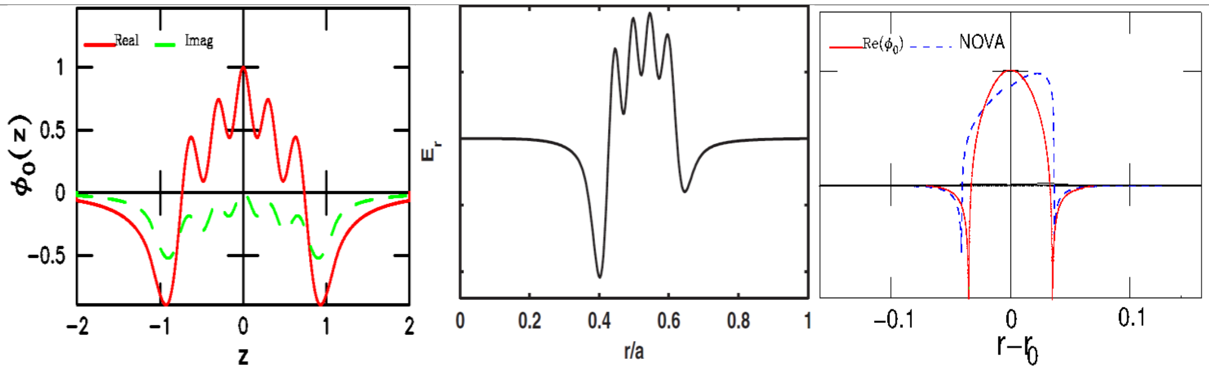

***Figure 4.2.2.2.2** Down-sweeping RSAEs structures in model plasmas are obtained with the shooting technique (left) showing the real and imaginary parts of the eigenfunction potential as a function of the normalized minor radius varable* z [287]. *Middle figure shows real part only of the down sweep RSAE displacement from Ref.* [288]. *Figure on the right shows only MHD part of the mode structure from theory and NOVA computed real part of RSAE structure* [287].

A unique opportunity to check both the ideal MHD and kinetic theories was offered recently [286] [287] in explaining these rarely experimentally observed RSAEs when their frequency goes down as q_{min} decreases. They are also known as down-sweeping RSAEs, whereas the modes at the bottom of the sweep are called bottom sweep RSAEs. It makes sense to consider both these modes together as the physics of their formation is similar.

A common element for both modes is that they are formed with eigenfrequencies above the AC minimum and thus intersect the continuum at two points, giving rise to the singular-like structures on the radial harmonic at the two points of AC intersections (or resonance with the AC). This situation is known from the literature when AE solutions intersecting the AC are sought (see for example [293]). It was shown in Ref. [286] that it is impossible to construct the ideal MHD mode structure due to unmatched solutions shot (numerically) from the left and from the right in the vicinity of the origin (which is the q_{min}point). Either a solution itself or its derivative experience jumps. The only way to reconcile the physical solution with the requirement of the continuity of the mode structure is to introduce a kinetic part of the solution. Such coupling of the KAW with the ideal Alfvénic solution is known to occur at the AC resonance [203] [294].

Thus, the solution constructed in Refs. [286] [287] starts as ideal MHD at infinity and approaches the AC resonance point, $r = r_{AC}$, as the ideal solution dictates, i.e. with $\ln|r - r_{AC}|$ singularity in the vicinity of r_{AC}. Then the RSAE couples to the KAW due to the non-vanishing 4th order FLR terms in the eigenmode equation. What differs in these down sweeping RSAE solutions is that the KAW oscillations have to be present not only near r_{AC} but also far away and propagate to the origin where they serve as mediators required for the solution to be physical, i.e. to match up to the first derivatives. Because of this it seemed possible to compute the damping rates.

The outlined theory takes care of these peculiarities and gives rise to the conditions in which the ideal MHD theory required for large scale RSAE structures is also responsible for the dispersion relations. One consequence of this is that there is often in the experiments a range of q_{min} when RSAEs cannot exist, which explains why down sweeping RSAEs are generally not observed.

We present here the down sweeping RSAE mode structure plots computed by two groups with notably different codes, of Ref. [287] and Ref. [288]. In particular Fig. 4.2.2.2.2 (left) computes the electrostatic potential of these modes with its real and imaginary parts in the tokamak ordering and with the following parameters of the tokamak plasma: $R_0 = 10m$, $R_0/a = 10$, $r/a = 0.5$, $\beta_0 = 0.1\%$, $q''_{min} = 2$. What is most remarkable is that in this case even the pure ideal code NOVA is able to recover the "long scale" ideal structure of the mode and that the eigenfrequency is close to the expected value.

It also follows from Ref. [287] that the obtained structure can be used to compute the mode growth and damping rates perturbatively when the radiative damping coming from FLR terms is negligible. According to the theory [286] the down sweeping RSAEs can be weakly damped modes existing in the low shear plasma region and are ideally suited to explain the anomalous plasma energy and particle transport.

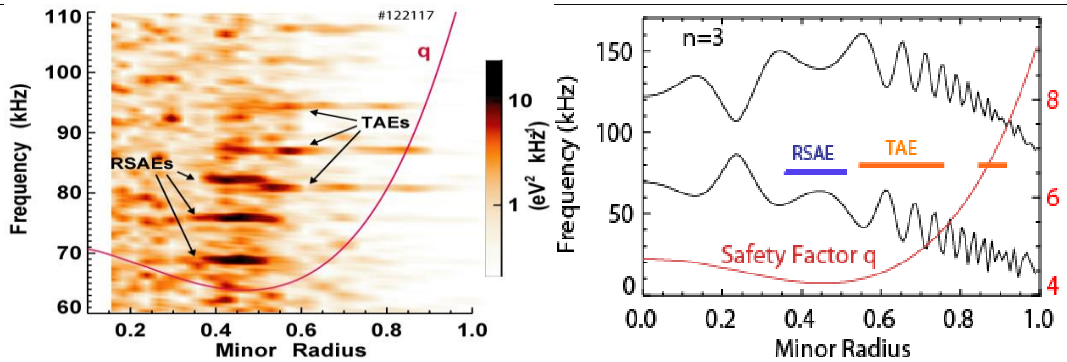

Figure 4.2.2.2.3. *DIII-D results on TAE and RSAE excitation by beam ions in a reversed shear plasma* [276]. *Figure (a) represents the ECE signal radiometer spectrum. Figure (b) shows AC profiles with the solid lines corresponding to RSAE and TAE frequencies and their radial extend computed by NOVA code.*

Experimental validation of linear TAE/RSAE theory. As we discussed (and the experimental evidence shows) EP driven instabilities are excited in part due to the existence of the eigenmodes. In fact, one can identify a corresponding eigenmode or the eigenmode should be sought for almost all the observed instabilities. Eigenmodes in turn exist due to higher order MHD effects such as the toroidicity and the plasma pressure. Such higher order corrections to the "homogeneous" plasma approximation can be rigorously tested. Thus, the study of eigenmodes via the study of MHD theory's higher order effects is arguably the most powerful tool to verify the whole MHD model. Perhaps the most compelling case for this is the excitation of AEs. One such example is the plasma with NBI driven modes in DIII-D.

One key element of DIII-D's recent experimental campaign [295] was the use of a special diagnostic, FIDA, (fast ion D_α) spectroscopy for beam ion relaxation measurements and the electron-cyclotron-emission (ECE) diagnostic for AE measurements. The basic description of these diagnostics is given in Sec.2. Among many reported results the authors focused on linear AE physics [276], which helped to validate the whole MHD theory. Together with the Mirnov magnetic probes, ECE was used to identify and document several AE modes. In addition, for each mode with the measured toroidal mode number a numerical analysis provided the radial structure of the perturbed plasma displacement, which was, in turn, compared with the displacements derived from the ECE signals using the relationship Eq. (2.2.1) for MHD fluctuations in Sec.2.2

The next figures represent the results of such comparisons [276]. First we show the radial profile of the spectral power of electron temperature fluctuations obtained from the ECE radiometer on Fig. 4.2.2.2.3 (left). It represents the TAE and RSAE modes, which were identified with the help of the NOVA code and additional diagnostics data. Fig. 4.2.2.2.3 (right) shows the continuum for this case with two mode frequencies indicated as horizontal lines, which are radially extended according to the mode structure.

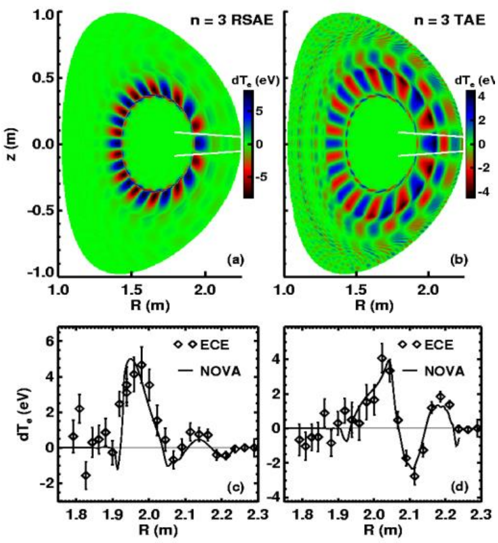

Figure 4.2.2.2.4 *Comparison of TAE and RSAE radial structures measured by ECE diagnostics (diamonds) in a dedicated DIII-D experiments* [276] *with the predictions by NOVA code (solid curve) in the lower figures. The upper 2D mode structures are calculated by NOVA.*

Perhaps the most impressive data comes from the ECE radial structure of these modes and how it compares with the computed ones. Figure 4.2.2.2.4 shows the comparison of two modes, n=3 RSAE and n=3 TAE. The radial dependence of the electron temperature fluctuations with all the phase inversions obtained from the ECE diagnostics can be seen to agree with the one calculated by the MHD theory. Given the finite accuracy of the ECE data and the other modeling tools used, the agreement seems to be impressive and important for MHD theory in general.

A very recent addition to the study of the RSAEs came from further DIII-D experiments [80]. ECEI was used as a fast measurement technique for the temperature perturbation as mentioned in Sec.2. It showed the RSAE 2D structure that was in good agreement with the ideal MHD modeling for many features such as mode frequency, mode radial width and so on. However other characteristics, such as the poloidal structure of the mode, showed the distinct phase shearing that in other words is an extra poloidal variation of the phase needed to describe the 2D structure satisfactorily as shown in Fig.4.2.2.2.5. This feature was found to be well described by the hybrid MHD-gyrofluid code TAEFL [296] and was explained by the fast ions diamagnetic flow. In AUG, 2D structures of the fundamental and second radial harmonics of RSAE and BAE are successfully measured by ECEI and are agree with the numerical results by a linear gyrokinetic code LIGKA [79] [297].

We would like to add that reversed-shear plasmas are considered for the so-called advanced tokamak scenario regimes [182]. These scenarios seem to be very susceptible for EP losses [295] due to RSAE/TAE activities and are investigated in sections 5.2 and 7.4.

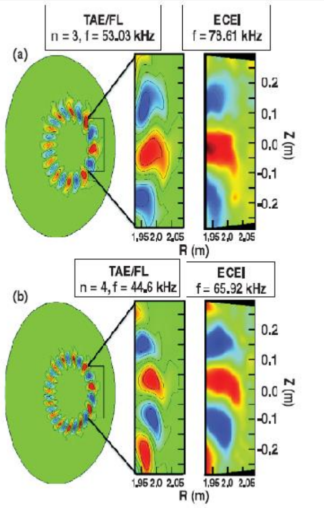

Figure 4.2.2.2.5 *Comparison of 2D structures of n=3 (a) and n=4 (b) RSAEs measured by ECEI (right) in DIII-D with the mode structures calculated by the gyrofluid code TAEFL (left). Poloidal shearing of the mode patterns agrees very well with each other. The differences in the frequencies are caused by the calculations omitting plasma compressibility. . The figures are adopted from Ref.* [80].

4.2.2.3 Characteristic AEs in 3D plasmas

The dependence of the coefficients of the eigenmode equation (4.2.2.5) on toroidal angle as well as on poloidal one in 3D plasmas leads to gap formation through mode couplings due to poloidal and toroidal variations. As in tokamaks, one can formulate the local ballooning theory for AEs, which would have the same local equations for the mode structure but with the toroidal angle acting as a field line marker parameter, a shift to the poloidal angle in the expressions [298]. Different field lines would correspond to different coefficients in this equation, which is indicative of the localization of the mode in real space. As in the theory of ideal ballooning modes, high n TAEs have been successfully studied in stellarators [299] [300] with the use of this formalism. We review the properties of AEs specific for 3D geometries.

As mentioned in Sec. 4.2.2.1, toroidal mode coupling is not important for TAEs/EAEs and GAEs/RSAEs in helical/stellarator devices such as LHD with large Nmagnetic configuration. A class of AEs for which toroidal mode coupling is essential exists only in 3D plasmas. In toroidal mode coupling, Fourier modes having the toroidal mode number $n=n_1$ can couple with the Fourier modes having different $n=n_2$, provided the condition $n_1 \pm n_2 = kN$ is satisfied, where N is the toroidal period number and k=0, 1, 2,… These modes consist of the mode family of $n=n_1$. The number of the mode families is finite, i.e., $1 + N/2$ [301]. Coupling among all modes belonging to the mode family of $n=n_1$ takes place and generates the helicity-induced Alfvén eigenmode (HAE) gaps [302] [303] [304]. The gap frequency can be evaluated analogously to the TAE frequency, by intersection of adjacent Alfven continua as, $k_{\parallel m,n} = -k_{\parallel m+\nu,n+\nu N}$. Here, the magnetic field strength B is decomposed in Fourier expansion with Boozer coordinates (ψ, θ, ϕ) as, $B = B_o\left(1 + \sum_{\mu,\nu} \varepsilon_B^{\mu,\nu}(\psi)\cos(\mu\theta - \nu N\phi)\right)$. The gap frequency is expressed as follows [302] [303] [304]: $f^{\mu,\nu} = \left(\nu q^* N - \mu\right)\left(\frac{v_A}{4\pi \mathrm{R} \mathrm{q}^*}\right)$ and $q^* = \frac{2m+\mu}{2n+\nu N}$. This expression describes the gap frequency of TAE with $\mu = 1, \nu = 0$, and EAE with $\mu = 2, \nu = 0$. Typical stellarator configurations have helical coils of $l = 2$ polarity and the dominant helical component $\cos(2\theta - N\phi)$ corresponds. The HAE is called HAE$_{21}$ or just HAE. As seen from the equation, the HAE frequency is approximately a factor of N larger than the TAE frequency. The HAE frequency is close to the TAE frequency in stellarators with medium and low $N(\approx 2-5)$, and may have noticeable impacts on EP transport, while the frequency in high N stellarators such as LHD (N=1) is much higher than the TAE frequency. The coherent magnetic fluctuations in high beta LHD plasmas at lower toroidal field ($B_\varphi = 0.6$T) were consistently interpreted to be HAE. The observed mode frequency lies above the lower bound of the HAE gap [305]. The gap structure calculated, including toroidal mode coupling, is shown in Fig 4.2.2.3.1. From the gap structure, this mode is expected to exist in the edge region.

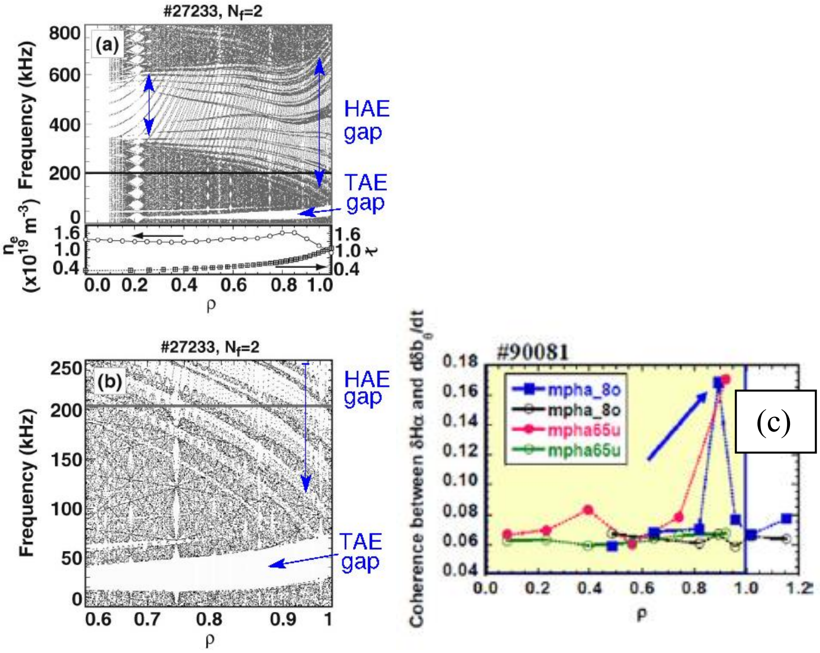

Figure 4.2.2.3.1 *(a) Calculated n=2 shear Alfven spectra continua of high beta LHD plasma at* $B_\varphi = 0.6$T*, where 919 Fourier modes having n=2, 8, ... 48, 52 belonging to the mode family* $N_f = 2$*. are taken into account. The horizontal bold line indicates the observed frequency. Electron density and the rotational transform (=1/q) profiles are also shown. Figure (b) depicts the zoomed spectra in the plasma outer region. The figure is reproduced from* [305]*, where (as well as in the figure) the mode family is marked* N_f*. The HAE and TAE gaps are indicated by arrows. (c) Radial profile of the coherence between the electron density fluctuations obtained by the Hα detector arrays with fast time response and magnetic fluctuations by HAE, in a similar shot where the HAEs were observed. The high coherence region agrees well with the location of HAE inferred from Figs.(a) and (b). The figures are is adapted from* [10].

Correlation analysis between magnetic probe signal and H-alpha emissions confirmed the mode location in the plasma edge [10]. The coherent fluctuations that are suggested to be HAEs were observed in W7-AS [250] [306]. Detection of HAEs was reported from Heliotron J and TJ-II stellarators [262].

In LHD plasmas with $N \gg 1$, the properties of TAEs, EAEs, GAEs and reversed shear Alfvén eigenmodes (RSAE) are very similar to these modes in tokamak plasmas. The observed differences are believed to be due to the differences in the q-profile, i.e., positive vs negative shear monotonic q-profiles and positive vs negative curvature of q at the zero shear layer in reversed magnetic shear q-profiles for tokamak and LHD plasmas.

Although the linear Alfvénic instability theory is well developed, one of the outstanding issues in 3D low frequency instability studies is developing the eigenmode solvers capable of computations of the stability of the modes in realistic equilibria. The challenge here is more complex toroidal and poloidal harmonics couplings that need to be addressed. This can influence both the growth and damping rates. On the experimental side the validations of those theories are required.

4.2.2.4 Kinetic TAEs

The KTAE modes were predicted for toroidal plasmas by theory [225] and were found experimentally on JET [307]. They are radially localized modes and have extent in $r$determined by the thermal ion Larmor radius. To describe the KTAE structure satisfactorily the coupled system of equations (4.2.2.6) needs extra FLR terms [225]. The exact form of these terms in the cylindrical geometry was suggested in Ref. [203] to be proportional to $\lambda_k^2 = \frac{7}{4}\left(\frac{\rho_i}{r}\right)^2 \frac{m^2 s^2}{\varepsilon}$. Our illustration in figure 4.2.2.3 suggests that many KTAE modes can arise (confirmed on JET [307]) but the radial extent is small, on the order of $(l+1)\pi \mathrm{r} \lambda_k,\ l = 0,1,2\ldots$ depending on which particular mode we consider. Thus KTAEs tend to have large parallel electric fields and large damping by thermal electrons. Because of their radial localization KTAE instabilities by themselves do not seem to be dangerous for EP confinement. However they can potentially contribute to EP transport in strongly nonlinear regimes when the fast ion profiles are relaxing and KTAEs serve as mediators. This is a potential subject for further studies especially for self-consistent simulations using initial value codes.

In addition to the pioneering papers we listed above, there were several follow-up studies that treated KTAEs in order to determine the radiative damping analytically [308] [309] and numerically non-perturbatively [310] [311]. One focus was on the computations of the radiative damping mechanisms that was originally derived and computed for TAEs [312]. We would like to note that the radiative damping of TAEs is close in physics to the continuum damping and can be treated the same way as shown in Ref. [313] [314]. This is because both dampings are due to the parallel electric field generated when an oscillation resonates (in frequency and location) with the short wavelength KAW. Different branches of the Alfvénic oscillations, such as TAEs, KAW and KTAE [315] may exist, depending on whether the equilibrium geometry and kinetic effects are important for the mode structure.

4.2.2.5 Active excitation of stable AEs and measurements of the damping rates

The linear stability of the AEs such as TAEs depends on the competition of the energetic particle drive γ_{drive} and damping rates by background plasma γ_{damp}. That is, if the effective growth rate of AEs $\gamma_{eff}=\gamma_{drive} - \gamma_{damp}$ is positive (negative), AEs are unstable (stable). Reliable estimation of γ_{drive} and $\gamma_{damping}$ is critical to assess the linear stability of AEs in ITER. The theoretical evaluations of these quantities are sensitively dependent on modelling of MHD and kinetic effects. In particular, the damping rates vary by an order of magnitude depending on theoretical models. As mentioned above, various AEs are identified in tokamak and stellarator plasmas using ideal MHD theory. That is, these AEs can exist as stable eigenmodes in the toroidal plasmas without energetic ions. Accordingly, the experiments to excite these stable AEs by a set of antennas were for the first time attempted in Ohmically heated plasmas without energetic particles on JET, and the damping rates (γ_{damp}) of low n TAEs and EAEs were successfully measured for various plasma conditions [266] [316]. The data are quite important to validate various theoretical models and the numerical codes through comparison with them. In subsections 7.1 and 7.2, the code benchmarks and validations using these data are described as a work of the International Tokamak Physics Activities (ITPA).

The active excitation of the stable AEs in JET was done using in-vessel saddle coil antennas as an AE exciter. The plasma responses to applied alternating magnetic fields by the antenna system are detected by Mirnov probe arrays placed inside the vessel, ECE radiometer, reflectometers and so on. The mode structures of the applied magnetic fields are controlled by the relative phasing (+ and -) of currents of 8 saddle-coil antennas having 90 ^{o} coverage in toroidal direction for each antenna and the dominant peak of Fourier spectrum are around |n|=0, 1 or 2 [266]. The poloidal mode number spectra of the fields are determined by the poloidal coverage of the coil to the plasma surface and plasma shape including Shafranov shift. The antenna system in JET was used to excite n=0 GAEs and |n|=1 and |n|=2 TAEs propagating both co and counter toroidal directions. They can also excite |n|=1 and |n|=2 EAEs if the sweeping range of the antenna current includes the exciting EAEs. The applied field magnitude δB is weak in comparison with the toroidal magnetic field B_φ, ($\delta B/B_\varphi < 10^{-5}$ at the plasma boundary) and would not affect EP transport. The frequency of the field was swept within the range of 30 to 500 kHz so that the inferred frequencies of AEs should be included in the sweeping range. The Mirnov probe signal will include various electromagnetic noise. In order to remove the noise and detect only plasma response for the applied field perturbations having the angular frequency ω_{ext}, synchronous detection was employed and the transfer function of the plasma to the applied antenna fields was derived as a function of ω_{ext}. The presence of AEs is manifested as several resonance characters in the transfer function, that is, the following form of the transfer function having K numbers of the resonances was adopted in the experiments:

$$\mathrm{G}(\omega,r)=\frac{B(\omega,r)}{A(\omega)}=\sum_{k=1}^{K}\left\{\frac{R_k(r)}{i(\omega-\Omega_k)+\gamma_k}+\frac{R_k^*(r)}{i(\omega+\Omega_k)+\gamma_k}\right\}, \qquad (4.2.2.5.1)$$

where $A(\omega)$ and $B(\omega,r)$ are the Fourier transforms of the actuator or excitor such as antenna current and sensor signal to detect the plasma response, respectively. The angular frequency ω is the applied field frequency ω_{ext} and r is the measurement position. The residues and the complex conjugate are expressed as $R_k(x)$ and $R_k{}^*(x)$. The Ω_k and γ_k are respectively the eigenfrequency and the damping rate of the resonance of k-th AE, respectively. These parameters characterize the resonance can be derived by an appropriate curve fitting technique. The center frequency of the resonance $\Omega_k$corresponds to the eigenfrequency of the AE captured in the swept frequency range of ω_{ext}. The accuracy of the derivation of Ω_k and γ_k depends on the sweep rate of ω_{ext}. In order to improve the accuracy of the time variation of the center frequency was controlled to track the expected TAE frequencies. Figure 4.2.2.5.1 shows a typical resonance character of TAE in the transfer function obtained in a JET ohmic plasma shot. In the experiments, stable TAEs and EAEs with the toroidal mode numbers $|n|=1$ and $|n|=2$ were successfully excited by the antenna technique. The dependence of the damping rates of low n TAEs on the elongation of the plasma cross-section, the safety factor at the magnetic axis and toroidal rotation shear was investigated in JET Ohmic plasmas [317]

[318]. For n=0 GAE and n=1 TAE, the damping rates of both n=0 GAE and n=1 TAE increase from ~1% to ~5% of the angular AE frequency ω_o when the elongation increases from ~1 to ~1.6 [317]. For the trangularity, the damping rates increase from ~1.1% to ~ 1.7% when the trangularity is scanned from ~0 to ~0.3. It was also shown that the damping rates of n=1 TAEs reach high values more than 8% in the central safety factor q(0) less than 1 while they are less than 2% in the range of q(0)>1 [318]. This difference was interpreted that the change of magnetic shear profile near the plasma center would be altered due to sawtooth oscillations.

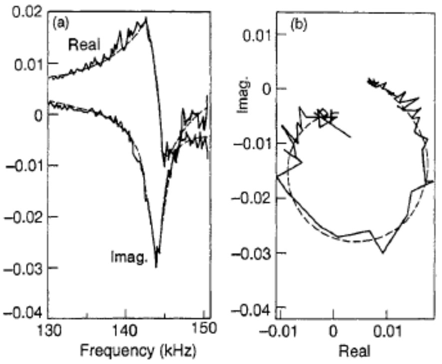

Fig.4.2.2.5.1 *Example of a TAE resonance identified in the transfer function obtained in an ohmic discharge on JET, where the transfer function is evaluated as the Fourier transform of the magnetic probe signal ($B(\omega,r)$) divided by that of the antenna current signal ($A(\omega)$). (a) Real and imaginary parts shown as function of the antenna current frequency $\omega_{ext}/(2\pi)$. (b) Transfer function shown on the complex plane. The derived eigenfrequency $\omega_o/(2\pi)$ and the damping rate γ are respectively* $144.2 \pm 0.1\ kHz$ *and* $1400 \pm 100s^{-1}$, *which corresponds to* γ/ω_o~0.8 % [266]. *The broken curves in Figs. (a) and (b) are fitted with the model transfer function expressed by Eq.(4.2.2.5.1).*

Although the direct measurement of the damping rates of low n TAEs were successfully performed on JET, the data of the damping rates of medium n TAEs that are thought to be more likely candidates in ITER are strongly required [205]. After the above JET experiments on low n TAE excitaion, the medium n TAEs were excited by two narrow-width antennas placed up and down in one toroidal location on C-Mod [319]. The toroidal mode spectrum produced by the antenna set expands having the width of the half maximum of $|n|$~20. In the actual experiment, n=4 TAE was excited and detected in the inner wall limited plasmas with low magnetic shear at the edge, and the damping rates were obtained to be relatively high of 1.4% to 4 %. However, the damping rates in the divertor discharges with high edge magnetic shear were lower than those in the limiter dischages, which is an opposite tendency on the edge magnetic shear for those obtained in JET. Note that the toroidal mode number of TAEs excited by the antennas was still low, n=4. Recently, in JET the excitation of medium n TAEs have been successfully done by two assemblies of 4 narrow-width in-vessel antennas at opposite toroidal locations [320] [321] [322]. The new antenna system has a capability to generate the antenna field in the range of |n|=3-20 up to $\delta B/B_\varphi < 10^{-5}$ at the plasma edge, the range of the frequency sweeping from 10 to 500 kHz. The medium n TAEs were excited by this system, as shown in Fig.4.2.2.5.2 [321]. It is shown that the damping rates of the excited n=3 and n=7 TAEs increase dramatically with the increase in the edge elongation κ_{95} from ~1.35 to 1.6 as same as the tendency of low n (=1) TAEs in the former active-antenna experiments [317]. This result suggests that the control of the plasma shape parameter such as the edge elongation can be employed for a real time control of AE stability on ITER. The similar active antenna system was also installed on the spherical tokamak MAST for the same purposes with JET [322].

As mentioned above, various AEs excited by energetic ions are observed in LHD. Due to 3D plasma configuration such as LHD, usual loop type antennas as used in tokamaks can also generate magnetic perturbations parallel to the equilibrium magnetic field lines as well as the perpendicular perturbations. In CHS which is a small stellarator/helical device with N=8, active excitation of stable TAEs was performed by helical currents which was induced along the equilibrium magnetic field by two inserted electrodes biased with alternating voltage up to 300 kHz. Because of the large sizes electrode, the current is extracted from the electrodes having finite length along the equilibrium field and the current produces magnetic perturbations purely perpendicular to the field as "plasma antennas", which can induce shear Alfven perturbations [323]. This technique was applied to low temperature plasmas heated by 2.45 GHz ECH power [323] and NBI heated plasmas [324]. The *n*=1 and *n*=2 TAEs were successfully excited by this unique technique and the damping rates were measured to be considerably high, i.e., 5-10 % of the mode frequency. The rotational transform profile in CHS plasmas increases from ~0.3 at the magnetic axis to ~1.1 at the last closed flux surface, as similar to low beta plasmas in LHD. The TAE gap frequencies increase toward the plasma edge. Accordingly, the eigenfrequencies of TAEs always hit the shear Alfven continuum, unless the AEs have a radially localized character. The observed large damping rate is thought to be continuum damping as the dominant damping mechanism.

Measurement of the damping rate of AEs by the active excitation technique is done for the plasmas without energetic particle drive so that the damping rates can be straightforwardly obtained from the analysis of the transfer function. In NBI and ICRF heated plasmas where the dependences of the damping rate on the plasma beta and temperatures can widely investigated, the obtained damping rates tend to be underestimated because of $\gamma_{damp}^{eff} = \gamma_{damp} - \gamma_{drive}$ at $\gamma_{drive} \neq 0$. To avoid this difficulty, the discharge condition should be carefully adjusted so that for TAEs the parallel velocity of EPs would be well below the excitation velocity of the side band excitation $\upsilon_A/3$, i.e., $\upsilon_{//} < \upsilon_A/3$. Although the further higher order excitation mechanisms are possible, the γ_{drive} will be able to be neglected. Nevertheless, the EP effects should be carefully assessed in the measurement of the AE damping rates in plasmas sustained by NBI and/or ICRF heating.

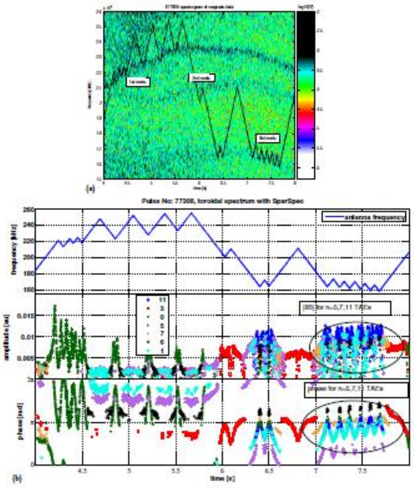

***Fig. 4.2.2.5.2** (a) Spectrogram of magnetic probe signal in an Ohmic JET plasma in limiter configuration where the antenna current frequency is swept in real time with a triangular waveform in the frequency range including three visible AE bands. (b) Time evolutions of the antenna current frequency, the amplitude and the phase of the antenna excited AEs having various toroidal mode numbers* [321].

4.2.3 Compressional AEs and ICE

The fast compressional Alfvénic wave is one of the fundamental MHD oscillations as noted in Subsection 4.2.2. It is closely related to the explanation of the Ion Cyclotron Emission (ICE) initially observed in conventional tokamaks at the harmonics of thermal ion cyclotron frequency and then in STs at the sub-cyclotron frequencies. Let us first review the *Compressional AEs (CAEs).* Two important implications for this topic development come to mind. The first is the use of ICE as a diagnostic (see sec. 4.3.2) to monitor the EP distribution in phase space and use it to control deleterious instabilities due to the EPs.

An eigenmode equation for CAEs can be obtained heuristically from the dispersion Eq. (4.2.2.3) [224] [325]. It can also be derived in a rigorous way using Faraday's and Ampere's laws [326]. We present here the heuristic "derivation" where we neglect the toroidal and poloidal cross-coupling terms and use a quasi-cylindrical coordinate system of high aspect ratio tokamak plasma. The Alfvén velocity in the dispersion relation needs to contain the minor radius dependence to rewrite the dispersion as:

$$\frac{1}{r}\frac{\partial}{\partial r} r \frac{\partial}{\partial r}\delta B_{\parallel} - V(r)\delta B_{\parallel} = 0, \tag{4.2.3.1}$$

where the effective potential is

$$V(r) = \frac{m^2}{r^2} - \frac{\omega^2}{v_{A0}^2}\frac{\mathrm{n}(r)}{n_0}. \tag{4.2.3.2}$$

If we assume for the sake of simplicity an analytic plasma density profile $n(r) = n_0(1 - r^2/a^2)^{\sigma_i}$, we find that the CAE eigenmode structure is $\delta B_{\parallel} = \delta B_{\parallel 0}\exp\left[-\frac{(r-r_c)^2}{\Delta_r^2}\right]$, where $r_c/a = 1/(1+\sigma_i)$ and $\Delta_r^2 = a^2\sqrt{2\,\sigma_i/(1+\sigma_i)}/[m(1+\sigma_i)]$. If toroidicity is added, the poloidal modulation has to be accounted for, which modifies the mode structure [326]

$$\delta B_{\parallel} = \delta B_{\parallel 0}\exp\left[-\frac{(r-r_c)^2}{\Delta_r^2}\right]\exp\left(-\frac{\theta^2}{\Delta_\theta^2}\right), \tag{4.2.3.3}$$

where $\Delta_\theta^2 = (\Delta/r_c)\sqrt{4\,(1+\varepsilon)/\varepsilon}$. The nominal location of the "effective" potential is illustrated in figure 4.2.3.1 and hints at the expected mode localization. Although it is illustrative the present analysis misses important dispersion properties of the CAEs. It was extended to the elongated cross section plasma in [327] [328]. The symmetry breaking Hall term was included in [327] [328] [329] [330]. Initial numerical approaches for the CAE problem attempted to make more detailed calculations. They either have not been suitable for large ellipticity, tight aspect ratio plasmas and

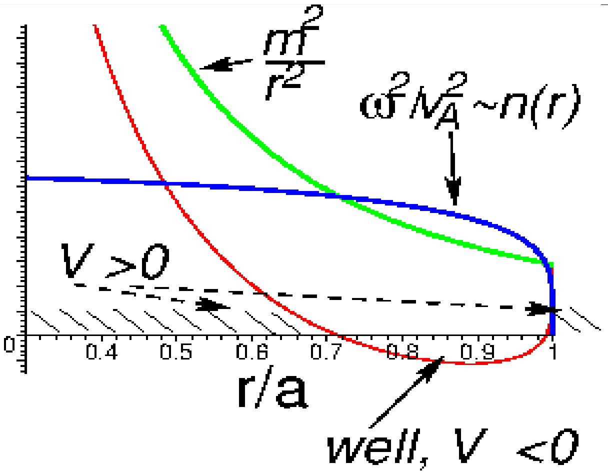

Fig. 4.2.3.1 *Radial dependence of the effective potential well of CAE mode in a cylinder. Negative potential values correspond to the wave location* [355].

high n numbers [331], or they do not include the Hall term [332]. Nevertheless, in Ref. [332] ideal MHD simulations using the NOVA code with $n = 0{,}1$ showed agreement of the CAE dispersion with the analytic expectations and in Ref. [331] a strong edge localization was demonstrated for medium and low toroidal mode numbers. An independent simulation of CAE structures in ST plasmas was performed using the cold plasma Hall-MHD model [333] where the slow mode was excluded as well as the coupling to the shear Alfvénic branch. This work also obtained CAE dispersion and showed mode localization towards the low field side. However, CAEs where also found with a relatively global structure spanning from the plasma center to the edge. This is an important result but may be limited in its applications due to the enforced decoupling of CAEs from the shear Alfvénic branch. It seems that a more realistic model for CAEs may come from initial value codes such as HYM [125] [334], which are capable of keeping all the fundamental MHD branches.

Experimental studies of CAE modes often served as motivations for theory development. We would like to show one of the first CAE spectra from NSTX presented in the literature [335] in figure 4.2.3.2. The experimental structure of the CAE spectrum shown reflect their dispersion relation. Unlike GAEs, CAE dispersion, Eq. (4.2.2.3), is proportional to k rather than $k_\parallel$, and cannot have the same frequency as another CAE with a different set of mode numbers, (m, n, l), where l is the radial mode number. In other words, once the instability is observed during the discharge its frequency does not intersect with another (different mode number) CAE. Such behavior is clearly seen in figure 4.2.3.2, right. A comparison with direct polarization measurements of $\delta\vec{B}$ at the edge supports such identification [336] [337] and is becoming a standard experimental technique for STs [338] [339].

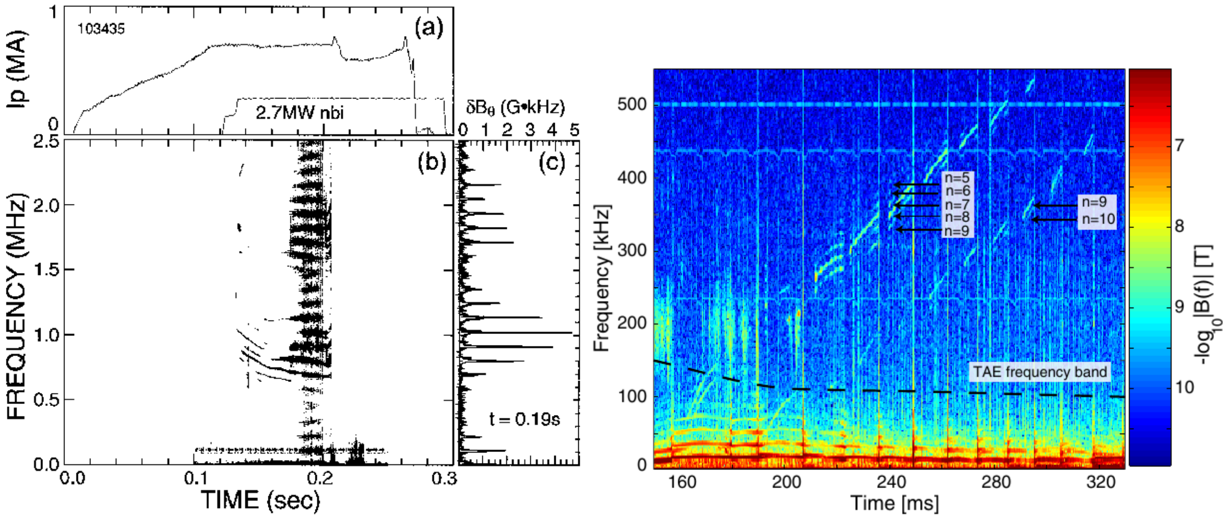

***Figure 4.2.3.2** CAE frequency spectrum from the edge oscillation of representative discharges of NSTX (left figure* [335]*) and MAST (right figure* [338]*) devices. The identification of these oscillations is helped by CAE dispersion relation coming from theory.*

Together with GAEs, CAEs form the observable spectra of the so-called high frequency oscillations (a term introduced in ST applications) also observed on conventional tokamaks [340]. The relatively low equilibrium magnetic field of tokamak plasmas allow the tracking of high-f mode evolution. In tokamaks, CAE signals from many modes merge into spectra which are hard to analyze [341]. However, that does not mean that CAEs were not excited in conventional plasmas; rather their polarization could not be measured. In fact, CAEs are now considered to be the main candidates to explain the observed superthermal **ion cyclotron emission (ICE)** in recent fusion experiments. Shear AEs at high frequencies tend to have continua that are too close (in frequency) to their neighbors in m and will likely result in strong (GAE) continuum damping.

Recent reflectometer measurements of CAEs and GAEs radial structures were performed on

NSTX [342]. What was surprising is that both types of identified oscillations, CAEs and GAEs, are global, having extended radial structure in minor radius unlike the simple theory would predict (see illustration on figure 4.2.3.1). CAE structures can be global as was earlier computed numerically for low mode frequencies [333] but perhaps need to be compared with new NSTX measurements.

The theory and experimental studies of ICE have progressed significantly since the comprehensive review in [1]. Most of the measurements were gathered in experiments on JET [341] [343] and TFTR [344]. In JET, ICE driven by energetic minority ions was observed during ICRF heating. The information provided by the measurements was found to be a useful diagnostic of energetic ions [345]. In DD plasmas heated by higher harmonic ICRH on JT-60U, ICE driven by energetic deuterons and fusion products (Triton-driven ICE) was also detected [346]. In deuterium plasmas heated by D-NBI [347] the characteristics of ICE driven by energetic D beam ions and the fusion products of ^{3}He and T ions were studied in detail using an ICRF antenna as a pickup coil. One of the results most motivating for a future research came from JET. There is was demonstrated that the intensity of ICE correlates linearly with the fusion product density (via the total neutron emission rate) for both Ohmic and NBI heated discharges. This correlation persists over six orders of signal intensity. Similar results have also been observed in TFTR and JT-60U. ICE has been seen on many tokamaks and recently, ICE was observed in LHD during perpendicular NBI which produces trapped energetic ions near the plasma edge in the horizontally elongated section and is also associated with TAE bursts [348] [349].

Initial studies of ICE theory and its applications were done using local approximations [350] [351] [352] [353] [354] assuming that the cyclotron CAE instability was undergoing strong ion drive: $\gamma_f \gg \omega_b$. The theory can be traced back to the above-mentioned first works on EP physics [198] [200] [199] [202] [15]. Later, the theory was able to analyze ICE under the opposite assumption, $\gamma_f \ll \omega_b$ [355] [356]. Both conditions could be met in experiments.

Further development allowed the study of ICE excitation in more realistic conditions with CAE 2D mode structures and the cyclotron resonances Doppler shifted by the toroidal drifts [355] [357] [358]. However, the complexity of these various elements of the theory would require a much longer and more focused review manuscript.

As we noted, CAEs with the sub-cyclotron frequencies were observed in STs. A recent paper on the anomalous fast ion diffusion due to CAEs [359] attempted to understand this peculiarity. The relevant discussion of that paper is summarized in figure 4.2.3.3. Several arguments help to identify the regions of allowed CAE instabilities. Of particular importance is the thermal ion cyclotron damping, which prevents CAE excitation when the mode frequency matches the harmonics of background ion cyclotron frequencies, so that at $\omega < \omega_{cD}$. CAEs avoid it in toroidal plasmas in general. One of the most striking differences between STs and conventional tokamaks is the ratio of the fast ion velocity to the Alfvén velocity, which in general is higher in STs. To reflect this in the qualitative diagram, the aspect ratio was chosen for the abscissa axis. It turns out that the ratio of fast ion velocity to Alfvén velocity can be connected to particular examples of beams in STs (NSTX) and alphas in tokamaks (TFTR) via $R/r \approx 4\mathrm{v}_A/v_f$.

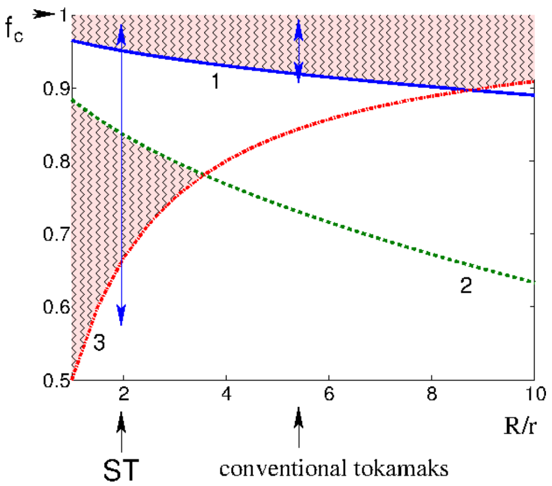

Figure 4.2.3.3. *Regions of allowed CAE frequencies as follows from the mode damping and possible Doppler shifted cyclotron resonances with EPs. Shown are regions in the plane of aspect ratio* R/r *and mode frequencies with the positions of STs and conventional tokamaks. The figure is adapted from Ref.* [359].

It follows from the theory that fast ions exchange their energy with CAEs under the cyclotron resonance condition with strong Doppler shift $\omega - \omega_c \approx k_\parallel v$. An additional special requirement for CAEs is $k_\perp \rho_f = O(1)$ [259]. This in turn implies that the frequency of the modes that are driven by fast ions should satisfy $\omega = \omega_c(1 - |k_\parallel|/k)$. On the other hand, damping on electrons can be minimized if the phase velocity of CAEs is either too small or too large in comparison with the thermal electron velocity, as in the example. If the damping rate is taken at fixed value 1% one can find the condition $\sqrt{\zeta_e} = (k_\perp/k)(m_e/m_i)\beta_e > 1.5$ (region above curve 1 in the figure 4.2.3.3) or $\zeta_e < 0.45$ (region below curve 2 in the figure). In plotting these dependencies in figure 4.2.3.3, we assumed that the nominal tokamak plasma beta scales with the aspect ratio, namely $\beta_e[\%] \sim 10/(R/a)$, which is at least empirically justified based on the results from TFTR and NSTX.

Coupling of CAEs to KAW at the edge results in a second restricting condition on the mode frequency. If we rewrite the resonance condition in the form $\omega = \omega_c - \omega(|k_\parallel|\, v_\parallel/k_\perp\, v_A)$ the avoidance of the mode conversion requires $k_\parallel/k_\perp \leq v_A/v_{Aedge}$, where v_{Aedge} is at the plasma edge. Experiments in NSTX and TFTR differ in $v_\parallel/v_A$ratios. We obtain the inequality describing the limiting condition for the CAE mode frequency as $\omega > \omega_c/(1 + Ca/R)$, where $C = 4\mathrm{k}_\parallel/k_\perp$. The parameter domain, which follows from this condition, is the region above curve 3 in figure 4.2.3.3 plotted for $C = 1$. We note that figure 4.2.3.3 is rather schematic without any specific plasma profiles. However, it illustrates though how STs and tokamaks are related in terms of the regions of most likely unstable CAE modes, based on minimizing the damping rates due to thermal particles.

It is clear that in general CAEs in conventional tokamaks are not expected to be excited far from the cyclotron frequency due to their rather high Alfvén velocity, i.e. low Doppler shift in comparison with the mode frequency. We should note that in special experimental conditions the conventional tokamaks can exhibit CAE instabilities at frequencies different from shown in Fig. 4.2.3.3. For example in Ref. [340] CAEs were reported at a fraction of the fundamental cyclotron frequency, which is due to special experimental conditions when the toroidal field was significantly lowered to 0.6T in comparison with the nominal value of 2T (see Table 2 of Sec. 4.2.6).

Note that CAEs were considered as mediators for energy channeling from fast ions to thermal ions [360]. In this mechanism fast ions excite CAEs during NBI in NSTX. The modes in their turn can stochastically transfer wave energy to thermal plasma ions. This mechanism can potentially improve the plasma performance in the STs.

4.2.4 Alfvén-acoustic modes

4.2.4.1 Low frequency Alfvénic modes: BAEs, BAAEs

We start this important topic by considering the Alfvén-acoustic continuum in tokamaks in a similar way to the formation of pure shear Alfvénic gap. The MHD continuity equation allows to couple two polarized oscillations, shear Alfvén and acoustic. The first one is incompressible but can push the plasma element to a different $\vec{B}$strength and force it to compress. Mathematically this connects the surface plasma displacement ξ_s with the divergence of the displacement $\nabla \cdot \xi_s$ via two equations:

$$\begin{gathered} \bar{\omega}^2\xi - R_0^2\hat{k}_\parallel^2\xi + \Gamma\beta\frac{q}{\varepsilon}\sin\theta\nabla\cdot\xi = 0, \\ \bar{\omega}^2\nabla\cdot\xi - \Gamma\beta\frac{R_0^2\hat{k}_\parallel^2}{2}\nabla\cdot\xi + \bar{\omega}^2\frac{2\varepsilon}{q}\sin\theta\xi = 0. \end{gathered} \tag{4.2.4.1.1}$$

If these oscillations are uncoupled we get two dispersions, Eqs. (4.2.2.2) and (4.2.2.4), with the resulting continuum shown in figure 4.2.4.1.1 (left). Both continua are degenerate at the rational q values. If the geometry allows coupling of these branches such as in toroidal devices the new gaps emerge [361] [362] [363]. The gaps are mediated by the finite pressure, plasma compressibility and the geodesic curvature and were described analytically for tokamaks in Refs. [364] [206] and numerically for stellarators and tokamaks in Ref. [365] [366] [297] [367] [368] [369]. Numerical results of Refs. [297] [366] [370] include the Alfvén and acoustic coupling effect on the dispersion in tokamak plasmas and demonstrated good agreement with AE activities observed in ICRH or NBI heated AUG plasmas [370]. The analytic form of this low frequency gap results in the gap structure shown in figure 4.2.4.1.1 (right).

The center of the gap can be estimated by comparing the sideband acoustic continuum, $\omega = v_a/q$, and the so-called "modified" Alfvén branch $\omega = k_\parallel v_A/\sqrt{1+2\mathrm{q}^2}$, which exists in the vicinity of the rational surface. Thus it is expressed via

$$\frac{\Gamma\beta}{2\mathrm{q}^2}\frac{v_A/R_0}{1+\sqrt{\Gamma\beta/2}\sqrt{1+2\mathrm{q}^2}}, \tag{4.2.4.1.2}$$

whereas the width of BAAE gap is $\Delta\omega = (\Gamma\,\beta/q)\sqrt{1+2\mathrm{q}^2}$.

Moreover, in Refs. [206] [371] these gaps were numerically shown to contain new eigenmodes - beta-induced Alfvén acoustic eigenmodes (BAAEs). The eigenmodes are localized near the accumulation points (extrema continuum points) of the gaps. Experimentally they are

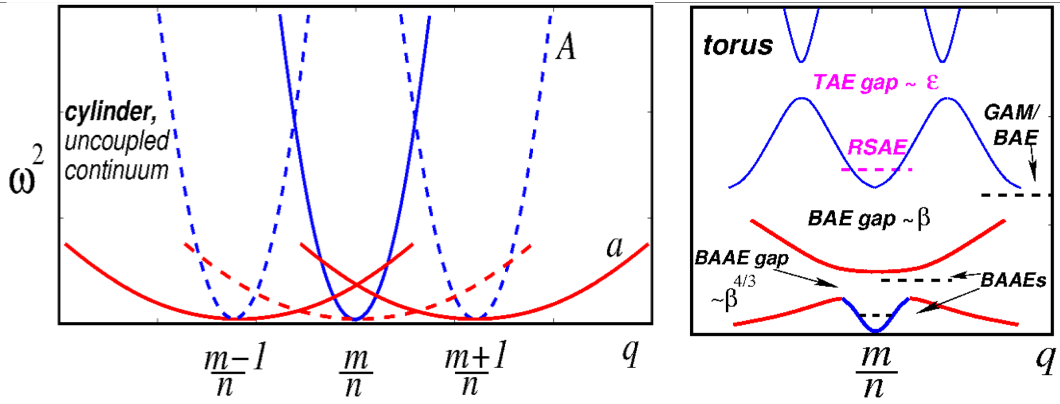

Figure 4.2.4.1.1 *Low frequency Alfvén acoustic continua in the cylinder (left) and in the torus (right) . For the purpose of illustrations BAAEs and RSAEs are shown at frequencies above the accumulation points of the corresponding continuums. Shown RSAE line corresponds to the down sweeping mode (see.sec. 4.2.2.2), whereas its plausible BAAE counterpart was not studied yet. The figure is adapted from Ref.* [372].

shown to be in agreement to have the radial structure as was modeled by the ideal MHD code NOVA [371]. One of the surprising experimental results is on the BAAE instability observations. Since they are the results of the coupling to the acoustic branch, BAAEs are subject to strong thermal ion Landau damping. It is thus expected that these modes should be excited at $T_i \ll T_e$. Nevertheless, BAAEs were identified in NSTX, JET [371] [206], DIII-D [372], HL-2A [373] and reported from AUG [370] when electrons had a temperature comparable with ions. The Alfvén acoustic gaps are much more complex [9] in helical devices such as stellarators and have only begun to be studied experimentally [367] [374].

In Ref. [363] a global mode with the frequency inside the BAAE gap was presented. That mode identified as BAE seems to have strong interaction with the continuum as can be seen from the figure 7(d) of that reference. For that reason this mode is ignored in the eigenmode solver within the ideal MHD NOVA code (run by one of us, NNG). The analysis of [363] uses the antennae version of the CASTOR code, which resulted in low continuum damping according to that reference. BAAE modes of Refs. [371] [206] are notably (well) localized near one BAAE gap (see Fig. 4.2.4.1.1 (right)). Local BAAE modes seem to be unlikely excited by the antennae from the plasma edge since they interact with the continuum in the evanescent regions as was found by NOVA. To this extent BAAEs and BAE of [363] are different modes. However, this is an issue to be studied in the future using the kinetic codes capable of resolving the resonances with continuum and as well as the thermal ion FLR effects. Such study should address if possible the reason of low continuum damping of the BAE mode found in Ref. [363].

Other effects on BAAEs due to thermal electrons and ion diamagnetic frequencies are important for the mode dispersion and stability [9] [236] [365] [372]. The accurate study of the low frequency modes requires numerical kinetic nonperturbative treatment such as the one described in Ref. [366]. Most comprehensive treatment of the Alfvén-acoustic coupling includes the kinetic effects, such as the resonant interaction between the plasma ions and oscillations can be found in Refs. [375] [376] [377]. This treatment allows to address the ion Landau damping which is shown can be large for the eigenmodes within the BAAE gap [372] if the electron and ion temperatures are comparable.

Being electromagnetic, BAEs have different polarization than the (mostly) electrostatic GAMs [378] [379]. In addition, BAEs have nonzero toroidal mode number whereas GAMs have $n = 0$. Both GAMs and BAAEs have polarization partially due to coupled acoustic (sound) MHD branch, which has low phase velocity, $v_a = \frac{\Gamma\beta}{2} v_A \ll v_A$. It also means that thermal ion velocity is close to v_a and that BAAEs and GAMs are potentially strongly damped as we noted above. Thus, BAEs are to be considered as candidates for burning plasma instabilities the same way as TAEs are and should be included in the reactor designs analysis. We should note that both BAEs and BAAEs are reported near the accumulation points of the continuum, see Fig. 4.2.4.1.1 (right).

From the relevance for burning plasmas in ITER, recently, BAEs are again studied theoretically and experimentally in tokamaks and stellarator/helical devices [376] [380] [366] [297] [381] [369] [367][312]. In AUG, BAEs destabilized by energetic ions are clearly detected during the sawtooth phase and the plasma current ramp-up phase. The experimental data are compared with the linear gyrokinetic eigenvalue code LIGKA [297]. The numerical results for real frequency and mode structure show good agreement with the experimental observations. Figure 4.2.4.1.2 depicts the mode structure of $m = 2/n = 1$ BAE which is located near the q=2 rational surface. The difference between the poloidal magnetic flux ψ and the electrostatic scalar potential ϕ measures the polarization of the mode and is proportional to the parallel wave electric field. It is much smaller than each of its components, ψ and ϕ . This clearly indicates the Alfvenic character. Moreover, the calculated 2D mode structure agrees well with that measured by ECEI diagnostic. The BAEs will play an important role in the ITER reversed shear scenario, because they are located in the outer region, i.e. closer to the plasma edge. If compared with RSAEs, BAEs can might expel

EPs more effectively. This is an important issue for ITER.

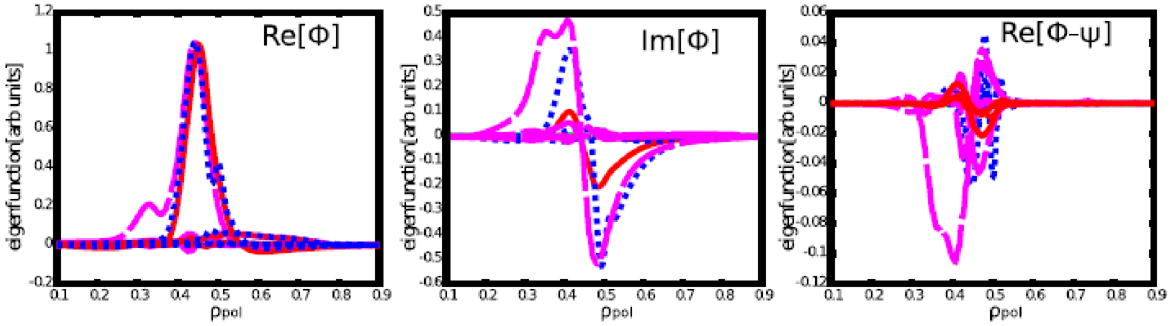

Fig.4.2.4.1.2 *m=2/n=1 BAE radial structures calculated by the LIGKA code. (left) Real part of the electrostatic scalar potential ϕ, (middle) the imaginary part, and (right) the difference between real pats of the poloidal magnetic flux ψ and electro static potential ϕ which is proportional to $E_{//}$ of the BAE* [297].

4.2.4.2 Low frequency modes driven by suprathermal electrons

We discuss here the excitation of low frequency global mode by suprathermal electrons that have a distribution function significantly deviating from the Maxwellian. New low frequency modes were observed in DIII-D [382] and other tokamaks: Frascatti Tokamak Upgrade (FTU) [383], HL-1M [384], HL-2A [385] and Tore Supra [386]. The fast electrons are created during ECR or lower hybrid (LH) heating. These observations motivated theoretical studies that seem to be interesting to highlight as they show all three elements of the research process identified in the introduction to section 4, namely eigenmodes, drive and the resonant particles. Theories that were published on the electron fishbones include [384] [387] [388] [389] [390] and we would like to recommend the recent thesis on this subject [391]. An important point that follows from theory is that suprathermal electrons can destabilize these instabilities since the excitation depends on the precessional drift and/or the circulating frequency of the charged particle, not on its mass.

We note that a very recent study performed on C-MOD suggests that the excitation of fishbones in the presence of energetic electrons can be via the non-resonant mechanism [392]. The mechanism is not completely understood but several observed properties are indicative that the excitation is non-resonant because of the weak to absent fishbone frequency chirps, low (almost zero in the lab frame) signal frequency in comparison with the characteristic frequencies of electrons drift motion, etc.

An initial theory development [384] allowed the identification of particles that resonate with fishbones in a more quantitative way than in the original experimental paper discussion [382]. Ref. [387] pointed out the drive that is coming from the barely trapped electrons. The mode structure was argued to be at $m/n = 1/1$ as the fishbone theory is predicting [183] [393]. The role of the circulating electrons is found to be even bigger than the barely trapped ones [388].

Typical fishbone frequency chirping is often used for this mode identification [385] and for its nonlinear regime identification [389], which was demonstrated for the first time using the FTU results and is shown in Fig. 4.2.4.2.1, see the signal having bursting character (denoted ECE Ch9 in the figure). As one can conclude from Ref. [389] the successful theory needs to rely on a realistic model for the electron distribution function. As in the original fishbone theory [183], the dispersion relation yielded the growth rate of the fishbones and their continuum damping [389], which appears due to AC proximity to zero (see Fig. 4.2.2.2 that implies almost zero fishbone real frequency). A critical excitation threshold emerges when the continuum damping balances the drive term

$$\beta_{ec} = \frac{r_s^2\sqrt{q_s''}}{\sqrt{2}R_0 q_s}\Lambda^{3/2}, \tag{4.2.4.2.1}$$

where $\Lambda \approx |q_s - q_0|$ and the subscript s refers to $q = q_s = 1$ surface. As it follows from this expression the threshold condition for electron fishbones gets more stringent for increasing $\Delta q_s = q_s - 1$, which is consistent with the experimental observations [389].

We would like to mention that energetic particle modes (EPMs) driven by suprathermal electrons were observed in the CHS stellarator [394]. This $m/n = 2/1$ mode had frequency around $60 - 70kHz$ and exhibited the recurrent bursting behavior. The instability propagated poloidally in the ion diamagnetic direction and toroidally in the precession direction of helically trapped electrons. Other low frequency oscillations are reported from stellarators and driven by the energetic electrons generated by ECH [395]. This is thought to be the acoustic mode rather than the gap mode due to Alfven-acoustic coupling because the mode frequency is weakly dependent on the rotational transform in the cold ion plasma ($Ti \ll Te$) [395] [367].

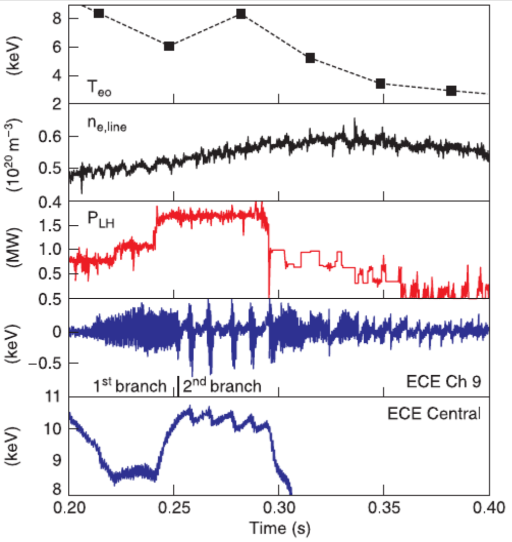

Figure 4.2.4.2.1 *Time evolution of the central thermal electron temperature, plasma line density, LH coupling power, fast electron temperature fluctuations and central radiation temperature in FTU discharge. The nonlinear behavior of fast electron temperature fluctuations of the electron fishbones reflects the level of LH power input* [389].

The theory and physics understanding of electron fishbones is sufficiently advanced to suggest numerical studies. Further investigations could improve our basic understanding of the physics and the control methods. As we state in Sec. 8, current drive modifications due to electron fishbone effects seems possible. This effect alone provides a good motivation for further studies.

4.2.4.3 EP driven GAM (EGAM)

A special phenomenon observed in JET [396] [397] [398] [399] was characterized by the toroidal mode number zero. More recent studies include the DIII-D tokamak [400] [401] and LHD stellarator experiments [87] [402]. In most of the reported observations GAM frequency modes had intense virulent chirping frequency evolution on a time scale of a few milliseconds. However, GAMs observed in LHD RS plasmas with counter NBIs are reported to be continuously excited at some times and have pitchfork splitting and rapid upward and downward chirping during superimposed ECH [87] [403]. These modes were interpreted as new (unlike regular GAMs [398]) and intrinsically energetic particle modes since both the mode frequency and mode structure can be described non-perturbatively by the EP dynamics [404]. The dispersion of $n = 0$ electrostatic EGAMs was derived for a tokamak plasma in the same paper using the hybrid-kinetic MHD framework with the non-perturbative contributions from EPs. EGAM radial electric field from the plasma momentum equation was used to derive the dispersion relation for local solutions:

$$\omega^2 = \omega_{EGAM}^2 \equiv \omega_{GAM}^2 + \beta_f \sum_p \quad \int d^3v \frac{G}{\omega^2 - p^2\omega_b^2}, \tag{4.2.4.3.1}$$

where G includes EP distribution function velocity derivative and the toroidal plasma equilibrium related coefficients. In the paper, slowing down DF with the pitch angle anisotropy is adopted. Here EP drift frequency ω_b stands for the transit frequency for passing particles and the bounce frequency for trapped particles.

Let's formulate three conditions of the instabilities (see discussion in the introduction to sec.4). First, the EGAM eigenmode solution has a radial structure [404] resembling the GAM structure [398]. Secondly, the resonant particles are determined by the resonant condition in Eq. (4.2.4.3.1), i.e. $\omega^2 = p^2\omega_b^2$. Thirdly, the part of EGAM drive proportional to EP pressure radial gradient is zero, since $n = 0$. Thus, the drive of EGAMs is due to the anisotropy of their DF that provides a unique bump-on-tail like source of energy for the instability. For low EP pressure, only one mode can exist and this mode transforms smoothly to the conventional GAM with the decrease of EP pressure down to zero. When EP pressure exceeds the threshold value, two new modes emerge in addition to the conventional GAM branch. The mode frequencies and the stability of the new modes depend critically on the value of ω_{bo}/ω_{GAM}, where ω_{bo} is the EP orbit frequency at the pitch angle $\chi = 0$.

The anisotropy drive of EGAMs is more accentuated in a follow-up paper by Berk [405]. The paper noticed that the EGAM instability develops very quickly after the start of NBI in DIII-D experiments [400]. That allowed the development of a model with the analytic EP distribution function. The existence of the loss boundary in the pitch angle direction provided the source for the instability in the expression for $G$and was called critical for the formation of the negative energy EGAM. Recently, linear behavior of EGAM in LHD was studied by a hybrid code using the LHD type q-profiles and a tokamak equilibrium without non-axisymmetric field effects, [406], and the results show the similar characters of EGAM discussed by Fu [404]. This simulation also shows the radial propagation of EGAM. In very low density LHD plasmas where beam beta is much higher than the bulk beta, strong EGAM bursts having rapid frequency chirping up are observed by magnetic probes and HIBP and the possibility of bulk ion heating by the EGAM is discussed [407] [408]. In LHD characteristics of quasi-stationary driven GAM are also investigated [409].

The coupling of the EGAM to (kinetic) GAM continuous spectrum is considered in Refs. [410] [411]. It was found that the nonlocal EGAM solution can tunnel to the outer plasma region and interact with the GAM continuum. Nonlinearly EGAM saturates via wave-particle trapping. The study of EGAM in the nonlinear regime allowed a discovery of an important second harmonic in the radial electric field due to the nonlinear self-interaction of the mode [412]. Fully kinetic description of the linear excitation of EGAMs and their nonlinear saturation is considered in Ref. [413]. The results of this full kinetic approach show slight differences with those of hybrid approach in [404].

We should note that GAMs can be generated by MHD nonlinearity and that those GAMs are not unstable modes like EGAM. They can play an important role in EP instabilities saturation as was recently shown [246].

A mechanism for energy transfer from energetic particles to bulk ions via EGAMs is discussed within the framework of quasilinear theory [414]. Landau damping of EGAM by bulk ions leads to bulk ion heating and can act as a kind of alpha channeling.

4.2.4.4 High frequency fishbones

In this review we do not cover many studies of fishbones driven by ions and refer the interested reader to recent topical review [11] for fishbone theory and observations (see Section 4 in [11]). Appropriate for this section are studies of the so-called high frequency fishbones [415] [416] [417] which combine Alfvénic and acoustic oscillations.

In the first paper, [415], observations from JET on two types of fishbones were reported for the ICRH pulses with deuterium plasmas at low density and high H (hydrogen) minority energy content. The first type of mode was associated with “classical”, precessional, fishbones [183] which in JET experiments had frequency in the range $f = 45 - 75\ kHz$. This range corresponds to trapped ICRH minority ion toroidal precessional drift frequency which was the main reason for the identification of the oscillations as fishbones. The precessional mode relatively high frequency required significantly high minority ion energy, estimated to be around $1\ MeV$.

The second type of modes, studied earlier in Ref. [393], has notably lower frequency, which was compared with the diamagnetic frequency of thermal ions. These modes exist in the plasma without fast ions and propagate in the direction of thermal ion drift. The source of energy for the instability in this case is the pressure gradient of the bulk ions. The frequency of the mode is low, up to $10\ kHz$ in JET plasmas. A plausible scenario for interplays between two types of fishbones and sawteeth were proposed. A third type of fishbones called hybrid was also considered and characterized by wider frequency variation, from $f \approx 75\ kHz$ to $f < 10\ kHz$.

The second paper [416] explains the very same observations in view of possible solutions in the BAE/GAM frequency range. It applies more quantitative criterion based on the sign of the fishbone-like dispersion relation which connects the mode frequency (via the inertial layer contribution) and the components of the potential energy of the mode such as given in Eq. (4.2.1.1). The high-frequency fishbone is consistent with the GAM/BAE excitation primarily on the basis of the mode frequency comparisons. The frequency of the mode is estimated to be near the values coming from BAE theory, $\omega_{BAE} = q\omega_{ti}(7/4\ + T_e/T_i)^{1/2}$. BAE then can resonate with ICRH H-minority ions which have precession frequency equal to the mode frequency if the ion energy is around $\sim 1\ MeV$.

Finally the third paper [417] introduces the plasma compressibility, which is shown to have strong effect on $m/n = 1/1$ modes in general, and finds three solutions. The lowest of these solutions has a frequency similar in magnitude to the BAAE eigenfrequency shown in Fig. 4.2.4.1.1, but the radial mode structure is much broader. The second solution of [417] apparently has the same frequency as the BAE high frequency fishbone mode of [416]. This also can be judged based on the accumulation point of the Alfvén continuum which is the same for both modes. Ref. [417] though considered the solution of [416] to be different from BAE. Perhaps detailed numerical calculations encompassing both solutions are appropriate to address this issue.

The studies concisely reviewed in this section are performed within the linear framework that definitely needs to be extended to include the nonlinear evolution stage.

4.2.5 Effects of kink modes and sawteeth on EP transport

The interaction of EPs with the internal kink modes can be treated either as collective effects or as a single particle effect depending on whether the EP density is high or low, respectively. In the former case well known phenomena, such as $m = n = 1$ EP driven fishbones or EPMs, appear (discussed in section 4.2.8.1). If the fast ion density is not high enough for the fishbones to be excited EPs still can work collectively to stabilize the sawtooth oscillations. This process will be considered in section 7.3 in applications to the burning plasmas and ITER in particular. If the sawtooth crash happens it causes the redistribution of fast ions and this is reviewed in this section.

The redistribution of EPs due to the sawtooth crash was studied extensively both theoretically and experimentally since Heidbrink's review [1] and its understanding was shaped by the experimental observations to large extent [418] [419] [420] [421] [422] [423] [19]. An investigation on TEXTOR device by the CTS diagnostic helped to resolve 1D EP distribution function for various viewing angles [424]. Very recent experimental study of EP transport during sawteeth was done on DIII-D tokamak with the use of the FIDA diagnostics [425] which is reviewed in this section.

Let us outline the theory first which is now well developed and summarized in [426]. In general MHD events are slow evolving except for fast reconnections which occur for $m = 1/n = 1$ sawtooth crash on a very short time scales $\tau_{cr} \approx 10^{-5} - 10^{-4} sec$ (crash time) [427]. This time is so fast that it is comparable with the characteristic drift frequencies of EPs namely with their precession frequencies. As a result passing particles stay attached to the field lines [418] whereas this model fails to describe the trapped particles [420] [421]. In recent experimental studies [425] the application of the EPs attached to the field line model (or simply inverse model [428] [429] derived from the Kadomtsev sawtooth reconnection) gives surprisingly reasonable agreement with the FIDA data (see fig.13(a) of Ref. [425]).

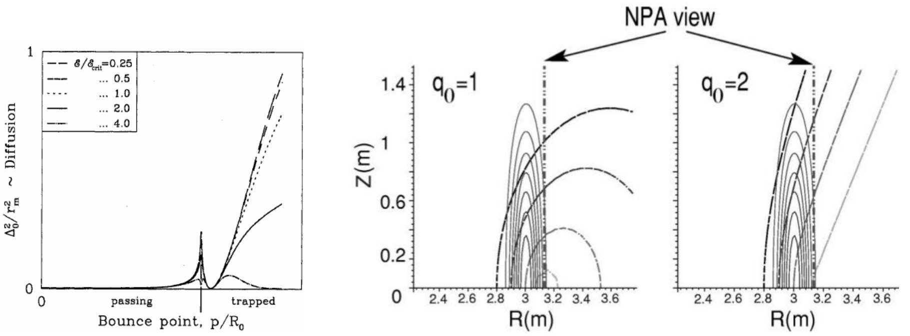

Fig. 4.2.5.1*. Left figure shows fast particle bounce point displacement in radius for different particle energies* [145] *. The figure on the right shows the contours of initial spatial distribution of EPs (solid lines) and the ion characteristic trajectories (dashed curves) of their bounce point motion during the crash event on JET* [432].

The trapped EPs precess relatively slow and can be affected by the electric fields induced by the sawtooth reconnection event. A relatively simple analytic model for the high aspect ratio plasma was developed to describe the redistribution of trapped particles [145] (for more sophisticated treatment refer to [426]). The model relies on the small orbit width approximation and uses the critical EP energy parameter [430]

$$E_{crit} = \frac{2\omega_c m_\alpha a R}{n\tau_{cr} q}, \tag{4.2.5.1}$$

which is approximately equal to the energy of trapped particles precessing toroidally on a time equal to the sawtooth crash time. Here, ω_c and m_α are the cyclotron frequency of energetic ions and the ion mass respectively. Energetic trapped particles at energies above critical, $E > E_{crit}$, average the electric field generated by the sawtooth. The change of EP bounce point during the crash obtained in Ref. [145] is shown in figure 4.2.5.1 (left) for both trapped and passing particles depending on their energy. Similar expressions follow from more rigorous formulations [431] [426].

Figure 3.2.1.1 (right) from section 3.2.1 shows how the PCX diagnostics [19] makes use of trapped H^+ minority ions signal and the FPPT code modeling to study both the sawtooth mixing mechanism and the ripple diffusion. In DIII-D [425] trapped particles are shown to be reasonably well modeled by the inversion formula.

It turns out that the same formalism is applicable not only to EP sawtooth mixing but also for the fast ion (also H^+minority) redistribution by the $m = 2/n = 1$ pressure driven kink mode [432]. The difference in the poloidal mode numbers gives different trapped ion trajectories as predicted by theory and is shown on the figure 4.2.5.1 (right).

The resonant effects of EPs with the sawtooth perturbations were considered in Ref. [433] and show that particles can be lost and redistributed in the poloidal and toroidal directions according to the resonance conditions for the zero frequency oscillation $s\omega_b = l\omega_\varphi$. The numerically obtained fluxes were compared with the observations of fusion alphas on TFTR and a reasonable agreement was demonstrated [434].

Another example of sawtooth effects is valuable for EP studies was inferred from CTS diagnostic with the first measurements reported recently [64] [435]. The studies investigated EP dynamics in TEXTOR during sawteeth to resolve the 1D fast ion velocity distribution function for various angles with respect to the magnetic field [436]. As we noted in Sec.2.6 the obtained data need thorough interpretation which is done for TEXTOR in Refs. [424] [436]. It was found in particular that trapped energetic ions are less susceptible to sawteeth-induced transport than the passing ion population, which agrees with theories.

The effects of kink modes on fast ions seem to be understood. They can be important to include in realistic predictive plasma modeling. Depending on the required accuracy of the predictions analytic estimates could be as good as the numerical ones.

	ITER [439]	JET [439]	TFTR [439]	AUG	JT-60U	DIII-D	C-Mod	ST	CHS N=8	LHD N=10	W7-AS N=5	W7X n=5	NCSX N=3
a,m	2	0.94	0.87	0.5	0.78	0.63	0.22	0.62	0.18	0.5-0.64	0.2	0.5	0.33
R,m	6.2	2.92	2.52	1.7	3.3	1.6	0.68	0.83	0.92-1.	3.6-3.9	2	5.5	1.42
I,MA	15	4	2.7	0.8	1.3	1.2	0.8	0.8	< 0.03	<0.15	-	-	0.7
B,T	5.3	3.5	5.5	2	3.7	2	8	0.45	0.8-1.2	0.6-1.5	2.5	3.0	1.7
n_{e0},$10^{20}m^{-3}$	1	0.45	1.02	0.4	0.3	0.26	~2	0.4	0.7-2.5	0.01-0.3	1.2	1	0.6
E_{fNBI},MeV	1	0.15	0.12	0.09	0.36	0.08	~0.3 (ICRH)	0.09	0.035	0.18	0.05	0.05(as)	0.04
E_a,MeV	3.52	3.52	3.52	-	-	-		-	-	-	-	-	-
a/r_{fNBI}	52	42	68	16	23.5	22	22	4.6	4-6	6-14	11	11(as)	14
a/r_a	39	12	18	-	-	-		-	-	-	-	-	-
b_{pl},%	6.5	4.9	6	1.8	~2.6	0.7	0.8	12.5	0.1-0.25	0.5-2.5	2	2(as)	4.25
b_{fNBI}/b_{pl}	0.08	0.14	0.17	0.39	~0.4	1.7	0.4	1	0.8-2.5	0.5-2	0.25	0.25(as)	~0.25
b_a/b_{pl}	0.19	0.08	0.05	-	-	-		-	-	-	-	-	-

***Table 2**. Nominal parameters of representative toroidal fusion devices for the plasma parameter diagrams shown in Fig. 4.2.6.1.*

4.2.6 Present day and future burning experiments in view of wave-particle resonances

After the introduction of various eigenmodes above we highlight their interactions with EPs. As we noted in the introduction to section 4 the wave-particle resonances (or WPI) are a key part of a theory to identify certain observed phenomena. This often helps to find a new physics or explain the similarity between the existing devices. The wave-particle resonances are key for the kinetic description of the plasma oscillations considered in Sec.4.2.1.

In order to prepare the numerical tools to make projections to BPs it is important to validate them against the present day experiments. This is discussed in sec.7.1 on ITPA initiative to benchmark the existing models. Good references to read on WPI are [15] [105] [181] [437]. We would like also to point out that the toroidal field ripple (sec. 3.2) and RMP effects (secs. 3.2.2, 4.1) can be handled via the WPI formalism.

Examples of new findings that are based on the wave-particle resonance analysis include

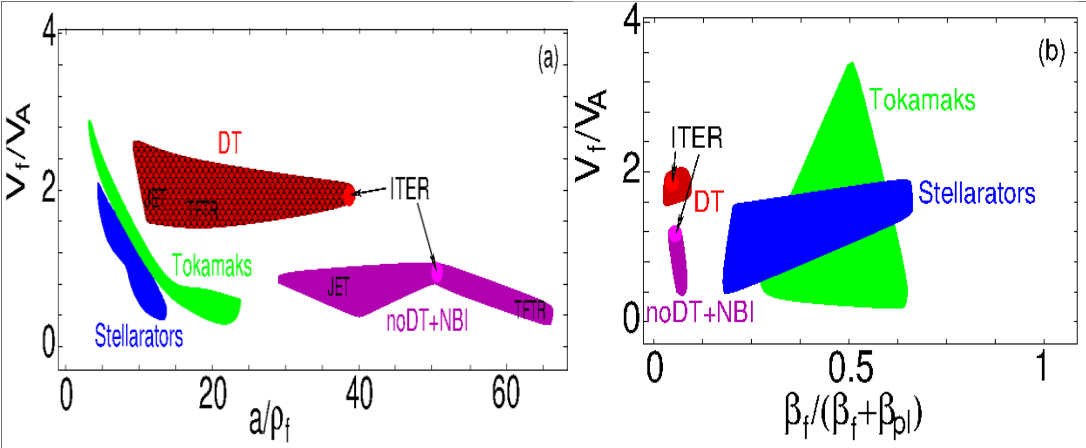

Figure 4.2.6.1. *Operating diagrams of present day tokamaks and stellarator with the nominal operating points for ITER also indicated. The JET, TFTR and ITER regions are plotted for DT operations and for those without DT but with NBI. The plasma parameters used for these plots are summarized in Table 2.*

electron fishbones (sec.4.2.4.2) and bounce or precession frequency fishbones discovered in NSTX [438]. The later paper points out at the oscillations in NSTX that exhibit characteristic fishbone-like frequency chirping from the TAE frequency range 50kHz down to very low values. Because of this the theory had to find a group of EPs that are characterized by such frequencies in a similar way to the case of electron fishbones. In such exercise, the mode numbers were taken from the experiment and the guiding center orbit following code was employed to compute the drift precession and bounce frequencies of trapped particles. It was noted that the dispersion relation (4.2.1.4) can take the form of "generic" fishbones [183] with similar stability properties. One of them is that the pressure drive exceeds the dissipation due to the interaction with the continuum (first term in Eq. (4.2.1.4)). For the slowing down DF of fast beam ions with a single pitch angle it was found that the unstable fishbone should have the real part of the mode frequency $\omega_r = 0.83(\omega_b + n\omega_\varphi)$ and the corresponding threshold instability condition. Estimates indicated that the beam drive is located at around $q = 2$ surface and that the thresholds and frequencies of the observed signal are consistent with the experimental observations. The fishbones considered were predicted to be important in high current, low shear discharges with a significant population of trapped particles with large mean bounce angles. Such distributions are often considered to be stable against the conventional fishbones in burning plasmas due to fusion products in general. Other types of high-frequency fishbones are discussed in section 4.2.4.4 in connection with the coupling of Alfvénic and acoustic branches.

The general resonance condition, Eq. (4.2.1.6), written for passing and trapped groups of particles in tokamaks [105] helps to understand the drive and to study one or another plasma excitations. Indeed, if we consider low frequency modes, $j = 0$, in Eq. (4.2.1.6), for trapped EPs we find $\omega = \bar{\omega}_D$ whereas for passing particles $\omega = l\omega_b$. With the typical condition for precessing frequencies, $\omega_b \gg \bar{\omega}_D$, one can separately study the trapped and passing particle effects on instabilities. In stellarators, EP orbits drift differently than those in tokamaks, and can be divided into three main groups: passing, helical ripple trapped and transition particles that travel around the torus and are trapped in the helical field ripple and de-trapped from it without collisions. Accordingly, many additional wave-particle resonances are possible besides the ones normally expected in tokamaks.

The wave-particle resonances help to arrange the present day, planned, and in particular ITER experiments according to physics understanding and expectations. Table 2 presents the summary of such arrangement. In that table for DT plasmas we assumed 50:50 mixture of the D and T isotops. Plasma parameters for ITER, JET, TFTR were collected in Ref. [439]. Other plasmas include AE oriented studies on present day toroidal devices: Further we included ASDEX experiments from Refs. [297] [440]. JT-60U [441], DIII-D [442], C-Mod [443], NSTX [337] (MAST parameter space are not shown separately due to its similarity to NSTX), CHS [248], LHD [10]. W7-AS [250] (future device is being built [97] w/some parameters used from W7-AS, denoted (as)), and NCSX [95] (construction stopped).

We made use of some of the nominal plasma parameters of tokamaks, stellarators, ITER and two DT experiments. The parameters relevant to EP studies are known from the corresponding publications cited in the table caption. From the table we compute three important quantities for the EP physics studies: v_f/v_A, a/ρ_f and $\beta_f/(\beta_f + \beta_{pl})$ and plot them in figure 4.2.6.1. In the plots for each group of plasmas the nominal point from the table is extended (except the ITER point) according to the B field or the plasma density variations down by 25% and joined with others of the group. The figure shown is not designed for precise positioning of a specific device from the above table but rather to relate the devices' operational spaces to each other and to ITER. This helps to understand if an ITER plasma is far (and how far) away in certain parameterization and if the major physics breakthroughs are required to reach its operational domain.

Let us demonstrate the usefulness of these figures for the analysis of DT experiments on JET and TFTR. From Fig.4.2.6.1 (b) it is clear that the locations are similar for both in terms of v_f/v_A and $\beta_f/(\beta_f + \beta_{pl})$ ratios. This suggests that the physics is expected to be similar, i.e. in the tokamaks of interest in the afterglow plasmas TAEs should be excited by fusion alphas when beam ions are sufficiently well thermalized [76] [243]. We note, that the ratio $\beta_f/(\beta_f + \beta_{pl})$ can be smaller (than given in the figure 4.2.6.1 (right)) in experiments due to the modification of the injection scheme.

Fig. 4.2.6.1 (a) illustrates that NBI ions have a higher ratio a/ρ_f in TFTR in comparison with alphas. Thus the sub-Alfvénic NBI ions in both JET and TFTR experiments should have contributed to the damping but in TFTR beam ions seem to interact more efficiently with relatively high n TAE-like modes, which are further away in n from the alpha driven AEs ($a/\rho_f \approx 65$ for alpha drive vs. $a/\rho_f \approx 18$ for beam ion drive). Hence, it seems easier to excite AEs in TFTR as the higher energy beam ions have less resonating particles contributing to the damping of the same n modes in comparison to the alpha drive. This was indeed confirmed in JET observations [217] where it was found that the NBI damping is hard to avoid and to prove that TAEs are driven by α's only.

Another example of the introduced diagram, Fig.4.2.6.1 (right), usage is given in Sec.5.4 to illustrate the relative positions of the NSTX plasmas in AE avalanche experiments. We should say that there are other ways to arrange the plasmas in the operational parameter space, such as those shown in Ref. [444]. The operational space in that reference is the plane $\langle\beta_f\rangle$ vs. $v_{f\parallel}/v_A$. In our opinion the ratio of EP to thermal plasma betas is more appropriate to use for the fast ion problems.

4.2.7 Alpha-channeling

The process known as alpha-channeling is speculative, but promises to relax the Lawson criterion by redirecting the fusion product heating to thermal ions, thus avoiding non-productive heating of thermal electrons [445]. It thus achieves the so-called hot ion mode [446]. In the original publication on α-channeling energetic DT fusion alphas were suggested to be cooled by the external wave and the power absorbed by the wave transferred (channeled) to thermal ions would avoid the electron heating.

The attractiveness of α-channeling can be understood from a simple power balance of the burning plasma reactor. The balance requires

$$\frac{Q_{pl}}{\tau_E} = P_\alpha = \frac{P_{reactor}}{5}, \tag{4.2.7.1}$$

where $Q_{pl} = \beta_{pl} B^2 V$ is the plasma energy content, the DT reactor power is $P_{reactor} = P_\alpha + P_n = 5\mathrm{P}_\alpha$. One can see that the reactor power is determined by τ_E if all alphas are confined, which is a limiting factor for the reactor performance [447]. In this case, burning conditions can be achieved in the hot ion mode with the relaxed Lawson criterion. Since the energy confinement time enters linearly with the energy content in Eq. (4.2.7.1), the relaxed Lawson criterion is up to two times lower than the nominal criterion known from the literature [181].

To relax the requirement of the power balance, Eq. (4.2.7.1), and to design the reactor with the improved performance, one has to allow losses of alphas [447]. An increase in the reactor power requires lowering τ_E on the assumption of fixed Q_{pl}, i.e. it is not possible unless some of the power associated with the fusion alphas is lost from the plasma and excluded from the power balance, Eq.(4.2.7.1). However, in the center of the alpha-channeling idea is not only fusion alpha losses but that their energy is recoverable within the plasma to thermal ions, thus allowing for decreased electron confinement time. The recovered energy might then be put directly into tail ions, or possibly used for ICRH current drive, thus further enhancing the utility of achieving the hot ion mode [448].

It was envisioned that the presence of two waves [449] would be compatible with the general α-channeling idea [445]. Although with one wave there is advantageously a very hard constraint on the motion of particles to move along a prescribed diffusion path, in practice it may be hard to find a wave with the precise wavenumber and frequency requirements to accomplish the optimal path. Using two waves may not guarantee a unique diffusion path, but on average the particles can be forced to lose energy to one wave or the other [450].

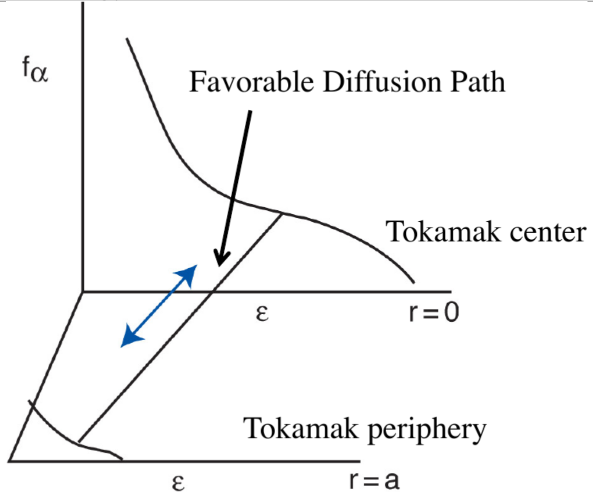

Fig. 4.2.7.1. *. A schematic of EP paths shown in the space energy vs minor radius. Shown are energy dependence of alphas EP DF in a reactor for $r = 0$ (center tokamak) and at $r = a$ (the periphery of the tokamak). At any radius, the alpha particle DF is monotonically decreasing in energy. However, there is a population inversion in energy along the indicated favorable diffusion path. The figure is adopted from Ref.* [451].

With two waves, the high frequency wave might be designed to extract the EP power whereas the second low frequency wave should result in EP radial diffusion and their eventual loss. The high frequency wave thought best to accomplish the energy extraction is the mode converted ion Bernstein wave (IBW) [451] , which was shown to have precisely the necessary wave characteristics [452]. The low frequency wave could be TAE modes. The introduced waves should be tuned to induce certain optimal paths of EPs in the phase space, which requires very delicate dedicated experiments.

A charged particle interacting with one wave traces a line in the $E-\mu-P_\varphi$ space. In such a representation EP trajectories tend to follow $P_\varphi \approx e_f\,\psi_p/c \approx const$ paths. Upon interaction with the wave, as was pointed out in Ref. [449], particle coordinates change according to laws

$$\begin{aligned} \Delta P_\varphi &= (n/\omega)\Delta E, \\ \Delta P_\varphi &= (nB/l\,\omega_c)\Delta\mu. \end{aligned} \qquad (4.2.7.2)$$

Thus, upon the interaction with one wave the COM of a particle traces a line with the possibility of extraction of the alpha particle energy determined by P_φ at low energy. The particle's path in the phase space is shown in Fig. (4.2.7.1) [451]. One can see from Eq. (4.2.7.2) that to choose a certain path in the phase space, in reality, might be very challenging. This would require a very coherent excitation of the waves as n's are typically high. Nevertheless theoretically α-channeling seems feasible and depends strongly on the experimental evidence of the baseline processes outlined above.

Experimental observations on this subject were conducted in parallel with the theoretical efforts. Most interesting were the observations of the anomalous EP diffusion on TFTR when the ICRH was applied [453]. There was one apparently great surprise in that the experimentally measured EP diffusion coefficient in particle energy was a factor of fifty higher than expected [207]. One possible explanation (not directly verified) was that the tokamak was ringing like a high-Q cavity, with the mode-converted ion-Bernstein wave exciting an internal mode [454]. That explanation gained support recently when related internal modes were observed on NSTX [359]. The experimental support is based on understanding the internal CAE instabilities offered by the theory, which we cover in some detail in Sec. 4.2.3 (see figure 4.2.3.3). That understanding helped to unambiguously identify the CAE modes through their polarization and spectrum. In addition, the stability properties of CAEs explained why in STs the eigenmodes are observed at frequencies lower than the fundamental cyclotron frequency, whereas in tokamaks the instabilities are expected in the proximity of the cyclotron frequency. This picture lent important support to Clark's idea [454].

One recent potential direction of the research is to optimize the alpha channeling effect and direct it towards the tokamak transformer recharging, recognizing that the low density stage of transformer recharging is particularly suited for a driven hot ion mode [455]. Transformer recharging is a method of using radio frequency (RF) current drive to recharge the toroidal current in a tokamak without letting the current itself reverse direction. The channeling effect is envisioned as a mean to power the current drive, whereas the transformer recharging optimizes the current drive effect. The current drive could arise from, in principle, any of the rf-driven non-inductive current drive mechanisms [456], although in achieving the hot ion mode together with current drive, it would be advantageous to use current drive mechanisms that heat ions rather than electrons.

Note that the original impetus for alpha channeling came from the realization that without arranging carefully the diffusion paths, the lower hybrid wave would damp on the alpha particles, making lower hybrid current difficult in the presence of energetic alpha particles [457]. This motivated both a more careful consideration of the energetic alpha particle damping [458] as well as motivation for development of the alpha channeling effect itself [445].

It is interesting to note as well that the basic mechanism of alpha channeling can be extended to other magnetic configurations. In particular, it was recently extended to simple mirror machines [459]. It was also extended to centrifugal mirror machines, where the effect was generalized to account for the fact that not all of the alpha particle kinetic energy lost would be captured by the injected wave [460]. Instead, in $E \times B$ rotating plasma, some kinetic energy is converted to potential energy as the channeling takes place in a potential well.

An interesting energy channeling scheme to bulk ions is proposed using ion Landau damping of EP driven GAMs which can be spontaneously destabilized in a plasma with energetic ions [414]. This is a promising alternative way to the above-mentioned original alpha channeling scenario.

A broader interpretation of alpha-channeling, which describes a more general redistribution of ions by means of waves in the plasma center, will be discussed in section 6. We think that the alpha-channeling deserves to be addressed in the future research. This is stated in Sec. 8. One can hope that trying to control the EP distribution we can learn different ways to change the distribution in the phase space. This is what we call phase space engineering. In a broader sense this is a direction the whole EP studies could reorient.

4.2.8 Strongly driven instabilities - EPMs

The Energetic Particle driven Modes (EPMs) are observed in present day devices and are expected in some ITER plasmas (cf. fishbones, see Sec. 7.3). They can be defined as oscillations whose structure and dispersion properties are strongly dependent on the energetic particles characteristics. In other words EPM is the mode which does not exist without the fast ions. This is opposite to the perturbative modes considered above which are not expected to change their properties when unstable, such as weakly driven TAEs (see sec. 4.2.2). One clear example of EPMs is fishbone instability [183] [393] which is seen in present day experiments and is relatively well understood. Another example of EPM is the EGAM (sec. 4.2.4.3) which does not exist without fast ions.

4.2.8.1 EPM examples including KBMs and rTAEs

We include into considerations here Kinetic Ballooning Modes (KBMs) as EPM example (KBM-EPM) because their frequency can depend strongly on the EP properties [461] [462]. KBMs are known theoretically to exist as the MHD gap modes when their growth rates are large [462]. Gap mode has a frequency in the order of the ion diamagnetic drift frequency. It can be destabilized only when the plasma is unstable with the regard of ideal MHD. In the opposite case, near gap mode threshold, the kinetic effects become important and modify KBM dispersion and structure.

For the KBM-EPM branch two excitation possibilities were considered in Ref. [462]: the modes are excited by circulating and by trapped fast ions. In the first case using single pitch angle slowing down EP distribution the dispersion (similar to Eq. (4.2.1.4)) results in real KBM-EPM frequency $\omega_r = 0.834 \mathrm{v}_{\parallel}/qR$. A threshold condition for this KBM-EPM instability was also obtained $\alpha_{thr} \equiv q^2 R_0 \beta_f^{'} = 0.683 s\, v_{\parallel}/v_A$. For the case of KBM-EPM instability driven by trapped particles let's consider the lower frequency solution, $\omega \sim \omega_{\varphi} < \omega_b$. In this case the KBM-EPM frequency is $\omega_r = 0.78\langle\omega_d\rangle$ and the threshold condition reads $\alpha_{thr} = 0.14\langle\omega_d\rangle\, qR/v_A$ where $\langle\omega_d\rangle$ is the time averaged drift precession frequency. The higher frequency solution $\omega \sim \omega_b$ can also exist. What can be seen from the properties above is that KBM-EPM frequency is determined by fast ions that is a good reason to qualify them as energetic particle modes.

Experimentally observed KBM-EPMs seem difficult to identify unambiguously. We would

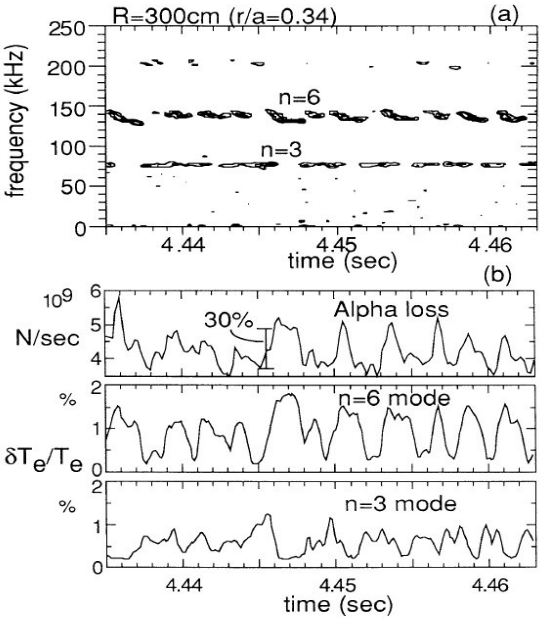

Figure 4.2.8.1.1 *A high frequency chirping $n = 6$ mode related to KBM in TFTR causes correlated losses of fusion alphas in the lost ion scintillator probe (SLIP) signal on figure (b). The figure is adopted from Ref.* [463].

like to point out at the experimental paper from TFTR which related certain high frequency modes to KBMs excited by fusion products, alphas [463]. Two types of modes were seen in those experiments. One type is called multifrequency quasicontinuous modes and the other - the bursting modes. The second class of modes is interesting as there is a correlation between the $n = 6$ mode signal and the SLIP loss signal (SLIP/FILD is discussed in sec 2.8). This is shown in figure 4.2.8.1.1 which clearly demonstrates the correlation of the alpha loss with the $n = 6$ mode. The signal in figure 4.2.8.1.1 (a) is related to KBMs based on the location of the strongest plasma pressure point corresponding to the location of the mode amplitude peak. Some other properties of the observed signal are also consistent with the KBM theory predictions. We stress that the $n = 6$ signal frequency evolution is up to 3 $msec$ as shown in figure 4.2.8.1.1 (a). This is consistent with the EPM characteristics of KBM.

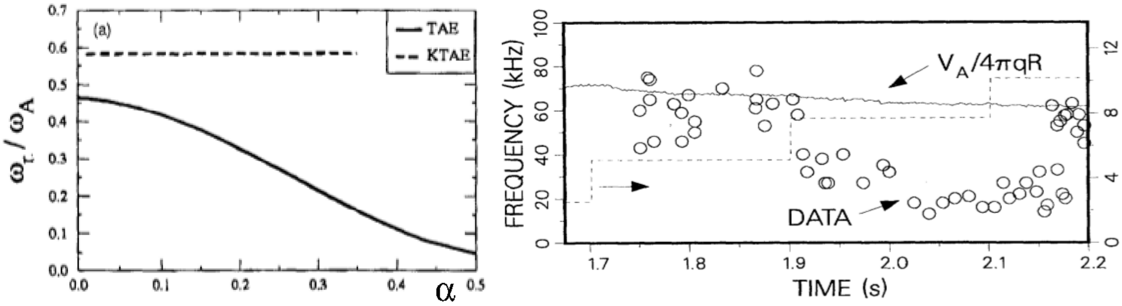

Figure 4.2.8.1.2. *TAE and KTAE solutions real frequencies on the left figure shown as dependences of the background plasma parameter and computed with the HINST code* [464]. *As this parameter increases the TAE solution moves into the rTAE one and eventually connects to a KBM. On the right figure shown is the observed frequency transition from the TAE mode to a low frequency mode in DIII-D suggested to be BAE using the comparison with the GATO code* [218].

A similar class of EPMs called resonance TAEs (rTAEs) was considered in Ref. [464]. Using the $s - \alpha$ model for the plasma equilibrium within the code HINST a smooth transition from TAE to rTAE was demonstrated during the increase of the plasma pressure gradient parameter α. A similar transition (from TAE to KBM) was reported in a concurrent work using similar numerical approach [465]. The name rTAE is due to demonstrated smooth transition of the mode properties from TAE solution to strongly nonperturbative solution with the properties determined by fast ions. At some value of α when EP contribution dominates, the found solution has the eigenfrequency inside the continuum and can be identified as KBM. It could be a BAE mode though as suggested in Ref. [218]. The distinction is possible to make by careful comparison of the poloidal amplitude dependence.

An independent approach to the EPM problem has been undertaken by another group [466] [467]. They took into account the effect of the electron drift in the crossed fields or compensating electron drift. For this effect to take place it is essential that EP orbits are large, that is if the energetic ion drifts radially it distorts electron distributions at new radial locations. Thus electrons can have an effective drift co compensate fast ion charge at each surface ion appears. This effect was suggested in Ref. [216] and was elaborated in Ref. [269]. It was shown in Refs. [466] [467] that EPMs need to be considered as positive energy waves with the damping coming from the continuum.

4.2.8.2 EP driven wall mode (EWM) on JT-60U and off-axis fishbones on DIII-D

It was observed in high-β plasmas in JT-60U and DIII-D tokamaks that EP driven modes interact with ELMs [468]. Abbreviated as EWM in JT-60U studies such EPMs emphasize the role of wall stabilization [469] [470]. On DIII-D similar EPMs were called *off-axis-fishbone-like* mode (OFM) stressing the similarity to classical fishbones [471]. Many properties of these EPMs are summarized in Ref. [472].

Like fishbones observed on PDX [473] they seem to be driven by energetic trapped ions at the fast ion precession frequency. The frequencies of these EPMs during bursts changes most rapidly reaching the amplitude maximum. Unlike the usual fishbones (internal kink modes driven by the energetic ions), the decay phase of EPM burst is highly variable and is usually shorter than the growth phase. EPM radial mode structure is similar to the external kink. It has radial peak around q=2 and alters its shape during the burst. In similarity to usual fishbones, the modes expel trapped EPs via a bunch with a definite phase relationship relative to the mode. The magnitudes of the loss bunch scale linearly with mode amplitudes. The toroidal rotation frequency across the entire plasma is suddenly changes due to the non-ambipolar fast-ion losses. The neutron signal oscillates in response to the wave. A special statistical analysis indicated that ELMs are triggered by EPMs if the repetition frequency of the later is higher than the repetition of the former. This points out at the pacing role EPMs play on ELMs.

It was noted that the EPMs of interest, EWMs or OFMs, can have not just one $n = 1$ component but their waveforms are distorted by others, $n = 2,3..$ [472] [474]. The EPMs do not always trigger ELMs. In figure 4.2.8.2.1 some EPM evolutions are plotted via their $n = 1$ and $n \neq 1$ component amplitudes. Both figures, (a) and (b), show similarity in the role of the $n \neq 1$ component which is required to be at a sufficient level to cause the ELM triggering. Also the amplitude of the EPMs to reach some level is a necessary, but not sufficient condition to trigger ELMs. Being driven by fast ions the EPMs transport them and affect the peeling/ballooning mode stability.

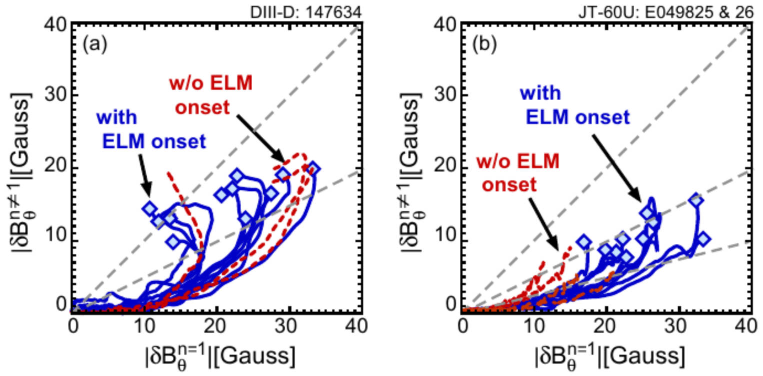

Figure 4.2.8.2.1 *Amplitudes of fundamental (*$n = 1$*) and distorted (*$n \neq 1$*) components of the EPMs on DIII-D and JT-60U tokamaks called EWMs or OFMs. ELM triggering in those experiments is indicated by diamonds on the figures where the ELM pacing by EPMs was observed* [468].

4.3 Implications of EP studies for plasma diagnostics

The fast ions induce events that carry important information about the plasma. It was proposed in the literature [475] to make use of these events as sources of information for diagnosing plasma. One clear example of this are energetic ion driven Alfvén eigenmodes, which are well documented in many devices. AE frequencies and mode structures are quantitatively explained by the established linear and perturbative theories, which provides the basis for so-called MHD spectroscopy. In this method the information about the macroscopic plasma properties and the energetic particles can be extracted as highlighted below. Another example is ICE covered in sec. 4.3.2 which is especially important in burning plasmas where other methods are hard to apply due to high levels of radiation that can potentially affect the diagnostic hardware.

4.3.1 MHD spectroscopy

The idea of MHD spectroscopy was first proposed as an *active* method using stable shear Alfvén waves excited by antennas or internal coils [476]. Later, MHD spectroscopy was extended to include Alfvén eigenmodes excited by EPs in a plasma [268] [475]. The use of RSAEs for the same purpose was clearly demonstrated on DIII-D [85], NSTX [278] and so on. In ASDEX BAEs were effectively employed for MHD spectroscopy in Ref. [366]. The extension of similar techniques to beta-induced Alfvén acoustic modes (BAAEs) is shown in Ref. [372]. The combination of *active* MHD spectroscopy using antenna excitation and *passive* spectroscopy with EP driven modes promise to be a powerful technique for the accurate reconstruction of plasma equilibrium information.

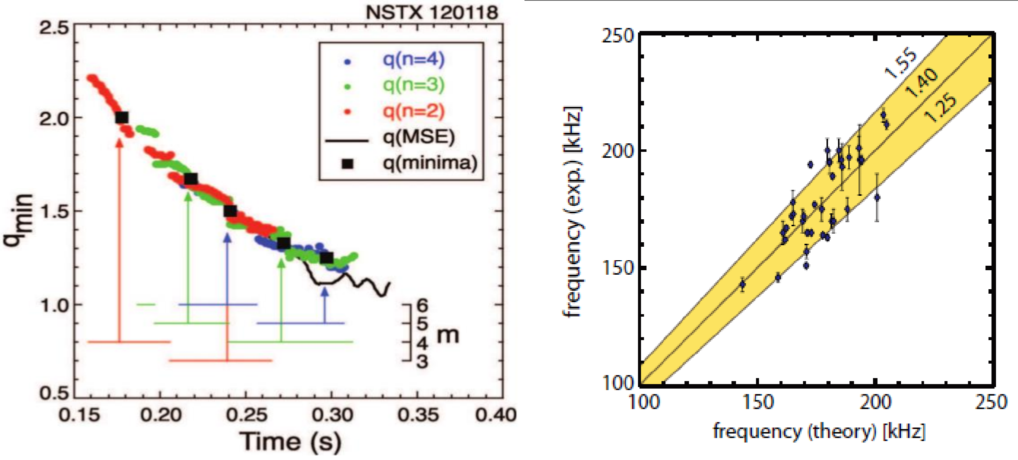

Figure 4.3.1.1 *Two examples of the application of MHD spectroscopy. The left figure shows an application to NSTX where RSAEs were observed with different toroidal mode numbers* [278]. *Also shown are the equilibrium reconstruction values of* q_{min} *(solid squares) and MSE inferred values shown as a solid line. The right figure shows the comparison of the adiabatic index or specific heat obtained by MHD spectroscopy in the C-mod plasmas* [481].

The requirements for collective modes to be suitable for MHD spectroscopy are pointed out in Ref. [475]. First, their dispersion relation should depend on macroscopic plasma properties, separate from the EP instability drive. Second, the modes should persist without suffering from strong damping, that is, the phase velocity should be away from the electron and ion thermal speeds. Third, the frequency range of the modes has to be away from the frequency range where the background micro-turbulence is actively excited. Finally, the amplitude should not be so high that the modes significantly affect the EP confinement and bulk plasma performance. Alfvén eigenmode instabilities typically satisfy these requirements. In MHD spectroscopy, the measurements of the mode frequency give accurate information about the plasma equilibrium, such as the radial profile of the safety factor q or the rotational transform, ion density, effective mass ratio and other quantities. Moreover, if the spatial structure of the mode is measured by various fluctuation diagnostics discussed in sec. 2.2, this input further improves the degree of accuracy of the extracted plasma equilibrium information. It should be noted in the application of MHD spectroscopy that Doppler effects due to toroidal and poloidal plasma rotations must be taken into account for the observed AE frequency. If the plasma rotation data are not available, the frequency differences between AEs with different toroidal mode number may provide the toroidal rotation velocity at the AE peak location under conditions of almost no poloidal rotation [477].

Here, we mainly focus on *passive* MHD spectroscopy using EP driven Alfvén eigenmodes. Although AEs in general satisfy the above requirements for MHD spectroscopy, to determine which modes are most suitable should be understood given the respective target information to be extracted with the help of experimentally available data. In most toroidal experiments, electron density profiles are available with high accuracy. In a mixed species plasma such as DT, the mass density can be properly evaluated by comparing the calculated frequencies of AEs such as TAEs with the observed ones. A standard diagnostic method to measure the safety factor q or the rotational transform profile is the motional stark effect spectroscopy (MSE) in toroidal confinement devices. This diagnostic provides the q-profile data with acceptable measurement errors and moderate time response of several milliseconds or more. However, the errors sometimes could be fairly large, around 20%. MHD spectroscopy using a specific AE such as RSAE provides very accurate predictions of the internal magnetic field structure of RS plasmas, and has a potentiality to back-up , or even replace in some cases, the MSE diagnostic or FIR polarimeter. In JET and DIII-D, it was demonstrated that the q_{min} can be derived very accurately in time in RS plasmas [268] [85]. Moreover, the minimum frequency f_{min} in the temporal sweeping of RSAE frequency contains the important information: $f_{min} = f_{GAM} + \Delta f$ as seen from the equation shown in sec. 4.2.2.2 Here, f_{GAM} is the GAM frequency of bulk plasma at the zero-shear layer (cf. $\bar{\omega}_{GAM}$ from sec.4.2.2.2) and Δf is the frequency offset having positive or negative sign due to the radial gradient of bulk plasma pressure and energetic ion density at the mode location [281]. Some properties of AEs such as TAEs and RSAEs excited in toroidal plasmas with energetic ions will deviate from pure shear Alfven waves (i.e polarization and dispersion eq.(4.2.2.2)), due to compressional effects.

The monotonic q-profile in a tokamak plasma is characterized by its value at the axis, q_0. This parameter plays an important role in sawtooth oscillations and also in the so-called hybrid scenario in ITER. The q_0 value can be predicted by MHD spectroscopy and was inferred successfully in JET using *active* MHD spectroscopy [478]. In an ICRF heated plasma with giant sawtooth crashes on JT-60U, q_0 was evaluated just before and after the crash with the help of MHD spectroscopy using EP driven TAEs and EAEs which were thought to be of a core-localized nature [479]. Here, q_0 was successfully predicted from the time sequence of multiple TAEs and EAEs having different toroidal numbers n. On C-Mod, RSAEs excited near the $q = 1$ rational surface in ICRF heated plasmas were observed by a phase contrast imaging system with a CO_2 laser beam [480]. These RSAEs also exhibited a characteristic frequency sweeping across the sawtooth crash. The temporal evolution of the q-profile by a sawtooth crash was derived by comparing the experimental data with the calculation results by NOVA-K. It should be stressed that MHD spectroscopy based on observations of AE provides a good opportunity to validate theoretical models of the sawtooth crash. Other important applications of MHD spectroscopy are to estimate the fuel ratio in D-T burning plasma though the observation of AEs. This potential was successfully demonstrated in JET by *active* MHD spectroscopy with antenna excitation of AEs [475]. Active spectroscopy method is introduced in Sec. 4.2.2.5. *Passive* spectroscopy using EP driven AEs is also a promising technique. In stellarator/helical plasmas of LHD RSAEs are detected in a RS plasma with the opposite sign of $q''(r_{min})$. The estimates of $(\iota/2\pi)_{\rm min}$ and the volume averaged EP beta were successfully derived then through the comparison of the minimum RSAE frequency and the frequency of EP-driven GAM excited concurrently [87] [10].

An example of the spectroscopic method highlighted above for the NSTX experiment was done in the paper Ref. [278] from which we reproduce the illustrative figure 4.3.1.1 (left). The physics included in the simulations is the same as discussed above, i.e. the GAM frequency shift of the AC and the toroidal plasma rotation. We should note that the frequency shift due to the pressure gradient, Eq. (4.2.2.2.3), vanishes at $q \approx 1$ and helps to explain the good agreement in the q_{min} plots. Note that GAM frequency shift still remains, but it does not depend on n number. Similar considerations were applied for sweeping-up BAAEs satisfying the modified Alfvénic branch dispersion (see sec. 4.2.4.1) $\omega = k_{\parallel} v_A/\sqrt{1+2\mathrm{q}^2}$ [372]. Results of the q_{min} reconstruction from such application demonstrated that BAAE can be employed in the MHD spectroscopy. The advantage of this is that there is no frequency shift such as due to GAM or the pressure gradient. However the BAAE modes can not be observed easily in the linear stage without being saturated as they seem to be more strongly damped than the RSAEs. The adiabatic index or specific heat ratio, Γ, plays an important role in the description of AEs. The suitable value of γ is discussed in details in the analysis of the minimum frequency during the RSAE-frequency sweeping in NSTX and C-Mod [280] [481]. The best γ values fitted to experimental data were inferred to be 1.40 ± 0.15 for RSAEs in ICRF heated low beta plasmas on C-Mod, and 1.34 to 1.38 in high beta beam heated plasmas of NSTX. Here we show another example of MHD spectroscopy, i.e. the values of γ obtained from the MHD spectroscopy and NOVA calculations for C-mod plasmas. They are compared to each other with good agreement as shown in Fig.4.3.1.1 (right).

As already mentioned, the energetic ion density gradient at the zero-shear layer and the evaluation of the averaged EP pressure can be estimated from the minimum frequency of RSAEs under the perturbative EP contribution condition. If the nonlinear theories of AEs are validated with the experimental data in the nonlinear regimes, these regimes could give us unique information about the velocity space resonant interaction between EPs and AEs. In a similar manner, the internal magnetic fluctuation amplitude was evaluated from the nonlinear behavior of AEs via the rapid frequency chirping of TAEs in MAST. This was done by comparing the experimental data with a calculation using a non-perturbative simulation code HAGIS [482]. In the next Section 5, the nonlinear effects of collective modes are discussed in details.

In further developments of this topic we would challenge the community to try to make the MHD spectroscopy to be more efficient. One way to do this is to attempt to set up a real time technique when certain acquired “measurement” would be done quickly without detailed comprehensive analysis. Examples of such technique are already known when the RSAEs appear as a certain sequence of many modes with different n-numbers. These are so-called Grand-cascades. The appearance of the Grand-cascades strongly correlates with the Internal Transport Barrier (ITB) formation and often appear just several milliseconds prior to the ITBs [483]. The real time spectroscopy such as shown in this section could be important for more precise information about the values of the safety factor for example.

4.3.2 ICE for EP Diagnostics

Here we overview the possibility to use ICE to diagnose alpha-particles in burning plasma experiments as was proposed in Refs. [341] [484]. This idea is based on the correlation of the ICE intensity, P_{ICE}, and the total neutron emission rate. The correlation data were collected using the ICE database over six years of JET operation and was included in the review Ref. [1]. The ICE diagnostic idea seems to be obvious and follows from the clear linear correlation up to the JET DT operation points. Thus in future DT burning plasma experiments with strong neutron and gamma fluxes potentially affecting the diagnostic hardware ICE in the expected frequency range above 10 MHz measured with the RF probes seem to be an attractive technique deserving further investigations.

At the time of both Refs. [1] [341] the theory behind ICE was rather in its initial state employing the local theory approaches. More widely accepted theories were developed later and we review them in sec. 4.2.3. New insights such as the oscillation polarization, frequency evolution etc. were gathered from the dedicated studies in STs as we argued in that section for the reasons that each of the unstable modes could be identified and studied separately. This is in contrast to earlier studies where primarily ICE envelops were used for research. As it follows from sec.4.2.3 more recent detailed studies give us the confidence in projections for burning plasmas. One of the results of such studies is that ICE can be explained slightly differently depending on if they are driven by fusion products or by the beam ions.

It is likely that in burning plasma tokamaks with strong magnetic fields the ICE spectrum will not be measured to the same resolution it is done in STs. This means that only the envelope of the ICE spectrum will be properly resolved. However even that may provide a wealth of information if analyzed adequately. The detailed attention given to this topic should be revitalized due to its relevance to the burning plasmas. Let us reiterate some points (see also sec. 4.2.3) to be considered in order to refine the ICE physics understanding. The cyclotron resonance conditions should be considered accurately and should include the Doppler shifted toroidal drift that gives rise to CAE propagation asymmetry against the sign of n in the dispersion relation. The Hall term contained in the dispersion further breaks the symmetry and adds the information about the toroidal direction of the EP motion as a group. The effect of the density profile (and the equilibrium magnetic field radial dependence) defines the CAE spectra directly with the dominant quantum number being the radial mode number. At present the subject of this section is speculative but nonetheless worth dedicated study.

We would like to add to the above discussion an illustration of more recent results of ICE observations on DIII-D tokamak during the excitation of the off-axis fishbones [472]. One can see from Fig.4.3.2.1 a clear correlation of the magnetic signal (upper figure) and the ICE signal measurements shown on the lower part of Fig. 4.3.2.1. This correlation already serves as a compelling argument in favor of the ICE diagnostic in BPs to detect energetic ions.

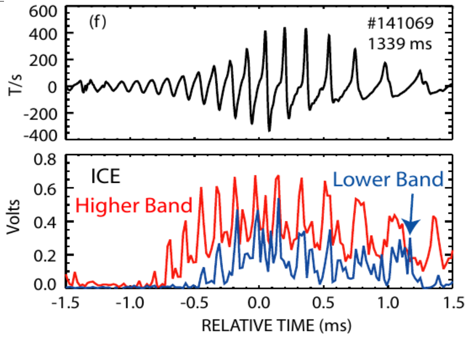

Figure 4.3.2.1. *An example of the ICE activity in DIII-D experiments which clearly correlates with the off-axis fishbones* [472]. *Lower figure shows the ICE signal of two frequency bands, lower band includes the fundamental cyclotron resonances, and higher band includes first few cyclotron harmonics. The upper figure corresponds to the Mirnov coil measurements of the off-axis fishbone event.*

A similar kind of ICE excitation was observed on LHD where TAE bursts induce ICE synchronously. This suggests fast ion radial transport due to TAE bursts into the plasma edge region [349].

The application of ICE for plasma diagnostics is proposed as a topic for future research in the summary section 8.

5 Nonlinear effects and energetic particle transport

The majority of experimental observations of energetic particle driven modes exhibit some form of nonlinear behavior, even if it is just that the unstable modes are observed in a saturated state where the energy transferred to them by the driving fast ions is balanced by dissipative processes.

First for the consistency of the review let us introduce the terminology used here to categorize the nonlinear mode evolution following Ref. [485]. In present day experiments some observed oscillations (such as TAEs) can be characterized by their gradual frequency evolution, i.e. their frequency changes on the same timescale as changes to the equilibrium. In contrast to these are chirping or bursting phenomena when the mode frequency changes rapidly (over $1-3$ msec), such as discussed below in Sec. 5.1.1. A third type is a special case of RSAEs (see section 4.2.2) which happens on equilibrium time scales but is characterized by a sweeping frequency evolution over $30-100$ msec in present day devices and depends on the toroidal mode number. To illustrate these different behaviours, we show an example of the observed AE activity in DIII-D during NBI [442] in section 5.2 (see figure 5.2.1). A mixture of gradual frequency changing TAEs and up-sweeping RSAEs are seen in the Mirnov spectrogram (b) whereas the FILD data primarily shows gradually evolving low frequency TAE induced losses. No bursting modes are present in the FILD spectra. Bursting modes, according to theory, correspond to the formation of structures such as holes and clumps in the distribution function [486]. Hence the QL models considered in section 5.2 should be sufficient to address the EP profile relaxation observed in these DIII-D experiments.

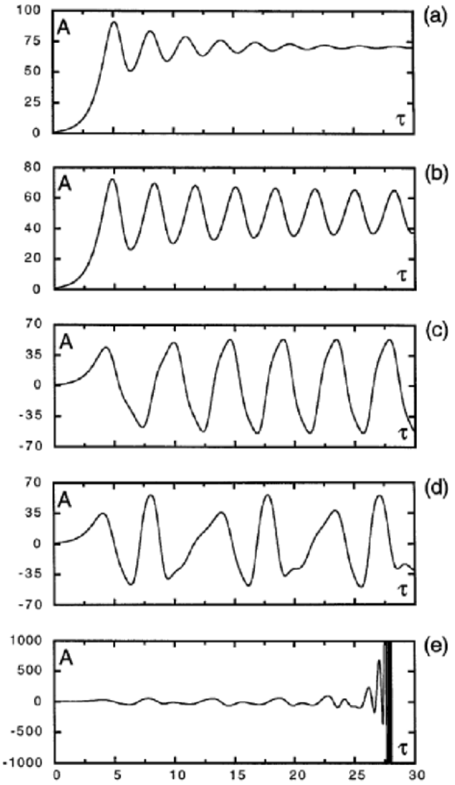

Figure 5.1.1 *Numerical solutions of equation (5.1.1) that describes the nonlinear amplitude evolution of marginally unstable fast ion drive modes for A(0) = 1 and various values of* $\hat{v}$*: (a)* $\hat{v}$ *= 5.0, (b)* $\hat{v}$ *= 4.3, (c)* $\hat{v}$ *= 3.0, (d)* $\hat{v}$ *= 2.5, and (e)* $\hat{v}$ *= 2.4. This figure is adopted from Ref.* [487].

5.1 Nonlinear models

In this section we review the progress in developing nonlinear models that describe the observed experimental evolution of energetic particle driven modes. This entails capturing the essential underlying physics in a numerically tractable manner. As we will see from this section the knowledge of the essential elements of the nonlinear dynamics of the instabilities helps to quantify the observation in a way which can be verified numerically. This is an important goal for the initial value codes development as we state in Sec. 8.

In the case of a weak source of fast ions, the population builds up on a timescale much longer than the characteristic growth time of an unstable mode of the system. In this case the system can't go far beyond the threshold for instability and it makes sense to restrict attention to near-threshold phenomena. Insight into the nature of the nonlinear mode evolution arose [487] as a result of focusing upon the evolution of kinetic instabilities near their marginal stability point. What has come to be known as the Berk-Breizman model (often abbreviated to BB model in the literature, e.g. in Ref. [488]) is an augmentation of the Vlasov-Maxwell system which includes a collision term (representing particle annihilation and injection processes) and external wave damping is included.

An important parameter in this nonlinear theory was found to be $\hat{\nu} \equiv \nu_{eff}/\gamma$, where ν_{eff} is the effective collision frequency, the linear growth rate is $\gamma = \gamma_L - \gamma_d$ with γ_L the growth rate arising from the energetic particles neglecting dissipation, and γ_d the damping rate of the mode due to background dissipation neglecting the energetic particle drive. A cubic nonlinear temporally non-local equation was derived [487] that depended upon the single control parameter $\hat{\nu}$:

$$\frac{dA}{d\tau} = A(\tau) - \frac{1}{2}\int_0^{\tau/2} dz\, z^2 A(\tau - z)\int_0^{\tau-2z} dx\, e^{-\hat{\nu}(2z+x)} A(\tau - z - x)A(\tau - 2z - x), \quad (5.1.1)$$

where A is the mode amplitude and $\tau = (\gamma_L - \gamma_d)t$ is the rescaled time. In essence, the parameter $\hat{\nu}$ describes the competition between the field of the wave that is trying to flatten the resonant particle distribution function and the relaxation processes that are continually trying to restore it.

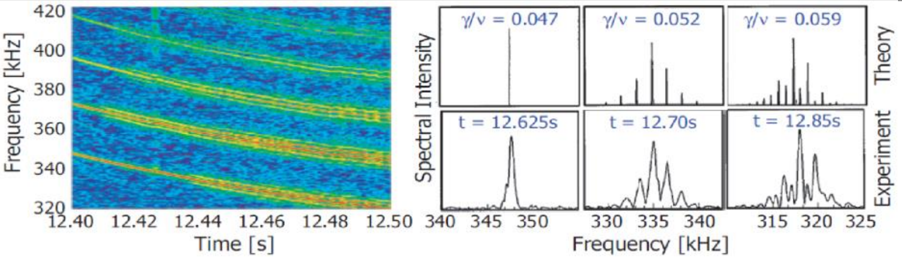

Figure 5.1.2 *(Left) Spectrogram of edge magnetic activity in JET hot-ion H-mode #40332 showing the appearance of ICRH driven TAEs (P_{ICRH} ~ 6.5 MW). (Right) Nonlinear splitting of TAE spectral lines for this case. Note the good agreement between theory and experiment for the asymmetries in the spectral line splitting* [489].

It was found that the effects of collisions on resonant particles are more important in the nonlinear regime than in the linear regime, which is quite insensitive to such details. Numerical solutions of this equation to determine the evolution of the mode amplitude showed that at high collision frequencies, $\hat{\nu} > 4.4$, a linear growth phase is followed by a saturated level ([487], figure 5.1.1). At lower collisionalities, $\hat{\nu} < 4.4$, the solution starts to pulsate with the oscillations becoming more complex and irregular as the collision frequency is further lowered. These solutions show a well-defined sequence of transitions as $\hat{\nu}$ is decreased from periodic, through multiply periodic, to chaotic behaviour and finally explosive behaviour when the assumptions in the derivation of the theory break down at sufficiently large amplitudes. It is possible to consider the saturated steady-state solution of the system as a fixed point of the system dynamics. The path to chaos then corresponds to a series of pitchfork bifurcations of this initially stable fixed point.

Experimental observations of the nonlinear frequency splitting of fast ion driven waves where made in JET by Fasoli et al. [489] and have been interpreted in terms of a slight extension of this model (where the second parameter was introduced as a result of finite γ_L/ω). Figure 5.1.2 shows the frequency behaviour of ICRF driven TAE and a comparison with theory.

In figure 5.1.2 several linear TAE modes (of different toroidal mode numbers) are simultaneously self-excited soon after the energetic neutral beam heating was applied. The frequencies slowly change in time due to the evolving plasma equilibrium. Initially, there are well-defined single spectral lines but these lines begin to split with increased structure as time evolves. The cubic nonlinear equation with a time evolving $\hat{\nu}$(primarily due to an increasing population of energetic particles) was used to explain the frequency splitting structure. Figure 5.1.2 also shows a comparison of JET data with results that emerge from the solution of the cubic nonlinear equation as the parameter $\hat{\nu}(t)$ varies. The precision of the matching enabled the determination of the mode growth rates and effective collision frequencies [489].

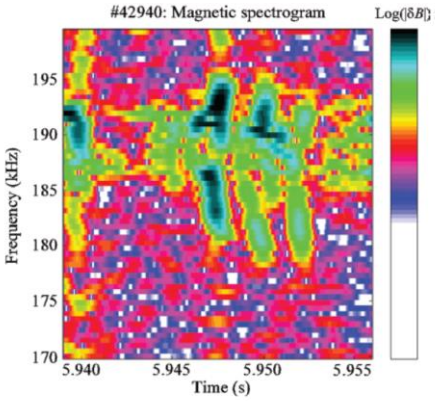

Figure 5.1.3 *Example of a frequency chirping mode during a shear optimized D–T pulse in the JET tokamak. In this case, δω/ω₀ ~ 5% in δt ~ 1 ms* [482].

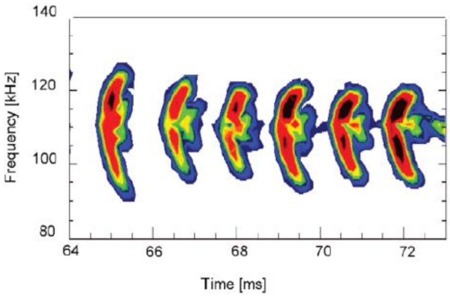

Figure 5.1.4 *Magnetic spectrogram showing frequency chirping n = 1 core-localized mode in MAST #5568. The first event shows a frequency shift of 18 kHz in a time of 0.8 ms* [482].

The cubic equation for nonlinear mode behaviour, Equation (5.1.1) outlined in the introduction to this section above, breaks down as soon as it is necessary to take the particle response into account. This was done in subsequent work by [486] where it was shown how structures form in the fast ion distribution function (so-called holes and clumps) that correspond to a deficit or surplus of fast ions relative to the equilibrium distribution. These structures support long-lived nonlinear Bernstein, Greene and Kruskal (or BGK, [490]) waves in which the background dissipation is balanced by the chirping of the observed frequency. Figures 5.1.3 and 5.1.4 shows two experimental examples of frequency chirping modes, one from a shear optimized DT pulse in JET and another from MAST [482]. Such nonlinear evolution of EP driven modes is insensitive for a detailed magnetic configuration, tokamak or stellarator/helical. In LHD, a clump-hole pair formation by TAE bursts was observed in time evolution of the energy spectra of charge exchanged EP flux measured by NPA diagnostic [491] (see Fig. 5.1.5).

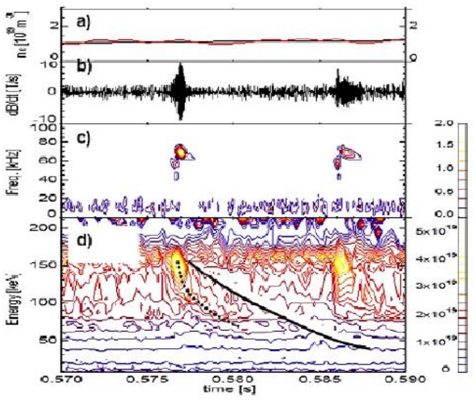

Figure 5.1.5 *Time evolutions of line averaged electron density (a), magnetic fluctuations of TAE bursts (b), the spectrogram (c) and energy spectra of charge exchanged neutrals(d) in an NBI heated plasma with TAE bursts. The dotted and solid curves in Fig.(d) respectively indicate the time evolution of the clumps and holes in LHD* [491].

High frequency GAE bursts observed in NSTX called Angelfish exhibit very similar chirping behaviour over $1-2\,msec$ [337]. The application of the theoretical expression for the evolution of the GAE burst to one specific chirping event is shown in Fig. 5.1.6. Also indicated in that figure is the expression of the mode frequency evolution [487]. With further validation this theory seems to be a very important tool for the WPI physics.

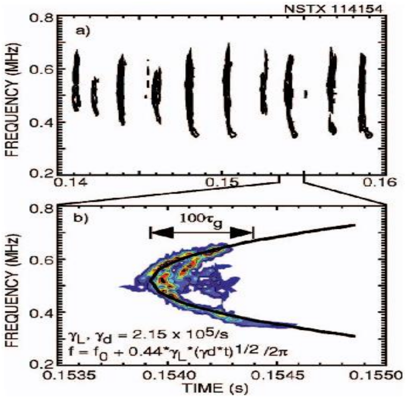

Figure 5.1.6. *One GAE burst spectrum from Mirnov coils for NSTX beam heated plasma. Shown also are the fitted curves using the adjusted parameters in Eq. (5.1.1)* [337].

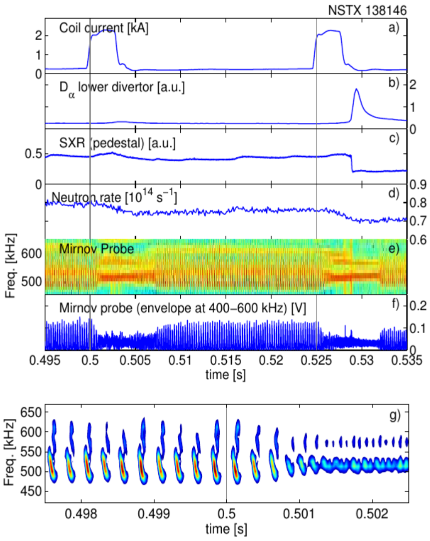

Figure 5.1.7. *GAE chirps shown in the figure (g) and how it is related to other plasma parameters shown as indicated for NSTX* [492].

Further insight into this problem has just been published [492]. It shows that the introduction of fairly large 3D field perturbations $\delta B/B\sim 0.01$ into the plasma boundary changes the evolution of the GAEs driven in NSTX by the beam ions as shown in Fig. 5.1.7. The mechanism of the change has been suggested via the EP drift orbits affected by the perturbations. The used technique is argued to be helpful for the development of the phase space engineering. This is a possible direction for EP physics in a future research as we identify in the summary section 8.

Other observations we would like to briefly discuss are from JT-60U tokamak [444]. They are done in experiments with high energy NBI into a plasma such that the EP component is sufficiently highly energetic $v_f/v_A\sim 1$. Thatis work reports on several observations of the instabilities which differ in their time evolution and frequencies. One instability was analyzed to have the frequency inside the AC and has slow frequency evolution. Another event is called the abrupt large amplitude event (ALE). It appears at the end of the fast frequency sweeping (FS, although according to our terminology should be called chirping) instability which occurs inside the TAE gap. FS has characteristic frequency chirp $10-20kHz$ on a time scale of few milliseconds. ALE is often characterized by the drop of the neutron emission rate and EP losses. The resonant interaction between energetic ions and the mode was suggested.

ALEs were modelled using the HMGC particle-in-cell (PIC) code [493]. Obtained results were shown to match well the dynamics of these events with regard to the time scale and the frequency spread. It was found that the obtained EP modes saturate as the resonant fast particles are scattered out of the resonance and redistributed radially.

5.1.1 Semi-analytic 1D models for bump-on-tail drive

It is sometimes useful to reduce the dimensionality of the problem to focus on the underlying physics. In this regard, several 1-D models have been developed by Vann [494], Lilley [495] and Lesur [488] to advance understanding in the field and capture the important features of the wave-particle resonant interaction.

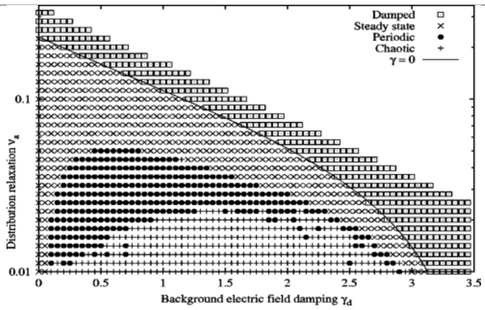

***Figure 5.1.1.1** Characterization of nonlinear behaviour of Berk-Breizman system in terms of mode damping and relaxation rate. The four types of behaviour occur in well-defined regions of the parameter space and depend upon the underlying fast ion distribution function, which here is taken as a bump on tail distribution* [494].

Vann used a Vlasov approach to numerically characterize the nonlinear behaviour in a marginally unstable dissipative system, the results of which are summarized in Figure 5.1.1.1.

Lilley and co-workers have elucidated the relative roles played by various collision effects, notably drag, Krook-like relaxation and phase-space diffusion [495]. Drag was found to be destabilizing and to act as a seed for energetic particle modes. It also led to asymmetries in the evolution of the frequency chirps, giving rise to a diverse range of nonlinear behaviors including hooked frequency chirping, undulating and steady-state regimes, see Figs. 5.1.1.2 – 5.1.1.5.

Lesur and co-workers [496] independently developed a 1D electrostatic code to study and characterize nonlinear behavior. Based on the behavior observed in their model, and in a similar manner to Vann, they defined a qualitative definition for each of the chirping regimes with drag and diffusion.

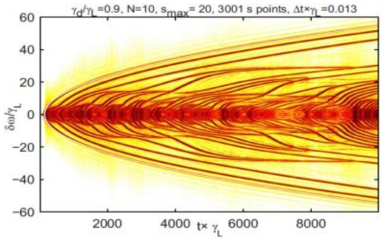

***Figure 5.1.1.2** Spectrogram of electric field amplitude for collisionless case close to threshold. The white curve is the best $\sqrt{t}$ fit passing through the upper and lower chirping structures* [496].

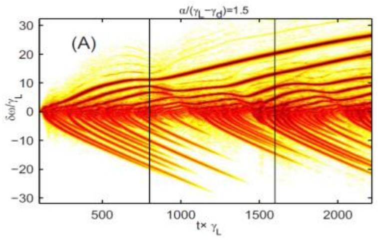

***Figure 5.1.1.3** Spectrogram showing asymmetric chirping for the case of pure drag* [496].

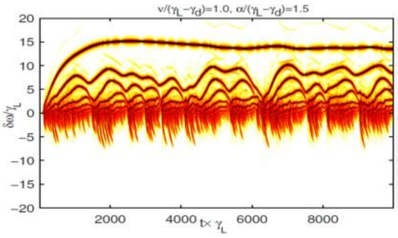

Figure 5.1.1.4 Establishment of a steady-state hole in the presence of both drag and diffusion [496].

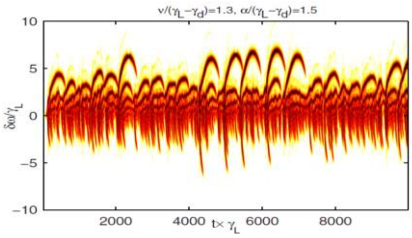

***Figure 5.1.1.5** Formation of a so-called hooked frequency spectrum arising from an increase in diffusion compared with Figure 5.1.1.2* [496]

The above nonlinear models show that mode behaviour close to marginal stability is well characterized both theoretically [487] and experimentally and can even provide opportunities to extract additional information on the particle phase space distribution from the measured instability spectral features [489] [482]. Focussing on fast frequency chirping phenomena, derivation of kinetic parameters on phase space was attempted through comparison between JT-60U data and the model of Ref. [497].

5.1.2: Initial Value Models

In the last section, attention was restricted to near-threshold phenomena by arguing that the system can't go far beyond threshold. Much less data exists for strongly unstable scenarios, characterised by nonlinear dynamical processes leading to energetic ion redistribution and losses, and identified in nonlinear numerical simulations of Alfvén eigenmodes and energetic particle modes.

Various initial value codes exist to model the interaction of an ensemble of energetic particles with a spectrum of unstable waves. Codes that treat the influence of the energetic particles perturbatively upon the linear eigenfunctions of the system include the ORBIT [197] and HAGIS [498] codes. In these models, the particle motion is described by a drift-kinetic, or guiding-centre, approach whilst the wave equations are updated using a δf technique in which the simulation markers only represent the change in the fast ion distribution. These models have been used successfully to describe the nonlinear interaction of fast ions with the linear waves in realistic systems and even shown how it is possible to recover the internal amplitude of a mode from observations of its frequency chirps [498]. Figure 5.1.2.1 shows the same alpha-driven n=3 TAE as in [498], with the addition of a Krook-like relaxation of the distribution function (ν_{eff}) and an electron-ion drag term, (ν_{ei}). With the parameters as shown it is demonstrated that models of this nature can recover the behaviour seen both in experimental observations (Figs. 5.1.3 and 5.1.4) and in simpler 1D models (Figs. 5.1.1.2 – 5.1.1.5).

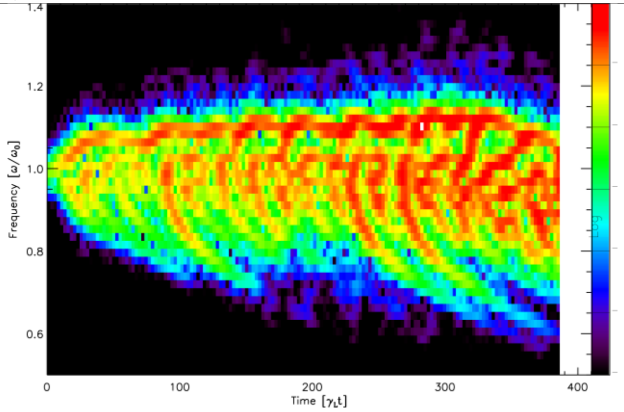

Figure 5.1.2.1: *Nonlinear evolution of an alpha driven n = 3 TAE in JET as described in* [482]. *Here the frequency of the mode has been reduced by 70% to maximize the linear growthrate,* $\gamma_L/\omega_0 = 0.0612$. *The other parameters used in this simulation were: an intrinsic mode damping rate of* $\gamma_d/\omega_0 = 0.06$; *a Krook-like relaxation rate of* $\nu_{eff}/\gamma_d = 0.01$; *and a drag coefficient of* $\nu_{ei}/\gamma_d = 0.002$.

Going beyond the linear MHD eigenmode structures necessitates formulating a model based upon a nonlinear MHD approach. This is the method adopted in the MEGA code [499] which is a kinetic-MHD hybrid model that has been used to simulate the interaction of alpha particles with various Alfvén eigenmodes. The plasma is divided into two species: the background plasma and the energetic particles. The behavior of the energetic ions is coupled to the MHD equations through the current that they carry. A linearized version of the code also exists to facilitate understanding of the nonlinear behavior observed.

Another code that can capture the non-perturbative effects of energetic particles is the HMGC code [500]. This is a hybrid MHD-particle simulation code that couples the sets of reduced MHD equations for the fluctuating fields with the gyrokinetic equations of motion for the fast ions. At each time step the particles move in the 3D electromagnetic field before the field is updated using fluid-equation solver.

The above approaches use a kinetic treatment for the energetic particle behaviour however it is also possible to take a fluid-based approach, as done by the TAEFL code [501]. In this model a gyro-fluid approach with a Landau closure is taken. This allows the study of TAE destabilised by fast ions whilst still capturing the mode damping due to neighbouring shear Alfvén continuua. Recent work [501] has shown good qualitative agreement between this approach, a DIII-D discharge (#142111) and the results of two gyro-kinetic codes, GTC [502] and GYRO [503], both for the mode evolution (frequency sweeping) and mode structure.

An international benchmarking exercise is currently taking place under the auspices of the Energetic Particles Topical Group of the International Tokamak Physics Activity (ITPA) {http://www.iter.org/org/team/fst/itpa} to verify the various implementations and to validate the codes' behaviour for ITER. Contributions to this exercise are not restricted to the nonlinear codes described above since developing validated robust predictive tools for future devices such as ITER is an important activity and one that is picked up on again in Section 7.1.

For the nonlinear physics of energetic particle driven modes the prediction of saturation amplitudes is an important issue. If the saturation is to be described near the marginality condition of the instability, the nonlinear amplitude behavior can be reliably predicted provided the linear solution of the modes is obtained in a proper way. The linear mode analysis using full gyrokinetic approach where both energetic particles and bulk plasma are treated within the gyro-kinetic formalism is required. For instance linear fully gyrokinetic shear Alfvén (LIGKA) spectral code can be used [504].

5.2 Quasi-linear models

The Quasi-linear (QL) models in general are designed for rather weakly turbulent systems to efficiently predict the plasma profiles with respect to certain oscillations [505]. These models may lack the desired accuracy in DF dynamics details but describe rather long term DF evolution (see for example Ref. [506] on transport QL model validations). QL models evolve the DF by solving the diffusion equations.

The wave trapping frequency enters the QL equation and can be written in conventional form [507] [508] [509]

$$\frac{\partial F}{\partial t}-\frac{\pi}{2}\sum_{ik}|\omega_{bik}^{4}|\frac{\partial}{\partial \Omega_{ik}}R(\omega_k-\Omega_{ik})\frac{\partial F}{\partial \Omega_{ik}}=S, \tag{5.2.1}$$

where k refers to the eigenmode index, i is a subscript associated with k mode and its frequency ω_k, Ω_{ik} is the combination of the particle characteristic frequencies $\omega_{D,b,c}$, which appear in the resonance condition Eq.(4.2.1.6). The resonant quantity R has a normalization property $\int d\Omega_{ik}R(\omega_k-\Omega_{ik})=1$. The resonant quantity serves a role of the correlation function which is peaked near the resonance with the k^{th} eigenmode. Its analytic form is known to be the resonant delta function in the limit of small growth rate:

$$R(\omega_k-\Omega_{ik})=\frac{\gamma_{\omega ik}/\pi}{(\omega_k-\Omega_{ik})^2+\gamma_{\omega ik}^2}\rightarrow\delta(\omega_k-\Omega_{ik}), \tag{5.2.2}$$

where width $\gamma_{\omega ik}$ can be substituted by the net growth rate to be computed by the difference between the linear drive and damping $\gamma_{ik}=\gamma_{Lik}-\gamma_{dik}$. More generally there is an intuitive interpretation of the width $\gamma_{\omega ik}$, which is the region of particle mixing near the resonance. It is proposed to be a combination of the trapping frequency $\omega_b$which is the resonance phase island width due to diffusive mixing through the effective scattering, ν_{eff} and growth rate, γ_{ik} [508]. The coefficients in the combination are of order unity as it follows from the numerical simulations. The trapping frequency square carries the mode amplitude linearly

$$\omega_b^2=2\frac{\partial \Omega_{ik}}{\partial E_f}\Big|_{P_\varphi}\langle e\vec{E}\cdot\vec{v}\rangle.. \tag{5.2.3}$$

The QL equation needs to be augmented by the amplitudes of the allowed modes. Provided the modes are in the regime of gradual evolution of interest, with the information about the growth/damping rate one can simply write:

$$\partial\,\omega_{bik}^4/\partial\,t+2\gamma_{di}\omega_{bik}^4=\int d^3v\omega_{bik}^4G(\vec{v}).$$

One important consequence of the QL theory is the possibility of overlapped resonances as was pointed out in Refs. [508] [509]. As we show in Fig. 5.2.1 multiple resonances are far more dangerous if they overlap. They can deplete the velocity distribution severely if develop simultaneously. This is shown to be a good explanation of for the avalanching phenomena observed in NSTX experiments, see sec. 5.3. The resonance overlapping is a subject of current research as we will review in Sec.5.4.

The outlined QL equations although attractive still require significant amount of computations in the phase space. One limiting case for QL theory is recently developed critical gradient model (or 1.5D QL model) [510] [511]. This case follows directly from the above QL equations in the approximations of (i) infinite number of localized modes in the system, (ii) resonances are strongly overlapped, so that the particles can diffuse stochastically in the unstable region, (iii) the relaxation time is longer than the collision time. In reality these assumptions can be too simplistic so that the validation exercise is needed to justify this model applicability to present day experiments and eventually to the burning plasmas. Since 1.5D model does not resolve the phase space structures and operates with the plasma pressure it is an approximate model of AE driven fast ion redistribution.

The 1.5D model is based on linear stability analysis under the assumption that the QL diffusion from overlapping resonances is applicable to EP profiles in the presence of these modes. Similar conditions can be envisioned in ITER-like burning plasmas in a variety of plasma scenarios [510]. In 1.5D model the beta critical gradient is determined by the following expression,

$$r\frac{\partial\beta_f}{\partial r}\,|_{crit}=\frac{\gamma_d}{\gamma_L^*}, \tag{5.2.4}$$

where the expression is to be taken at the mode position r in absence of quasi-linear relaxation, γ_L^* is the linear growth rate in absence of dissipation and γ_d is the damping rate without the destabilizing source. The linear growth rate is assumed to be of the form $\gamma_L = \gamma_L^* r\partial_r\beta_f$ with γ_L^* being independent of the energetic particle beta profile. Hence in the region of the unstable mode we require that the quasi-linear relaxation will results in $|\partial\,\beta_f/\partial\,r| \leq |\partial\,\beta_f/\partial\,r\,\,|_{crit}|$. If EP gradient predicted by TRANSP is larger than this critical value, it is relaxed by the 1.5D model to the critical value enabling the computations of the relaxed (redistributed) EP beta profile. Comparing the relaxed QL beta profile redistributed from the initial one evaluates EP losses as well as other quantities.

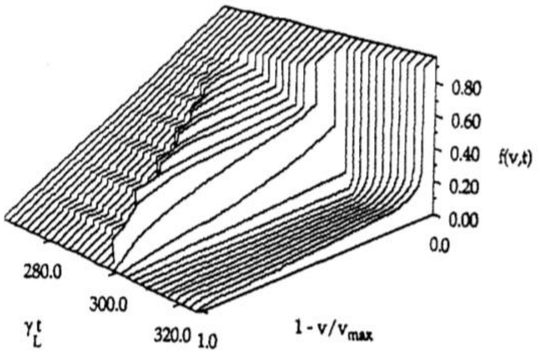

Figure 5.2.1. *EP DF modification by the multiple resonances in case when they broaden to overlap* [508].

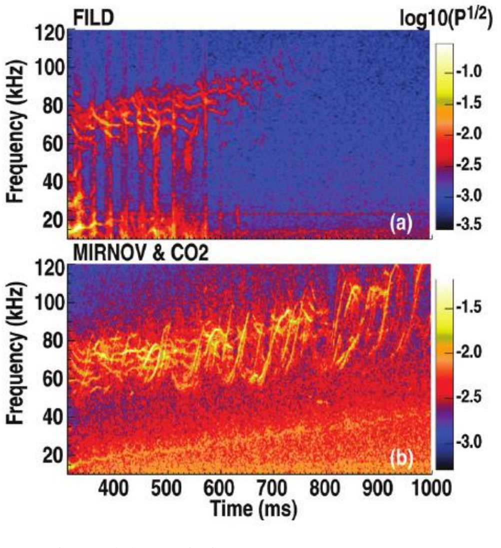

Figure 5.2.2 *Spectrograms of FILD data (a) and the crosspower spectrum of the edge magnetic field coils and interferometer data* [442] *take in DIII-D discharge focused on AE driven transport.*

The implementation of the 1.5D model has an option to improve the accuracy of the expressions for the growth and damping rates by using NOVA-K [191] rather than an analytic estimates. With these modifications the model accurately captures the TAE or RSAE eigenfunctions and their stability properties. Normally the growth/damping rates are normalized at two radial points so that the applied growth rate is multiplied by the ratio $\gamma_{NOVA}\,(r_i)/\gamma_{anlt}\,(r_i)$, and then a linear interpolation of the NOVA computed growth rate is used to continuously express the local growth rate in the radial domain locations r_i. The final EP distribution does not resolve the velocity space, as only the pressure profile is relaxed. To account for the velocity space relaxation, rules based on the work of Kolesnichenko are used [16].

The application of the 1.5D model to some recent DIII-D experiments gave surprisingly close agreement with experiments [511] [512] despite of its simplicity and the fact that the model is approximate. The plasma, formed with the reversed magnetic shear, created favorable conditions for EP induced AE excitations. The magnetic spectrogram of the discharge is depicted in Fig. 5.2.2. The multiple instabilities are clearly seen with strong (but still on the equilibrium time scale) frequency evolution of their spectrum peaks. Shown in figure 5.2.3 are 1.5D model predictions for neutron losses for several points in time using growth rates normalized to NOVA-K values [511] [513]. It was found that the dominant damping mechanisms are due to radiative damping and trapped electron collisions. Notably the trapped electron damping comes from the edge of the plasma whereas the drive is peaked near the half of the minor radius. The application of 1.5D model shown in Fig. 5.2.3 does not include time averaging (which is done in Ref. [512] and is notably better). Even in this form the model produces measurable "error bars" which can be estimated ~ 50% for the predictions of the neutron fluxes in the validation exercise. Here the neutron flux is assumed to be primarily due to beam and plasma density products ignoring the energy dependence of the fusion cross section. This is an important quantity to consider as the model will be applied in sec.7.4.

It is believed that the QL models described rather briefly here should be an invaluable tool for both interpreting the present day experiments and predicting the future burning plasmas in regimes where they cause shear Alfven like instabilities [507]. The predictive modeling guidelines were recently published [514]. These guidelines stress that the predictive models need validations under the widely accepted standards. Part of such validations in application to 1.5D model are recently published [511] [512] and will be discussed more in sec.7.4. It is important to note here that the experiments provide further confirmations that the off-axis beam ion injection into the DIII-D plasma does not lead to hollow EP profiles as maybe expected. Instead rather stiff peaked in the vicinity of plasma axis EP profiles were reported [512].

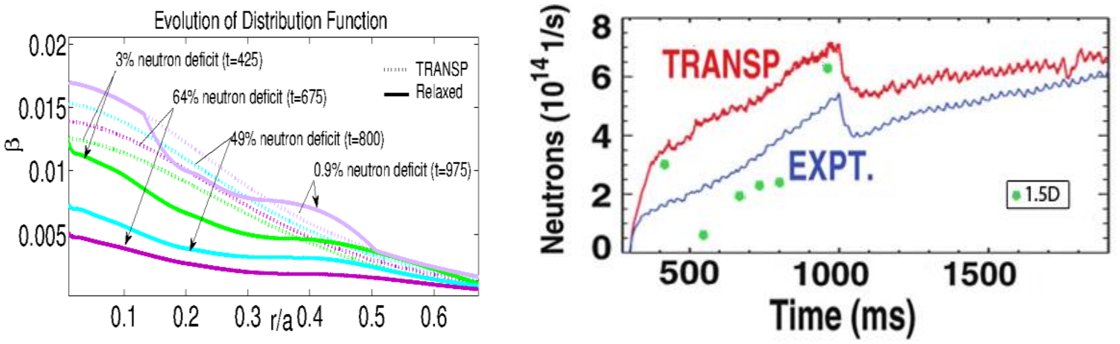

Figure 5.2.3 *Shown on left figure are beam ion* $\beta_f(r)$*beta profiles from TRANSP code before the 1.5D model is applied (dashed curves) and after its application (solid curves) for DIII-D discharge* [513]. *The model is applied to several time slices of the analyzed discharged whose neutron signal evolution is shown in the right figure as indicated. In the right figure TRANSP predicted (red) and experimentally measured (blue) neutron emission rate are shown as functions of time. Results of 1.5D model application are overlayed as green dots at t=425, 525, 675, 725, 800, and 975 ms* [511].

In many respects a complimentary (to 1.5D) model is being developed at General Atomics and is called "stiff" transport model [515]. It is based on local AE stability computed by the GYRO code [516] [517]. The "stiff" transport model computes the local drive to AEs using GYRO for EP profile relaxation. The stiffness [516] and the locality [517] of EP transport due to AEs are two major elements of the model. Microturbulence simulations supported by GYRO help to drive modest alpha losses at the edge. To be consistent with the requirements set in section 7.2 we note that the global structure of AEs has to be an essential part of any QL model. Described above 1.5D model can rely on NOVA stability calculations with the realistic AE eigenmodes.

The development of full 2D QL theory is posed as a challenge for a future research in Sec. 8. This is an important subject to direct the EP studies to develop the predictive capabilities for fusion reactors since available now 1.5D QL approach is approximate.

5.3: Nonlinear multimode interactions and excitation

Experimentally, modes rarely exist in isolation and whilst the resonant regions of fast ion phase-space may be well separated, if any one mode reaches such an amplitude that it starts to significantly perturb the (wide) orbits of the fast ions that are resonant with a neighboring mode, then it will start to exert some influence over its evolution. This phenomena is not only true of fast ion driven modes, but may also be expected to be true in the presence of large neoclassical tearing modes (NTMs) or Long-Lived Modes [284].

In the case of multiple energetic particle driven modes, the nonlinear behavior is governed by the degree of separation between the various mode resonances in the particle phase space [518]. If the separation of adjacent resonances is greater than the trapping frequency associated with either mode, then the resonances do not overlap and the modes evolve in isolation. In the opposite limit, the modes are so closely packed that they blend into a continuum and the quasi-linear approach discussed in Section 5.2 can be used.

In the framework of the Berk-Breizman paradigm outlined in Section 5.1, holes and clumps may form at one resonance and propagate through the fast ion distribution to influence neighboring resonances. The exact consequences of this interaction still need to be fully explored. However work has started to address the nonlinear evolution of two waves excited by the resonant interaction with fast ions just above the linear instability threshold [519]. The paper categorizes the evolution into various regimes and concludes that the nature of the nonlinear evolution obtained depends upon the type of relaxation processes at play, on the magnitudes of these various processes, and on the initial conditions. Whilst the regimes obtained are similar to those outlined in Section 5.1 for the case of a single mode, the two-mode dynamics is much richer due to the interplay that can arise between the modes.

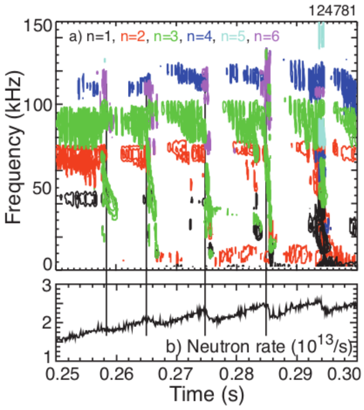

Figure 5.3.1 *TAE avalanches in NSTX* [337]*: (a) Spectrogram of magnetic fluctuations showing sequence of avalanche events; colours indicate the toroidal mode numbers [black-1, red-2, green-3, blue-4, cyan-5, magenta-6]. (b) Neutron rate showing drops of ~10% at avalanches.*

Experimentally, and as alluded to above, examples of multimode interactions are relatively common. In NSTX, a three-wave interaction has been shown to lie behind observations of simultaneous bursts of EPM and TAE [520]. In this case, the three-wave coupling concentrated the energy of the TAE into a toroidally rotating structure formed by the EPMs. This redistribution of energy is significant because it can modify the effect of TAEs on fast ion losses. The three-wave coupling between EP driven modes is also often observed in stellarator/helical plasmas heated by tangential NBI on LHD [10]. The effects of the multimode interaction on EP transport are important topics on LHD and stellarator/helical plasmas.

Other experiments in NSTX have been found to reveal strong bursts of multiple TAEs that undergo rapid frequency chirping [337] as shown in Fig. 5.3.1. These bursts are correlated with significant drops in the neutron rate which is indicative of fast beam ion losses since the neutron production rate is dominated by beam-plasma reactions. Such examples of the detrimental impact of fast ion driven instabilities are important to investigate since such events in future devices, including ITER, could have an adverse impact on their energy producing efficiency.

Simulations of these observations using the ORBIT code [197], albeit not self-consistent, and based upon linear eigenfunctions calculated with the NOVA code [185] [204] predict the same fraction of losses as the observed drop in neutron rate. Whilst such (essentially test particle) results are encouraging, the inherent strong nonlinearity in this case motivates further nonlinear simulations, possibly in which gyro-radius effects are also included.

The previously mentioned experiments on DIII-D (see Sec.4.2.2, Fig. 4.2.2.2.4) in the regimes when multiple instabilities are present were also analyzed using the ORBIT code [195]. Inferring the AE amplitudes and structures from the comparisons between the ECE diagnostic experiments and NOVA code modeling, ORBIT code simulations followed the evolution of the EP driven TAE/RSAE modes. The purpose of that work was to understand why previous attempts which picked only a few of the most strongly driven modes failed to explain the observed level of losses. The paper [195] concluded that it is important to include the electric potential of the modes which can significantly modify the degree of EP redistribution, even with amplitudes around the level of $\delta B/B \simeq 2\times10^{-4}$. The computed redistribution is due to the presence of WPI islands in the COM space. Phase-space island overlapping and collisions are revealed as stochasticity in the particle motion. The relaxation of the EP profiles seen in DIII-D in comparison with classical expectations (TRANSP predictions) can be explained by the low amplitude modes observed in the experiments. The EP transport due to AEs is shown to be very sensitive to small changes in mode spectrum, so that even with the relatively low mode amplitudes seen in the experiments, EP trajectories are found to be stochastic. This allowed large scale changes to the EP distributions. As mentioned in section 4.2.1, the paper [195] utilizes a powerful technique designed and employed for guiding center studies with the ORBIT code where the resonances can be identified without estimating the resonance conditions, Eq. (4.2.1.6). This is done by evaluating the changes of EP energy and P_φ due to the perturbations.

Observations of multimode interactions are not limited to axisymmetric devices. Indeed LHD displays a rich spectrum of fast ion driven modes that have been observed to interact [10]. The higher dimensionality of the stellarator configuration means that full particle simulations have not yet been conducted for these devices, although there is no fundamental reason why such calculations cannot be undertaken in the coming years. Recently, a numerical study of EP transport in a simple case where a single TAE is excited has been started using an orbit following code [521] [522]. In those papers the experimental data of TAE induced energetic ion losses on LHD are compared with the orbit following code DELTA 5D [158]. Inside the last closed flux surface (LCFS) the EP orbits and transport were calculated using DELTA-5D code for 3D MHD equilibrium of the VMEC code [523]. The energetic ion full orbits with energies and pitch angles that are obtained from the data of the lost ion probe are calculated starting from the detector position and moving toward the LCFS. When the energetic ion orbits match the orbits calculated by the DELTA-5D code at LCFS within a certain range of energies and pitch angles it is judged that these ions are transported by TAE from the plasma core to LCFS and then reach the detector, i.e., they are detected as lost ions. Otherwise, they are lost but not detected by the SLIP/FILD. These simulations find that the studied TAE induces both convective and diffusive types of losses observed in LHD.

As we saw the interactions of multiple AE instabilities can be dangerous in STs (see for example Fig. 5.3.1). Thus it is important to find the regimes of plasmas operations when instabilities are not virulent and the modes do not chip. If the modes chirp the outstanding problem here is: can the chirping regime be controlled in order not to allow the phase space structures propagate far and quench the instability.

5.4 New insights in EP loss mechanisms

This area provides one of the major motivations for EP research. To generate EP losses from closed field line configurations such as in tokamaks and stellarators, one possibility is via the resonances between the fast ion drift motion and perturbations. Due to the high energies of the EPs (by definition) these resonances are distinct from thermal plasma resonances, which help to identify and study the physical processes underlying the loss mechanisms.

We present some interesting results which shed new light on the underlying physics, beginning with recent AUG observations where RSAEs and TAEs were driven unstable by ICRH and NBI fast ions [71] [440]. The associated EP losses were measured using a FILD (see Sec.2). The technique employed allowed the losses to be characterized in the fast-ion phase space. It was observed that a single TAE or RSAE mode results in a convective process with the loss signal proportional to the fluctuation amplitude. These convective losses are modulated by the AE amplitude and can thus be clearly separated from diffusive incoherent losss. This is shown in figures 5.4.1. In figure (c) the coherent losses are plotted and show aclear linear dependence versus the amplitude of the perturbed magnetic field fluctuations measured at the magnetic probe position.

Convective and diffusive EP losses induced by TAE bursts with frequency chirping have also been observed in LHD [522]. The loss process changes from a convective mechanism to a diffusive one as the TAE amplitude increases and exceeds a certain threshold.

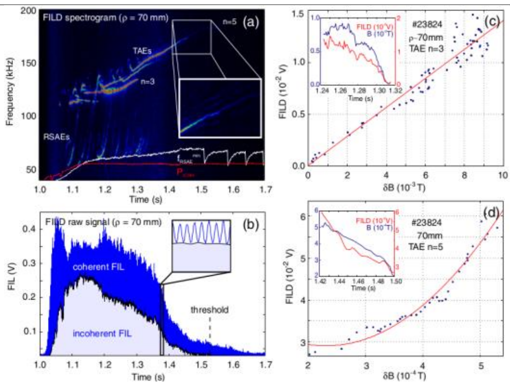

Figure 5.4.1. *EP loss observations in AUG* [440]. *Figure (a) shows the power spectrogram of the fast-ion loss signal. The inset in the figure (a) shows a single TAE trace responsible for the onset of the incoherent losses. (b) Fast-ion loss signal with the coherent and incoherent components highlighted. The vertical dashed line indicates the point (threshold) when the incoherent diffusive losses go to zero. (c) Linear dependence of the coherent non-diffusive losses. (d) Quadratic dependence of the incoherent losses for the TAE mode as indicated.*

At the same time if multiple RSAEs and TAEs are excited with overlapping spatial structures the losses are diffusive and proportional to the square of the amplitude. This was also seen in the AUG experiments above plotted in figure 5.4.1 (d). It was argued that the diffusion should reveal the quadratic proportionality of the loss rate with the AE amplitude, which was indeed observed. Convective and diffusive EP losses induced by TAE bursts with frequency chirping are also observed on LHD [521] [522]. The loss process changes from convective to diffusive when TAE amplitude increases and exceeds a certain threshold. In CHS stellarator/helical device the convective and diffusive losses of energetic beam ions induced by EPM bursts were measured by a directional Langmuir probe (see section **2.1.7**) inserted near the edge of low power and short pulse NBI heated plasmas [75]. The loss fluxes are composed of two components. The fast component oscillates with EPM frequency (coherent component) and slow one evolves with the discharge (incoherent one). They exhibit convective and diffusive transport, respectively.

We note that the diffusive nature of EP losses could be attributed to the resonant island broadening and eventual resonance overlapping which was discussed in Refs. [508] [524]. The potential overlap of the spatial structures of AEs as well as phase-space structures of WPI resonances are plausible reasons for large diffusive loss. Numerical analysis using the HAGIS code has provided insight on such resonances and confirmed this conjecture [194]. The HAGIS is applied to multiple modes with different frequencies focusing on the resonance interaction of EPs simultaneously with two different modes referred to as "double resonance" [525]. This shows that double resonance can enhance the growth rates and amplitudes of the modes, depending on the mode distance. It also can lead to strong nonlinear stabilization of a linearly dominant mode in the case of small radial mode distance.

Theoretically, resonances overlap was demonstrated by the quasi-linear theory in the 1D limit [508] [509] [524] as pointed out in Sec.5.2. The situations in realistic plasmas are far more complicated when the overlap will be in 3D velocity space and there is no satisfactory theoretical treatment. This problem could perhaps be addressed numerically with improved computation capabilities?

NSTX observations of AE avalanches [526] [527] were discussed above and illustrated in figure 5.3.1. In those experiments AEs were excited and formed structures in the spectrogram. It is conjectured that overlapping WPI resonances are responsible for each such structure. The linear analysis performed was satisfactory in reconciling the measured and computed mode structures. More recently, TAE driven losses were the focus of a more detailed study [528], the results of which are summarized in Fig. 5.4.2. A surprising finding is that the energy loss of the beam ions as a result of the Alfvénic modes gives such significant contribution to the overall neutron drop. It is likely that such an effect is more severe for ST plasmas whereas in ITER-like plasmas, a radial redistribution of the EPs is more plausible.

Fig. 5.4.3 shows a more recent classification of the TAE instability bursts in the avalanches [529] using the operating space diagram introduced in Sec. 4.2.6. It is surprising that this diagram helps to sort the TAE avalanches from the quiescent cases but this can perhaps help connect the observations with the plausible theoretical explanations such as discussed this these references: [508] [509] [524].

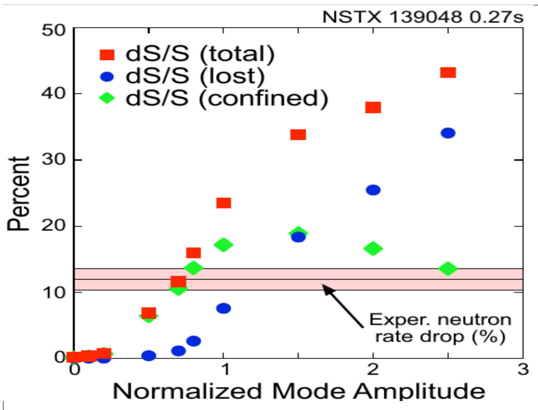

Figure 5.4.2. *Computed neutron rate drop versus scaled TAE amplitude in NSTX due to lost beam ions (blue dots), due to fast ion energy loss (green squares), and the rest from the EP redistribution. Shown also is the level of the neutron drop seen in experiments* [528].

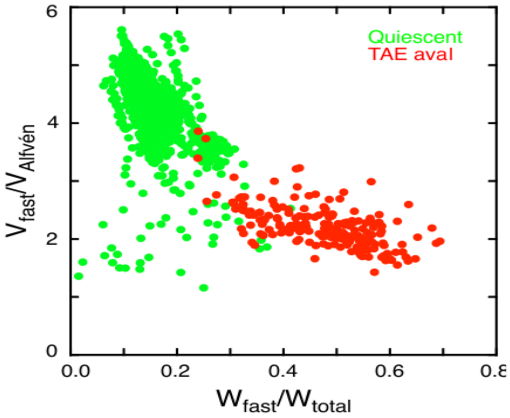

Figure 5.4.3. *NSTX observational points of the ratio of full-energy fast ion velocity to average Alfvén speed vs. ratio of energy in fast ion population normalized to the total plasma stored energy (e.g. ~ $\beta_f/(\beta_{pl}+\beta_f)$). Color coded are quiescent plasmas as green, and plasma with TAE avalanches as red points* [529].

5.5 Micro-turbulence effects

One of the problems micro-turbulence studies should address is how fusion produced EPs are confined in a reactor in the absence of any MHD activity. To a large extent this is done by investigating MHD quiescent plasmas (see Sections 3.1.1, 3.3.1). If a quiescent regime is assumed then non-MHD activity could affect fast ions such as micro-turbulence, which is the focus of this section.

Micro-turbulence effects could be considered in section 4.1 but we include them here as recent studies show that one needs nonlinear gyrokinetic codes that self-consistently include EPs in turbulence simulations [530] [531]. EPs in existing studies do not drive the instabilities (thought to be) responsible for the plasma transport via their radial pressure gradient as simulations show [532] and can be treated as *passive test particles*. Nevertheless, it is important to include turbulence with realistic field amplitudes. Initial studies of micro-turbulence induced transport made use of test particle calculations with EP guiding center trajectories [533].The conclusions were nevertheless broadly consistent with more recent realistic calculations. They are based on the expectation that micro-turbulence will peak around $k_\perp \rho_i \sim 1$ and that the EP's Larmor radius is orders of magnitude larger than this [1]. In addition, not only do FLR effectss help to reduce the influence of micro-turbulence on EP transport but the radial extent of their drift orbits also decorrelates the wave-particle interactions (WPI).

It is worth pointing out the outstanding open questions from the investigations in ASDEX Upgrade that showed a relatively fast broadening of the radial plasma current profile [534]. It was driven by the off-axis NBI in the absence of any measurable magneto-hydrodynamic activity, which makes the micro-turbulence mechanism the most plausible candidate. Gyrokinetic simulations performed with the GENE code [535] of EPs arising from NBI with either an asymmetric or anisotropic Maxwellian distribution, could explain the degradation of the current drive efficiency. DIII-D experiments also showed that the fast-ion distribution function differs from classical theory [536] for $E_f/T_{pl} \leq 10$. The observed anomalies were greatest in high temperature plasmas and at low fast-ion energies. The micro-turbulence transport mechanism could be invoked to explain the high-performance plasmas at moderate E_f/T_{pl} ratios.

One recent publication that is worthwhile to cite here is the clearly entitled: "Energetic ion transport by microturbulence is insignificant in tokamaks" [537]. It summarizes the EP transport results in the DIII-D MHD quiescent plasmas by probing it with a range of NBI configurations. Plasma conditions were varied in order to modify the background turbulence. The authors concluded that EP transport due to micro-turbulence is too small to observe experimentally. The accompanying modeling was in agreement with the DIII-D experiments, which led to the conjecture that the coherent fluctuations (such as those due to AEs) are more important in ITER (see also the DEP code below). Earlier electrostatic simulations reached the same conclusions with regard to predicting the passive $E \times B$ electrostatic transport of fusion alpha particles in ITER, namely that such transport will be negligible [538].

There are several other studies on EP micro-turbulence, which we note briefly. The GYRO code demonstrated that α-particles will be weakly affected by the micro-turbulence in ITER [539]. Simulations using the GENE code indicated that the EP transport is independent of the particle energy [540]. The energy increase of the magnetic drift velocity, $\sim E_f$, is balanced by the inverted dependence caused by the perpendicular decorrelation. The conclusions were made that magnetic expressions profoundly deviate from theoretical expectations based on orbit averaging. This work stressed that EP transport can occur when their gyroradius becomes comparable or smaller than the turbulence correlation length. This remains to be checked in quiescent burning plasmas such as in ITER with $E_f/T_{pl} \gg 10$. Simulations with the PIC GTC code [541] found a different scaling for the diffusivity coefficient versus EP energy in the presence of ion temperature gradient (ITG) turbulence. The energy dependence for the dominant passing energetic ion contributors goes as T_{pl}/E_f. The difference in simulations is the subject of some debate [542] [543]. Nevertheless, the GENE micro-turbulence diffusion model with the inclusion of ITG/TEM instabilities was recently applied to DEMO and TCV plasmas [544]. Negligible alpha particle transport was found in both tokamaks whereas important beam ion redistribution in DEMO was demonstrated.

The aforementioned studies involve computationally expensive calculations and are therefore not very practical for routine application. Very recently micro-turbulence investigations focused on the parameterization of the diffusion operator to capture quantitatively the effective scattering. This scattering operator was proposed via the effective collision frequency

$$\nu_{eff} = D_r[mv_{\|}\, q'/q^2\, R]^2 \tag{5.5.1}$$

and was included in the initial value M3D modeling code [545]. This form of the scattering frequency allowed the study of the micro-turbulence diffusion effect on the EP confinement and TAE saturation levels. When a specially constructed criterion,

$$R_d = \frac{D_r(2\mathrm{m}\, q'/q)^2}{\nu_d(1 + 2\mathrm{m}q'R\, \rho/r)^2} \frac{\chi^2}{1-\chi^2} \tag{5.5.2}$$

is greater than 1, the micro-turbulence induced radial diffusion becomes more important for TAE saturation than Coulomb collision scattering, where $\rho = m_f\, v_{\|}/eB_{\varphi}$. It was claimed by using this formula that in TFTR, DIII-D and ITER plasmas micro-turbulence plays a more important role than Coulomb scattering.

This is an important conclusion and may be considered as a motivation for developing a quasi-linear operator allowing practical and efficient calculations in the same way as the TGLF plasma transport module [546] [547]. The TGLF module works as a driver for the newly developed DEP code [548]. This code is based on a diffusivity that operates on the linear branches of the quasi-linear kernel. The development of the QL code DEP is promising (see Ref. [537]) but requires further validation efforts.

6 Impact of fast ion driven modes on bulk plasma confinement

EP driven instabilities can play a negative or a positive role in the performance of fusion plasmas. An interesting experimental study was done on DIII-D [549] where EP driven AEs redistributed fast ions and helped create and maintain off-axis current drive. This sustained a steady-state internal transport barrier. The whole methodology was called “alpha-channeling” (see Sec 4.2.7) as EPs sustained the transport barrier and were advantageous for a reactor. This effect may appear due to EP driven mode induced non-ambipolar EP losses, rather than the mode itself. The losses are thought to induce a sheared flow, although no direct experimental measurements indicates this. This is a favorable effect of EP driven modes and can be viewed as a kind of alpha-channeling as presented in [549].

Another important EP driven mode effect on plasma confinement has to do with internal transport barrier (ITB) formation and shear flow generation by the transport of EPs [550], which is well covered in the topical review in Ref. [11]. In the LHD stellarator/helical device, TAE bursts were seen to transiently improved the bulk plasma confinement. During each burst the amplitude of density fluctuation measured by a CO_2 laser phase contrast imaging were noticeably reduced with an enhanced phase velocity [10]. The exact mechanism leading to ITB formation is not clear but may be important for future experiments.

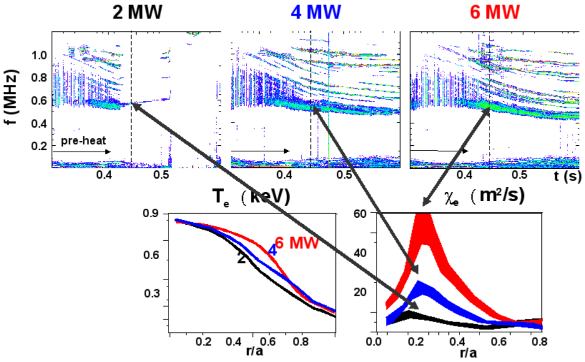

Fig. 6.1 *Correlation of sub-cyclotron high frequency activity in NSTX with thermal electron temperature profiles and electron heat conductivity inferred from TRANSP code simulations* [551].

A new development seen recently has to do with the observations of anomalous thermal electron transport on NSTX [551]. This seems to be important as it can limit the fusion plasma performance via the electron transport channel. It was noted in Ref. [551] that in NSTX the increase of NBI power by a factor of 3, from 2MW to 6MW, did not lead to the expected increase in the thermal electron temperature. This is illustrated in Figure 6.1 for 2MW, 4MW and 6MW of NBI power. Instead of going up, the electron temperature profile is flattened near the plasma center during the injection ramp up. A subsequent analysis of this discharge led to elevated values of χ_e in excess of 10 $\mathrm{m}^2 s^{-1}$. An analysis of various other possibilities excluded them from being the explanation for the observed trends in the electron behavior [551] [552].

Two approaches to this problem emerged. The first one [553] discusses the energy heat channeling that delivers some of the injected power from the center to the edge and elevates T_e. This approach was originally proposed to explain the thermal crashes in the W7-AS stellarator during the low-frequency Alfvén instabilities [261]. In later experiments the observations arguably were characterized by the Alfvénic activity identified as NGAE (Sec. 4.2.2.2) driven by the beam ions. Because NGAEs can be converted to KAW due to “tunnelling”, the amplitude of the latter can be large and even comparable to the GAE amplitude. NGAEs in the simulations were shown to be localized near the center.

A similar channeling due to GAE generation (part of the high frequency activity seen on Figs. 6.1 top) in the NSTX plasma was proposed in the later paper [553] to explain the electron temperature profile anomaly. The observed modes were argued to be GAEs with eigenfrequencies just below the AC. To ensure the electron channeling (e-channeling) in this case a mechanism was proposed in which the radially extended m^{th} harmonic of the GAE solution couples to the $m+1^{\text{th}}$ kinetic structure of the edge AC [553]. As discussed in Sec 4.2.2.2, GAEs in NSTX exist near the plasma center and are excited by the tangential NBI ions. The corresponding GAE parallel electric field is then

$$\tilde{E}_\parallel \approx \frac{i\omega k_\parallel}{ck_\vartheta} k_\perp^2 \rho_i^2 BL \frac{\tilde{n}_e}{n_e}, \qquad (6.1)$$

where $L$is the plasma density scale length. Estimates for the trapped electron heat conductivity from this equation gives $\chi_e^t \approx \sum_{m,n}(n^2 q^2 c^2/r^2 k_\parallel^3 v_e)\,|\tilde{E}_\parallel|/B_0^2 \sim 1\text{m}^2/s$ which is well (two orders of magnitude) below the TRANSP inferred values. On the other hand, the energy channeling to the AC is applicable in NSTX and couples the NBI heated center and the plasma edge where neutral beam destabilized waves are damped. It was qualitatively concluded that the parallel electric field of the GAE to AC coupled structure can provide a mechanism for channeling both the energy and momentum of EPs to the edge [553].

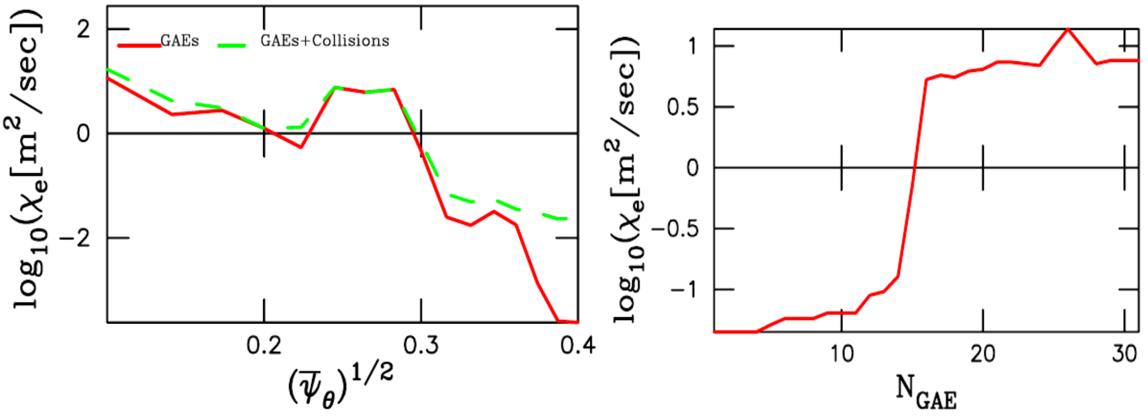

Figure 6.2 *Thermal electron heat conductivity versus minor radius (left figure) with the test GAE mode structures, centered at normalized poloidal flux* $\bar{\psi}_{\vartheta 0} = 0.04$. *The figure on the right shows the* χ_e *dependence versus the number of applied GAEs.* χ_e *is taken at the location of* $\bar{\psi}_\vartheta = 0.06$. *The figure is adopted from Ref.* [552] *for NSTX.*

The second approach to this problem [552] is based on the stochastic diffusion of the electrons across the magnetic field lines in the presence of multiple GAEs. Multiple GAEs' magnetic and electric fields mediate thermal electron motion. The guiding center code ORBIT [197] was used to follow the electron drift motion perturbed by the GAEs. A set of test GAE eigenfunctions was employed with the number of modes and their locations taken near the plasma center, which follow from the measurements and theoretical understanding. It was found that in the MHD limit (zero parallel electric field) the electron thermal diffusion is indeed present. To get the electron heat conductivity to the level inferred from the experiments, $\chi_e \geq 10\text{m}^2 s^{-1}$, a parallel electric field was introduced and controlled by including higher (second in the electrostatic potential amplitude) order corrections. $E_\parallel$ is important for electron dynamics on relatively long time scales on the order of ten microseconds. Simulations with a medium number of GAEs, $N > 16$, and with mode amplitudes close to those measured by the interferometer high-k diagnostic in terms of $\alpha_{GAE} \approx (\delta B_r/B_0)(ir/mR_0) \approx (\xi_r/R)(k_\parallel/k_\vartheta) \approx 4\times 10^{-4}$ produced $\chi_e \sim 10\text{m}^2 s^{-1}$ where ξ_r is the characteristic electron radial displacement. In those simulations the parallel electric field was included according to the perturbation of the MHD model for GAEs. Figure 6.2 illustrates the results obtained.

One can construct a qualitative expression for thermal electron thermal conductivity reflecting the baseline assumptions and numerically obtained results

$$\chi_e = \frac{3}{2}\xi_r^2\tau_{deph}^{-1} = \alpha_{GAE}^3 R_0^3 \frac{3\mathrm{k}_\vartheta^3}{2\mathrm{k}_\parallel{}^3}\frac{k_r k_\perp v_d}{\pi}, \tag{6.2}$$

where τ_{deph} is the dephasing time of the electron GAE interaction. This expression applied to NSTX plasma results in an electron thermal conductivity, $\chi_e \approx 4\mathrm{m}^2 s^{-1}$, which is in reasonable agreement with simulations. An important thing to note is the cubic dependence on the mode amplitudes. A closer agreement with the inferred $\chi_e$value seems possible [552] if the amplitude of the mode is higher (it was observed intermittently), or the number of modes is increased, or the parallel electric field is raised.

An initial value code HYM [125] was used in search of those effects [554]. It did not find the heating channeling of GAEs to AC even though it was able to resolve it. Instead, a new phenomenon was reported in which radially broad medium-*n* CAEs extend through the plasma center and couple to a new poloidally localized kinetic structure (tentatively identified as propagating KAW) mediated by beam ions. The KAW is localized poloidally on the HFS and is in local resonance with the CAEs. The radial width of the KAW is comparable to the beam ions' Larmor radius. The eigenfrequency of the CAE satisfies the following dispersion relation which includes the contribution from the beam ions: $\omega^2 = k_\parallel^2 V_A^2\left(1 + \frac{3}{4}\frac{n_f}{n_e}\lambda_f - \frac{n_f}{n_e}\frac{\omega^2}{\omega_{ci}^2}\right)$, $\lambda_f = \frac{\mathrm{k}_\perp^2 T_f}{m_i \omega_{ci}^2}$. It is expected that the energy flux from CAE to KAW would have a direct effect on the electron temperature profile due to the small wavelength of the KAW. This will hopefully be addressed in future works.

Further experimental analysis carried out in Ref. [555] comparing the mode frequencies to dispersion equations indicated that the observed modes with frequencies $400 - 1000$ kHz could be a mixture of both GAEs and CAEs. ORBIT code simulations demonstrated the stochastic diffusion e-transport contributions from CAEs, which scales similar to GAEs, that is proportional to the mode amplitude to the third power [556]. The predictions illustrate that the interplay of CAE and GAE modes can produce high electron transport rates (up to $70\, m^2/s$) in the particular discharge of interest. The consistency between the simulations and the inferred values of the e-transport indicates that stochastic diffusion could be a good way to explain the levels of core electron transport in NSTX with high NBI power H-mode plasmas. To improve the predictive capability of the GAE/CAE driven e-transport model one would need first principles numerical tools capable of simulating the unstable mode spectra, structure and nonlinear amplitudes of GAEs and CAEs.

We should note that the effect of GAE/CAEs on thermal electrons needs to be considered in order to explain the NBI current drive observations in NSTX [557] and other tokamaks [534] [558]. These observations indicate that the current driven by NBI is potentially affected by EP driven instabilities. This is because the saturated central electron temperature may degrade the current drive efficiency as already known from the present current drive experiments. The reviewed observations indicate that the current driven by NBI is potentially affected by EP driven instabilities.

7 Implications for burning plasmas, ITER

In this section we review the effects EPs can have on burning plasmas with particular reference to ITER. Of particular interest are the AE instabilities (sections 7.2, 4.2.2), sawteeth and fishbone instabilities (sec. 7.3) and the thermonuclear burning instability (sec 7.4), since they can all affect the operation of a reactor.

We would like to note here that the high-n modes excited by EPs can lead not only to the redistribution of fast ions but can also have significant effects on the bulk plasma profiles. One such effect actively pursued in STs recently is electron channeling covered in Sec.6. Another potential effect is due to RSAEs and their link to ITB formation (see Sec. 4.2.2.2 and the discussion in this topical review [11]). This has the potential to explain the origin of ITBs and the sheared plasma rotation observed in their vicinity. If RSAEs are seen in experiments this by itself is a clear indication of the reversed shear of the of the q-profile with or without the ITB formation as we discuss in the subsection 4.3.1.

The observed multiplicity of RSAEs in a plasma with reversed magnetic shear and their analysis [282] suggests that not only do thermal ions contribute to their damping but they can also help drive these modes. This follows from the magnitude of the thermal ion finite diamagnetic drift frequency $\omega_{*i} \sim \omega_A$ when n gets sufficiently large. For example, in DIII-D at $n = 20$ and $T_i > 25\ keV$ plasma ions contribute to the drive [282]. This mechanism is similar to the thermal ion ITG mode drive [559]. Hence, in AE stability calculations for burning plasmas, ω_{*i} terms should be kept. This is also true for ST DT reactors with a relatively low magnetic field. An Alfvénic mode excited by this mechanism is called the ion temperature gradient driven Alfven eigenmodes (AITG) [380].

For the AE stability problem the limitation on the mode number comes from the finite orbit width effect [560] [561] [191], which can be simply cast into the condition that the maximum growth rate is obtained when the radial width of the TAE eigenstructure is comparable to the EP orbit,

$$k_\perp \rho_f \sim 1. \tag{7.1}$$

This condition is important for AE stability analysis in BPs such as ITER (see Sec. 7.2). The first term on the left hand side of Eq. (7.1) being proportional to n chooses the most unstable toroidal mode number: n $\sim a/q\rho_f$.

As the linear AE theory is well developed the next important step is to verify and validate various linear (and nonlinear) AE stability codes in existence so that they can be used to predict the AE stability in different ITER operating scenarios. This activity was recently led by the ITER International Tokamak Physics Activity (ITPA) and is discussed in the next section.

7.1 Verification and validation of AE growth and damping rates

There are several important goals that the EP Topical Group of the ITPA is pursuing within the framework for internationally coordinated fusion research activities. One of them is to establish cases for the verification of linear and initial value codes operated in the linear regimes. Two cases have been considered to date: a specific JET plasma [562] for which the damping of global TAEs was measured; and an analytic case [563].

The details of the JET discharge can be found in [321]. The models employed covered a range of approaches and included the perturbative MHD codes CASTOR-K [564] and NOVA-K [191], the warm dielectric tensor model code LEMan [565], the gyro fluid code TAEFL [566] and the linear gyrokinetic code LIGKA [311]. In addition to constituting a benchmarking exercise between codes, since the damping rate of a specific TAE mode was measured, this activity can also be considered as a validation of these codes.

Most of the codes found two $n = 3$ TAE with a rather global mode structure. One of the global TAE modes is a probable candidate to explain the measured TAE damping rate as its structure is not locally intersects the continuum. It was found to have an eigenfrequency in the range $f = 179 - 181\text{kHz}$ in the calculations. Its structure interacted with the continuum at the edge and near the center. The different approaches used to compute the damping rates gave good agreement for the $n = 3$ TAE of interest. We show the damping rate evolution in Figure 7.1.1 (left). It should be noted that there are intrinsic error bars in the computed dampings. These come from uncertainties in the plasma profile measurements and the equilibrium reconstructions and are hard to account for.

The two dominant damping mechanisms found by the codes are continuum and radiative dampings. A specific scan of the damping rates is shown in Figure 7.1.1 (right). Although there were some discrepancies between the codes at times, the results shown in Figure 7.1.1 (right) are remarkable given that the methods employed to compute the damping rates are different in the different codes. In this regard we should note that the agreement was demonstrated for two damping rate mechanisms added together. Very recent study [567] shows that the continuum damping computed perturbatively within NOVA ideal MHD approach can not be used for accurate stability calculations due to intrinsic singularities the solutions have at the continuum.

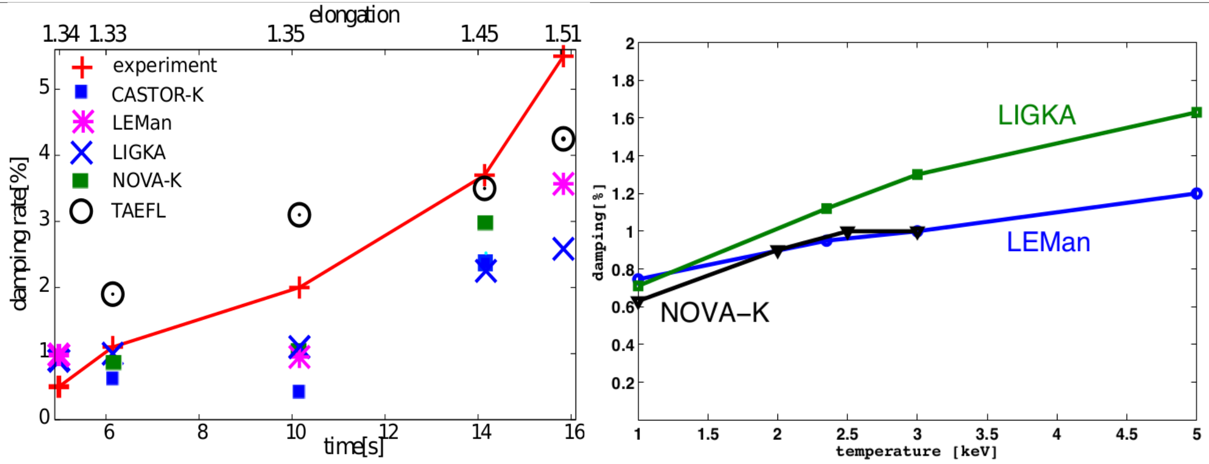

Fig. 7.1.1. *(Left) Damping rate computations and their comparison with the JET experimentally inferred dampings. (Right) Variation of TAE damping rates with temperature for* $t = 6$s *for three of the codes as depicted* [562].

Another paper we would like to highlight is on the modelling of growth rates by the majority of the codes involved in the previous study. The codes use various approaches to compute the fast ion growth rates with those involved in this study being CAS3D-K [568], GYGLES [569], TAEFL [566], AE3D-K [367], NOVA-K [191], HMGC [500], MEGA [499], CKA-EUTERPE [570], and VENUS [571]. Figure 7.1.2 presents the comparison of these nine codes employing methods ranging from kinetic MHD/hybrid [191] [568] [367] [570] [571] [499] [500] to completely gyro-kinetic [569] and gyro-fluid approaches [566].

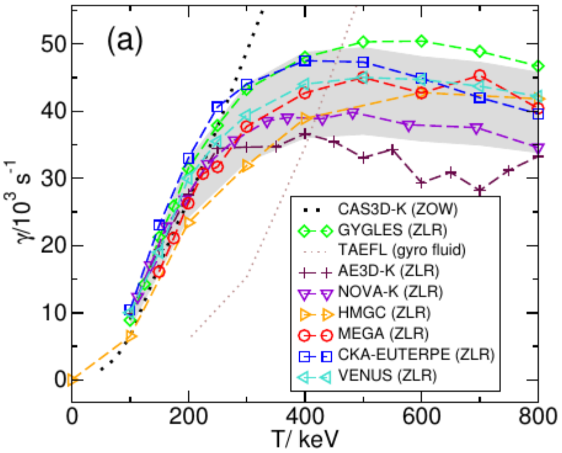

Figure 7.1.2. *A linear stability analysis of* $n = 6$ *TAE growth rate and analytic plasma parameter profiles for a scan of the central energetic ion temperature of a model profile* [563].

The equilibrium was of a large aspect ratio ($R/a = 10/1$) and comprised consistent analytic plasma profiles. Within the reasonable error range indicated as a shaded region in Fig. 7.1.2, the codes agree with each other. They all reflect the existence of a plateau in growth rate dependence with respect to fast ion temperature, which is important for BP projections. The EP DF was taken to be Maxwellian for easy comparison but some minor discrepancies may still be present in the various codes' implementations (necessitating further verification). The growth rates shown include finite orbit width effects but neglect finite Larmor radius effects (i.e. they are performed with zero Larmor radius – ZLR). The agreement among the codes is satisfactory and was concluded to be within $\sim 15\%$ for energies < 400keV in the case considered.

Both of the cases considered above helped to establish confidence in using these numerical tools for interpreting present day experimental results and predicting future experimental behaviour. The results mark the starting point for a subsequent non-linear benchmark and validation exercise and the linear calculations of the stability boundaries due to fast particle effects in ITER.

7.2 AE stability in ITER-like plasma

There are already cases of ITER, or ITER-like, AE stability analyses in the literature that we outline here. It is worthwhile starting this section by considering the early attempts to tackle this problem for ITER-like plasmas [572]. The numerical tools employed were widely used and the plasmas analyzed represented cases in which the expected toroidal mode number was shifted to higher values than in ITER. The paper [572] focuses on the ITER-98 EDA design [115] which was a slightly larger tokamak device than that of the ITER design presently being build [573]. According to our review (see Eq. (7.1) and Figure 4.2.6.1 (left)) the plasmas considered in the ITER-98 EDA design resulted in higher values of a/ρ_f which would translate to unstable AEs with higher n numbers in comparison with the present expectations for ITER (as we will see below).

In Ref. [572] the range of unstable core localized TAEs was predicted to be $10 < n < 50$ where the nominal parameters for the ITER-98 EDA plasmas were considered. The physical effects included in the analysis were advanced at the time and considered the dominant damping mechanisms such as electron and ion Landau dampings, collisional electron damping and radiative/continuum damping. The fusion alpha-particle drive also included the finite orbit width effect. As the paper states the simulations indicated that within the relevant values of n the radially localized group of core-localized TAEs (cTAE) lead to a rather insignificant number of α losses. This was even the case for the "worse-than-expected" conditions when the growth rate was boosted to 8%. However the possibility of significant redistribution and losses due to radially extended modes was acknowledged. None of the effects due to super Alfvénic beam ions were included.

At this stage it is important to discuss how the effects included in the analysis of Ref. [572] modify the AE linear stability. The correct treatment of the AE drive by EPs should include finite orbit width and Larmor radius effects, as was noted after Eq. (7.1). This effect alone peaks at the most unstable AE toroidal mode number. In computations of the drive, the distribution function of EPs has to be realistic, which means that for alphas it should not be isotropic in pitch angle, reflecting the finite orbit width effects [574] [575] [576]. It should also be strongly anisotropic for fast beam ions if NBI is envisioned in the design [510]. Ion and (to a lesser extent) electron Landau damping are generally the dominant damping mechanisms and help to determine the boundary between stability and instability (see Sec.7.5) [560]. Continuum damping [208] limits the radial width of TAEs and often helps to stabilize EP driven modes that extend towards the plasma edge. Depending upon the mode frequencies, it can be small in the low shear region near the center or near q_{min} of plasmas with reversed magnetic shear. It is zero for modes that reside in the TAE frequency gap when the TAE gap is radially aligned (or close to being aligned), which is the case for the nominal TAE frequency close to constant in radius, i.e. $q(r)\sqrt{n_e(r)} \sim const.$ Radiative damping is important for the modes with a high toroidal mode number and a relatively large radial wavelength [308] [240]. Trapped electron collisional damping [577] [578] is important to retain as it becomes large towards the edge of the plasma and may stabilize global TAE modes that are otherwise destabilized toward the center. In this regard the computations of the AE mode structure needs to be done in realistic equilibrium since the results sensitively depend upon the equilibrium details.. Ref. [579] shows that by using the realistic geometric elongation in the ITER case analyzed (see below) the TAE net drive was lowered by more than a factor of 3.

The effects mentioned above are included in the stability simulations of ITER normal shear plasmas [510] and in a more systematic (unpublished) study [213]. In Ref. [510], as expected, a lower and more narrow toroidal mode number spectrum than in ITER-EDA 98 (above) are reported with the normal shear plasma being unstable to TAEs in the range $6 < n < 14$. What was noted is that the contribution by fusion alphas is about the same as from beam ions. However, TAEs are only marginally unstable with either alphas or only beam ions. An example of the unstable mode stability analysis with the growth and damping rates is shown in Table 3. The numbers shown in the table support many points identified in the previous paragraph.

$\bar{\omega}_0^2 q_{edge}^2$	γ_{ecoll}/ω (%)	γ_{eLand}/ω (%)	γ_{rad}/ω (%)	γ_α/ω (%)	γ_{beam}/ω (%)	γ_{Tot}/ω (%)
0.96	0.18	0.61	0.43	0.82	0.71	0.31

Table 3: Damping and driving rates of $n = 10$ *unstable TAE for* $0.55m$ *off axis tangential* $1MeV$ *deuterium normal shear NBI in ITER where* $\gamma_{Tot} = \gamma_\alpha + \gamma_{beam} - (\gamma_{ecoll} + \gamma_{eLand} + \gamma_{rad})$ *[213].*

It seems appropriate to highlight here the results from the less accessible Ref. [213] that analyzed three ITER scenarios, standard ELMy H-mode, hybrid and AT (advanced tokamak or reversed shear) plasmas. We have chosen the plasmas with the most unstable AE for each of several NBI injection geometries and show them in Fig. 7.2.1. In that figure star or triangle points correspond to AEs driven by DT alphas or by a combination of alphas and beam ions, respectively. One can see that all these plasmas are marginally unstable against AEs, which means that out of many analyzed modes only a few are linearly unstable whereas most of them are stable. It is the strong damping mechanisms that play a role in separating the few unstable modes from the large number of stable ones. It is also noticeable that the reversed shear plasma has less unstable AEs and lower n numbers. The unstable modes are either localized or global in radius so that radial transport due to these modes can be expected.

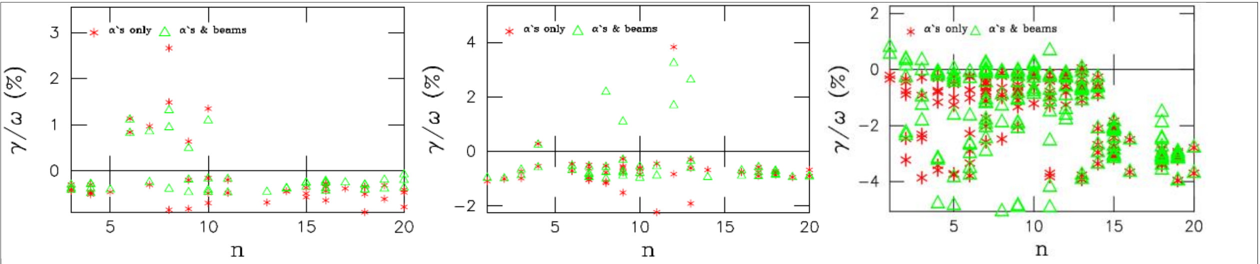

Figure 7.2.1. . *Growth rates of the most unstable AEs for three ITER plasmas representative of three different scenarios: standard ELMy H-mode (left), hybrid (center) and advance tokamak (AT or reversed - right). The analysis includes TAE, EAE, NAE gaps* [213].

With instabilities like those predicted in Figures 7.2.1 it is hard to envisage that the 1.5D QL diffusion conditions are satisfied (see sec.5.2) although the validation against DIII-D experiments suggests that it is applicable. What helps to significantly reduce the error bar of the model predictions is the strong dependence of the DT fusion reaction rate on the plasma temperature (see Sec. 7.5).

We also should mention a work on the linear AE stability in ITER using the initial value code HMGC [580]. This is perhaps one of the first uses of initial value codes for studying linear AE stability in ITER. It is hard to compare the results obtained in that publication with others (see Refs. [205] [510] [213] and [579] below) because Ref. [580] employed different plasma parameters and does not have some elements and, in particular, damping mechanisms identified above. However, we can say that there are some similarities in the results. Numerical study showed that the Alfvénic fluctuations driven by EPs are weakly unstable in all the analyzed cases. The most unstable modes have relatively low-n numbers and are localized near q_{min}. Projections were made for the expected redistribution of alphas and the paper concluded that it is not significant. Most notably, the difference as compared to other works is in the unstable toroidal mode numbers, which are lower in Ref. [580] in comparison with the results from Refs. [205] [510] [213] [579] although the analysis was not done at $n > 8$ in Ref. [580]. We should also note that the HMGC code was a part of the benchmark exercise for the EP drive, which we reviewed in sec.7.1.

Another more recent case of ITER TAE stability calculations has been carried out using the PIC code GEM [579]. In the study a hybrid gyrokinetic ions/massless fluid electron model was used. The paper considered the so-called Miller equilibrium model [581] and includes many of the important effects discussed in the third paragraph of this section, although trapped electron collisional damping was neglected, which may have some effect on the spectrum. We show the growth rate from Ref. [579] in Figure 7.2.2. Although GEM was not part of the ITPA exercise from Sec.7.1 the rollover of the growth rate as a function of the TAE toroidal mode number is consistent with the theory and the ITPA case. It was found that the dominant damping mechanism is thermal ion Landau damping and that the shaping of the equilibrium plasma plays a strong stabilizing role. This is possibly due to the contributions from the continuum and radiative dampings. The threshold of the most unstable TAE is at $\beta_\alpha(0) = 0.7\%$. The treatment of TAE instabilities was noted to be novel in that fully kinetic thermal ions are included in the nonperturbative model. This is very important for the radiative damping, which was not found to be significant.

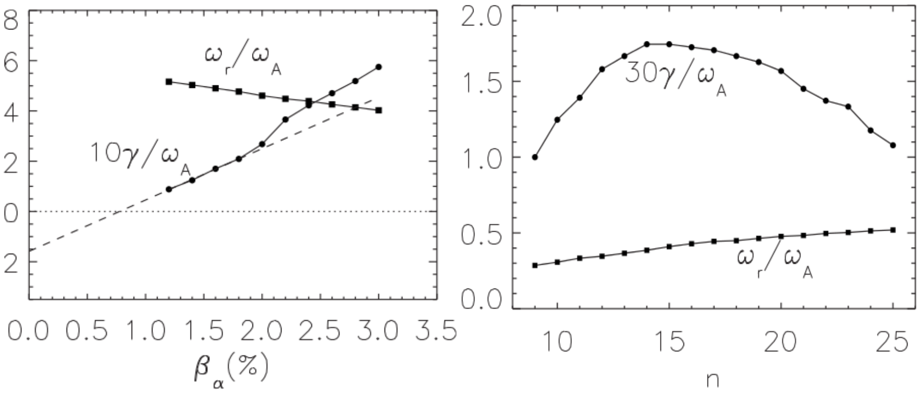

Figure 7.2.2 *GEM linear calculations of TAE stability in ITER described using a Miller equilibrium. (Left) Linear dependence of TAE growth rate illustrating that the alpha-particle drive can be boosted with respect to the projection based on lower beta values. (Right) TAE growth rate rollover as a function of toroidal mode number with the boosted* α*-particle beta to* $\beta_\alpha(0) = 3\%$. [579].

Despite the above studies of TAE stability in ITER-like plasmas using different models and approaches, they agree in predicting only weakly unstable AE with rather weak consequences. Such predictive simulations are important for identifying the stable operational regions for burning plasma and ITER in particular. They are also important for indicating suitable discharge trajectories to approach the most unstable point by exploiting the physics of the instabilities. This could be done in the initial non-nuclear stage of plasma operations when the plasma does not exhibit any self-heating and can be more easily controlled. Such considerations will be discussed further in Section 7.5.

7.3 The effect of fast particles on $n/m = 1/1$ internal kink mode and fishbones in burning plasmas

We highlight here theoretical studies of two related problems applicable to ITER scenarios which are the possibility of so-called monster sawteeth crashes and the excitation of fishbone instabilities. It is not desirable to have such instabilities in burning plasmas for the reasons summarized in a recent topical review on the control of sawtooth oscillations [582]. First the stabilization by fusion α-particles will make the sawtooth period longer and cause so-called monster sawteeth with potentially severe consequences for plasma confinement. The triggering of neoclassical tearing modes (NTMs) or ELMs, which by themselves can degrade the plasma confinement, will require mitigation. Monster sawteeth can potentially also trigger disruptions of the plasma and lead to EP redistribution as discussed in Sec.4.2.5. EP redistribution can cause avalanches of AEs [524] [526] [527] which distort the AE stability boundaries as presented in Sec. 7.5.

Among the ITER scenarios most likely to exhibit sawteeth or fishbones, only the ELMy H-mode scenario with a central $q_0 < 1$ will have a resonant $q = 1$ surface where these modes can develop. We do not consider here scenarios with flat q profiles in the center (see however the note at the end of this section). Several studies exist on fishbone and sawtooth stabilization by EPs in ITER [583] [584] [585] [586] [587]. The first two references [583] [584] evaluated the $n/m = 1/1$ (or simply $m = 1$) stability for ITER EDA-98 [588] parameters. In the first of them, an analytic study of the $m = 1$ ideal MHD branch and fishbone stabilization was carried out using the standard internal kink mode dispersion relation [183] [589], whereas in the second the EP dynamics were retained within the equilibrium geometry. The EP contribution is characterized by trapped and passing ions which are described by a uniform in pitch angle slowing-down distribution function. Both groups of particles can resonate with the $m = 1$ internal kink mode which typically has a low frequency. The trapped ions constitute the dominant contribution to the imaginary part of the dispersion relation which represents the drive. Results of this study form a classic example of the $m = 1$ internal mode stability and are considered to be wholly appropriate for inclusion in this review. Fig. 7.3.1 is taken from this work and clearly shows the two separate branches that corresponds to ideal kinks and fishbones. The ideal kink mode branch can be completely stabilized by alphas but fishbones are near the unstable threshold in the ITER-EDA 98 design.

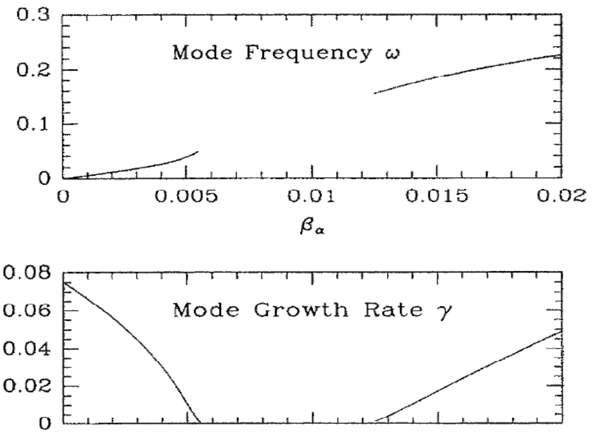

Figure 7.3.1 *Real mode frequency (top) and growth rate (bottom) of ideal branch (low* β_α *values) and fishbone branch (above* $\beta_\alpha = 0.0125$*) of internal kink mode for ITER EDA-98 plasma. For comparison the projected value of* α*-particle beta was* $\sim 1\%$ [583]. *The real mode frequency and the growth rate are normalized to the Alfvén frequency* ω_A*.*

In the paper by Porcelli [584] a comprehensive approach to the $m = 1$ kink mode problem was developed using appropriate orderings for the EP dynamics. A criterion for the onset of the sawtooth crash was proposed, but only simplified expressions were used in the calculations based on a circular plasma cross section, low-β and large aspect ratio. EP dynamics was accounted for using these approximations. Application of the model to ITER-EDA 98 plasma parameters showed the possible stabilization of $m = 1$ mode by alphas for a longer period of time than the confinement time. For the reference with alphas, the sawtooth period was expected to be between $10 - 10^3 s$ which is longer than the energy confinement time, $\tau_E = 5$s. With such long sawtooth periods, the possibility of crashs that can so strongly perturb the plasma that they become a threat to plasma operations arises.

More advanced calculations in terms of the internal kink stabilization model and numerical equilibria employed are described in Ref. [586]. The results indicate that according to the expectations in ITER-like plasmas within the $q = 1$ surface and not too low magnetic shear, the fluid instability drive is small enough that the MHD branch is fully stabilized by alphas up to a plasma beta twice as high as the expected value. The paper thus focuses on the fishbone branch in moderate magnetic shear. Figure 7.3.2 is taken from Ref. [586] and depicts the MHD and fishbone branches stability boundaries. We present the summary of the fishbone stability calculations in the right figure 7.3.2. In the this figure one can see that the destabilizing contribution due to alphas is mostly limited to inside the $q = 1$ surface and thus proportional to the area encompassed by this surface. This is reflected in the fishbone branch stability boundary shown on the left of the figure that the EP contribution is mostly determined by the number of fast ions inside the $q = 1$ surface.

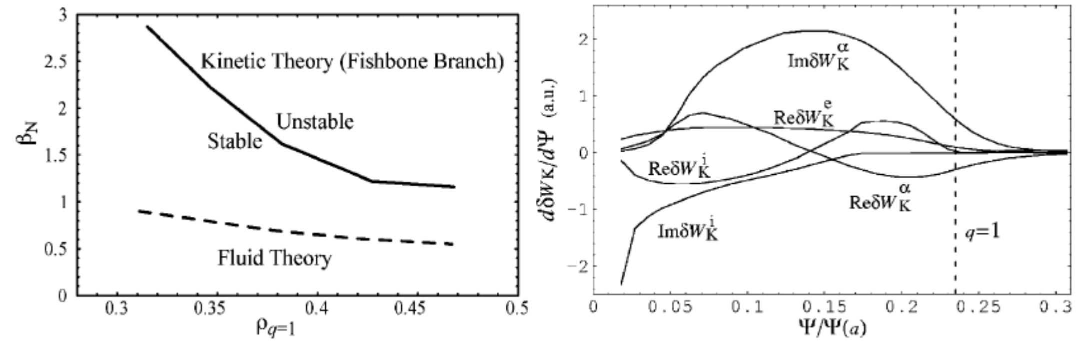

Figure 7.3.2 *(Left) Stability threshold region for fishbone (marked as kinetic theory) and ideal branches (marked as fluid theory curve) for a normal shear plasma (with* $\beta_N = 1.8$*) shown as a function of the* $q = 1$ *surface minor radius. (Right) Contributions of various fluid and kinetic components to the quadratic form of the potential energy* [586] .

In another work, Ref. [585], a numerical study of $m = 1$ internal kink mode stabilization by alphas was done. The parameters used were close to an ELMy H-mode with central $q_0 = 0.9$. The results are consistent with the identification of the solution as the internal kink mode. A significant, but not complete, stabilization of the ideal branch was reported. In particular, the growth rate of the MHD branch was reduced from $\gamma_{MHD}/\omega_A = 0.007$ to $\gamma_{MHD}/\omega_A = 0.0039$ if alphas were included. It was found that the mode is stabilized by alphas more easily in the circular cross section tokamak with the following formula derived for the α contribution:

$$\delta W_f = \frac{2\sqrt{3}}{\sqrt{(1+\kappa^2)(5+\kappa^2)}} \delta W_f^{circular}, \qquad (7.3.1)$$

where κ is the plasma ellipticity. Simulations have confirmed this directly. Interestingly, the fishbone branch was not excited in these conditions, although the physics of fishbones was fully included in the simulations of the $n = 1$ mode. Using Fig. 7.3.1 above, the results of Ref. [585] imply that fishbones are still stable and the fast particle drive is below their excitation threshold.

So far we have shown the results of the stability of the internal kink mode in ITER without the inclusion of NBI ions. A contribution of beam ions to the internal kink stability was considered in Ref. [587] where both fusion alpha and fast beam ion contributions were shown to stabilize the ideal kink mode. The tangential off-axis 1MeV neutral beam ions will be passing. Together with alphas they should completely stabilize sawteeth if 40MW of NBI power is injected. Again as in the Ref. [585], the fishbone branch is expected to be stable in nominal ITER plasmas.

What we can conclude from the $m = 1$ internal kink mode theories and calculations is that the ideal kink branch in ITER is predicted to be strongly stabilized. The fishbone branch however, is prone to be unstable. This strongly motivates future work to make more refined assessments of fishbone instability, and perhaps more importantly, their consequences as well as starting to investigate possibilities for controlling them. An extensive overview of the control methods which could be applied in ITER for such purposes are described in Ref. [582].

We should also note that the internal kink mode in ITER is associated with the quasi-interchange mode if the magnetic shear is very low within the $q = 1$ surface [590]. In this regime it was shown in Ref. [586] that as beta increases, first the fishbone branch is found unstable and then the MHD branch. It should be noted that such flat q profiles are thought hard to achieve in present day experiments [591] but should not be ruled out in burning plasmas. Indeed, high beta spherical tokamaks such as MAST regularly observe a transition from fishbones to an ideally saturated n=1 internal kink mode [284].

7.4 Thermonuclear (burning) instability

The fusion alpha-particle heating rate has a strong plasma temperature dependence, meaning that alpha particles have been identified as one of the drivers of thermonuclear instabilities in the coupled plasma particle, momentum, and energy balances [592]. We review it here as a key topic in achieving self-sustained burning conditions. We would like to note that the effects of AEs on alpha-particle profiles, sawteeth and fishbone oscillations could be considered as other types of burning instability, see the next section on POPCONs (Plasma OPeration CONtour) for a further example.

We shall start with the work by Furth et al. [593] in which for the first time the instability of the radial temperature profile was predicted to be due to the dependence of the temperature profile on the inductive current profile in Ohmically heated plasmas. This instability was found to be suppressed by fixing the total plasma current, i.e. fixing the heating rate. This analysis was expanded to account for α heating in Ref. [594]. That work found the thermonuclear instability present at fixed loop voltage over a range of plasma parameters. As in earlier research, stability was predicted at a fixed total current. Further publications [595] [596] included non-inductive currents. Ref. [595] found current-thermal instabilities with a growthrate inversely proportional to the plasma skin time. In Ref. [596], currents driven by lower hybrid waves, neutral beams and the bootstrap current were also brought into consideration. In the applications of their theory to the ITER-EDA 98 design it was concluded that the instability should be present. In later work [597], the plasma control system was shown to be able to suppress the instability on confinement timescales. We can thus summarize several publications: the current thermonuclear instability does not seem to be a problem in tokamaks with auxiliary heating due to feedback control of the total current.

Several publications on the energy balance for the burning instability are motivated by the strong dependence of the fusion alpha source on the ion temperature [598] [599] [600] [601] [602] [603] [604]. That is, after reaching the ignition point the plasma heating could further accelerate on a thermal transport timescale until a competing energy loss process balances the fusion energy production at a higher temperature. In this part of the review we present the results of Refs. [603] [604]

Fig. 7.4.1 summarizes the results of the cases considered in this model for the dynamic evolution of the particle and energy confinement times. These are calculated with the following assumptions: (a) the ratio of the particle to energy confinement times $\rho = \tau_p/\tau_E$ is assumed to be a constant; (b) the energy confinement time is taken to be a factor of two larger than the value provided by the ITER-89 L-mode scaling [605]. Burn control was evaluated using these scaling assumptions in a steady-state regime. Shown in the figures are the constraints imposed by the

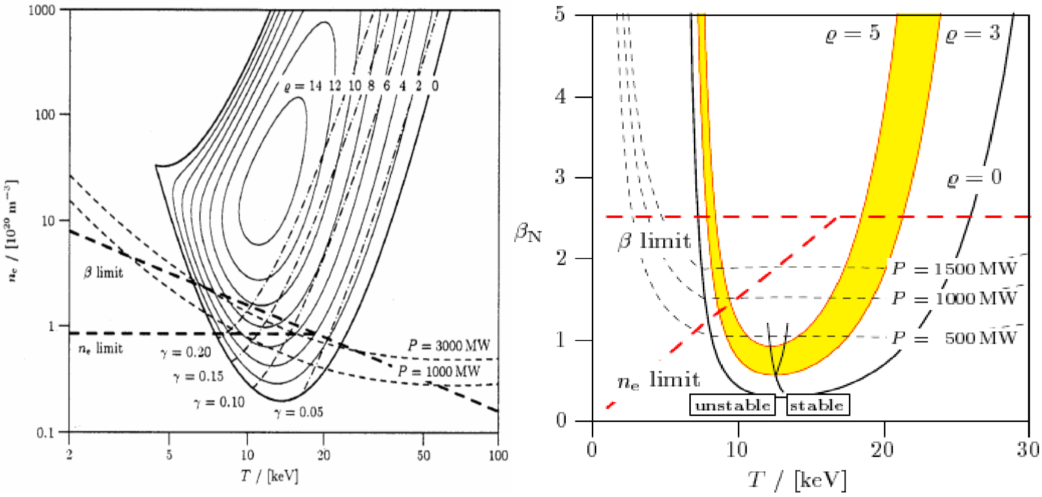

Figure 7.4.1 *The left figure shows the optimization of the fusion plasma operation points as discussed in the text. On the right figure, the ignition curve* $\rho = 5$ *(together with* $\rho = 3$ *and* 0 *curves) is shown versus normalized beta and plasma temperature where* $\rho = \tau_p/\tau_E$ *for He ash. The boundary of the stability with respect to thermal instabilities is depicted* [603] [604].

Troyon β limit, achievable fusion power P, fraction of radiated over applied powers, $\gamma = P_{rad}/P_{\alpha}$, and the Greenwald density limit. Contours indicated by different ρ values correspond to He ash concentrations that determined by the ratio $\rho = \tau_p/\tau_E = const.$

Figure 7.4.1 (right) represents the burn stability in the β_N, T plane. On the left side of the figure (region I, indicated unstable) an unstable mode is found when the thermal fluctuation is coupled to small density fluctuation. Region II (between the solid lines) is oscillatory with two found modes that are either real or complex. Finally, on the right branches (right figure), Region III (indicated as stable), all possible modes are stable. We would like to point out that the maximum fusion production rate of a DT plasma with Maxwellian distributed ion species is achieved at a plasma temperature of $T \approx 15keV$ [17], so that it is natural to expect that the optimal tokamak performance is easier to achieve around that value. This is reflected in Figure 7.4.1.

The above POPCON analysis was done using the ITER89 L-mode scaling multiplier H-factor. It should be noted that the optimum operating point for the ITER H-mode IPB98(y,2) scaling becomes appreciably different from that shown in Fig. 7.4.1 [606]. The thermonuclear instability depends upon parameter dependencies in the energy confinement time scaling, dilution by helium ash and so on [607]. Alpha heating and the thermonuclear instability can be tested experimentally only in ITER scale devices. Multi-parametric feedback control, including profile control, may be needed in ITER and DEMO machines to see if the burning plasma is sustained near the optimum operating point without thermonuclear instability.

7.5 Critical gradient model on operational regimes in burning plasmas

The progress in understanding Alfvénic mode stability is sufficient to be ready to make predictions with some degree of confidence about future operational regimes, which is the subject of the present section. The model applied here is based on linear stability theory which is well established and reviewed in Section 4.2.2.

We employ a 1.5D or critical gradient model to predict α-particle profiles relaxation by AE instabilities as described in Sec. 5.2. We show how with the help of this approximate reduced model one can make predictions rather quickly about relatively dangerous/safe parameter spaces in light of present understandings. One motivation for this is that the burning steady-state tokamak reactor needs a higher T_e to drive the plasma current efficiently and in steady-state should have a higher α pressure which could drive Alfvénic instabilities. The 1.5D model provides guidance on the modifications of plasma parameters to avoid AE driven effects.

We apply the 1.5D model to two ITER-like cases, an ELMy H-mode (normal shear) and an AT case with reversed magnetic shear q as discussed in Sec.7.2. We use the version of this model which relies on a normalization using linear NOVA growth rate calculations. We have to remark though that the version of the 1.5D model using analytic growth/damping rates expressions results in a lower AE unstable region by approximately $5\ keV$ on Figures 7.5.1. NBI fast ions contribution to the drive is added to the fusion alphas within the model. The POPCON diagrams obtained (figure 7.5.1) depict EP loss domains where the loss magnitudes increase very sharply with the plasma temperature which is a consequence of the approximate proportionality of the alpha source to the plasma pressure squared. Since the critical gradient model is by itself approximate we estimate the error in its predictions in the following way. If the 1.5D model suggests 50% error bars for the predicted EP losses (see Fig.5.2.3 (right) for the predictions of the neutron emission in the validation against DIII-D experiments), then applying the color index scale in figure 7.5.1 reduces the error bar to around 10% accuracy in terms of the plasma temperature. Nevertheless the qualitative dependencies used in the model are expected to be correct.

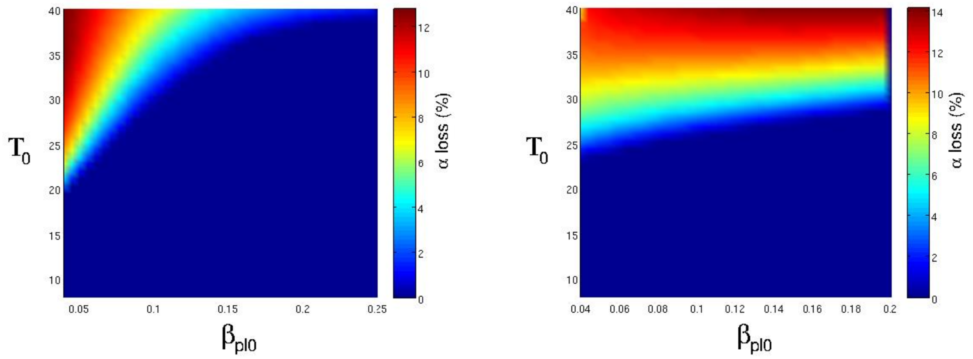

Figure 7.5.1 *POPCON diagrams of ITER like operation space plotted for the normal shear (left) and the reversed shear (right) plasmas. The nominal plasma parameters for the left figure correspond to* $\beta_{pl0} = 6\%$ *and* $T_0 = 23\text{keV}$ *and have a low alpha loss level. The negative magnetic shear plasma on the right figure has* $\beta_{pl0} \approx 6\%$ *and* $T_0 = 34\text{keV}$.

There are a few reservations about the applicability of this model which should be stated. If only alphas are used to compute the growth rates then the predicted losses should not be so severe, which makes Figs. 7.5.1 to be rather pessimistic. Also the number of unstable modes is far from infinite (see sec. 7.2): it is not clear if the model works in those conditions. In NOVA normalization version used in the plots we do not include potentially important radiative damping. This is because there is no appropriate analytic form of the radiative damping suitable for such applications. Neglecting the radiative damping makes 1.5D model predictions somewhat pessimistic. Since the 1.5D model is ambitious it does need more validations on wide plasma range in various devices as we stated in Sec. 5.2.

Nevertheless the POPCONs of Fig. 7.5.1 suggest that the AT scenario is more unstable than the normal shear elmy H-mod case. The ignored radiative damping should not change this due to medium unstable toroidal mode numbers [213]. Notably the loss regions are shaped in different ways in two cases. We can reflect on this by comparing the damping rates which are stronger function of the plasma pressure in the first case. The comparison of the thermal ion Landau damping dependences explains sharp plasma beta stable region dependence in the left figure. In the second case (figure 7.5.1 (right)) much weaker dependence is due primarily to the dominant trapped electron collision mechanism. It was noted using experimental DIII-D studies that AT plasma scenarios have low β_f excitation thresholds of AE instabilities in general [295] [442].

An independent method to estimate EP losses in ITER like plasma was just published [608]. It studies the same AT plasma with the TAE kinetic stability summarized in Fig.7.2.1 (right). The kinetic theory employs a theoretical approximate formula in order to evaluate the AE saturated amplitudes [609] [610]. Thus AE eigenstructures and their predicted amplitudes are used for the perturbative simulations of both fusion α's and injected beam ions relaxations. Only unstable TAEs were used in simulations which produced somewhat different results then 1.5D model does. What was found in simulations is that the AT scenario is characterized by a finite small loss of alphas on the order of 1%. This is lower than the 1.5D model predictions by a factor 3 to 5. Without beam ions AEs seem to be benign.

8 Summary and possible future developments

In preparation for burning plasma experiments we described advances in the physics of energetic particles since last comprehensive review paper by W.W. Heidbrink and G.J. Sadler. We showed many experimental and theoretical results on tokamak, ST and stellarator/helical plasmas. Most practically important results are in three key areas directly connected to the Alfvénic instabilities:

(1) Linear properties of Alfvén eigenmodes observed in tokamak, ST and stellarator/helical plasmas are explained consistently with the ideal MHD or MHD theory with kinetic effects taken into account perturbatively. Moreover, measurements of 2D structures of AEs provide an opportunity to verify non-perturbatiove AE theories. Stabilization and mitigation of the EP driven modes are attempted by various ways in burning plasma conditions, and the development of effective control techniques are needed.

(2) Properties of the nonlinear evolution of AEs predicted by a simple nonlinear bump-on tail instability (called BB – Berk-Breizman) model are documented for tokamak, ST and stellarator/helical plasmas. Only qualitative comparison has been done so far between the experimental data and the nonlinear simulations.

(3) Radial transport and losses of EPs induced by the resonant interaction of Alfvén eigenmodes or magnetic perturbations with EPs are intensively studied by various advanced EP and fluctuation diagnostics. Numerical simulations are developed using various approaches and demonstrate the qualitative agreement with the experimental data. High quality experimental data on induced EP transport are still needed for quantitative comparison with numerical simulations.

Building on this we would like to offer for considerations some interesting directions and topics for future energetic particle research of the fusion.

(1) Since it is clear now that the low frequency instabilities such as Alfvénic or MHD kink modes (fishbone modes) are central among the deleterious effects a lot of effort should be on the development of the control methods. This is not an urgent task to be addressed in search for the robust self-sustained tokamak operations though. In our opinion the most urgent task is to be able to confidently and accurately predict the stability domain of AEs and other modes for BPs. Both the damping and the drive can be modified and controlled for this purpose. Phase space engineering with combined heating, for instance, NBI and ICRF is an important and promising approach for EP driven mode control. If the radial penetration of externally applied 3D magnetic perturbations and its impact of EP transport are solved, they may be a candidate for an actuator for phase space control.
MHD spectroscopy development based on linear AE studies in various magnetic configurations is an important beneficial outcome for EP studies. In addition the employment of the Ion Cyclotron Emission (ICE) should be expected for fast ion diagnostics. These ideas follow from the discussions in Sec. 4.3. One issue not addressed in the literature at the moment is the nonlinear phase of ICE instabilities. The MHD spectroscopy and ICE diagnostics are expected to be powerful in burning plasma conditions with high radiation, in addition to various neutron and gamma ray diagnostics.

(2) One particular rather urgent problem for the nonlinear physics is to be able to predict the nonlinear evolution of the EP driven instabilities. Whether the expected instability behavior is characterized by the rapid chirping or by slow evolving amplitudes is important for the usability of the quasilinear models. For this purpose diagnostics of the EP distribution function with high resolution in time, real space, energy and pitch angle should be developed for detailed verification studies with more realistic nonlinear simulation tools.

(3) (and (1)) The deleterious effects that can make difficult for the fusion plasma to achieve its goal - sustained steady state burning - are the enhanced radial transport and losses induced

by various EP driven modes and other MHD instabilities. The central problem here is the Alfvénic instabilities that are capable of transporting fusion alphas in minor radius and degrade or quench the self-sustained thermonuclear reaction by inducing their losses. We touched upon the predictive capabilities of the Alfvén instability theory in sec. 7.5 within 1.5D quasi-linear approach. As the linear stability theory is mature enough, a more persistent push towards the nonlinear physics is now required. The role of the ITPA group at the moment should be instrumental in coordinating such activity (see sec. 7.1). In our opinion the most urgent task is to be able to confidently and accurately predict the operational regimes for BPs. This means that more advanced model of the quasi-linear transport has to be developed. At the same time for verification and validation of QL models the development of the first principle numerical tools should be done in a complimentary way to address the problem of the fast ion transport. Although at the moment these first principle numerical tools seem to be too expensive to run in the predictive regimes in the long run they could develop into alternative and more accurate approaches.

Related mostly to (3). Non-inductive current drive by high energy neutral beam injection is a critical component of the tokamak type reactor such as ITER, where the role of EPs is crucial. Its modification or degradation due to various instabilities, such as AEs, fishbones and internal kink modes is expected in the hybrid plasma scenarios and is thus crucial issue. Through the exploitation of 3D effects such as arise when 3D fields are applied to control ELMs (i.e. via resonant magnetic perturbation applications) the most interesting effect appear to be on the energetic particle confinement due to partial breaking of axisymmetric configuration in the plasma edge. The key issue is to solve radial penetration of these externally applied 3D magnetic perturbations. This points towards a greater collaboration between the stellarator and tokamak communities and motivates the routine inclusion of 3D effects when calculating, for instance, the underlying fast ion distribution. Such effects as snakes and long lived kink like mode perturbed core of the plasma present an interest from the EP confinement point of view [611]. More accurate and realistic modeling of the 3D effects in the tokamak plasma is getting more traction and numerical support.

Further, one of the most challenging and beneficial for the fusion is the possibility to create and explore the alpha-channeling covered in Sec. 4.2.7. Although this is a speculative area it has a potential for the fusion research to relax the Lawson criterion to achieve fusion burning and ultimately the cost of a fusion reactor two times. If explored well it may show the ways for modifications of EP distributions in a controllable way that would stabilize other instabilities such as AEs, GAEs, and other deleterious excitations. Such distribution modification is the purpose of phase space engineering concept for the future. A wide range of possibilities opens up if this technique is accessible.

One area not covered in details in this review is the physics of trapped fast ions created during ICRH. This physics is complex but accessible theoretically and experimentally as this heating method is one of few dominant ones which in present day experiments create a source of EPs with a controllable distribution function. ICRH can be used in burning plasmas for such problems as alpha-channeling, phase space engineering, sawtooth and fishbone control.

Finally, we point out at a few issues which are most critical for BPs in specific magnetic configurations, that is STs and stellarator/helical burning plasma devices. These studies would contribute to the efforts on the above issues directly linked to ITER.

One basic outstanding problem here has to do with the plasma equilibrium which still needs to be properly addressed in modern equilibria solvers with EP pressure and its anisotropy contribution included as this is shown to have a significant effect on the geometry, its metrics elements and such integral properties as the Shafranov shift. This problem together with the plasma rotation becomes especially acute in the ST devices with strong EP beta values capable for example of shifting the AE continua depending on the fast ion characteristics. Those effects could be quantified to be of order ε in present day STs and in the projected ST reactors.

A model for GAE/CAE electron thermal transport in ST plasmas primarily is required for predictive plasma transport simulations. First thing to address here is the clarification of the underlying mechanism responsible for the anomalous electron heat transport. Next is the development of the quantitative model for transport coefficients.

In stellarator/helical devices, confinement of trapped energetic particles is crucial for future BPs of this type configurations. Good confinement of energetic passing ions is demonstrated on LHD. MHD modes such as AEs destabilized by passing EPs are intensively studies. Recently, on LHD, MHD modes destabilized by helically trapped EPs, which have similar character to that of off-axis fishbone/EWM in tokamaks but have a structure of resistive interchange different from external kink modes were observed inducing large change of plasma rotation [612]. Harmful MHD modes destabilized by trapped EPs should be suppressed or mitigated by development of reliable control techniques such as phase space engineering, in addition to control of AEs driven by passing EPs.

Acknowledgement

We would like to thank the board of editors of the Nuclear Fusion journal for offering us to write this review and Dr. R. Nazikian for ideas on its formatting. We would like to thank Drs. H. L. Berk, B. Breizman, E. Fredrickson, G.Y. Fu, W. W. Heidbrink, M. Isobe, A.V. Krasilnikov, S.S. Medley, N. Nakajima, M. Osakabe, M.P. Petrov, S. E. Sharapov, D.A. Spong, M. Salewski, Y. Todo, M.A. Van Zeeland and other colleagues we contacted for useful discussions and Dr. F. Zonca for sharing certain publication details about his review [12] co-authored with Prof. L. Chen.

The work on this review is supported in part (KT) by the Grant-in-Aid for Scientific Research from JSPS (No. 21360457, 24360386) and in part (NNG) under Contract Number DE-AC02-09CH11466 with the U.S. DOE. The views and opinions expressed herein do not necessarily reflect those of the ITER Organization.

Appendix A. Nomenclature

α- fusion products, alpha-particles
$\alpha_p = -2\mathrm{q}^2\, Rp'/B_0^2$ - plasma pressure gradient combination
α_r exponent phase for the ripple dependence
$\langle \dots \rangle$ - time (drift orbit) averaging
β_i - (ion species or core plasma if $i = pl$) plasma pressure to the magnetic field pressure ratio
β_N - normalized plasma beta
$\vec{B}$ - magnetic field vector.
$B_{\theta,\varphi}$ - poloidal and toroidal (or TF) magnetic field components
$B_{min,max}$ - minimum and maximum values of the Bfield in the tokamak poloidal plane
c - speed of light
$()'_x$ - scalar derivative in $x$direction
$\Delta = \nabla \cdot \nabla$ - differential operator of partial derivatives
$\Delta_{r,\vartheta}$ - radial and poloidal width of CAE eigestructure
Δ'_{Sh} - radial derivative of the Shafranov shift, Δ_{Sh}
$\delta p_c, (\delta f)$ - perturbation of a core pressure (or a function f)
$\delta K, \delta W$ - kinetic and potential energies in MHD theory
e_f - EP charge
E_f, E_n, E_α - fast ion, neutron, or alpha-particle energy. Indexes are applied here for energy as an example
$\mathcal{E}_\perp = m\, v_\perp^2/2\,;$ - particle perpendicular energy
$\hat{\varepsilon} = 2\left(r/R + \Delta'_{Sh}\right)$- toroidicity parameter corresponding to toroidal configuration with $\varepsilon = r/R$
$\varepsilon_\rho, \varepsilon_{\rho cr}$ - stochastic (critical) diffusion parameter due to non-adiabaticity
F_f - (or simply F) fast ion distribution function
$\vec{F}$ - force applied to the plasma element
$f_{p,ce}$ - electron plasma,cyclotron frequency
Γ - the ratio of specific heat, $5/3$ for ideal MHD
$\vec{\nabla}, \nabla$- vector derivative, gradient, of a function along the direction of its fastest change
κ - ellipticity of the poloidal cross-section
$k_{\parallel m,n} = \frac{m-nq}{qR}$- parallel wavevector
λ - magnetic moment normalized to particle energy
λ_k - kinetic coefficient for KTAE problem
m_i - mass of specie i
$\mu = \mathcal{E}\,\lambda/B_0$ - magnetic moment
m, n - poloidal and toroidal mode numbers
N - number of toroidal field coils
$\nu_{d(eff)}$ - (effective) diffusion frequency
ψ_p - poloidal flux
P_φ - toroidal angular momentum
$q = rB_\varphi/RB_\vartheta$- magnetic field safety factor (expression is valid in circular plasma, large-aspect ratio limit)
$\iota \equiv 1/q$- the rotational transform of magnetic field line
$\Im, \Re$ - imaginary and real parts
$q_{min,0,1}$ - minimum, center and edge values of $q(r)$
ϱ - plasma mass density
ϱ_L - Larmor radius
R, r - major and minor radii

r_b, ϑ_b - radial and poloidal coordinates of the banana tip point
$s - \alpha$ - analytic model for plasma equilibrium
$s = rq'/q$ - magnetic field shear
se - subscript for slowing down on electrons
$S_m = m\theta - n\varphi$ - eikonal of perturbed quantities
S_f - source of fast particles
St - collisonal integral
σ_E- the standard deviation in energy
τ_E - energy confinement time
τ_b - bounce time, period of drift motion
τ_{cr} - sawtooth crash time
τ_{se} - EP slowing down time (on electrons)
τ_δ - ripple stochastic diffusion confinement time
τ_{loss} - effective loss time
T_i- thermal ion temperature
ϑ, φ - poloidal and toroidal angles
b - subscript for bounce motion characteristics
v_* - critical velocity parameter when slowing down on ions equal to the slowing down on electrons
$v_A = B/\sqrt{4\pi m_i n_0}$- Alfvén velocity
v_a- acoustic, sound speed
$v_{f(0)}$- EP (birth) velocity
$v_i = \sqrt{2T_i/m_i}$- thermal ion speed
v_d - drift velocity of a particle in TF
ω - frequency
$\bar{\omega} = \omega R_0/v_A$ - frequency normalized to Alfvén freqency
ω_{cj} - cyclotron frequency of $j$specie
$\omega_{a,A,cA}$ - sound (acoustic), Alfvén and compressional Alfvén wave frequencies
$\omega_{b,\varphi}$ - bounce and toroidal drift frequencies
ω_D - particle magnetic field drift (toroidal) frequency
$\vec{\xi}$- vector of a plasma displacement
x^3- plasma volume element.
$\chi = v_\parallel/v$ - pitch angle
ξ - radial displacement

Acronyms

AE, AC- Alfvén Eigenmodes (see 4.2.2 for the "zoo" of AE) and Alfvén Continuum
ACM - Alfvén Cascade Mode - another name for $RSAEs$
AUG - ASDEX (**A**xially **S**ymmetric **D**ivertor **Ex**periment) Upgrade tokamak
$BAAE$ - beta-induced Alfvén acoustic Eigenmodes
BES - beam emission spectroscopy
BP - burning plasma
CHS – Compact Helical System
COM - constant of motion
CTS - collective Thomson scattering
DF - distribution function
DT - deuterium-tritium mixture of a plasma
$ECEI$ - electron cyclotron emission imaging
ECR - electron cyclotron resonance
$EGAM$ - EP driven geodesic acoustic mode (GAM)
ELM - edge localized modes

EP – energetic particles, or fast, or energetic ions here
EPM - energetic particle mode
EWM - EP driven Wall Mode
FTU - Frascati Tokamak Upgrade (FTU)
FILD - fast ion loss detector
FP - Fokker-Plank
FS - ferritic steel inserts
FTU - Frascati Tokamak Upgrade
JET - Joint European Torus
HFS - high field side
ICE - ion cyclotron emission
ICRH- ion cyclotron resonant heating
ITER - International Thermonuclear Experimental Reactor
ITB - internal transport barrier
KAW - kinetic Alfvén wave
KSTAR - Korea Superconducting Tokamak Advanced Research
LCFS - last closed flux surface
LH - low hybrid heating
LHD - *Large Helical device*
LFS - low field side
MHD – magnetohydrodynamic
MAST – Mega Amp Spherical Tokamak
MP - magnetic probes
NBI(NBCD) – neutral beam injection (current drive)
NDD – natural diamond detector
NPA - neutral particle analyzer
NSTX - national spherical torus experiment
NTM - neoclassical tearing mode
OFM - Off-axis Fishbone Mode
PCX - pellet charge exchange
PFC - plasma facing components
PIC - particle in cell
PSE - phase space engineering
QL - quasi-linear
RF - radio frequency
RS - reversed share
RMP - resonance mode perturbation
RWM - resistive wall mode
ST - spherical tokamak (or torus)
(c)TAE - (core localied) toroidicity induced AE
TBM - test blanket module
TF - toroidal field
TFTR - Tokamak Fusion Test Reactor
TEXTOR - Tokamak EXperiment for Technology Oriented Research
WPI wave particle interactions

Bibliography.

[1] W. W. Heidbrink and G. J. Sadler, *Nuclear Fusion,* vol. 34, p. 535, 1994.

[2] R. Hawryluk, *Phil. Trans. R. Soc. Lond. A,* vol. 357, p. 443, 1999.

[3] S. Zweben, R. V. Budny, D. S. Darrow and et.al., *Nucl. Fusion,* vol. 40, p. 91, 2000.

[4] K. Wong, R. Fonk, S. Paul and et.al., *Phys. Rev. Lett.,* vol. 66, p. 1874, 1991.

[5] W. W. Heidbrink, E. Strait, E. Doyle and et.al., *Nucl. Fusion,* vol. 31, p. 1635, 1991.

[6] K. Wong, *Plasma Phys. Control. Fusion,* vol. 42, p. R1, 1999.

[7] G. Vlad, F. Zonca and S. Briguglio, *Riv. Nuovo Cimento,* vol. 22, p. 1, 1999.

[8] W. Heidbrink, *Phys. Plasmas,* vol. 15, p. 055501, 2008.

[9] Y. Kolesnichenko, A. Könies, V. Lutsenko and Y. Yakovenko, *Plasma Phys. Control. Fusion,* vol. 53, p. 024007, 2011.

[10] K. Toi, K. Ogawa, M. Isobe and et.al., *Plasma Phys. Control. Fusion,* vol. 53, p. 024008, 2011.

[11] B. Breizman and S. Sharapov, *Plasma Phys. Control. Fusion,* vol. 53, p. 054001, 2011.

[12] L. Chen and F. Zonca, "Physics of Alfven waves and energetic particles in burning plasmas," *Rev. Mod. Phys.,* 2014 (to appear).

[13] P. Lauber, *Phys. Reports,* vol. 533, p. 33, 2013.

[14] A. Mikhailovskii, Reviews of Plasma Physics, vol. 6, M. Leontovich, Ed., New York - London: Consultants Bureau, 1975, p. 70.

[15] A. Mikhailovskii, Reviews of Plasma Physics, vol. 9, M. Leontovich, Ed., New York - London: Consultants Bureau, 1986, p. 103.

[16] Y. Kolesnichenko, *Nucl.Fusion,* vol. 20, p. 727, 1980.

[17] S. Putvinskij, Reviews of Plasma Physics, vol. 18, B. Kadomtsev, Ed., New York: Consultants Bureau, 1993, p. 239.

[18] S. Medley, D. Mansfield, A. Roquemore and et.al., *Rev. Sci. Instrum.,* vol. 67, p. 3122, 1996.

[19] M. P. Petrov, M. Bell and R. V. Budny et.al., *Phys. Plasmas,* vol. 6, p. 2430, 1999.

[20] T. Stix, *Nucl. Fusion,* vol. 15, p. 737, 1975.

[21] C. Chang and P. Colestock, *Phys. Fluids B,* vol. 2, p. 310, 1990.

[22] A. V. Krasilnikov et al., in Fusion Energy 1996 (Proc. 16th Int. Conf. Montreal, 1996), Vol. 1, p. 293, IAEA, Vienna (1997).

[23] A. Krasilnikov, S. S. Medley and N. Gorelenkov et al., *Nucl. Fusion,* vol. 39, p. 1111, 1999.

[24] A. Korotkov, A. Gondhalekar and A. Stuart, *Nucl. Fusion,* vol. 37, p. 35, 1997.

[25] A. Bader, R. S. Granetz and R. R. Parker et al., *Nucl. Fusion,* vol. 52, p. 094019, 2012.

[26] J. M. Adams, O. N. Jarvis and G. J. Sadler et al., *Nucl. Instrum. Methods,* vol. A329, p. 277, 1993.

[27] E. Ronchi, S. Conroy and E. Anderson Sunden et al., *Nucl. Fusion,* vol. 50, p. 035008, 2010.

[28] M. Ishikawa, M. Takechi and K. Shinohara et al., *Nucl. Fusion,* vol. 47, p. 849, 2007.

[29] A. J. H. Donne et al., "Progress in the ITER Physics Basis Chapter 7: Diagnostics," *Nucl. Fusion,* vol. 47, p. S337, 2007.

[30] B. Wolle, *Phys. Reports,* vol. 312, p. 1, 1999.

[31] M. Gatu Johnson, L. Giacomelli and A. Hjalmarsson et al., *Nucl. Instrum. Methods,* vol. A591, p. 417, 2008.

[32] L. Giacomelli, A. Hjalmarsson and H. Sjostrand et al., *Nucl. Fusion,* vol. 45, p. 1191, 2005.

[33] G. Ericsson et al., *Rev. Sci. Instrum.,* vol. 72, p. 759, 2001.

[34] A. V. Krasilnikov, E. A. Azizov and A. L. Roquemore et al., *Rev. Sci. Instrum.,* vol. 68, p. 553, 1997.

[35] H. Brysk, *Plasma Phys.,* vol. 15, p. 611, 1973.

[36] C. Hellesen, M. Gatu Johnson and e. a. E. Anderson Sunden, *Nucl. Fusion,* vol. 53, p. 113009, 2013.

[37] J. Kallne, L. Bellabio and J. Frenje et al., *Phys. Rev. Lett.,* vol. 85, p. 1246, 2000.

[38] C. Hellesen et al., *Plasma Phys. Control. Fusion,* vol. 52, p. 085013, 2010.

[39] V. G. Kiptily, F. E. Cecil and S. S. Medley, *Plasma Phys. Control. Fusion,* vol. 48, p. R59, 2006.

[40] S. Medley, F. Cecil, D. Cole and et.al., *Rev. Sci. Instrum.,* vol. 56, p. 975, 1985.

[41] V. Kiptily, F. Cecil, O. Jarvis and et.al., *Nucl. Fusion,* vol. 42, p. 999, 2002.

[42] V. Kiptily, *Fusion Technology,* vol. 18, p. 583, 1990.

[43] V. Kiptily, Y. Baranov, R. Barnsley and e. al., *Phys. Rev. Lett.,* vol. 93, p. 115001, 2004.

[44] V. Kiptily, J. Adams, L. Bertalot and e. al., *Nucl. Fusion,* vol. 45, p. L21, 2005.

[45] V. G. Kiptily, G. Gorini and M. Tardocchi et al., *Nucl. Fusion,* vol. 50, p. 084001, 2010.

[46] M. Tardocchi, M. Nocente and I. Proverbio et al., *Phys. Rev. Lett.,* vol. 107, p. 205002, 2011.

[47] T. Kondoh, Y. Kusama and H. Kimura et al., *J. Nucl. Mater.,* Vols. 241-243, p. 564, 1997.

[48] W. W. Heidbrink, *Rev. Sci. Instrum.,* vol. 81, p. 10D727, 2010.

[49] W. Heidbrink, K. Burrell, Y. Luo and et.al., *Plasma Phys. Control. Fusion,* vol. 46, p. 1855, 2004.

[50] W. W. Heidbrink, M. Murakami, J. M. Park and et.al., *Plasma Phys. Control. Fusion,* vol. 51, p. 125001, 2009.

[51] B. Geiger, M. Garcia-Munoz, W. Heidbrink and et.al., *Plasma Phys. Control. Fusion,* vol. 53, p. 065010, 2011.

[52] C. Michael, N. Conway, B. Crowley and et.al., *Plasma Phys. Control. Fusion,* vol. 55, no. 9, p. 095007, 2013.

[53] S. Pinches, R. Akers and B. Breizman et al., 2012 Proc. 24th Int. Conf. on Fusion Energy (San Diego 2012) [TH/P3-43] http://www-naweb.iaea.org/napc/physics/FEC/FEC2012/index.htm.

[54] O. Jones and et.al., *Plasma Phys. Control. Fusion,* vol. 55, p. 085009, 2013.

[55] T. Ito, M. Osakabe and K. Ida et al., *Plasma Fusion Res.,* vol. 5, p. S2099, 2012.

[56] M. Van Zeeland, J. Yu, N. Brooks and et.al., *Plasma Phys. Control. Fusion,* vol. 52, p. 045006, 2010.

[57] A. Patel, P. Carolan, N. Conway and R. Akers, *Rev. Sci. Instrum.,* vol. 75, p. 4944, 2004.

[58] J. Yu, M. Van Zeeland, M. Chu, V. Izzo and R. La Haye, *Phys. Plasmas,* vol. 16, p. 056114, 2009.

[59] M. A. Van Zeeland, W. W. Heidbrink and J. H. Yu, *Plasma Phys. Contr. Fusion,* vol. 51, p. 055001, 2009.

[60] J. Chung, R. Konig, J. Howard and et.al., *Plasma Phys. Control. Fusion,* vol. 47, p. 919, 2005.

[61] J. Howard, *Rev. Sci. Instrum.,* vol. 77, p. 10F111, 2006.

[62] D. Moseev, F. Meo and S. B. Korsholm et al., *Plasma Phys. Control. Fusion,* vol. 53, p. 105004, 2011.

[63] M. Salewski, O. Asunta, L.-G. Eriksson and et.al., *Plasma Phys. Control. Fusion,* vol. 51, p.

035006, 2009.

[64] H. Bindslev, J. Hoekzema and et.al., *Phys. Rev. Lett.,* vol. 83, p. 3206, 1999.

[65] H. Bindslev, S. Nielsen, L. Porte and et.al., *Plasma Phys. Control. Fusion,* vol. 49, p. B551, 2007.

[66] W. W. Heidbrink, Y. Luo and K. H. Burrell et al., *Plasma Phys. Control. Fusion,* vol. 49, p. 1457, 2007.

[67] M. Salewski, B. Geiger, S. Nielsen and et.al., *Nucl. Fusion,* vol. 52, p. 103008, 2012.

[68] M. Salewski, B. Geiger, S. Nielsen and e. al., *Nucl. Fusion,* vol. 54, p. 063019, 2013.

[69] S. Kubo, M. Nishiura, T. K. and et.al., *Rev. Sci. Instrum.,* vol. 81, p. 10D535, 2010.

[70] D. Darrow, H. W. Herrman and D. W. Johnson et al., *Rev. Sci. Instrum.,* vol. 66, p. 476, 1995.

[71] M. Garcia-Munoz, N. Hicks, R. van Voomveld and et.al., *Phys. Rev. Lett.,* vol. 104, p. 185002, 2010.

[72] M. Isobe, K. Toi, H. Matsusita and et.al., *Nucl. Fusion,* vol. 46, p. S918, 2006.

[73] K. Ogawa, M. Isobe, K. Toi and et.al., *Nucl. Fusion,* vol. 50, p. 084005, 2010.

[74] D. Darrow, S. Baumel, F. Cecil and e. al., *Rev. Sci. Instrum.,* vol. 75, p. 3566, 2004.

[75] K. Nagaoka, M. Isobe and K. Toi et al., *Phys. Rev. Lett.,* vol. 100, p. 065005, 2008.

[76] R. Nazikian, G. Fu, S. Batha and e. al., *Phys. Rev. Lett.,* vol. 78, p. 2976, 1997.

[77] M. Van Zeeland, G. Kramer, M. Austin and et.al., *Phys. Rev. Lett.,* vol. 97, p. 135001, 2006.

[78] B. Tobias, C. Domier, T. Liang and et.al., *Rev. Sci. Instrum.,* vol. 81, p. 10D928, 2010.

[79] I. Classen, P. Lauber, D. Curran and et.al., *Plasma Phys. Control. Fusion,* vol. 53, p. 124018, 2011.

[80] B. J. Tobias, I. G. J. Classen and C. W. Domier et al., *Phys. Rev. Lett.,* vol. 106, p. 075003, 2011.

[81] R. Nazikian, G. Kramer and E. Valeo, *Phys. Plasmas,* vol. 8, p. 1840, 2001.

[82] R. Nazikian, G. Fu, Z. Chang and et.al., *Phys. Plasmas,* vol. 5, p. 1703, 1998.

[83] D. Gupta, R. Fonk, G. McKee and et.al., *Rev. Sci. Instrum.,* vol. 75, p. 3493, 2004.

[84] R. D. Durst, R. J. Fonck and K. L. Wong et al., *Phys. Fluids B,* vol. 4, p. 3707, 1992.

[85] M. Van Zeeland, M. Austin, T. Carlstrom and et.al., *Nucl. Fusion,* vol. 46, p. S880, 2006.

[86] S. Sharapov, B. Alper, J. Fessey et al. and ., *Phys. Rev. Lett.,* vol. 93, p. 165001, 2004.

[87] K. Toi, F. Watanabe, T. Tokuzawa and et.al., *Phys. Rev. Lett.,* vol. 105, p. 145003, 2010.

[88] E. Edlund, M. Porkolab, G. Kramer and et.al., *Phys. Rev. Lett.,* vol. 102, p. 165003, 2009.

[89] T. Ido, A. Shimizu and M. Nishimura et al., *Plasma Phys. Control. Fusion,* vol. 52, p. 124025, 2010.

[90] A. V. Melnikov et al., *Nucl. Fusion,* vol. 50, p. 084023, 2010.

[91] H. Soltowisch, *Plasma Phys. Control. Fusion,* vol. 34, p. 1669, 1992.

[92] L. Lin, W. X. Ding and D. L. Brower et al., *Phys. Plasmas,* vol. 20, p. 030701, 2013.

[93] W. Cooper, J. Graves and O. Sauter, *Plasma Phys. Control. Fusion,* vol. 34, p. 1011, 1992.

[94] H. Yamada, K. Watanabe, K. Yamazaki and et.al., *Nucl. Fusion,* vol. 41, p. 901, 2001.

[95] G. Neilson, M. Zarnstorff, J. Lyon and et.al., *J. Plasma Fusion Res.,* vol. 78, p. 214, 2002.

[96] G. Rewoldt, L.-P. Ku and W. Tang, *Phys. Plasmas,* vol. 12, p. 102512, 2005.

[97] C. Beidler, G. Grieger, F. Herrnegger and et.al., *Fusion Technol.,* vol. 17, p. 148, 1990.

[98] J. Talmadge, V. Sakaguchi, F. Anderson and et.al., *Phys. Plasmas,* vol. 8, p. 5165, 2001.

[99] D. Spong, S. Hirshman, L. Berry and et.al., *Nucl. Fusion,* vol. 41, p. 711, 2001.

[100] A. Boozer, *Phys. Fluids B,* vol. 23, p. 904, 1980.

[101] D. Spong et al., in Fusion Energy 2006 (Proc. 21st Int. Conf. Chengdu, 2006) (Vienna: IAEA) CD-ROM file TH/P7-2 and http://www-naweb.iaea.org/napc/physics/FEC/FEC2006/html/index.htm.

[102] D. Spong, *Phys. Plasmas,* vol. 12, p. 056114, 2005.

[103] H. Mynick, *Phys. Plasmas,* vol. 13, p. 058102, 2006.

[104] S. Masuda, R. Kumazawa, K. Nishimura and et.al., *Nucl. Fusion,* vol. 37, p. 53, 2006.

[105] R. White, The Theory of Toroidally Confined Plasmas, London, UK: Imperial College Press, 2006.

[106] T. Saida, M. Sasao, M. Isobe and et.al., *Nucl. Fusion,* vol. 44, p. 488, 2004.

[107] T. Mutoh, R. Kumazawa, T. Seki and et.al., *Nucl. Fusion,* vol. 43, p. 738, 2003.

[108] M. Osakabe, M. Isobe, S. Murakami and et.al., *Fusion Sci. Technol.,* vol. 58, p. 131, 2010.

[109] S. Murakami, A. Fukuyama, T. Akutsu and et.al., *Nucl. Fusion,* vol. 46, p. S425, 2006.

[110] Y. Todo, S. Murakami, T. Yamamoto and et.al., *Fusion Sci. Technol.,* vol. 58, p. 277, 2010.

[111] C. Beidler, W. Hitchon, W. van Rij and et.al., *Phys. Rev. Lett.,* vol. 58, p. 1745, 1987.

[112] C. Beidler and W. Hitchon, *Plasma Phys. Control. Fusion,* vol. 36, p. 317, 1994.

[113] M. Smirnova, *Phys. Plasmas,* vol. 8, p. 5204, 2001.

[114] M. Redi, H. Mynick, M. Suewattana and et.al., *Plasma Phys. Control. Fusion,* vol. 36, p. 317, 1994.

[115] R. R. Parker, *Plasma Phys. Control. Fusion,* vol. 35, p. B23, 1993.

[116] L. Ku, P. Garabedin, J. Lyon and et.al., *Fusion Sci. Technol.,* vol. 54, p. 673, 2008.

[117] M.-K. Peng, *Phys. Plasmas,* vol. 7, p. 1681, 2000.

[118] M. Ono et al., in Fusion Energy 1996 (Proc. 16th Int. Conf. Montreal, 1996), Vol. 2, p. 71, IAEA Vienna (1997).

[119] A. Sykes, *Phys. Plasmas,* vol. 4, p. 1665, 1997.

[120] S. Kaye, M. Bell, R. Bell and et.al., *Nucl. Fusion,* vol. 45, p. S168, 2005.

[121] J. Menard, M. Bell, R. Bell and et.al., *Nucl. Fusion,* vol. 47, p. S645, 2007.

[122] A. Sykes, J.-W. Ahn, R. Akers and et.al., *Phys. Plasmas,* vol. 8, p. 2101, 2001.

[123] V. Gusev, E. Azizov, V. Belyakov and et.al., in *Proc. Int. Congr. on Plasma Phys. 25th European Phys. Conf.*, Prague, vol. 22C, p. 576, 1998.

[124] A. Morozov and L. Soloviev, in *Reviews of Plasma Phys.*, vol. 2, New York, Consultants Bureau, 1966, p. 101.

[125] E. Belova, N. Gorelenkov and C. Cheng, *Phys. Plasmas,* vol. 10, p. 3240, 2003.

[126] Y. Kolesnichenko, R. White and Y. Yakovenko, *Phys. Plasmas,* vol. 9, p. 2639, 2002.

[127] V. Yavorskij, D. Darrow, V. Goloborodko and et.al., *Nucl. Fusion,* vol. 42, p. 1210, 2002.

[128] V. Yavorskij et al., in Fusion Energy 2002 (Proc. 19th Int. Conf. Lyon, 2002) (Vienna: IAEA) CD-ROM file TH/P3-20 and http://www.iaea.org/programmes/ripc/physics/fec2002/html/fec2002.htm.

[129] J. Carlsson, *Phys. Plasmas,* vol. 8, p. 4725, 2001.

[130] R. Hastie, G. Hobbs and J. Taylor, in *Plasma Phys. Control. Nuclear Fusion Res. 1968 (Proc.. 3rd Int. Conf. Novosibirsk 1968)*, Vienna, vol. 1, p. 389, 1969.

[131] W. Heidbrink, M. Miah, D. Darrow and et.al., *Nucl. Fusion,* vol. 43, p. 883, 2003.

[132] A. Bortolon, W. Heidbrink and M. Podesta, *Bulletin of the American Physical Society, http://meetings.aps.org/link/BAPS.2010.DPP.BP9.63,* 2010.

[133] J. Cary, C. Hedrick and J. Tolliver, *Phys. Fluids,* vol. 31, p. 1586, 1988.

[134] J. Rome, *Nucl. Fusion,* vol. 35, p. 195, 1995.

[135] R. Goldston, D. McCune, H. Towner and et.al., *J. Plasma Phys.,* vol. 26, p. 283, 1981.

[136] P. Yushmanov, Reviews of Plasma Physics, vol. 16, New York: Consultants Bureau, 1990, p. 55.

[137] A. Fasoli, C. Gormezano, H. Berk and et.al., "Chapter 5 of ITER Physics Basis," *Nucl. Fusion,* vol. 47, p. S264, 2007.

[138] V. Basiuk, L.-G. Eriksson, V. Bergeaud and et.al., *Nucl. Fusion,* vol. 44, p. 181, 2004.

[139] G. Saibene, N. Oyama, J. Lönnroth and et.al., *Nucl. Fusion,* vol. 47, p. 969, 2007.

[140] S. Putvinski, *JETP Lett.,* vol. 36, p. 397, 1982.

[141] S. Putvinskii and R. Shurygin, *Sov. J. Plasma Phys.,* vol. 10, p. 534, 1984.

[142] V. Goloborodko and V. Yavorskij, *Nucl. Fusion,* vol. 24, p. 627, 1984.

[143] R. Goldston, R. White and A. Boozer, *Phys. Rev. Lett.,* vol. 47, p. 647, 1981.

[144] R. B. White, *Phys. Rev. E,* vol. 58, p. 1774, 1998.

[145] N. Gorelenkov, R. Budny, H. Duong and et.al., *Nucl. Fusion,* vol. 37, p. 1053, 1997.

[146] P. Yushmanov, *Nucl. Fusion,* vol. 23, p. 1599, 1983.

[147] G. Hammet, Ph.D. Thesis, Princeton Univerity, 1983.

[148] S. Konovalov and et.al., in *Proc. 28th EPS Conf. on Control. Fusion and Plasma Physics*, Funchal, June 2001, vol. 25A (ECA), p. 613.

[149] K. Tobita, K. Nakayama, S. Konovalov and et.al., *Plasma Phys. Control. Fusion,* vol. 45, p. 133, 2003.

[150] L. Giancarli, V. Chuyanov, M. Abdou and et.al., *Fusion Eng. Des. ,* vol. 85, p. 1829, 2010.

[151] M. Schaffer, J. Snipes, P. Gohil and et.al., *Nucl. Fusion,* vol. 51, p. 103028, 2011.

[152] G. Kramer, R. Budny, R. Ellis and et.al., *Nucl. Fusion,* vol. 51, p. 103029, 2011.

[153] G. Kramer, R. Budny, A. Bortolon and et.al., *Plasma Phys. Control. Fusion,* vol. 55, p. 025013, 2013.

[154] J. Heikkinen and S. Sipilä, *Phys. Plasmas,* vol. 2, p. 3724, 1995.

[155] K. Tani, M. Azumi and H. Kishimoto et al., *J. Phys. Soc. Japan,* vol. 50, p. 1726, 1981.

[156] D. Spong, S. Hirshman and W. J.C., *Plasma Phys. Rep. ,* vol. 23, p. 483, 1997.

[157] G. J. Kramer, A. McLean and N. Brooks et al., *Nucl. Fusion,* vol. 53, p. 123018, 2013.

[158] D. Spong, *Phys. Plasmas,* vol. 18, p. 056109, 2011.

[159] W. Cooper, J. Graves and O. Sauter, *Plasma Phys. Control. Fusion,* vol. 53, p. 024002, 2011.

[160] Y. Luo, W. Heidbrink, K. Burrell and et.al., *Phys. Plasmas,* vol. 14, p. 112503, 2007.

[161] R. Budny, *Nucl. Fusion,* vol. 34, p. 1247, 1994.

[162] S. Medley, R. V. Budny and D. Mansfield, *Plasma Phys. Control. Fusion,* vol. 38, p. 1779, 1996.

[163] A. Korotkov, A. Gondhalekar and R. Akers, *Phys. Plasmas,* vol. 7, p. 957, 2000.

[164] S. Medley, A. Donne, R. Kaita and et.al., *Rev. Sci. Instrum,* vol. 79, p. 011101, 2008.

[165] K. McClements, R. Dendy and A. Gondhalekar, *Nucl. Fusion,* vol. 37, p. 473, 1997.

[166] D. Testa, W. G. F. Core and A. Gondhalekar, *Phys. Plasmas,* vol. 6, p. 3498, 1999.

[167] D. Testa and A. Gondhalekar, *Nucl. Fusion,* vol. 40, p. 975, 2000.

[168] S. Medley, N. Gorelenkov, R. Andre and et.al., *Nucl. Fusion,* vol. 44, p. 1158, 2004.

[169] J. Cordey, R. Goldston and D. Mikkelsen, *Nucl. Fusion,* vol. 21, p. 581, 1981.

[170] J. D. Gaffey Jr., *J. Plasma Phys.,* vol. 16, p. 149, 1976.

[171] V. G. Kiptily, C. P. Perez von Thun and S. D. Pinches et al., *Nucl. Fusion,* vol. 49, p. 065030,

2009.

[172] K. G. McClements, M. P. Gryaznevich and S. E. Sharapov et al., *Plasma Phys. Control. Fusion,* vol. 41, p. 661, 1999.

[173] M. R. Tournianski, R. J. Akers and P. G. Carolan et al., *Plasma Phys. Control. Fusion,* vol. 47, p. 671, 2005.

[174] S. Medley, Y. Kolesnichenko, Y. Yakovenko and et.al., *Nucl. Fusion,* vol. 52, p. 013014, 2012.

[175] G. Federici, *Phys. Scripta,* vol. T124, p. 1, 2006.

[176] T. Evans, M. Fenstermacher, R. Moyer and et.al., *Nucl. Fusion,* vol. 48, p. 024002, 2008.

[177] O. Asunta, S. Akaslompolo, T. Kurki-Suonio and et.al., *Nucl. Fusion,* vol. 52, p. 094014, 2012.

[178] K. Tani, K. Shinohara, T. Oikawa and et.al., *Nucl. Fusion,* vol. 52, p. 013012, 2012.

[179] J. Kim, J. Kim, S. Yoon and et.al., *Rev. Sci. Instrum.,* vol. 83, p. 10D305, 2012.

[180] M. Garcia-Munoz, S. Akaslompolo and O. Asunta et al., *Nucl. Fusion,* vol. 53, p. 123008, 2013.

[181] J. Wesson, Tokamaks, Oxford: Clarendon Press, 1997.

[182] T. Hender, J. Wesley, J. Bialek and et.al., *Nucl. Fusion,* vol. 47, p. S128, 2007.

[183] L. Chen, R. White and M. Rosenbluth, *Phys. Rev. Lett.,* vol. 52, p. 1122, 1984.

[184] M. Bussac, R. Pellat, D. Edery and et.al., *Phys. Rev. Lett.,* vol. 35, p. 1638, 1975.

[185] C. Cheng, *Phys. Reports,* vol. 211, p. 1, 1992.

[186] C. Cheng, *J. Geophys. Res.,* vol. 96, p. 21159, 1991.

[187] I. Bernstein, E. Frieman, M. Kruskal and et.al., *Proc. Roy. Soc. A,* vol. 244, p. 17, 1958.

[188] R. Grimm, J. Greene and J. Johnson, *Meth. Comput. Phys.,* vol. 16, p. 253, 1976.

[189] S. Tsai and L. Chen, *Phys. Fluids B,* vol. 5, p. 3284, 1993.

[190] F. Porcelli, R. Stankiewicz and W. Kerner, *Phys. Plasmas,* vol. 1, p. 470, 1994.

[191] N. Gorelenkov, C. Cheng and G. Fu, *Phys. Plasmas,* vol. 6, p. 2802, 1999.

[192] L. Chen, Z. Lin and R. White, *Phys. Plasmas,* vol. 8, p. 4713, 2001.

[193] G. Kramer, L. Chen, R. Fisher and et.al., *Phys. Rev. Lett.,* vol. 109, p. 035003, 2012.

[194] S. D. Pinches, V. G. Kiptily and S. E. Sharapov et al., *Nucl. Fusion,* vol. 46, p. S904, 2006.

[195] R. White, N. Gorelenkov, W. Heidbrink and et.al., *Plasma Phys. Control. Fusion,* vol. 52, p. 045012, 2010.

[196] R. White, *Commun. Nonlin. Sci. Numer. Simulat. ,* vol. 17, p. 2200, 2012.

[197] R. White and M. Chance, *Phys. Fluids,* vol. 27, p. 2455, 1984.

[198] L. Korablev, *Zh. Eksp. Teor. Fiz (transl. Sov. Phys. JETP vol.26, p. 922, 1968),* vol. 53, p. 1600, 1967.

[199] L. Korablev and L. Rudakov, *Zh. Eksp. Teor. Fiz (transl. Sov. Phys. JETP, vol. 27, p. 499, 1968),* vol. 54, p. 818, 1968.

[200] Y. I. Kolesnichenko and N. N. Oraevskii, *Atomnaya Energiya (transl. Sov. Atomic Energy, vol. 23, p. 1028, 1967),* vol. 23, p. 289, 1967.

[201] V. S. Belikov, Y. I. Kolesnichenko and V. N. Oraevskii, *Zh. Eksp. Teor. Fiz. (transl. Sov. Phys. JETP, vol. 28, p. 1172, 1969),* vol. 55, p. 2210, 1968.

[202] A. Mikhailovskii, *Zh. Eksp. Teor. Fiz. (transl. Sov. Phys. JETP, vol. 41, p. 890, 1975),* vol. 68, p. 1772, 1975.

[203] M. Rosenbluth and P. Rutherford, *Phys. Rev. Lett.,* vol. 34, p. 1428, 1975.

[204] C. Cheng and M. Chance, *Phys. Fluids,* vol. 29, p. 3695, 1986.

[205] N. Gorelenkov, H. Berk, R. Budny and et.al., *Nucl. Fusion,* vol. 43, p. 594, 2003.

[206] N. N. Gorelenkov, H. L. Berk, E. Fredrickson and et.al., *Phys. Lett. A,* vol. 370/1, p. 70, 2007.

[207] N. J. Fisch, *Nucl. Fusion,* vol. 40, p. 1095, 2000.

[208] H. Berk, J. Van Dam, Z. Guo and D. Lindberg, *Phys. Fluids B,* vol. 4, p. 1806, 1992.

[209] B. Breizman, H. Berk, M. Pekker and et.al., *Phys. Plasmas,* vol. 10, p. 3649, 2003.

[210] G. Fu and H. Berk, *Phys. Plasmas,* vol. 12, p. 082505, 2005.

[211] C. Cheng, L. Chen and M. Chance, *Ann. Phys.,* vol. 21, p. 161, 1985.

[212] C. Kittel, Introduction to solid state physics, 5th ed., New York: Wiley, 1976.

[213] N. Gorelenkov, R. Berk, R. Budny and et.al., Preprint PPPL #4287;
http://w3.pppl.gov/~ngorelen/Gorelenkov_ITERstone08.pdf, 2008.

[214] M. Chu, J. Greene, L. Lao and et.al., *Phys. Fluids B,* vol. 4, p. 3713, 1992.

[215] B. Breizman, M. Pekker, S. Sharapov and et.al., *Phys. Plasmas,* vol. 12, p. 112506, 2005.

[216] H. Berk, D. Borba, B. Breizman and et.al., *Phys. Rev. Lett.,* vol. 87, p. 185002, 2001.

[217] S. Sharapov, B. Alper, H. Berk and et.al., *Phys. Plasmas,* vol. 9, p. 2027, 2002.

[218] W. Heidbrink, E. Strait, M. Chu and et.al., *Phys. Rev. Lett.,* vol. 71, p. 855, 1993.

[219] A. Turnbull, E. Strait, W. Heidbrink and et.al., *Phys. Fluids B,* vol. 5, p. 2546, 1993.

[220] S. Mahajan, *Phys. Fluids,* vol. 27, p. 2238, 1984.

[221] R. Betti and J. Freidberg, *Phys. Fluids B,* vol. 3, p. 1865, 1991.

[222] R. Betti and J. Freidberg, *Phys. Fluids,* vol. 4, p. 1465, 1992.

[223] G. Kramer, M. Saigusa, T. Ozeki and et.al., *Phys. Rev. Lett.,* vol. 80, p. 2594, 1998.

[224] S. Mahajan, D. Ross, G. Chen and et.al., *Phys. Fluids,* vol. 26, p. 2195, 1983.

[225] S. Mahajan and D. Ross, *Phys. Fluids,* vol. 26, p. 2561, 1983.

[226] N. Gorelenkov, *Phys. Rev. Lett.,* vol. 95, p. 265003, 2005.

[227] C. Cheng, *J. Korean Phys. Soc. (Proc. Suppl.),* vol. 31, p. S128, 1997.

[228] G. Fu, *Phys. Plasmas,* vol. 2, p. 1029, 1995.

[229] H. Berk, J. Van Dam, D. Borba and et.al., *Phys. Plasmas,* vol. 2, p. 3401, 1995.

[230] G. Fu, C. Cheng, R. Budny and et.al., *Phys. Rev. Lett.,* vol. 75, p. 2336, 1995.

[231] J. Candy, B. Breizman, J. Van Dam and et.al., *Phys. Lett A,* vol. 215, p. 299, 1996.

[232] G. Kramer, S. Sharapov, R. Nazikian and et.al., *Phys. Rev. Lett.,* vol. 92, p. 015001, 2004.

[233] S. Bernabei, M. Bell, R. Budny and et.al., *Phys. Rev. Lett.,* vol. 84, p. 1212, 2000.

[234] S. Bernabei, R. Budny, E. Fredrickson and et.al., *Nucl. Fusion,* vol. 41, p. 513, 2001.

[235] P. Sandquist, S. Sharapov, M. Lisak and et.al., *Phys. Plasmas,* vol. 14, p. 122506, 2007.

[236] F. Zonca and L. Chen, *Phys. Plasmas,* vol. 3, p. 323, 1996.

[237] N. N. Gorelenkov and C. Z. Cheng, *Phys. Plasmas,* vol. 5, p. 3389, 1998.

[238] F. Zonca, S. Briguglio and L. Chen et al., *Phys. Plasmas,* vol. 9, p. 4939, 2002.

[239] K. Wong, G. Schmidt, S. Batham and et.al., *Phys. Rev. Lett.,* vol. 76, p. 2286, 1996.

[240] G. Fu, C. Cheng, R. Budny and et.al., *Phys. Plasmas,* vol. 3, p. 4036, 1996.

[241] D. A. Spong, C. L. Hedrick and B. A. Carreras, *Nucl. Fusion,* vol. 35, p. 1687, 1995.

[242] M. Takechi, M. Ishikawa, A. Fukuyama and et.al., *Phys. Plasmas,* vol. 12, p. 082509, 2005.

[243] R. Nazikian, Kramer, G.J., C. Cheng and et.al., *Phys. Rev. Lett.,* vol. 91, p. 125003, 2003.

[244] D. Borba, H. Berk, B. Breizman and et.al., *Nucl. Fusion,* vol. 42, p. 1029, 2002.

[245] Y. Todo, H. Berk and B. Breizman, *Phys. Plasmas,* vol. 10, p. 2888, 2003.

[246] Y. Todo, H. Berk and B. Breizman, *Nucl. Fusion,* vol. 52, p. 094018, 2012.

[247] S. Sharapov, D. Borba, A. Fasoli and et.al., *Nucl. Fusion,* vol. 39, p. 373, 1999.

[248] K. Toi, M. Takechi, M. Isobe and et.al., *Nucl. Fusion,* vol. 40, p. 1349, 2000.

[249] S. Yamamoto, K. Toi, S. Ohdachi and et.al., *Nucl. Fusion,* vol. 45, p. 326, 2005.

[250] A. Weller, M. Anton, J. Geiger and et.al., *Phys. Plasmas,* vol. 8, p. 931, 2001.

[251] M. Takechi, K. Toi, S. Takagi and et.al., *Phys. Rev. Lett.,* vol. 83, p. 312, 1999.

[252] Y. I. Kolesnichenko, S. Yamamoto and K. Yamazaki et al., *Phys. Plasmas,* vol. 11, p. 158, 2004.

[253] M. Maraschek, S. Gunter and T. Kass et al., *Phys. Rev. Lett.,* vol. 79, p. 4186, 1997.

[254] J. Goedbloed, *Phys. Fluids,* vol. 18, p. 1258, 1975.

[255] K. Appert, R. Gruber, F. Troyon and J. Vaclavik, *Plasma Phys. ,* vol. 24, p. 1147, 1982.

[256] A. de Cambrier, A. Cheetham, A. Heym and et.al., "Proc. the 3rd Joint Varenna-Grenoble Intern. Symposium," Euroatom, Brussels, 1982, p.161.

[257] A. de Cambrier, A. Cheetham, A. Heym and et.al., *Plasma Phys.,* vol. 893, p. 165004, 1982.

[258] B. Kuvshinov and A. Mikhailovskii, *Sov. J. Plasma Phys.,* vol. 18, p. 495, 1992.

[259] N. Gorelenkov, E. Fredrickson, E. Belova and et.al., *Nucl. Fusion,* vol. 43, p. 228, 2003.

[260] K. Toi, S. Yamamoto, N. Nakajima and et.al., *Plasma Phys. Control. Fusion,* vol. 46, p. S1, 2004.

[261] Y. Kolesnichenko, Y. Yakovenko, A. Weller and et.al., *Phys. Rev. Lett.,* vol. 94, p. 165004, 2005.

[262] S. Yamamoto et al., 2012 Proc. 24th Int. Conf. on Fusion Energy (San Diego, 2012) [EX/5-2] http://www-naweb.iaea.org/napc/physics/FEC/FEC2012/index.htm.

[263] D. Spong, E. Azevedo, Y. Todo and et.al., *Phys. Plasmas,* vol. 17, p. 022106, 2010.

[264] L. Villard and J. Vaclavik, *Nucl. Fusion,* vol. 37, p. 351, 1997.

[265] Z. Chang, E. D. Fredrickson and S. J. Zweben et al., *Nucl. Fusion,* vol. 35, p. 1469, 1995.

[266] A. Fasoli, J. B. Lister and S. E. Sharapov et al., *Nucl. Fusion,* vol. 35, p. 1485, 1995.

[267] K. McClements, L. C. Appel, M. J. Hole and et.al., *Nucl. Fusion,* vol. 42, p. 1155, 2002.

[268] S. Sharapov, D. Testa, B. Alper and et.al., *Phys. Lett. A,* vol. 289, p. 127, 2001.

[269] S. Sharapov, A. Mikhailovskii and G. Huysmans, *Phys. Plasmas,* vol. 11, p. 2286, 2004.

[270] H. Kimura, S. Moriyama, M. Saigusa and et.al., in *Proc. 16th Intern. Conf. Plasma Phys. and Controll. Nuclear Fusion Res.*, Montreal, IAEA-F1-CN-64/E-6, 1996.

[271] Y. Kusama, H. Kimura, T. Ozeki and et.al., *Nucl. Fusion,* vol. 38, p. 1215, 1998.

[272] Y. Fukuyama and E. Yokota, in *Proc. 6th IAEA Techn. Comm. Meeting Energetic Particles in Magn. Conf. Systems*, Naka, JAERI, p.61, 1999.

[273] G. Kramer, N. Gorelenkov, R. Nazikian and C. Cheng, *Plasma Phys. Control. Fusion,* vol. 46, p. L23, 2004.

[274] G. Fu and H. Berk, *Phys. Plasmas,* vol. 13, p. 052502, 2006.

[275] N. Gorelenkov, G. Kramer and R. Nazikian, *Plasma Phys. Control. Fusion,* vol. 48, p. 1255, 2006.

[276] M. A. Van Zeeland, G. J. Kramer and M. E. Austin et al., *Phys. Rev. Lett.,* vol. 97, p. 135001, 2006.

[277] M. Van Zeeland, M. Austin, N. Gorelenkov and et.al., *Phys. Plasmas,* vol. 14, p. 056102, 2007.

[278] E. Fredrickson, N. Crocker, N. Gorelenkov and et.al., *Phys. Plasmas,* vol. 14, p. 102510, 2007.

[279] M. A. Van Zeeland, W. W. Heidbrink and R. Nazikian et al., *Plasma Phys. Control. Fusion,*

vol. 50, p. 035009, 2008.

[280] N. Crocker, E. Fredrickson, N. Gorelenkov and et.al., *Phys. Plasmas,* vol. 15, p. 102502, 2008.

[281] B. N. Breizman, in *Theory of Fusion Plasmas, AIP Conf. Proc. No. 871 (AIP, New York, 2006).*

[282] R. Nazikian, H. Berk, R. Budny and et.al., *Phys. Rev. Lett.,* vol. 96, p. 105006, 2006.

[283] I. Classen, J. Boom, W. Suttrop and et.al., *Rev. Sci. Instrum.,* vol. 81, p. 10D929, 2010.

[284] M. Gryaznevich, S. Sharapov, M. Lilley and et.al., *Nucl. Fusion,* vol. 48, p. 084003, 2008.

[285] S. Konovalov, A. Mikhailovskii, M. Shirokov and et.al., *Phys. Plasmas,* vol. 11, p. 4531, 2004.

[286] N. Gorelenkov, *Phys. Plasmas,* vol. 14, p. 110701, 2008.

[287] N. Gorelenkov, G. Kramer and R. Nazikian, *Phys. Plasmas,* vol. 18, p. 102503, 2011.

[288] L. Yu, G. Fu and Z. Sheng, *Phys. Plasmas,* vol. 16, p. 072505, 2009.

[289] I. Abel, B. Breizman and S. Sharapov, *Phys. Plasmas,* vol. 16, p. 102506, 2009.

[290] V. Marchenko, *Phys. Plasmas,* vol. 18, p. 040701, 2011.

[291] J. Haverkort, *Plasma Phys. Control. Fusion,* vol. 54, p. 025005, 2012.

[292] W. W. Heidbrink, M. E. Austin and D. A. Spong et al., *Phys. Plasmas,* vol. 20, p. 082504, 2013.

[293] A. Timofeev, Reviews of Plasma Physics, M. Leontovich, Ed., vol. 9, p. 265.: Consultants Bureau, New York, 1986.

[294] A. Hasegawa and L. Chen, *Phys. Rev. Lett.,* vol. 35, p. 370, 1975.

[295] W. Heidbrink, N. Gorelenkov, Y. Luo and et.al., *Phys. Rev. Lett.,* vol. 99, p. 245002, 2007.

[296] D. Spong, B. Carreras and C. Hedrick, *Phys. Fluids B,* vol. 4, p. 3316, 1992.

[297] P. Lauber, I. Classen, D. Curran and et.al., *Nucl. Fusion,* vol. 52, p. 094007, 2012.

[298] N. Nakajima, *Phys. Plasmas,* vol. 3, p. 4545, 1996.

[299] N. Nakajima, *Phys. Plasmas,* vol. 3, p. 4556, 1996.

[300] Y. Yakovenko, A. Weller, A. Werner and et.al., *Plasma Phys. Control. Fusion,* vol. 49, p. 535, 2007.

[301] C. Schwab, *Phys. Fluids B,* vol. 5, p. 3195, 1993.

[302] N. Nakajima, C. Cheng and M. Okamoto, *Phys. Fluids B,* vol. 4, p. 1115, 1992.

[303] Y. Kolesnichenko, V. Lutsenko, H. Wobig and et.al., *Phys. Plasmas,* vol. 8, p. 491, 2001.

[304] D. Spong, R. Sanchez and W. A., *Phys. Plasmas,* vol. 10, p. 3217, 2003.

[305] S. Yamamoto, K. Toi, N. Nakajima and et.al., *Phys. Rev. Lett.,* vol. 91, p. 245001, 2003.

[306] Y. Kolesnichenko, V. Lutsenko, V. Marchenko and et.al., *Fuson Sci. Technol,* vol. 46, p. 54, 2004.

[307] A. Fasoli, J. Lister, S. Sharapov and et.al., *Phys. Rev. Lett.,* vol. 76, p. 1067, 1996.

[308] H. Berk, R. Mett and D. Lindberg, *Phys. Fluids B,* vol. 5, p. 3969, 1993.

[309] J. Candy and M. Rosenbluth, *Phys. Plasmas,* vol. 1, p. 356, 1994.

[310] N. Gorelenkov, *Plasma Phys. Rep.,* vol. 21, p. 451, 1995.

[311] P. Lauber and S. Gunter, *Nucl. Fusion,* vol. 48, p. 084002, 2008.

[312] R. R. Mett and S. M. Mahajan, *Phys. Fluids B,* vol. 4, p. 2885, 1992.

[313] F. Zonca and L. Chen, *Phys. Rev. Lett.,* vol. 68, p. 592, 1992.

[314] M. Rosenbluth, H. Berk, J. Van Dam and et.al., *Phys. Rev. Lett.,* vol. 68, p. 596, 1992.

[315] F. Zonca, *Plasma Phys. Control. Fusion,* vol. 35, p. B307, 1993.

[316] A. Fasoli, D. Borba and G. Bosia et al., *Phys. Rev. Lett.*, vol. 75, p. 645, 1995.

[317] D. Testa and A. Fasoli, *Nucl. Fusion,* vol. 41, p. 809, 2001.

[318] D. Testa, C. Boswell and A. Fasoli et al., *Nucl. Fusion,* vol. 45, p. 907, 2005.

[319] J. A. Snipes, D. Schmittdiel and A. Fasoli et al., *Plasma Phys. Control. Fusion,* vol. 46, p. 611, 2004.

[320] D. Testa et al., "The new Alfven wave active excitation system at JET," in *Proc. 23rd Symp. on Fusioin Technology (SOFT), (Venice, Italy, September 2004) http://infoscience.epfl.ch/record/143354/files*.

[321] D. Testa, N. Mellet and T. Panis et al., *Nucl. Fusion,* vol. 50, p. 084010, 2010.

[322] A. Fasoli, D. Testa and T. Panis et al., *Plasma Phys. Control, Fusion,* vol. 52, p. 075015, 2010.

[323] G. Matsunaga, K. Toi and S. Kawada et al., *Phys. Rev. Lett.*, vol. 94, p. 225005, 2005.

[324] T. Ito, K. Toi and G. Matsunaga et al., *Phys. Plasmas,* vol. 16, p. 092105, 2009.

[325] B. Coppi, S. Cowley, R. Kulsrud and et.al., *Phys. Fluids,* vol. 29, p. 4060, 1986.

[326] N. Gorelenkov and C. Cheng, *Nucl. Fusion,* vol. 35, p. 1743, 1995.

[327] Y. Kolesnichenko, T. Fulop, M. Lisak and et.al., *Nucl. Fusion,* vol. 38, p. 1871, 1998.

[328] T. Fulop, M. Lisak, Y. Kolesnichenko and et.al., *Phys. Plasmas,* vol. 7, p. 1479, 2000.

[329] B. Coppi, G. Penn and C. Riconda, *Ann. Phys.*, vol. 261, p. 117, 1997.

[330] G. Penn, C. Riconda and F. Rubini, *Phys. Plasmas,* vol. 5, p. 2513, 1998.

[331] T. Hellsten and M. Laxaback, *Phys. Plasmas,* vol. 10, p. 4371, 2003.

[332] N. Gorelenkov, E. Fredrickson, W. Heidbrink and et.al., *Nucl. Fusion,* vol. 46, p. S933, 2006.

[333] H. Smith and E. Verwichte, *Plasma Phys. Control. Fusion,* vol. 51, p. 075001, 2009.

[334] E. Belova et al., 2012 Proc. 24th Int. Conf. on Fusion Energy (San Diego, 2012), TH/P6-16 and http://www-naweb.iaea.org/napc/physics/FEC/FEC2012/index.htm.

[335] E. Fredrickson, N. Gorelenkov, C. Cheng and et.al., *Phys. Rev. Lett.*, vol. 87, p. 145001, 2001.

[336] E. Fredrickson, R. Bell, D. Darrow and et.al., *Phys. Plasmas,* vol. 13, p. 056109, 2006.

[337] E. Fredrickson, N. Crocker, R. Bell and et.al., *Phys. Plasmas,* vol. 16, p. 122505, 2009.

[338] L. Appel, T. Fulop, M. Hole and et.al., *Plasma Phys. Control. Fusion,* vol. 50, p. 115011, 2008.

[339] E. Fredrickson, N. Gorelenkov, E. Belova and et.al., *Nucl. Fusion,* vol. 52, p. 043001, 2012.

[340] W. Heidbrink, E. Fredrickson, N. Gorelenkov and et.al., *Nucl. Fusion,* vol. 46, p. 324, 2006.

[341] G. Cottrell, V. Bhatnagar, O. Da Costa and et.al., *Nucl. Fusion,* vol. 33, p. 1365, 1993.

[342] N. A. Crocker, E. D. Fredrickson and N. N. Gorelenkov et al., *Nucl. Fusion,* vol. 53, p. 043017, 2013.

[343] K. G. McClements, C. Hunt and R. O. Dendy et al., *Phys. Rev. Lett.,* vol. 82, p. 2099, 1999.

[344] G. Greene, in *Control. Fusion Plasma Heating (Proc. 17th Eur. Conf. Amsterdam, 1990), vol. 14B, Part IV, EPS, Geneva (1990), p. 1540.*.

[345] G. A. Cottrell, *Phys. Rev. Lett.,* vol. 84, p. 2397, 2000.

[346] H. Kimura, Y. Kusama and M. Saegusa et al., *Nucl. Fusion,* vol. 38, p. 1303, 1998.

[347] M. Ichimura, H. Higaki and S. Kakimoto et al., *Nucl. Fusion,* vol. 48, p. 035012, 2008.

[348] K. Saito, H. Kasahara, T. Seki and et.al., *Fusion Eng. Des.,* vol. 84, p. 1676, 2009.

[349] K. Saito, R. Kumazawa, T. Seki and et.al., *Plasma Sci. Technol.,* vol. 15, p. 209, 2013.

[350] R. Dendy and et.al., *Nucl. Fusion,* vol. 35, p. 1733, 1995.

[351] Y. Kolesnichenko et al., in Fusion Energy 1996 (Proc. 16th Int. Conf. Montreal, 1996), Vol. 2, p. 487, IAEA, Vienna (1997)..

[352] T. Fulop, Y. Kolesnichenko, M. Lisak and et.al., *Nucl. Fusion,* vol. 37, p. 1281, 1997.

[353] S. Cauffman, R. Majeski, K. McClements and et.al., *Nucl. Fusion,* vol. 35, p. 1597, 1995.

[354] K. McClements, R. Dendy, C. Lashmore-Davies and et.al., *Phys. Plasmas,* vol. 3, p. 543, 1996.

[355] N. Gorelenkov and C. Cheng, *Phys. Plasmas,* vol. 2, p. 1961, 1995.

[356] V. Belikov, Y. Kolesnichenko and O. Silivra, *Nucl. Fusion,* vol. 35, p. 1603, 1995.

[357] T. Fulop and M. Lisak, *Nucl. Fusion,* vol. 38, p. 761, 1998.

[358] Y. Kolesnichenko, M. Lisak and D. Anderson, *Nucl. Fusion,* vol. 40, p. 1419, 2000.

[359] N. Gorelenkov, N. Fisch and E. Fredrickson, *Plasma Phys. Control. Fusion,* vol. 52, p. 055014, 2010.

[360] D. Gates, N. Gorelenkov and R. White, *Phys. Rev. Lett.,* vol. 87, p. 205003, 2001.

[361] J. Goedbloed, *Phys. Plasmas,* vol. 5, p. 3143, 1998.

[362] B. van der Holst, A. Belien and J. Goedbloed, *Phys. Plasmas,* vol. 7, p. 4208, 2000.

[363] G. Huysmans, W. Kerner, D. Borba and et.al., *Phys. Plasmas,* vol. 2, p. 1605, 1995.

[364] N. Gorelenkov, H. Berk and E. Fredrickson, *Bull. Am. Soc.,* vol. 51, p. 183, 2006.

[365] Y. Kolesnichenko, V. Lutsenko, A. Weller and et.al., *Phys. Plasmas,* vol. 14, p. 102504, 2007.

[366] P. Lauber, M. Brudgam, D. Currant and et.al., *Plasma Phys. Control. Fusion,* vol. 51, p. 124009, 2009.

[367] D. Spong, B. Breizman, D. Brower and et.al., *Contrib. Plasma Phys. ,* vol. 50, p. 708, 2010.

[368] D. K. A. Eremin, *Phys. Plasmas,* vol. 17, p. 012108, 2010.

[369] A. Konies and D. Eremin, *Phys. Plasmas,* vol. 17, p. 012107, 2010.

[370] D. Curran, P. Lauber, P. Mc Carthy and et.al., *Plasma Phys. Control. Fusion,* vol. 54, p. 055001, 2012.

[371] N. N. Gorelenkov, H. L. Berk and N. A. Crocker et al., *Plasma Phys. Control. Fusion,* vol. 49, p. B371, 2007.

[372] N. N. Gorelenkov, M. A. Van Zeeland, H. L. Berk and et.al., *Phys. Plasmas,* vol. 16, p. 056107, 2009.

[373] L. Yi, I. Mitsutaka, P. Xiao-Dong and et.al., *Nucl. Fusion,* vol. 52, p. 074008, 2012.

[374] J. Bertram, B. Blackwell, M. Hole and et.al., *Plasma Phys. Control. Fusion,* vol. 54, p. 055009, 2012.

[375] A. B. Mikhailovskii, *Nucl. Fusion,* vol. 13, p. 259, 1973.

[376] F. Zonca, L. Chen and R. A. Santoro, *Plasma Phys. Control. Fusion,* vol. 38, p. 2011, 1996.

[377] A. B. Mikhailovskii and S. E. Sharapov, *Plasma Phys. Rep.,* vol. 25, p. 838, 1999.

[378] I. Chavdarovski and F. Zonca, *Plasma Phys. Control. Fusion,* vol. 51, p. 115001, 2009.

[379] A. I. Smolyakov, C. Nguyen and X. Garbet, *Nucl. Fusion,* vol. 50, p. 054002, 2010.

[380] F. Zonca, L. Chen and J. Q. Dong et al., *Phys. Plasmas,* vol. 6, p. 1917, 1999.

[381] H. S. Zhang, Z. Lin and I. Holod et al., *Phys. Plasmas,* vol. 17, p. 112505, 2010.

[382] K. Wong, M. Chu, T. Luce and et.al., *Phys. Rev. Lett.,* vol. 85, p. 996, 2000.

[383] R. Cesario, L. Panaccione, A. Botruguo and et.al., *Nucl. Fusion,* vol. 49, p. 075034, 2009.

[384] L. Yan, J. Dong, X. Ding and et.al., *Chin. Phys. Lett.,* vol. 18, p. 1227, 2001.

[385] W. Chen, X. Ding, Y. Liu and et.al., *Nucl. Fusion,* vol. 50, p. 084008, 2010.

[386] Z. Guimaraes-Filho, D. Elbeze, R. Sabot and et.al., *Plasma Phys. Control. Fusion,* vol. 53, p.

074012, 2011.

[387] Y. Sun, B. Wan, S. Wang and et.al., *Phys. Plasmas,* vol. 12, p. 092507, 2005.

[388] Z. Wang, Y. Long, A. Wang and et.al., *Nucl. Fusion,* vol. 47, p. 1307, 2007.

[389] F. Zonca, P. Buratti, A. Cardinali and et.al., *Nucl. Fusion,* vol. 47, p. 1588, 2007.

[390] S. Chen, Z. Wang, C. Tang and et.al., *Chin. Phys. Lett.,* vol. 29, p. 025203, 2012.

[391] A. Merle, "Stability and properties of electron-driven fishbones in tokamaks", Ph.D. Thesis, Ecole Polytechnique, 2012.

[392] L. Delgado-Aparicio, L. Sugiyama and S. Shiraiwa et al., "Destabilization of internal kink by suprathermal electron pressure," *Phys. Rev. Lett.,* 2014 (submitted).

[393] B. Coppi and F. Porcelli, *Phys. Rev. Lett.,* vol. 57, p. 2272, 1986.

[394] M. Isobe, K. Toi, Y. Yoshimura and et.al., *Nucl. Fusion,* vol. 50, p. 084007, 2010.

[395] C. Deng, D. Brower, B. Breizman and et.al., *Phys. Rev. Lett.,* vol. 103, p. 025003, 2009.

[396] R. Heeter, "Alfven eigenmode and ion Bernstein wave studies for controlling fusion alpha-particles", PhD Thesis, Princeton University, 1999.

[397] A. Figueiredo and M. Nave, *IEEE Trans. Plasma Sci.,* vol. 33, p. 468, 2005.

[398] C. Boswell, H. Berk, D. Borba and et.al., *Phys. Lett. A,* vol. 358, p. 154, 2006.

[399] H. Berk, C. Boswell, D. Borba and et.al., *Nucl. Fusion,* vol. 46, p. S888, 2006.

[400] R. Nazikian, G. Fu, M. Austin and et.al., *Phys. Rev. Lett.,* vol. 101, p. 185001, 2008.

[401] R. Fisher, D. Pace, G. Kramer and et.al., *Nucl. Fusion,* vol. 52, p. 123015, 2012.

[402] T. Ido, A. Shimizu and M. Nishiura, *Nucl. Fusion,* vol. 51, p. 073046, 2011.

[403] K. Toi, *Plasma Fusion Res.,* vol. 8, p. 1102002, 2013.

[404] G. Fu, *Phys. Rev. Lett.,* vol. 101, p. 185002, 2008.

[405] H. Berk and T. Zhou, *Nucl. Fuison,* vol. 50, p. 035007, 2010.

[406] H. Wang and Y. Todo, *Phys. Plasmas,* vol. 20, p. 012506, 2013.

[407] M. Osakabe, T. Ito and K. Ogawa et al., "Effect of Energetic Particle Induced n=0 Instabilities on Buld Ions in LHD," in *12th IAEA TM on Energetic Particles in Magnetic Confinement Systems, 2011, Austin, USA, No. O-3..*

[408] T. Ido, M. Osakabe and A. Shimizu et al., "Potential fluctuation of energetic particle-induced geodesic acoustic mode in the Large Helical Device," in *18th International Stellarator/Heliotron Workshop, 29 Jan.-3 Feb., 2012, ANU, Canberra and Murramarang, Australia, paper No. S15-1..*

[409] K. Toi, K. Ogawa and M. Isobe et al., "Characteristics of Energetic-Ion-Driven Geodesic Acousticc Modes in the Large Helical Device," in *12th IAEA TM on Energetic Particles in Magnetic Confinement Systems, Sep. 2011, Austin, USA, No. O-4..*

[410] Z. Qiu, F. Zonca and L. Chen, *Plasma Phys. Control. Fusion,* vol. 52, p. 095003, 2010.

[411] Z. Qiu, F. Zonca and L. Chen, *Plasma Sci. Technol.,* vol. 13, p. 257, 2011.

[412] G. Fu, *J. Plasma Phys. ,* vol. 77, p. 457, 2011.

[413] D. Zarzoso, X. Garbet, Y. Sarazin and et.al., *Phys. Plasmas,* vol. 19, p. 022102, 2012.

[414] M. Sasaki, K. Itoh and S.-I. Itoh, *Plasma Phys. Control. Fusion,* vol. 53, p. 085017, 2011.

[415] F. Nabais, D. Borba and M. Mantsinen et al., *Phys. Plasmas,* vol. 12, p. 102509, 2005.

[416] F. Zonca, L. Chen and A. Botrugno et al., *Nucl. Fusion,* vol. 49, p. 085009, 2009.

[417] Y. I. Kolesnichenko, V. V. Lutsenko and R. B. White, *Nucl. Fusion,* vol. 50, p. 084017, 2010.

[418] B. Stratton, R. Fonck, G. McKee and et.al., *Nucl. Fusion,* vol. 36, p. 1586, 1996.

[419] O. Jarvis, J. Adams, P. Howarth and et.al., *Nucl. Fusion,* vol. 36, p. 1513, 1996.

[420] M. Petrov and et.al., *Bull. Am. Phys. Soc.,* vol. 40, p. 1869, 1995.

[421] M. Petrov and et.al., in *Control. Fusion Plasma Phys. (Proc. 23rd Eur. Conf. Kiev, 1996), vol. 20C, part I, EPS*, Geneva, 1996, p. 63..

[422] M. Petrov, R. Budny, H. Duong and et.al., *Nucl. Fusion,* vol. 35, p. 1437, 1995.

[423] S. Medley, R. Budny, H. Duong and et.al., *Nucl. Fusion,* vol. 38, p. 1283, 1998.

[424] S. Nielsen, H. Bindslev, M. Salewski and et.al., *Plasma Phys. Control. Fusion,* vol. 52, p. 092001, 2010.

[425] C. Muscatello, W. Heidbrink, Y. Kolesnichenko and et.al., *Plasma Phys. Control. Fusion,* vol. 54, p. 025006, 2012.

[426] Y. Kolesnichenko, V. Lutsenko, R. White and et.al., *Nucl. Fusion,* vol. 40, p. 1325, 2000.

[427] K. McGuire, V. Arunasalam, C. Barnes and et.al., *Phys. Fluids,* vol. 2, p. 1287, 1990.

[428] Y. Kolesnichenko and Y. V. Yakovenko, *Nucl. Fusion,* vol. 32, p. 449, 1992.

[429] D. Anderson, Y. I. Kolesnichenko, M. Lisak and et.al., *Nucl. Fusion,* vol. 34, p. 217, 1994.

[430] Y. Kolesnichenko and Y. Yakovenko, *Nucl. Fusion,* vol. 36, p. 159, 1996.

[431] Y. Kolesnichenko and et.al., in *Controll. Fusion Plasma Phys. (Proc. 23rd Eur. Conf., Kiev, 1996), vol. 20C, part I, EPS*, Geneva (1996) 331.

[432] N. Gorelenkov, A. Gondhalekar, A. Korotkov and et.al., *Phys. Plasmas,* vol. 10, p. 713, 2003.

[433] Y. Kolesnichenko, V. Lutsenko, R. White and et.al., *Phys. Plasmas,* vol. 5, p. 2963, 1998.

[434] Y. Kolesnichenko, V. Lutsenko, R. White and et.al., *Phys. Plasmas,* vol. 6, p. 1117, 1999.

[435] H. Bindslev, S. Nielsen, L. Porte and et.al., *Phys. Rev. Lett.,* vol. 97, p. 205005, 2006.

[436] S. Nielsen, M. Salewski, H. Bindslev and et.al., *Nucl. Fusion,* vol. 51, p. 063014, 2011.

[437] L. Chen and F. Zonca, *Nucl. Fusion,* vol. 47, p. S727, 2007.

[438] E. Fredrickson, L. Chen and R. White, *Nucl. Fusion,* vol. 43, p. 1258, 2003.

[439] R. Budny, *Nucl. Fusion,* vol. 42, p. 1383, 2002.

[440] M. Garcia-Munoz, I. Classen, B. Geiger and et.al., *Nucl. Fusion,* vol. 51, p. 103013, 2011.

[441] K. Shinohara, M. Takechi, M. Ishikawa and et.al., *Plasma Phys. Control. Fusion,* vol. 46, p. S31, 2004.

[442] M. Van Zeeland, W. Heidbrink and R. Fisher, *Phys. Plasmas,* vol. 18, p. 056114, 2011.

[443] J. A. Snipes, N. Basse and P. Bonoli et al., *Fusion Sci. Technol.,* vol. 51, p. 437, 2007.

[444] K. Shinohara, Y. Kusama, M. Takechi and et.al., *Nucl. Fusion,* vol. 41, p. 603, 2001.

[445] N. J. Fisch and J.-M. Rax, *Phys. Rev. Lett.,* vol. 69, p. 612, 1992.

[446] J. Clarke, *Nucl. Fusion,* vol. 20, p. 563, 1980.

[447] L. Zakharov, N. Gorelenkov, R. White and et.al., *Fusion Eng. Des.,* vol. 72, p. 149, 2004.

[448] N. J. Fisch and M. C. Herrmann, *Nucl. Fusion,* vol. 34, p. 1541, 1994.

[449] M. Herrmann and N. Fisch, *Phys. Rev. Lett.,* vol. 79, p. 1495, 1997.

[450] N. J. Fisch and M. C. Herrmann, *Nucl. Fusion,* vol. 35, p. 1753, 1995.

[451] N. J. Fisch, A. Fruchtman, C. F. F. Karney and e. al., *Phys. Plasmas,* vol. 2, p. 2375, 1995.

[452] E. J. Valeo and N. J. Fisch, *Phys. Rev. Lett. ,* vol. 73, p. 3536, 1994.

[453] D. Darrow, R. Majeski, N. Fisch and et.al., *Nucl. Fusion,* vol. 36, p. 509, 1996.

[454] D. Clark and N. Fisch, *Phys. Plasmas,* vol. 7, p. 2923, 2000.

[455] N. Fisch, *J. Plasma Phys.,* vol. 72, p. 627, 2010.

[456] N. J. Fisch, *Rev. Modern Phys.,* vol. 58, p. 175, 1987.

[457] K.-L. Wong and M. Ono, *Nucl. Fusion,* vol. 24, p. 615, 1984.

[458] N. J. Fisch and J.-. M. Rax, *Nucl. Fusion,* vol. 32, p. 549, 1992.

[459] N. J. Fisch, *Phys. Rev. Lett.,* vol. 97, p. 225001, 2006.

[460] A. J. Fetterman and N. J. Fisch, *Phys. Rev. Lett.,* vol. 101, p. 205003, 2008.

[461] H. Biglari and L. Chen, *Phys. Rev. Lett.,* vol. 67, p. 3681, 1991.

[462] S. Tsai and L. Chen, *Phys. Fluids B,* vol. 5, p. 3284, 1994.

[463] Z. Chang, R. Budny, L. Chen and et.al., *Phys. Rev. Lett.,* vol. 76, p. 1071, 1996.

[464] C. Cheng, N. Gorelenkov and C. Hsu, *Nucl. Fusion,* vol. 35, p. 1639, 1995.

[465] R. A. Santoro and L. Chen, *Phys. Plasmas,* vol. 3, p. 2349, 1996.

[466] A. Mikhailovskii, E. Kovalishen, S. Konovalov and et.al., *Doklady Physics,* vol. 50, p. 329, 2005.

[467] A. Mikhailovskii, E. Kovalishen, V. Tsypin and et.al., *Phys. Plasmas,* vol. 12, p. 042507, 2005.

[468] G. Matsunaga et al., 2012 Proc. 24th Int. Conf. on Fusion Energy (San Diego, 2012) EX/5-1, http://www-naweb.iaea.org/napc/physics/FEC/FEC2012/index.htm.

[469] G. Matsunaga, N. Aiba, K. Shinohara and et.al., *Phys. Rev. Lett.,* vol. 103, p. 045001, 2009.

[470] G. Matsunaga, K. Shinohara, N. Aiba and et.al.:, *Nucl. Fusion,* vol. 50, p. 084003, 2010.

[471] M. Okabayashi, I. Bogatu, M. Chance and et.al., *Nucl. Fusion,* vol. 49, p. 125003, 2009.

[472] W. Heidbrink, M. Austin, R. Fisher and et.al., *Plasma Phys. Control. Fusion,* vol. 53, p. 085028, 2011.

[473] K. McGuire, R. Goldston, M. Bell and et.al., *Phys. Rev. Lett.,* vol. 50, p. 891, 1983.

[474] M. Okabayashi, G. Matsunaga and J. deGrassie, *Phys. Plasmas,* vol. 18, p. 056112, 2012.

[475] A. Fasoli, D. Testa, S. Sharapov and et.al., *Plasma Phys. Control. Fusion,* vol. 44, p. B159, 2002.

[476] J. Goedbloed, H. Holties, S. Poedts and et.al., *Plasma Phys. Control. Fusion,* vol. 35, p. B277, 1993.

[477] E. Strait, W. Heidbrink and A. Turnbull, *Plasma Phys. Control. Fusion,* vol. 36, p. 1211, 1994.

[478] H. Holties, A. Fasoli, J. Goedbloed and et.al., *Phys. Plasmas,* vol. 4, p. 709, 1997.

[479] G. Kramer, M. Iwase, Y. Kusama and et.al., *Nucl. Fusion,* vol. 40, p. 1383, 2000.

[480] E. Edlund, M. Porkolab, G. Kramer and et.al., *Phys. Plasmas,* vol. 16, p. 056106, 2009.

[481] E. Edlund, M. Porkolab, G. Kramer and et.al., *Plasma Phys. Control. Fusion,* vol. 52, p. 115003, 2010.

[482] S. Pinches, H. Berk, M. Gryaznevich and et.al., *Plasma Phys. Control. Fusion,* vol. 46, p. S47, 2004.

[483] E. Joffrin, C. D. Challis and G. D. Conway et al., *Nucl. Fusion,* vol. 43, p. 1167, 2003.

[484] R. Dendy, C. Lashmore-Davies, G. Cottrell and et.al., *Fusion Technol.,* vol. 25, p. 334, 1994.

[485] N. Gorelenkov, S. Bernabei, C. Cheng and et.al., *Nucl. Fusion,* vol. 40, p. 1311, 2000.

[486] H. Berk, B. Breizman and N. Petviashvili, *Phys. Lett. A,* vol. 234, p. 213, 1997, errata Phys. Lett. A, vol. 238, p. 408, 1998.

[487] H. Berk, B. Breizman and M. Pekker, *Phys. Rev. Lett.,* vol. 76, p. 1256, 1996.

[488] M. Lesur, Y. Idomura and X. Garbet, *Phys. Plasmas,* vol. 16, p. 092305, 2009.

[489] A. Fasoli, B. Breizman, D. Borba and et.al., *Phys. Rev. Lett.,* vol. 81, p. 5564, 1998.

[490] I. Bernstein, J. Greene and M. Kruskal, *Phys. Rev. ,* vol. 108, p. 546, 1957.

[491] M. Osakabe, S. Yamamoto, K. Toi and et.al., *Nucl. Fusion,* vol. 46, p. S911, 2006.

[492] A. Bortolon, W. Heidbrink, G. Kramer and et.al., *Phys. Rev. Lett.,* vol. 110, p. 265008, 2013.

[493] S. Briguglio, G. Fogaccia, G. Vlad and et.al., *Phys. Plasmas,* vol. 14, p. 055904, 2007.

[494] R. Vann, R. Dendy and G. Rowlands et al., *Phys. Plasmas,* vol. 10, p. 623, 2003.

[495] M. Lilley, B. Breizman, S. Sharapov and et.al., *Phys. Plasmas,* vol. 17, p. 092305, 2010.

[496] M. Lesur and Y. Idomura, *Nucl. Fusion,* vol. 52, p. 094004, 2012.

[497] M. Lesur, Y. Idomura, K. Shinohara and et.al., *Phys. Plasmas,* vol. 17, p. 122311, 2010.

[498] S. Pinches, L. Appel, J. Candy and et.al., *Comput. Phys. Commun.,* vol. 111, p. 133, 1998.

[499] Y. Todo and T. Sato, *Phys. Plasmas,* vol. 5, p. 1321, 1998.

[500] S. Briguglio, G. Vlad, F. Zonca and et.al., *Phys. Plasmas,* vol. 2, p. 3711, 1995.

[501] D. Spong, E. Bass, W. Deng and et.al., *Phys. Plasmas,* p. 082511, 2012.

[502] Z. Lin, T. Hahm, W. Lee and et.al., *Science,* vol. 281, p. 1835, 1998.

[503] J. Candy and R. Waltz, *J. Comput. Phys. ,* vol. 186, p. 545, 2003.

[504] P. Lauber, S. Gunter, A. Konies and S. D. Pinches, *J. Comput. Phys.,* vol. 226, p. 447, 2007.

[505] A. Vedenov, Y. Velikhov and R. Sagdeyev, *Nucl. Fusion,* vol. 1, p. 82, 1961.

[506] A. Casati, C. Bourdelle, X. Garbet and et.al., *Nucl. Fusion,* vol. 49, p. 085012, 2009.

[507] H. Berk, in *MHD and Energetic Particles, 5th International Summer School*, Aix-en-provence, France, ed. S. Benkkadda, Melville, NY 2012, p. 29.

[508] H. Berk, B. Breizman and J. Fitzpatrick et al., *Nucl. Fusion,* vol. 35, p. 1661, 1995.

[509] H. Berk, B. Breizman and J. Fitzpatrick et al., *Phys. Plasmas,* vol. 3, p. 1827, 1996.

[510] N. Gorelenkov, H. Berk and R. Budny, *Nucl. Fusion,* vol. 45, p. 226, 2005.

[511] K. Ghantous, N. Gorelenkov, H. Berk and et.al., *Phys. Plasmas,* vol. 19, p. 092511, 2012.

[512] W. Heidbrink, M. Van Zeeland, M. Austin and et.al., *Nucl. Fusion,* vol. 53, p. 093006, 2013.

[513] S. Sharapov, B. Alper, H. Berk and et.al., *Nucl. Fusion,* vol. 53, p. 104022, 2013.

[514] P. Terry, M. Greenwald, J.-N. Leboeuf and et.al., *Phys. Plasmas,* vol. 15, p. 062503, 2008.

[515] E. Bass and R. Waltz, Bulletin of the American Physical Society, 2013, Denver, http://meetings.aps.org/Meeting/DPP13/Event/200657.

[516] E. Bass and R. Waltz, *Phys. Plasmas,* vol. 17, p. 112319, 2010.

[517] E. Bass and R. Waltz, *Phys. Plasmas,* vol. 20, p. 012508, 2013.

[518] H. Berk and B. Breizman, "Overview of Nonlinear Theory of Kinetically Driven Instabilities", preprint IFSR, #841, 1998.

[519] J. Zalesny, G. Galant, M. Lisak and et.al., *Phys. Plasmas,* vol. 18, p. 062109, 2011.

[520] N. Crocker, W. Peebles, S. Kubota and et.al., *Phys. Rev. Lett.,* vol. 97, p. 045002, 2006.

[521] K. Ogawa, M. Isobe and K. Toi et al., *Nucl. Fusion,* vol. 52, p. 094013, 2012.

[522] K. Ogawa, M. Isobe, K. Toi and et.al., *Nucl. Fusion,* vol. 53, p. 053012, 2013.

[523] S. P. Hirshman and O. Betancourt, *J. Comput. Phys.,* vol. 96, p. 99, 1991.

[524] H. Berk, B. Breizman and M. Pekker, *Phys. Plasmas,* vol. 2, p. 3007, 1995.

[525] M. Schneller, P. Lauber and M. Brüdgam et al., *Nucl. Fusion,* vol. 52, p. 103019, 2012.

[526] E. Fredrickson, N. Gorelenkov, R. Bell and et.al., *Nucl. Fusion,* vol. 46, p. S926, 2006.

[527] M. Podesta, W. Heidbrink and e. D. Liu, *Phys. Plasmas,* vol. 16, p. 056104, 2009.

[528] E. Fredrickson, N. Crocker, D. Darrow and et.al., *Nucl. Fusion,* vol. 53, p. 013006, 2013.

[529] E. Fredrickson et al., "Fast-ion energy loss during TAE avalanches in the National Spherical Torus Experiment," Proc. 13th IAEA TM on Energetic Particles in Magnetic Conf. Systems, 2013, Beijing, submitted to Nucl. Fusion.

[530] M. Pueschel, in *MHD and Energetic Particles, 5th ITER International Summer School*, Aix-en-provence, France, Ed. S. Benkkadda, Melville, NY 2012, p. 23.

[531] R. Ganesh, in *MHD and Energetic Particles, 5th ITER International Summer School*, Aix-en-provence, France, Ed. S. Benkkadda, Melville, NY 2012, p. 91.

[532] R. Basu, T. Jessen, V. Naulin and et.al., *Phys. Plasmas,* vol. 10, p. 2696, 2003.

[533] G. Manfredi and R. Dendy, *Phys. Plasmas,* vol. 4, p. 628, 1997.

[534] S. Gunter, G. Conway, S. daGraca and et.al., *Nucl. Fusion,* vol. 47, p. 920, 2007.

[535] T. Dannert, S. Gunter, T. Hauff and et.al., *Phys. Plasmas,* vol. 15, p. 062508, 2008.

[536] W. Heidbrink, J. Park, M. Murakami and et.al., *Phys. Rev. Lett.,* vol. 103, p. 175001, 2009.

[537] D. Pace, M. Austin, E. Bass and et.al., *Phys. Plasmas,* vol. 20, p. 056108, 2013.

[538] C. Angioni, A. Peters, G. Pereverzev and et.al., *Nucl. Fusion,* vol. 49, p. 055013, 2009.

[539] C. Estrada-Mila, J. Candy and R. Waltz, *Phys. Plasmas,* vol. 13, p. 112303, 2006.

[540] T. Hauff, M. Pueschel, T. Dannert and et.al., *Phys. Rev. Lett.,* vol. 102, p. 075004, 2009.

[541] W. Zhang, V. Decyk, I. Holod and et.al., *Phys. Plasmas,* vol. 17, p. 055902, 2010.

[542] W. Zhang, Z. Lin and L. Chen, *Phys. Rev. Lett.,* vol. 107, p. 239501, 2011.

[543] F. Jenko, T. Hauff, M. Pueschel and et.al., *Phys. Rev. Lett. ,* vol. 107, p. 239502, 2011.

[544] M. Albergante, A. Fasoli, J. Graves and et.al., *Nucl. Fusion,* vol. 52, p. 094016, 2012.

[545] J. Lang and G. Fu, *Phys. Plasmas,* vol. 18, p. 055902, 2011.

[546] G. Staebler, J. Kinsey and R. Waltz, *Phys. Plasmas,* vol. 14, p. 055909, 2007.

[547] G. Staebler, J. Kinsey and R. Waltz, *Phys. Plasmas,* vol. 15, p. 055908, 2008.

[548] R. Waltz, E. Bass and G. Staebler, *Phys. Plasmas,* vol. 20, p. 042510, 2013.

[549] K. Wong, R. Budny, R. Nazikian and et.al., *Phys. Rev. Lett. ,* vol. 93, p. 085002, 2004.

[550] S. Sharapov, B. Alper, Y. Baranov and et.al., *Nucl. Fusion,* vol. 46, p. S868, 2006.

[551] D. Stutman, L. Delgado-Aparicio, N. Gorelenkov and et.al., *Phys. Rev. Lett.,* vol. 102, p. 115002, 2009.

[552] N. Gorelenkov, D. Stutman, K. Tritz and et.al., *Nucl. Fusion,* vol. 50, p. 084012, 2010.

[553] Y. Kolesnichenko, Y. V. Yakovenko and V. Lutsenko, *Phys. Rev. Lett.,* vol. 104, p. 075001, 2010.

[554] E. Belova, N. Gorelenkov, N. Crocker and et.al., *Bull. Amer. Phys. Soc. (abstract PP8.22), http://meetings.aps.org/link/BAPS.2012.DPP.PP8.22.*

[555] N. Crocker, W. Peebles, S. Kubota and et.al., *Plasma Phys. Control. Fusion,* vol. 53, p. 105001, 2011.

[556] K. Tritz, D. Stutman, M. Finkenthal and et.al., *Bull. Amer. Phys. Soc. (abstract PP6.4), http://meetings.aps.org/link/BAPS.2012.DPP.GO6.4.*

[557] J. Menard, R. Bell, D. Gates and et.al., *Phys. Rev. Lett.,* vol. 97, p. 095002, 2006.

[558] S. Gunter et al., in Fusion Energy 2006 (Proc. 21st Int. Conf., Chengdu, 2006) (Vienna: IAEA) CD-ROM file EX6-1 and http://www-naweb.iaea.org/napc/physics/FEC/FEC2006/html/index.htm.

[559] A. Dimits, B. Cohen, W. Nevins and et.al., *Nucl. Fusion,* vol. 41, p. 1725, 2001.

[560] G. Fu and C. Cheng, *Phys. Fluids B,* vol. 4, p. 3722, 1992.

[561] B. Breizman and S. Sharapov, *Plasma Phys. Control. Fusion,* vol. 37, p. 1057, 1995.

[562] S. Gunter et al., in Fusion Energy 2010 (Proc. 23rd Int. Conf. Daejeon, 2010) (Vienna: IAEA) CD-ROM file THW/P7-08 and http://www-naweb.iaea.org/napc/physics/FEC/FEC2010/index.htm.

[563] A. Konies et al., 2012 Proc. 24th Int. Conf. on Fusion Energy (San Diego, 2012) ITR/P1-34 and http://www-naweb.iaea.org/napc/physics/FEC/FEC2012/index.htm.

[564] G. Huysmans, J. Goedbloed and W. Kerner, *Phys. Fluids B,* vol. 5, p. 1545, 1993.

[565] P. Popovich, W. Cooper and L. Villard, *Comput. Phys. Comm.,* vol. 175, p. 250, 2006.

[566] D. Spong, B. Carreras and C. Hedrick, *Phys. Plasmas,* vol. 1, p. 1503, 1994.

[567] G. W. Bowden, A. Konies and M. Hole et al., "Comparison of methods for numerical calculation of continuum damping," *Phys. Plasmas,* 2014 (submitted).

[568] A. Konies, A. Mishchenko and R. Hatzky, in *Theory of Fusion Plasmas*, ed. X. Garbet, O. Sauter, E. Sindoni (AIP, New York, 2008), vol. 1069, p. 133.

[569] A. Mishchenko, A. Konies and R. Hatzky, *Phys. Plasmas,* vol. 16, p. 082105, 2009.

[570] R. Kleiber, in *Theory of Fusion Plasmas*, ed. X. Garbet, O. Sauter, E. Sindoni (AIP New York, 2006) vol. 871, p. 136.

[571] W. Cooper, J. Graves, S. Brunner and et.al., *Plasma Phys. Control. Fusioin,* vol. 53, p. 024001, 2011.

[572] J. Candy, D. Borba, H. Berk and et.al., *Phys. Plasmas,* vol. 4, p. 2597, 1997.

[573] R. Aymar, V. Chuyanov, M. Huguet and et.al., *Nucl. Fusion,* vol. 41, p. 1301, 2001.

[574] F. Zaitsev, A. Gondhalekar, T. Johnson and et.al., *Plasma Phys. Control. Fusion,* vol. 49, p. 1747, 2007.

[575] V. Goloborod'ko, S. Reznik and V. Yavorskij, *Nucl. Fusion,* vol. 37, p. 771, 1997.

[576] N. Gorelenkov, *Fiz. Plasmy [Sov. J. Plasma Phys., vol.18, p. 289, 1992],* vol. 18, p. 555, 1992.

[577] N. Gorelenkov and S. Sharapov, *Phys. Scr. ,* vol. 45, p. 163, 1991.

[578] G. Fu, C. Cheng and K. Wong, *Phys. Fluids B,* vol. 5, p. 4040, 1993.

[579] Y. Chen, S. Park, J. Lang and et.al., *Phys. Plasma,* vol. 17, p. 102504, 2010.

[580] G. Vlad, S. Briguglio, G. Fogaccia and et.al., *Nucl. Fusion,* vol. 46, p. 1, 2006.

[581] R. Miller, M. Chu, J. Greene and et.al., *Phys. Plasmas,* vol. 5, p. 973, 1998.

[582] I. Chapman, *Plasma Phys. Control. Fusion,* vol. 53, p. 013001, 2011.

[583] Y. Wu, C. Cheng and R. White, *Phys. Plasmas,* vol. 1, p. 3369, 1994.

[584] F. Porcelli, D. Boucher and M. Rosenbluth, *Plasma Phys. Control. Fusion,* vol. 38, p. 2163, 1996.

[585] G. Fu, W. Park, H. Strauss and et.al., *Phys. Plasmas,* vol. 13, p. 052517, 2006.

[586] B. Hu, R. Betti and J. Manickam, *Phys. Plasmas,* vol. 13, p. 112505, 2006.

[587] I. Chapman, S. Pinches, J. Graves and et.al., *Plasma Phys. Control. Fusion,* vol. 49, p. B385, 2007.

[588] "ITER Final Design Report, Cost Review and Safety Analysis (FDR) and Relevant Documents," ITER Documentation Series No. 14, IAEA, Vienna (1999).

[589] R. B. White, P. H. Rutherford, P. Colestock and M. N. Bussac, *Phys. Rev. Lett.,* vol. 60, p. 2038, 1988.

[590] J. Wesson, *Plasma Phys. Control. Fusion,* vol. 28, p. 243, 1986.

[591] E. Lazarus, F. Waelbroeck, T. Luce and et.al., *Plasma Phys. Control. Fusion,* vol. 48, p. L65, 2006.

[592] W. Stacey, *Fusion Sci. Technol. ,* vol. 52, p. 30, 2007.

[593] H. Furth, M. Rosebluth and P. Rutherford, *Phys. Fluids,* vol. 13, p. 3020, 1970.

[594] S. Putvinskii, *Sov. J. Plasma Phys. ,* vol. 14, p. 754, 1988.

[595] Y. Kolesnichenko, V. Lutsenko and S. Reznik, *Nucl. Fusion,* vol. 31, p. 1479, 1991.

[596] D. Anderson, M. Lisak and Y. Kolesnichenko, *Plasma Phys. Control. Fusion,* vol. 33, p. 455, 1991.

[597] F. Engelmann, *Plasma Phys. Control. Fusion,* vol. 34, p. 881, 1992.

[598] S. Haney, L. Perkins, J. Mandrekas and et.al., *Fusion Technol. ,* vol. 18, p. 609, 1990.

[599] J. Mandrekas, W. Stacey and H. He, *Fusion Technol.,* vol. 19, p. 1307, 1991.

[600] Y. Kolesnichenko, V. Lutsenko and S. Reznik, *Fusion Technol.,* vol. 25, p. 84, 1994.

[601] H. Burbaumer, G. Kamelander, D. Sigmar and et.al., *Fusion Sci. Technol.,* vol. 35, p. 280, 1999.

[602] H. Burbaumer and G. Kamelander, *Fusion Sci. Technol. ,* vol. 37, p. 131, 2000.

[603] E. Rebhan and U. Vieth, *Nucl. Fusion,* vol. 37, p. 251, 1997.

[604] G. Van Oost and E. Rebhan, *Trans. Fusion Sci. Technol.,* vol. 53, p. 16, 2008.

[605] P. N. Yushmanov, "Scalings for tokamak energy confinement," *Nucl. Fusion,* vol. 30, pp. 1999-2006, 1990.

[606] E. Doyle, W. Houlberg, Y. Kamada and et.al., *Nucl. Fusion,* vol. 47, p. 518, 2007.

[607] V. Mukhovatov, M. Shimada, K. Lackner and et.al., *Nucl. Fusion,* vol. 47, p. S18, 2007.

[608] N. Gorelenkov and R. White, *Plasma Phys. Control. Fusion,* vol. 55, p. 015007, 2013.

[609] N. Gorelenkov, Y. Chen and R. White, *Phys. Plasmas,* vol. 6, p. 629, 1999.

[610] H. Berk, B. Breizman and M. Pekker, *Plasma Phys. Rep. ,* vol. 23, p. 778, 1997.

[611] W. A. Cooper, J. P. Graves and O. Sauter, *Nucl. Fusion,* vol. 51, p. 072002, 2011.

[612] X. D. Du, K. Toi and S. Ohdachi et al., "First Observation of Fishbone-like Modes Driven by Helical-Ripple Trapped Fast Ions on LHD," 13th IAEA Technical Meeting on Energetic Particles in Magnetic Confinement Systems, 2013, Beijing.

The Princeton Plasma Physics Laboratory is operated
by Princeton University under contract
with the U.S. Department of Energy.

Information Services
Princeton Plasma Physics Laboratory
P.O. Box 451
Princeton, NJ 08543

Phone: 609-243-2245
Fax: 609-243-2751
e-mail: pppl_info@pppl.gov
Internet Address: http://www.pppl.gov